universität wien

DISSERTATION / DOCTORAL THESIS

Titel der Dissertation /Title of the Doctoral Thesis

Towards automated atom manipulation in the scanning transmission electron microscope

verfasst von / submitted by

Dipl.-Ing. Andreas Postl, BSc

angestrebter akademischer Grad / in partial fulfilment of the requirements for the degree of

Doktor der Naturwissenschaften (Dr. rer. nat.)

Wien, 2022 / Vienna 2022

Studienkennzahl lt. Studienblatt / degree programme code as it appears on the student record sheet:	A 796 605 411
Dissertationsgebiet lt. Studienblatt / field of study as it appears on the student record sheet:	Physik
Betreut von / Supervisor:	Assoz. Prof. Dr. Toma Susi

„Aus dem Durcheinander findet sich Einfachheit, aus der Uneinigkeit entwickelt sich Harmonie, inmitten der Schwierigkeit liegt die Gelegenheit.“ - Out of clutter comes simplicity, from discord find harmony, in the midst of difficulty lies opportunity.

(Albert Einstein)

Acknowledgements

Funding by the European Research Council (ERC) Grant No. 756277-ATMEN is gratefully acknowledged. I cordially thank the Vienna Doctoral School in Physics (VDS-P) for providing additional cost coverage through their mobility fellowship.

Furthermore, I thank the University of Vienna and its institutions for offering a great variety of seminars and workshops on various topics. The soft skills I acquired from these furthered my personal development as well as my professional career.

My sincere thanks go to Assoz. Prof. Dr. Toma Susi, my supervisor and principal investigator of the ATMEN[1] project, to Univ.-Prof. Dr. Jani Kotakoski, the speaker of the Physics of Nanostructured Materials group at the Faculty of Physics, and to Univ.-Prof. Dr. Christoph Dellago, my mentor on the part of the VDS-P.

I express my cordial thanks to all colleagues who supported me and my work in any regard, and to all internal as well as external collaborators, contributors, and supporters. In the hope of not forgetting anyone, I thank: Pit Hilgert, Kimmo Mustonen, Christoph Hofer, Thuy An Bui, Mukesh Tripathi, Alexander Markevich, Georg Zagler, Alexandru Chirita, Somar Dibeh, Daniel Imrich, Andreas Mittelberger, Cong Su, Manuel Längle, Stefan Noisternig, Makoto Schreiber, Clemens Mangler, Ursula Ludacka, and Jacob Madsen.

[1] Atomic precision materials engineering, https://cordis.europa.eu/project/rcn/212060/factsheet/en.

Abstract

The two-dimensional material graphene is being intensively studied due to its unique properties. Exploration of its potential for novel applications appears to be far from complete, with defect engineering being one promising avenue for tailoring its properties. Not only can aberration-corrected scanning transmission electron microscopy (STEM) image graphene, but the focused electron beam can also be used to create defects and even manipulate individual substitutional impurities with atomic precision.

In this work, both graphene as well as its impurities, most notably silicon, are investigated using STEM. First, the temperature-dependent electron knock-on cross section of pristine graphene was measured. The quantification of the observed radiation hardness at elevated temperature led to an experimental estimate of the carbon adatom migration barrier on graphene. Second, the cross sections for electron-beam induced dynamics associated with silicon and phosphorus dopants were measured. Previous and the new experimental data for silicon were used to discuss in detail the success probability for single-atom manipulation of silicon substitutionals. In addition, two different experimental approaches for the implantation of aluminum into graphene were evaluated.

Finally, the controlled single-atom manipulation of impurity atoms in graphene was extended toward automation. While the degree of control over more than two silicon atoms could not be improved, a software application capable of performing autonomous manipulation of multiple impurities was developed and successfully deployed. This involved implementing a convolutional neural network to recognize the atomic structure in STEM images, an algorithm to determine the shortest path for manipulating multiple impurity atoms to a pattern, and automatic positioning of the electron probe to irradiate the required sites.

Although sample quality and undesirable chemical interactions continue to impede progress toward multi-atom structures, this work lays the basis for scaling up the technique of atom manipulation in the scanning transmission electron microscope.

Zusammenfassung

Das zweidimensionale Material Graphen wird aufgrund seiner einzigartigen Eigenschaften intensiv untersucht. Die Erforschung seines Potenzials für neuartige Anwendungen scheint noch lange nicht abgeschlossen zu sein, nicht zuletzt, da Defect Engineering eine vielversprechende Methode ist, um seine Materialeigenschaften anzupassen. Mithilfe aberrationskorrigierter Rastertransmissionselektronenmikroskopie (STEM) kann Graphen nicht nur abgebildet werden. Vielmehr kann der fokussierte Elektronenstrahl auch zur Erzeugung von Defekten und sogar zur Manipulation einzelner substitutioneller Fremdatome mit atomarer Präzision verwendet werden.

In dieser Arbeit werden Graphen und seine Verunreinigungen, allen voran Silizium, mittels STEM untersucht. Zunächst wurde der temperaturabhängige Wirkungsquerschnitt für Stöße von hochenergetischen Eletronen mit Gitteratomen gemessen, die zur Entfernung letzterer aus makellosem Graphen führen. Die Quantifizierung der beobachteten Strahlungshärte bei erhöhter Temperatur konnte zur experimentellen Abschätzung der Migrationsbarriere für Kohlenstoffatome auf Graphen genutzt werden. Zweitens wurden die Wirkungsquerschnitte für Elektronstahl-induzierte Dynamiken in Zusammenhang mit Silizium- und Phosphordotanden gemessen. Frühere und die neuen Daten für Silizium wurden verwendet, um die Erfolgswahrscheinlichkeit für die Manipulation einzelner Siliziumatome ausführlich zu diskutieren. Außerdem wurden zwei verschiedene experimentelle Ansätze für die Implantation von Aluminium in Graphen bewertet.

Zudem wurde die kontrollierte Manipulation einzelner Fremdatome in Richtung Automatisierung erweitert. Während der Grad der Kontrolle über mehr als zwei Siliziumatome nicht verbessert werden konnte, wurde jedoch eine Softwareanwendung entwickelt und erfolgreich eingesetzt, die die Manipulation mehrerer individueller Substitutionsatome eigenständig durchführt. Dazu wurden ein Convolutional Neural Network zur Erkennung atomarer Strukturen in STEM-Bildern, ein Algorithmus zur Ermittlung des kürzesten Weges für die Manipulation von mehreren Fremdatomen zu einem Muster sowie die automatische Positionierung des Elektronenstrahls implementiert.

Obgleich Probenqualität und unerwünschte chemische Wechselwirkungen den Fortschritt hinsichtlich der Erzeugung von Strukturen mit mehreren Atomen weiterhin behindern, legt diese Arbeit den Grundstein für die Ausweitung der Atommanipulation im Rastertransmissionselektronenmikroskop.

Contents

List of Tables xv

List of Figures xv

Glossary of Abbreviations and Acronyms xix

1 Introduction 1
- 1.1 Scanning transmission electron microscopy . . . 2
  - 1.1.1 Annular dark field image contrast . . . 3
  - 1.1.2 Electron-probe shape . . . 4
  - 1.1.3 STEM as a nano-engineering tool . . . 4
- 1.2 Density functional theory . . . 4
- 1.3 Point defects in graphene . . . 5
  - 1.3.1 Stone–Wales defect . . . 5
  - 1.3.2 Single vacancy . . . 6
  - 1.3.3 Multivacancy . . . 6
  - 1.3.4 Substitutional impurities . . . 7
    - 1.3.4.1 Two-step substitution of carbon . . . 7
  - 1.3.5 Carbon adatoms . . . 8
- 1.4 Diffusion in solids . . . 8
  - 1.4.1 Surface diffusion of carbon adatoms on graphene . . . 9
    - 1.4.1.1 Healing of vacancies by recombination with carbon adatoms . . . 9
  - 1.4.2 Vacancy diffusion in graphene . . . 10
- 1.5 Electron-beam induced irradiation effects in graphene . . . 10
  - 1.5.1 Knock-on displacement of a carbon lattice atom . . . 11
  - 1.5.2 X–C bond inversion in graphene . . . 13
  - 1.5.3 Stone–Wales transformation involving an impurity atom . . . 14
  - 1.5.4 Knock-on displacement of a dopant or replacement by carbon . . . 14
- 1.6 Single-atom manipulation in graphene . . . 15
  - 1.6.1 Target impurities . . . 15
  - 1.6.2 Controlled single-atom manipulation . . . 17
    - 1.6.2.1 Non-disruptive versus terminating processes . . . 18

2 Methods 19
- 2.1 Instrumentation . . . 19
  - 2.1.1 Nion UltraSTEM 100 . . . 19
    - 2.1.1.1 Electron energy-loss spectroscopy . . . 20
  - 2.1.2 UHV system . . . 22
  - 2.1.3 In situ and in UHV devices for sample alteration . . . 22

2.2 Preparation of graphene samples . . . 24
2.2.1 Increasing the density of substitutional impurities . . . 24
2.2.2 In situ sample cleaning . . . 25
2.2.2.1 Laser cleaning parameters . . . 25
2.3 Characterization of the electron beam . . . 26
2.3.1 Calibration of the beam current . . . 26
2.3.2 Reconstruction of the probe shape . . . 27
2.4 Cross sections of atom displacements . . . 27
2.4.1 Experimental measurements . . . 27
2.4.1.1 Signal-to-noise ratio and perception limit . . . 28
2.4.1.2 ROI and choosing the optimal scan parameters . . . 29
2.4.1.3 Data acquisition . . . 31
2.4.1.4 Poisson analysis . . . 33
2.4.2 Theoretical model for the knock-on displacement cross section of pristine graphene . . . 33
2.4.2.1 Generalization to other elastic effects with threshold energies . . . 34
2.4.2.2 Shortcomings . . . 35
2.5 Calculation of the carbon adatom migration barrier on graphene . . . 35
2.6 Regression algorithms and error propagation . . . 35
2.6.1 Propagation of uncertainties and random errors . . . 36
2.7 Developed software packages . . . 38
2.7.1 Image recording . . . 38
2.7.2 Live image filtering . . . 39
2.7.3 Automated single-atom manipulation . . . 39
2.7.3.1 Structure recognition . . . 40
2.7.3.2 Bond detection . . . 40
2.7.3.3 Structural pathfinding . . . 40
2.7.3.4 ADF detector feedback . . . 44
2.7.3.5 Microscope control . . . 44
2.7.3.6 Systems integration . . . 45

3 Results and discussion **47**
3.1 Characterization of the electron beam . . . 47
3.1.1 Calibration data for the beam current . . . 47
3.1.2 Electron-probe shape . . . 48
3.2 Electron knock-on damage of pristine graphene . . . 50
3.2.1 Temperature-dependent knock-on cross section at 90 keV . . . 50
3.2.2 Refinement of the displacement threshold energy and the root mean square velocity of the nuclei . . . 50
3.2.3 Vacancy healing by recombination with diffusing carbon adatoms . . . 51
3.3 Electron-beam induced atom displacements at impurities . . . 58
3.3.1 Voltage-dependent cross-section measurement for Si@SV . . . 58
3.3.1.1 Success probability for single-atom manipulation of Si@SV . . . 60
3.3.2 Temperature-dependent cross-section measurement for Si@SV and P@SV . . . 65
3.4 Evaluation of implantation experiments . . . 69
3.4.1 Al ion implantation . . . 69
3.4.2 Al and Si incorporation after Ar plasma treatment . . . 70

3.5 High-control automated single-atom manipulation to patterns 70
3.5.1 Automation software 70
3.5.2 Experimental proceedings 73

4 Conclusion **75**
4.1 Pitfalls and experimental difficulties 76
4.2 Outlook 77

Outputs **79**
First-authored journal article publications 79
Other publications 79
Software 80

Bibliography **81**

Appendix **95**

List of Tables

2.1 Atom Manipulator: Overview of tasks, modules, and contributors. 39

3.1 Parameters and their standard errors for all beam-current calibrations. 48
3.2 Fit values for the reconstruction model of the electron-probe shape. 48
3.3 Pristine graphene: Temperature-dependent cross section for knock-on damage at an electron kinetic energy of 90 keV. 51
3.4 Pristine graphene: Voltage-dependent cross section for knock-on damage at ambient temperature. 51
3.5 Observed cross sections for different electron kinetic energies and beam-induced processes involving a Si@SV impurity, at ambient temperature. 61
3.6 Suitability of different electron kinetic energies E_e for single-atom manipulation of Si@SV: expectation value $E(M)$ for different electron energies. 64
3.7 Observed cross sections for different temperatures and beam-induced processes involving Si@SV and P@SV impurities, at an electron kinetic energy of 60 keV. 68

List of Figures

1.1 Raw and Gaussian-blurred MAADF-STEM image of a strained defective graphene structure with a Si atom incorporated in the 2D lattice. 3
1.2 Atomic structure of a reconstructed SW(55-77) defect in graphene. 5
1.3 Atomic structure of a reconstructed single vacancy in graphene. 6
1.4 Atomic structure of a reconstructed double vacancy defect V_2(5-8-5) in graphene. 7
1.5 The carbon adatom adsorption sites and the adatom migration path. 8
1.6 Maximum transferable energy as a function of the electron kinetic energy for a ^{12}C atom moving at different out-of-plane velocities. 12
1.7 Molecular dynamics simulation after a kinetic energy transfer of 15 eV to a C neighbor of a Si@SV impurity in graphene. 13
1.8 MAADF-STEM images of an experimentally observed SW transformation involving a Si@SV impurity. 14
1.9 Kinetic energy ranges – transferred to the PKA – that lead to the direct exchange of the positions between a three-coordinated X@SV impurity and the PKA, compared for Al, Si, and P. 16
1.10 Schematics of an atomic pattern comprising substitutional atoms in graphene. . . 17

2.1 Photo and schematics of the core components of the Nion UltraSTEM 100 installed in Vienna. . . . 20
2.2 Electron energy-loss spectra of Si impurities in graphene. . . . 21
2.3 Schematics of the UHV system run by the Physics of Nanostructured Materials group in Vienna. . . . 23
2.4 Typical contamination coverage of suspended monolayer graphene and effect of laser cleaning (MAADF-STEM images). . . . 26
2.5 Schematics of the regions of interest for different irradiation effects involving three-coordinated impurities in graphene. . . . 30
2.6 MAADF-STEM images of a graphene monolayer before and after electron KO damage ($E_e = 90$ keV). . . . 31
2.7 MAADF-STEM image of a graphene monolayer with holes created by 90 keV electron irradiation. . . . 32
2.8 Concept of a three-parametric coordinate system (κ, λ, η) for monolayer graphene. 41
2.9 Structural pathfinding: Resulting subpaths for manipulating multiple impurities to a given pattern. . . . 43
2.10 Structural pathfinding: Resolution of conflicting subpaths using different strategies. 45

3.1 Beam current as a function of the virtual objective aperture current at an acceleration voltage of 70 kV. . . . 49
3.2 Reconstructed beam-current density as a function of the radial distance to the beam center. . . . 49
3.3 Pristine graphene: Cross section for knock-on damage as a function of the incident electron kinetic energy at ambient temperature. . . . 52
3.4 Vacancy healing rate as a function of the inverse temperature in semi-logarithmic representation (Arrhenius plot). . . . 54
3.5 Schematic representation of a graphene monolayer with a single vacancy caused by the electron probe's "leading" tail. . . . 56
3.6 Pristine graphene: Cross section for knock-on damage as a function of the temperature, at an electron kinetic energy of 90 keV. . . . 57
3.7 SiCEx: Observed cross section for the positional exchange between a Si@SV impurity and a neighboring C atom as a function of the electron kinetic energy, at ambient temperature. . . . 59
3.8 SiCKO: Observed cross section for the knock-on displacement of a C atom neighboring a Si@SV impurity as a function of the electron kinetic energy, at ambient temperature. . . . 59
3.9 SiRepC: Observed cross section for the beam-induced replacement of a Si@SV impurity by a C atom as a function of the electron kinetic energy, at ambient temperature. . . . 60
3.10 Suitability of different electron kinetic energies for single-atom manipulation of Si@SV: expectation value $E(M)$ as a function of the electron kinetic energy. . . . 63
3.11 Suitability of different electron kinetic energies for single-atom manipulation of Si@SV: complementary cumulative distribution function of M. . . . 64
3.12 SiCEx & PCEx: Observed cross section for the positional exchange between a Si@SV or P@SV impurity and a neighboring C atom as a function of the temperature, at an electron kinetic energy of 60 keV. . . . 65

3.13 SiCKO & PCKO: Observed cross section for the knock-on displacement of a C atom neighboring a Si@SV or P@SV impurity as a function of the temperature, at an electron kinetic energy of 60 keV. 66
3.14 SiRepC & PRepC: Observed cross section for the beam-induced replacement of a Si@SV or P@SV impurity by a C atom as a function of the temperature, at an electron kinetic energy of 60 keV. 67
3.15 MAADF-STEM images of graphene samples after Al ion implantation experiments. 69
3.16 Atom Manipulator: MAADF-STEM image series recorded during an automated single-atom manipulation experiment with two individual Si@SV impurities. . . . 71
3.17 Atom Manipulator: Infographics to give an overview of the functionalities. 72
3.18 Atom Manipulator: Infographics describing the two main operation modes. 72
3.19 Contamination coverage and non-manipulable Si dopants in suspended monolayer graphene (MAADF-STEM images). 73
3.20 Atomically resolved MAADF-STEM images of non-manipulable and manipulable Si impurities in suspended monolayer graphene. 74

Links to license legal codes

Creative Commons Attribution 3.0 Unported license (CC BY 3.0)
https://creativecommons.org/licenses/by/3.0/legalcode

Creative Commons Attribution 4.0 International license (CC BY 4.0)
https://creativecommons.org/licenses/by/4.0/legalcode

GNU General Public License, Version 3 (GPL-v3)
https://www.gnu.org/licenses/gpl-3.0.txt

Glossary of Abbreviations and Acronyms

2D	two-dimensional
ABF	annular bright field
ADF	annular dark field
API	application programming interface
CNT	carbon nanotube
CVD	chemical vapor deposition
DF	dark field
DFT	density functional theory
DFT-MD	density functional theory based molecular dynamics
DOS	density of states
DV	double vacancy
EDXS	energy-dispersive X-ray spectroscopy
EEL	electron energy loss
EELS	electron energy-loss spectroscopy
EMCCD	electron-multiplying charge-coupled device
FCNN	fully convolutional neural network
FEG	field emission gun
FFT	fast Fourier transform
FOV	field of view
FWHM	full width at half maximum
GUI	graphical user interface
HAADF	high-angle annular dark field
HRTEM	high-resolution transmission electron microscope/microscopy
KO	knock-on
LAP	linear assignment problem
LSQ	least squares
MAADF	medium-angle annular dark field
MD	molecular dynamics
NEB	nudged elastic band
ODR	orthogonal distance regression
P@DV	phosphorus (atom) in a double vacancy
P@SV	phosphorus (atom) in a single vacancy
PBE	Perdew-Burke-Ernzerhof (functional)
PKA	primary knock-on atom
ROI	region of interest
SC	semiconductor
Si@DV	silicon atom in a double vacancy
Si@SV	silicon atom in a single vacancy
SNR	signal-to-noise ratio
STM	scanning tunneling microscope/microscopy
STEM	scanning transmission electron microscope/microscopy
SV	single vacancy
SW	Stone(–Thrower)–Wales
TEM	transmission electron microscope/microscopy
TIFF	Tagged Image File Format
UC	unit cell
UHV	ultra-high vacuum
VOA	virtual objective aperture
X@DV	impurity atom (element X) in a double vacancy
X@SV	impurity atom (element X) in a single vacancy
ZLP	zero-loss peak

1 Introduction

In this thesis, electron irradiation effects on *graphene* are studied with scanning transmission electron microscopy (STEM). Conversely, the applicability of *STEM* as a nanoengineering tool at the atomic scale is investigated using graphene. I report on my contribution to various aspects of *"single-atom manipulation"*. Whilst certain knowledge of the basics of STEM and particle physics is assumed, the present chapter aims to make the methods and the results covered in this work fully comprehensible for physicists and at least partially explicable for technicians and natural scientists.

Graphene, a two-dimensional (2D) allotrope of carbon, was first predicted in 1947 [1]. Its reproducible isolation from graphite did not occur until 60 years later [2]. It is a monolayer of carbon atoms arranged in a honeycomb structure and, thus, only one atom thick. Numerous other superlative properties are attributed to it as well, e.g. in terms of stiffness, tear resistance [3], and electrical [4, 5] as well as heat conductivity [6].

Techniques classified as scanning probe microscopy have become the predominant engineering tools for fabrication and investigation at the nanoscale [7]. Since the late 1980s, the atomically sharp tips of scanning tunneling microscopes have been used to move atoms over clean metal surfaces held at cryogenic temperatures [8]. A recent highlight in 2016 was the use of scanning tunneling microscopy to manipulate individual surface vacancies and realize "a kilobyte rewritable atomic memory" [9] that is stable at temperatures up to 77 K.

With the invention of the probe-corrected STEM [10, 11], Richard P. Feynman's vision of an electron microscope one hundred times better, when compared to 1959, has been made reality [12]. While scientists have been able to see single atoms in STEM images since 1970 [13, 14], it is now possible to visualize each atom or atomic column in most materials. The highest reported resolution is around 50 pm [15, 16].

In 2014, it was discovered that the scattering of energetic imaging electrons can cause three-coordinated Si impurities to move through a monolayer of graphene. By purposefully directing the Ångström-sized electron probe, that movement can be controlled with atomic precision [17, 18]. Our research team has focused on investigating the possibilities and limitations of this method, henceforth referred to as single-atom manipulation. Despite facing up challenges on the edge of scientific knowledge and the art of engineering, continuous progress has been achieved.

STEM has thus emerged as a new tool for the direct assembly of nanostructures with the ability to manipulate single atoms. Rearrangements in the atomic structure are possible if the transferable kinetic energy is comparable to the strength of covalent bonds [17]. The advantage over scanning tunneling microscopy techniques is the stability of configurations at room temperature. Experiments have revealed the potential for atomically precise manipulation of Al, Si, and P impurities in a graphene lattice using the Å-sized focused electron beam [18–21].

One of my goals was, by using substitutional impurity atoms as an "ink" and the 2D material graphene as "paper", to develop electron microscopy software that is capable of controlling a STEM and, by doing so, writing arbitrary pre-defined patterns. To make that aim comprehensible, details relevant to my research will be mentioned in the present chapter. This will include an opening description of the technique STEM, a brief introduction to density functional theory (DFT), an overview of point defects in graphene, and an outline of diffusion in solids, examining surface diffusion on graphene in more detail. Then, electron-beam induced irradiation effects in graphene will be described. Last, basic information related to my experimental work on single-atom manipulation will be given.

1.1 Scanning transmission electron microscopy

The present section is a summary of STEM aspects relevant to this thesis, based on ref. [22]. I will give a brief explanation of why an electron microscope instead of a visible-light microscope needs to be used for the imaging of graphene and other 2D materials. In addition, I will explain how this type of microscope works and which detectors are most commonly used for material analysis with STEM.

While the wavelength of visible light ranges from roughly 380 to 740 nm, electrons accelerated by a potential of a few kV have a wavelength in the 10 pm regime. According to generally applicable[1] resolution limits (Abbe diffraction limit, Rayleigh criterion), this allows resolving a much smaller distance, i.e. to distinguish features on a much smaller length scale. While the best resolution in visible-light microscopy is usually about 200 nm, the resolution in electron microscopy is limited by the aberrations of the electromagnetic lenses.

Electrons are emitted by a gun, which is driven either electrostatically or thermally, and then accelerated by an electrostatic potential. The charged particles then get focused by electromagnetic lenses. In aberration-corrected instruments, a series of multipole magnets is used to correct the lens errors. After passing this so-called probe corrector, the electrons are deviated perpendicular to the direction of their momentum by so-called scan coils. The beam of electrons is rastered across a region of the sample, called the field of view (FOV). In addition to the condenser lenses and the aberration corrector, the lens system also consists of an objective lens before the sample and projector lenses after the sample.

At and inside of the sample, the beam electrons interact with the material and scatter. A part of them is transmitted through the sample, deviated by the projector lens, and enters the detector system. In a modern STEM, there are commonly multiple annular or circular semiconductor (SC) detectors present. If an electron hits such a detector, it causes a certain number of electron-hole pairs. The resulting voltage can be measured and gives a certain intensity per pixel, synchronized with the scan coils. Depending on the semi-angle of collection, we call the detector an annular bright field (ABF) or medium-/high-angle annular dark field (MAADF/HAADF) detector. The SC detectors generally have high capacitance to not be highly responsive to fast changes in the intensity of the signal. Their bandwidth is in the range of 100 kHz. In addition to SC detectors, a magnetic prism as part of an electron energy-loss spectroscopy (EELS) setup is often available. In EELS, the amount of energy an imaging electron loses due to an inelastic scattering process is measured, from which the chemical compounds present can be determined.

[1] This applies to visible-light microscopy as well as to electron microscopy.

1.1.1 Annular dark field image contrast

For dark field (DF) imaging with STEM, usually an annular axis-on-axis[2] semiconductor detector is used. An individual instrument may be equipped with multiple such annular dark field (ADF) detectors. They are located behind the specimen in the direction of the beam propagation, which is typically upwards for dedicated STEMs, and collect electrons scattered in the angular range[3] of ca. 50 to 200 mrad with respect to the optical axis [22, 23], depending on the acceleration voltage.

The ADF-STEM image contrast is due to a different number of electrons hitting the detector for different sample regions. It mainly arises from incoherent scattering – intense diffraction peaks satisfying the Bragg condition [24] are avoided because of the angular range – and is predominantly affected by differences in the mass density and the thickness of the sample [22]. In this mass-thickness contrast, elements with a greater atomic number and thicker specimen regions appear brighter.

The contrast due to differences in mass density becomes particularly important when imaging suspended monolayers of 2D materials. In the atomic limit, this is determined by the atomic number Z and is therefore commonly called *Z-contrast*. Specifically for ADF-STEM images of graphene, this is why substitutional impurities can be distinguished from ${}_6\mathrm{C}$. An example of a MAADF-STEM image of defective graphene with a substitutional Si impurity is illustrated in fig. 1.1.

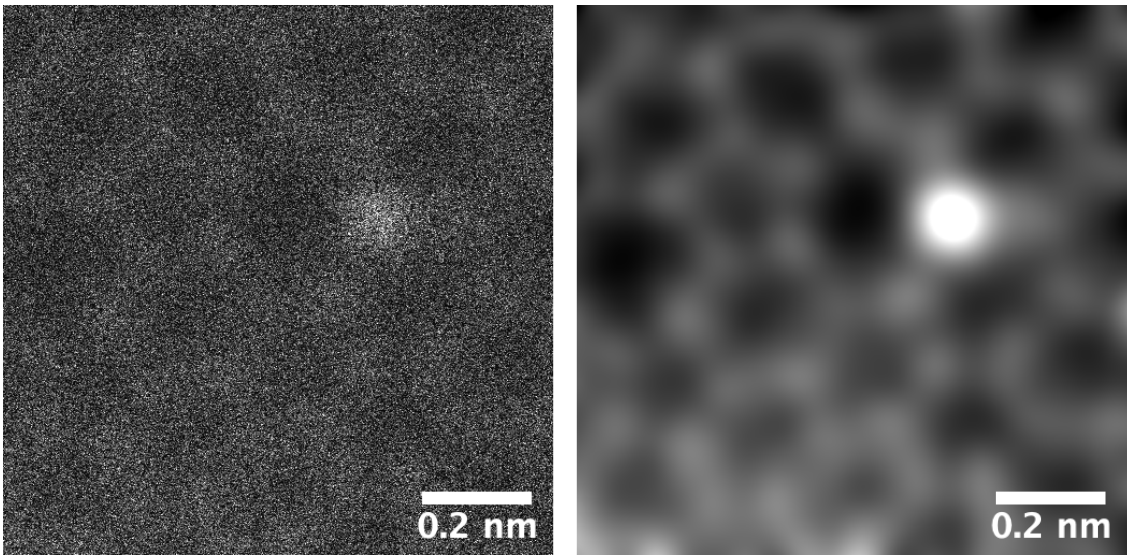

Figure 1.1: Raw (left) and Gaussian-blurred (right) MAADF-STEM image of a strained defective graphene structure with a Si atom incorporated in the 2D lattice. The impurity appears brighter than the surrounding C atoms. The FOV was ca. 1×1 nm^2, the pixel dwell time was 8 µs, and the number of pixels was 512×512 px.

[2]The detector axis and the optical axis of the microscope are coincident.
[3]Technically, the semi-angle of collection.

1.1.2 Electron-probe shape

The electron-probe shape of the STEM determines how the electron dose is distributed in the two spatial dimensions perpendicular to the axis of the beam cone. In electron-beam manipulation, the irradiation must be precisely directed at single atoms. The spatial distribution of the dose is thus very important for a good estimate of the count of electrons impinging on each atom. The electron-probe shape (later referred to as beam intensity profile) is determined by the electron-optical instrumentation, i.e. lenses and apertures [22]. In 2014, the full width at half maximum of the Nion microscope which we are using was estimated to be 1.4 Å, although it was not clear how much this varies over time [25]. Approximating the shape by a single Gaussian- or Lorentzian-shaped curve, or by a superposition of such yields precise analytical probe functions [26–29].

1.1.3 STEM as a nano-engineering tool

This section is based on original work in Publication 1 [30].

Both STEM and conventional transmission electron microscopy (TEM) allow the exposure of specimens to highly energetic electron irradiation. The typical acceleration voltage in modern instruments ranges up to ca. 200–300 keV. The irradiation effects caused by the electron-material interaction can be imaged in-situ with atomic resolution in spatial terms and with a time resolution determined by the exposure time in TEM and by the frame time in STEM, respectively. During the last decade, electron irradiation has been used to sculpt materials at the nanoscale [31–35], to induce phase transitions [36, 37], change the local structure of materials [38–41], and even induce the positional exchange between individual atoms [17, 18, 20, 42, 43]. The application of the last-mentioned method to graphene is a main topic of this thesis. It will be referred to as "single-atom manipulation" and be explicitly discussed in section 1.6.

1.2 Density functional theory

DFT is a method to describe many-body systems and calculate their properties. In the context of quantum mechanical modeling, it is based on the inhomogeneous distribution of the electron density [44] and used to calculate e.g. energies in atoms, molecules, and solids, though the applications of DFT are much more far-reaching. DFT methods offer broad variations and are often combined with other methods. An example of the latter is molecular dynamics (MD), for which forces calculated based on DFT potentials can be used (DFT-MD).

When numerically solving the Schrödinger equation [45], using DFT drastically reduces the computational effort, because it eliminates the necessity to solve the complete equation of the many-body system. This makes DFT calculations with many more electrons possible when compared to more exact methods. The Born–Oppenheimer approximation [46] (the nuclei are seen as fixed due to the larger time scale of their movement when compared to the movement of electrons) is inherently assumed. The total energy of the system is formally written as a sum of the kinetic energies of the electrons, the electron-nuclei interactions, and the electron-electron interactions. According to the Hohenberg–Kohn theorems [44], the electron density (given by the wavefunction as a function of the spatial coordinates) determines the ground state of a system. DFT calculations seek to iteratively minimize the total energy functional of the electron density, by optimizing the latter.

There are different approaches to modeling the energy functional. The ansatz according to Kohn and Sham [47], which splits the minimization problem into single-electron Schrödinger equations, has become widely accepted. The Kohn–Sham formalism shifts the many-electron problem to the exchange-correlation energy, for which no explicit derivation is possible. The exact form of the exchange-correlation functional is not known (except for the free electron gas). A variety of approximations for it exists, and one of the most commonly used functionals was introduced by Perdew, Burke, and Ernzerhof (PBE) [48].

1.3 Point defects in graphene

In material sciences and especially in nanotechnology, deviations from perfection are common research foci, because it is crucial to understand their effect on the material properties. As for graphene, structural, topological, intrinsic, and substitutional defects have been extensively studied [49–52]. The present section gives a brief overview of point defects (0-dimensional defects). Defects of higher dimensions are not dealt with in this thesis: whenever those were observed during an experiment, the FOV was re-positioned to a sample region that was neither significantly strained, nor notably bent, and free from dislocations, grain boundaries, and edges.

Formation energy of defects
DFT-based values for defect formation energies E_f, some of which are mentioned below, are typically calculated according to [53, 54]

$$E_\mathrm{f} = E_\mathrm{d} - E_\mathrm{bulk} - n\mu_\mathrm{C}, \tag{1.1}$$

where E_d is the total energy of the defective structure, E_bulk is the total energy of the pristine structure, μ_C is the chemical potential of C, and n is the number of added ($n > 0$) or removed ($n < 0$) C atoms. Thereby, the chemical potential is taken as $\mu_\mathrm{C} = E_\mathrm{bulk}/N_\mathrm{C}$, where N_C is the number of atoms in the pristine structure. An alternative definition of E_f in terms of energies assigned to the bonds of the defective and the pristine structure is given in ref. [55].

1.3.1 Stone–Wales defect

The Stones-Wales defect [56], which is denoted SW(55-77) and illustrated in fig. 1.2, is intrinsic, meaning that no heteroatoms are present, and topological, meaning it changes the local symmetry

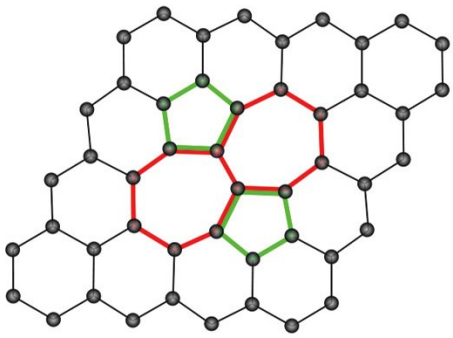

Figure 1.2: Atomic structure of a reconstructed SW(55-77) defect in graphene, obtained from DFT calculations. (Adapted with permission from ref. [50]. Copyright 2011 American Chemical Society.)

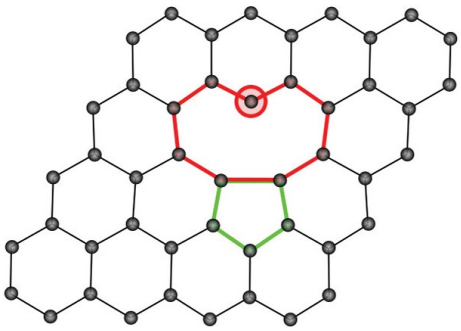

Figure 1.3: Atomic structure of a reconstructed single vacancy in graphene, obtained from DFT calculations. The atom encircled in red has a dangling bond that remains due to geometrical reasons. (Adapted with permission from ref. [50]. Copyright 2011 American Chemical Society.)

of the lattice. The number of lattice atoms is conserved upon formation. By rotating a C-C bond by 90° with respect to its midpoint, two pentagons and two heptagons are formed. The formation energy of this defect is ca. 5 eV [53, 57], though if the formation involves the above-mentioned bond rotation, a kinetic barrier of ca. 10 eV needs to be overcome [53]. Stone–Wales transformations in graphene are frequently observed in high-resolution transmission electron microscopy (HRTEM) [58] and STEM [59] at energies at and above 60 keV, hence the energy to overcome the transition barrier can be provided by the electron beam.

1.3.2 Single vacancy

A missing lattice atom is a structural and intrinsic point defect, and it is the simplest defect in any material. In graphene, a single vacancy (SV) reconstructs through a Jahn-Teller distortion [60]: two of the three dangling bonds saturate by forming a bond between two former neighbors of the missing atom, while one bond remains unsaturated [50]. The structure surrounding the single vacancy (SV, or MV for monovacancy) contains a pentagon and a nonagon instead of two hexagons and the notation of the defect is, thus, V_1(5-9). The DFT-calculated atomic structure is depicted in fig. 1.3. The defect formation energy is ca. 7.5 eV [53, 61, 62].

1.3.3 Multivacancy

In a double vacancy or divacancy (DV), two neighboring atoms are missing. Since no non-carbon atoms are involved, it is an intrinsic defect. There are combined topological and structural as well as purely structural divacancies. In a fully reconstructed DV, which is depicted in fig. 1.4a and denoted V_2(5-8-5), all bonds are saturated and the surrounding structure contains two pentagons and one octagon instead of four hexagons. The DV formation energy is ca. 9 eV (4.5 eV per missing atom) [61, 62], which is why DVs are thermodynamically more favorable than SVs. Other appearances of a DV are omitted here for brevity, but they include additional bond rotations. The removal of more than two atoms leads to larger and more complex defect configurations (see e.g. [63]), an in-depth characterization of which is also beyond the scope of this work.

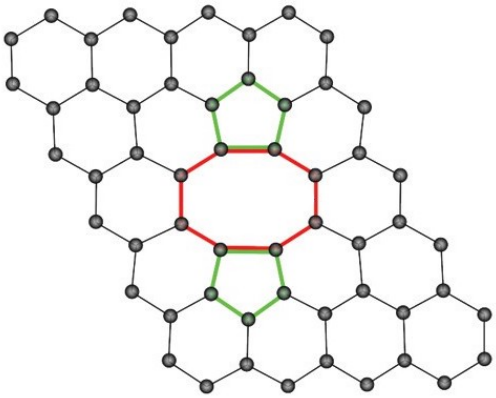

Figure 1.4: Atomic structure of a reconstructed double vacancy V_2(5-8-5) in graphene, obtained from DFT calculations. (Adapted with permission from ref. [50]. Copyright 2011 American Chemical Society.)

1.3.4 Substitutional impurities

Certain heteroatoms adopt a stable configuration if incorporated into the graphene lattice as substitutional impurities. They can substitute one or two C atom(s) in an SV or a DV, respectively. Si is the element that is observed most often when investigating free-standing monolayer graphene by STEM, since (hydro-)carbon contamination layers typically contain Si and due to its similar valence binding, it has a high affinity to bond with C. A substitutional Si impurity in a single vacancy (Si@SV) enters a three-coordinated configuration (thus also denoted as Si–C_3), whereas it is four-coordinated if in a double vacancy (Si@DV, or Si–C_4) [17]. Single Si impurities are of particular interest for this thesis because they can be moved through the graphene monolayer at atomic precision using the focused beam of a STEM.

Graphene doped with B and N has been extensively studied as well [64, 65], and ways for implanting the semi-metal Ge [66] and the transition metal Au [67] into graphene have been shown. However, Al [68] and P [69] impurities are, after Si, the most promising candidates for single-atom manipulation [21]. They bond in tetrahedral-like configurations with sp^2 and sp^3 character, and the impurity atom buckles out of the lattice plane. Please refer to section 1.6 for more details on single-atom manipulation in graphene.

Si atoms are almost always present on graphene samples (see e.g. [17, 18], and also according to my own experience). N atoms can sometimes be observed without intentional doping (see e.g. [68]). Any other atom has to purposefully be incorporated into the lattice.

1.3.4.1 Two-step substitution of carbon

The growth of doped graphene by CVD with heteroatom-containing precursors, for example $(HCN)_3$ [70], and ion implantation [21, 64, 66] into free-standing monolayers were considered feasible ways to dope graphene. In 2012, bombardment with Au and B atoms/ions has been used to create vacancies, which can be filled by different elements in a second step, showcased for Pt, Co, and In [71]. In 2017, a 100 keV electron probe was used to create vacancies in graphene, which were then filled with Si by irradiating the surrounding amorphous contamination [42]. Shortly afterward, single Si atoms were found within single-walled carbon nanotubes (SWCNTs)

as well as graphene after Ar^+ plasma irradiation treatment [72], which causes a high density of vacancies in the corresponding lattices [63]. The conclusion was that other impurities could also be incorporated that way if they could be brought near the vacancies created by the irradiation. This was successfully carried out in rapid succession for Al [68] and Au [67].

1.3.5 Carbon adatoms

In graphene, interstitial atoms do not exist, because a configuration with an additional atom at an in-plane position (e.g. in the center of a hexagon) is not stable. Instead of straining the material in two dimensions, additional atoms sit on one of the two surfaces outside of the lattice as adatoms. As depicted in fig. 1.5, the energetically favored position of a C adatom is on top of a carbon-carbon bond center (bridge site), where it has an adsorption energy of ca. 1.4 eV [73]. Please refer to section 1.4.1 for more details on the bonding and the dynamics of C adatoms on the surface of graphene.

1.4 Diffusion in solids

The present section is a brief introduction to relevant basics based on ref. [74]. However, the surface diffusion of carbon adatoms on graphene is discussed in more detail due to its major relevance for this thesis and original work in Publication I [30].

Diffusion (from Latin "diffundere": to spread out, to scatter) refers to the natural motion of particles such as atoms or molecules caused by a concentration or chemical potential gradient (chemical diffusion, intermediate to high coverage of diffusible species), or by spontaneous migration of particles in the absence of such a gradient (tracer diffusion, very low coverage of diffusible species) [74]. For the purpose of this work, we are solely interested in the tracer regime.

Random-walk diffusion kinetics
The following applies to self-diffusion (e.g. C adatoms on graphene) and hetero-diffusion (e.g. Si adatoms on graphene). In solids, the movement of a diffusing particle across larger areas or volumes is typically just a concatenation of jumping or tunneling processes from one adsorption site (in equilibrium, local potential energy minimum) to another one. During every individual migration step, the migration energy E_m has to be overcome by the particle. At non-cryogenic temperatures and spanning multiple classical migration mechanisms (see [74]), the temperature-dependence of the diffusion coefficient $D(T)$ (mean-square displacement per unit time) is found to follow the

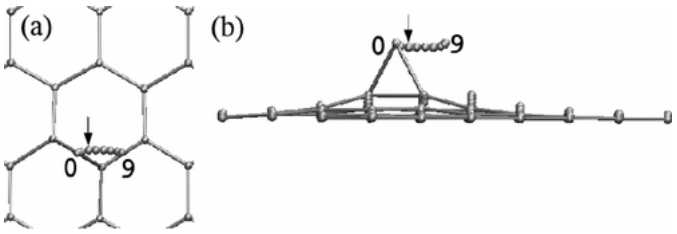

Figure 1.5: The carbon adatom adsorption sites (0 and 9) and the adatom migration path (0-9) in top (a) and side (b) view. (Reproduced with permission from ref. [73]. Copyright 2013 American Physical Society.)

semi-empirical Arrhenius equation [75]

$$D(T) = D_0 \exp\left(-\frac{E_\mathrm{m}}{k_\mathrm{B}T}\right), \tag{1.2}$$

where D_0 is the self-diffusion or hetero-diffusion coefficient at infinite temperature, E_m is the migration energy, k_B is the Boltzmann constant, and T is the temperature. Furthermore, $D(T)$ is proportional to the migration rate $\Gamma(T)$ (with the dimension of inverse time), which is characterized by an attempt frequency f_0 and the same thermodynamic factor:

$$\Gamma(T) = D(T)\frac{z}{d^2} = f_0 \exp\left(-\frac{E_\mathrm{m}}{k_\mathrm{B}T}\right), \tag{1.3}$$

where z is the number of neighboring adsorption sites the particle can hop to, and d is the spacing of the sites.

1.4.1 Surface diffusion of carbon adatoms on graphene

For this thesis, the diffusion of carbon adatoms is highly relevant in two respects. First, the recombination of diffusing carbon adatoms with vacancies explains the observed radiation hardness of graphene at elevated temperatures (as will be discussed in section 3.2), which has been reported before [76, 77]. Second, the replacement of a substitutional impurity in graphene by carbon also involves approaching carbon atoms (sections 3.3.1 and 3.3.2). Surface diffusion of non-carbon adatoms on graphene, although relevant for Si and Al substitution in graphene [68, 72] is not explicitly considered.

Carbon adatoms on the surface of graphene are widely agreed to diffuse exclusively via a basic hopping mechanism [50, 73, 78], in contrast to diffusion by atomic exchange[4] and tunneling diffusion [74]. Equations (1.2) and (1.3) apply to the surface diffusion of (ad)atoms, molecules, and clusters on the surface of graphene. Regarding carbon adatoms, DFT calculations show that their equilibrium position (adatom adsorption site) is between two carbon (lattice) atoms with a perpendicular distance to the lattice of 1.87 Å, forming a bridge-like structure (see fig. 1.5a). The adatom bonds with two lattice atoms and features an sp^2-like hybridization of the valence orbitals bonds, and the lattice atoms each present sp^2-sp^3 hybridization. As far as the hopping mechanism is concerned, the minimum energy adatom diffusion path, calculated in a static approximation using the nudged elastic band (NEB) method [79], is a low-curvature line that ranges from an adsorption site to one of the three adjacent ones. On its trajectory, the adatom slightly approaches both the center of the interstitial space and the lattice plane (see fig. 1.5). Literature values for the calculated carbon adatom migration barrier E_m lie between 0.40 and 0.47 eV [62, 73, 78, 80, 81], and the attempt frequency f_0 is usually assumed to be ca. 4×10^{12} s^{-1} (value for carbon interstitials in graphite) [82].

1.4.1.1 Healing of vacancies by recombination with carbon adatoms

Fundamentally important diffusion processes in some materials have been directly studied by (S)TEM [83–85]. The migration of carbon adatoms on the surface of graphene, though, is not accessible to direct observation. To measure how quickly they migrate, an experimental setup to

[4] A self- or hetero-diffusion mechanism involving the exchange between an adatom and an adjacent surface atom.

monitor secondary effects has to be contrived. One way to accomplish that is an experiment to quantify the vacancy healing rate as a function of the temperature, since the rate-limiting process for vacancy healing is presumably the hopping mechanism described above. This temperature-dependent mechanism is governed by the energy barrier for surface migration of carbon adatoms and can mathematically be described according to eq. (1.3).

Small vacancies and even larger holes up to 100 vacancies have been shown to heal under electron irradiation with a kinetic energy of 60 keV, even at ambient temperatures [77]. Provided that there is a source for carbon adatoms, a locally greater binding energy at vacancies in combination with random diffusion according to (1.3) explains that phenomenon: the values given above for E_m and f_0 result in a migration rate at ambient temperature of $\Gamma(300\ \mathrm{K}) \approx 8 \times 10^5\ \mathrm{s}^{-1}$. This yields a diffusion coefficient of $D(300\ \mathrm{K}) \approx 3 \times 10^3\ \mathrm{nm}^2\,\mathrm{s}^{-1}$, where $z = 4$ and $d = a_\mathrm{gra}/2$ have been used (with $a_\mathrm{gra} = 0.246$ nm being the lattice constant of graphene). Further, adatom migration may be enhanced under electron irradiation due to electrostatic interactions between the beam and adatoms [42, 77], but this has not been proven.

1.4.2 Vacancy diffusion in graphene

The migration of single vacancies in graphene is rarely observed at ambient temperature [86]. Literature values for the DFT-calculated migration barrier of an SV in graphene range from 0.56 to 1.4 eV [61, 62, 87]. According to eq. (1.3), this suggests a drastic increase in the migration rate at elevated temperatures above 100 °C. However, such an increase is not confirmed by our experiment at temperatures up to 800 °C, as we will see later in section 3.2.1.

1.5 Electron-beam induced irradiation effects in graphene

In electron microscopy, it is crucial to understand the interaction between probe electrons and the sample, both for image interpretation as well as material characterization. Beam-induced processes occur due to electron irradiation. Thus, a *cross section* can be assigned to each of them.

Electron irradiation effects on carbon nanostructures have been intensely studied during the past decade [50, 88, 89]. A detailed overview of 2D materials and state-of-the-art quantification methods was recently given by Susi, Kotakoski, and Meyer [90]. Graphene, which is a zero-gap semiconductor [4] with very high charge carrier mobility [91], is hardly damaged by secondary ionization effects, but mainly by elastic electron-nucleus interactions, which conserve kinetic energy and momentum. Electron-beam induced effects involving structural and topological changes at the atomic scale in graphene were of particular interest for this work. Recent advances in theoretical modeling have made it possible to quantitatively describe so-called knock-on damage due to elastic electron-nucleus collisions [90, 92, 93]. In section 1.5.1, the phenomenon of knock-on displacement is illuminated, followed by effects that are its consequences (sections 1.5.2 and 1.5.3).

Electron-electron scattering, on the other hand, is almost invariably inelastic, meaning that part of the kinetic energy is converted into excitations in the material. It causes ionization of the irradiated material, core excitation, valence excitation, and phonon excitation. Charging effects due to ionization can usually not be observed in graphene (high conductivity). Beam-induced chemical effects like etching and deposition occur at defects and edges of graphene [94, 95], most notably in the presence of oxygen. The replacement of individual impurity atoms by carbon will be outlined

in section 1.5.4. Secondary effects of electronic excitation are typically used for spectroscopic techniques (e.g. EDXS, EELS) and/or energy-filtered imaging techniques. The contribution of electron-electron interactions to knock-on damage is currently still difficult to understand and has rarely been described quantitatively [96, 97].

1.5.1 Knock-on displacement of a carbon lattice atom

Note: The terminology for "knock-on" (KO) events is nuanced. In principle, any elastic momentum transfer is called a knock-on event, disregarding whether it causes an atomic displacement or not. In literature, typically there was only interest in knock-on damage, which is used synonymously with knock-on displacement. Hence, this effect will also be referred to as "knock-on damage".

The term *knock-on displacement* means that the bonding of a lattice atom is broken by the impact of a particle and the atom is knocked out of its lattice position. This can happen due to an electron scattering elastically from a nucleus and transferring an amount of kinetic energy that is greater than or equal to the displacement threshold energy T_d, which is ca. 21 eV for pristine graphene if the atom is ejected perpendicular to the lattice [93]. DFT studies revealed that, owing to variations in the momenta of the atoms neighboring the displaced atom, the displacement threshold follows a temperature-dependent normal distribution, with the symmetric width slightly increasing from ca. 0.9 K at 75 eV to ca. 1.5 eV at 300 K, where it reaches a constant level up to at least ca. 450 K [98]. If there is a substitutional three-coordinated impurity in the lattice (X@SV), the KO displacement threshold energy for the three C neighbors can be significantly lower than for a pristine lattice, as in the cases of Si (16.75 eV) [17], Al (15.6 eV), and P (17.2 eV) [21]). If a C neighbor of Si or P is knocked out, the impurity atom will relax towards the original position of the displaced atom and will bind to the rest of the lattice in a four-coordinated configuration (X@DV).

The second crucial quantity in the context of electron knock-on damage is the maximum transferable energy E_max, which is defined as the highest amount of kinetic energy that can be transferred from a moving electron with an initial kinetic energy of E_e to a nucleus with mass m_Z in a collision. In general, E_max is transferred if (and only if) the electron backscatters at a polar angle of $\theta = \pi = 180°$. The higher E_e and the smaller m_Z, the higher is E_max. The relativistic solution for the latter can be derived from energy and momentum conservation, using the relativistic energy $E = \gamma mc^2$ and the relativistic momentum $p = \gamma mv$ with $\gamma = 1/\sqrt{1 - v^2/c^2}$, where m is the (rest) mass of an electron (or C atom, resp.), v is the velocity, and c is the speed of light [99].

In the static-nucleus approximation, in which the nucleus is at rest when scattering occurs, in the case of a ^{12}C nucleus, the maximum transferable energy in our typical acceleration voltage regime ranges from 10.6 eV at $E_\mathrm{e} = 55$ keV to 17.9 electronvolt at $E_\mathrm{e} = 90$ keV (see fig. 1.6, blue curve), which is below the displacement threshold in graphene.

However, if the vibrational movement of the nucleus is taken into account, E_max will be significantly increased at and above ambient temperature. Limited to the out-of-plane movement ("z-only"), the phonon-assisted maximum transferable energy derived from relativistic energy–momentum conservation is given by [90]

$$E_\mathrm{max}\left(E_\mathrm{e}, v\right) = \frac{1}{2Mc^2}\left[Mvc + 2\sqrt{E_\mathrm{e}(E_\mathrm{e} + 2m_0c^2)}\right]^2, \tag{1.4}$$

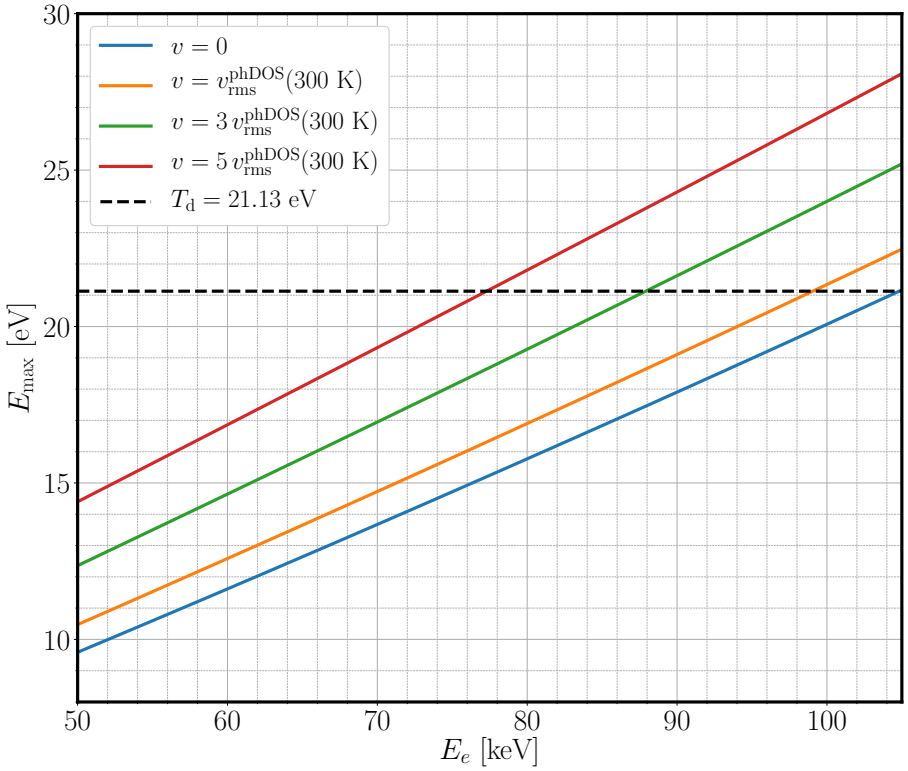

Figure 1.6: Maximum transferable energy E_{max} as a function of the electron kinetic energy E_{e} for a ^{12}C atom, with its out-of-plane velocity v being set to zero or different multiples of the root mean square velocity $v_{\mathrm{rms}}^{\mathrm{phDOS}}$ at ambient temperature. The displacement threshold energy $T_{\mathrm{d}} = 21.13$ eV [93] is depicted as a dashed horizontal line.

where M is the mass of the nucleus, v is the out-of-plane velocity[5] of the nucleus (which is parallel to the electron beam in case of perpendicular irradiation), m_0 is the electron mass, E_{e} is the initial electron kinetic energy, and c is the speed of light. In fig. 1.6, E_{max} is depicted as a function of the electron kinetic energy E_{e} for different values of v. The velocity of the target atoms v is assumed to be normally distributed with a variance equal to the temperature-dependent mean square velocity $v_{\mathrm{ms}}(T) := \overline{(v(T))^2} = \int p(v(T))(v(T))^2 \mathrm{d}v(T)$, where $p(v(T))$ is the (Gaussian) probability distribution function of $v(T)$ [93]. Using the phonon density of states (DOS) derived from a frozen phonon calculation, $v_{\mathrm{ms}}(T)$ can be estimated by

$$v_{\mathrm{ms}}(T) = \frac{\hbar}{2M} \int_0^{\omega_z} g_z(\omega) \left(\frac{1}{2} + \frac{1}{\exp\left(\frac{\hbar\omega}{k_{\mathrm{B}}T}\right) - 1} \right) \omega \, \mathrm{d}\omega, \tag{1.5}$$

where $\hbar$ is the reduced Planck constant, ω is the out-of-plane phonon frequency, ω_z is the highest (out-of-plane) phonon frequency, $g_z(\omega)$ is the out-of-plane phonon DOS, k_{B} is the Boltzmann constant, and $1/\left(\exp(\hbar\omega/k_{\mathrm{B}}/T) - 1\right)$ is the Bose–Einstein distribution function. At ambient temperature, the evaluation of eq. (1.5) yields $v_{\mathrm{ms}}^{\mathrm{phDOS}}(300\ \mathrm{K}) \approx 3.1 \times 10^5\ \mathrm{m^2\,s^{-2}}$ [93], which corresponds to a root mean square velocity of $v_{\mathrm{rms}}^{\mathrm{phDOS}}(300\ \mathrm{K}) = (v_{\mathrm{ms}}^{\mathrm{phDOS}}(300\ \mathrm{K}))^{1/2} \approx 560\ \mathrm{m\,s^{-1}}$.

[5] A defining subscript "z" is omitted for simplicity in the notation.

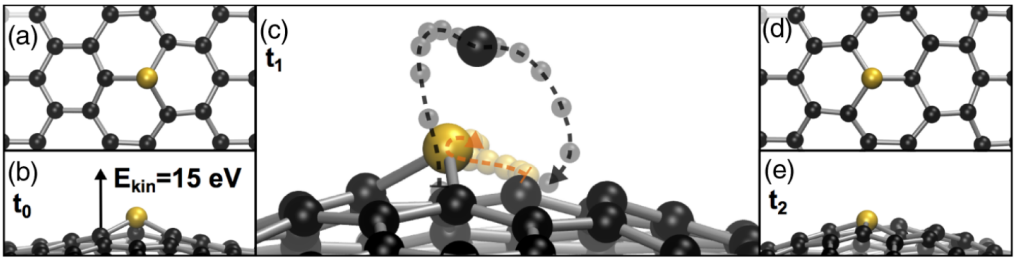

Figure 1.7: Molecular dynamics simulation after a kinetic energy transfer of 15 eV to a C neighbor of a Si@SV impurity in graphene. (a) Initial configuration at time t_0, top view. (b) Time t_0, side view. The kinetic energy transferred to a C neighbor is indicated. (c) Time $t_1 = t_0 + 70$ fs, side view. The trajectories of the ejected C atom and the Si atom are marked by dashed lines. (d) End configuration at time $t_2 = t_0 + 140$ fs, top view. (e) Time t_2, side view. (Reproduced from ref. [17]. Published 2014 by the American Physical Society under the CC BY 3.0 license.)

1.5.2 X–C bond inversion in graphene

In 2014, it was shown that and explained why a three-coordinated Si atom that is incorporated in the graphene lattice can be induced to exchange its position with a C neighbor by irradiating a specimen with electrons in a STEM [17]. The bond inversion process was proposed to be carried by a kinetic energy transfer just below the displacement threshold energy from an incident electron to *one of the C atoms neighboring the Si@SV*, which is also referred to as the primary knock-on atom (PKA) [21]. According to DFT-MD calculations, if the amount of transferred energy is within a well-defined range, i.e. from 15 to 16.25 eV, the PKA gets ejected from the lattice but pulled towards the Si atom due to their mutual attraction. The Si atom relaxes towards the vacancy and the ejected PKA gets incorporated in the lattice again, on the opposite side of the Si atom [17]. This atomic motion is depicted in fig. 1.7 for 15 eV. If the energy transfer is in the range from 14.625 to 15 eV, the PKA, after bouncing off the Si atom once and being drawn downwards a second time, is left as an adatom on the side opposite to its starting position. Between 16.25 and 16.75 eV, it also lands as an adatom on the opposite side of the Si. Since the three-coordinated Si@SV is thermodynamically favored over Si@DV and a C adatom close by, the configuration will likely recombine back to Si@SV. Thus, a kinetic energy transfer in the entire range from 14.625 to 16.75 eV leads to a flip of the bond between the PKA and the Si@SV impurity (later referred to as "*bond inversion*" or "*direct exchange*"). Energies below the lower bond inversion threshold do not lead to a structural change, and energies above 16.75 eV lead to KO displacement of the PKA, as discussed in section 1.5.1.

The cross section (typically specified in barn; 1 barn = 1 b = 10^{-28} m^2) for an energy transfer within the above-mentioned range was of particular interest for my work. For 60 keV electrons and the "z-only" model, the originally calculated values lied between 0.47 and 0.64 b [17], which was later corrected to 0.005 b [19]. Experimental measurements in 2014 [17] yielded 0.61 b with a 95 % confidence interval $[0.42, 0.89]$ b. The same set of electron doses yielded (0.53 ± 0.09) b (as will be discussed in section 3.3.1) based on the analysis method described in section 2.4.1. For a kinetic energy of 55 keV, the cross section is roughly one order of magnitude lower [18].

Looking ahead, the bond inversion process introduced in this section will serve as the fundamental basis for single-atom manipulation, which is dealt with in section 1.6. It has been observed and studied by DFT simulations for three-coordinated Si, Al, and P [17, 21].

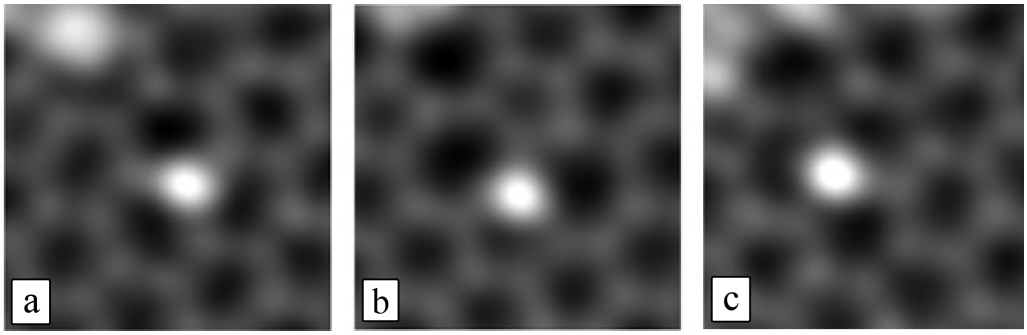

Figure 1.8: MAADF-STEM images of an experimentally observed SW transformation involving a Si@SV impurity. The plane-normal of the graphene monolayer is tilted with respect to the electron beam by ca. 17°. (a) Hexagonal structure with a Si impurity (bright contrast in the middle) before the transformation. (b) Metastable SW 5577 defect involving the Si atom, resulting from a clockwise SW transformation. (c) Hexagonal structure after clockwise relaxation, with exchanged positions between the Si and one of its C neighbors. (Adapted from ref. [21]. Published 2019 by the American Association for the Advancement of Science under the CC BY 4.0 license.)

1.5.3 Stone–Wales transformation involving an impurity atom

Although SW defects due to a rotation of a Si–C bond are rarely seen under the microscope (see fig. 1.8), the SW transformation could also contribute to single-atom manipulation. If the relaxation from the metastable SW 5577 to the hexagonal configuration involves another rotation by 90° in the same direction, the end result is equivalent to a direct exchange. According to NEB calculations, the energy barrier for the transition back to hexagonal from an SW 5577 configuration with Si is as low as 0.8 eV [21]. Thus, this relaxation process can be activated quite easily under electron irradiation, which leads to a low lifetime of the SW 5577 defect involving Si. Therefore, a fraction of the electron-induced exchange events observed with (S)TEM could indeed be unobservable SW transformations that have relaxed to the hexagonal configuration before the instrument could resolve the SW defect. As far as P is concerned, SW defects are observed much more often, which is likely in virtue of the higher energy barrier for relaxation (1.6 eV) [21].

1.5.4 Knock-on displacement of a dopant or replacement by carbon

The substitutional dopant is of central importance in the context of single-atom manipulation in graphene. Thus, if it gets knocked out or replaced by carbon, nothing will remain to manipulate.

Knocking out an isolated three-coordinated Al, Si, or P impurity, leaving behind a single vacancy, is rarely if ever observed. Owing to the higher mass and despite the lower displacement threshold energy, the knock-on displacement cross section for Si impurities is orders of magnitude lower than for neighboring C atoms according to DFT calculations [17], which most likely holds for Al and P as well. Therefore, this effect is neglected in the further course of this work.

The replacement of a dopant by a freely diffusing C adatom that approaches the impurity is much more likely, although the exact mechanism is uncertain. The resulting configuration, which is pristine graphene and an impurity adatom on top, is energetically favorable over the doped lattice with a C adatom. For most impurities, though, there presumably is an energy barrier to overcome during the replacement process. In such cases, the process can be activated or accelerated

by electron irradiation, although the role of the beam in the induced process is unclear. After replacement, the displaced impurity diffuses away quickly. This effect is sometimes observed for Si, and often for P and Ge [17, 21].

1.6 Single-atom manipulation in graphene

During the most recent years, several research groups including ours in Vienna have made significant progress on the manipulation of single atoms in graphene and other materials [18, 41, 42, 100–104]. In graphene, the phrase "single-atom manipulation" refers to selectively inducing an exchange in position between a dopant X and a neighboring C atom. This is achieved by directing the focused electron beam of a STEM precisely at the adjacent C atom located where the impurity atom is supposed to move. In the case of Si impurities, which are frequently found during STEM investigations, the suitable acceleration voltage regime has been empirically pinpointed [18, 100].

In the case of Si, Al, and P dopants, only three-coordinated X@SV are manipulable. In fig. 1.9, the corresponding direct exchange energy (kinetic energy transferred to the PKA) ranges are depicted. A four-coordinated X@DV, which can result from X@SV by the KO displacement of a C neighbor, is a trap state for all three elements: once the impurity is four-coordinated, it can no longer be moved [17, 20, 21, 105]. Thus, it must be noted that knock-on displacements are undesirable and can hinder single-atom manipulation experiments.

1.6.1 Target impurities

Without knowledge beyond their valence shell configuration and their bonding orbitals when incorporated in the graphene lattice as substitutional impurities, a couple of different elements could be good candidates for manipulation in the graphene lattice. To classify them, we can divide them into:

1. Isoelectric with C: Si, Ge, Sn
2. Direct neighbors of Si in the periodic table: Al, P
3. Direct neighbors of C in the periodic table: B, N
4. Transition metals: Fe, ...

Tin has not yet been investigated, and this work does not deal with it either. Germanium can be implanted into graphene at a modest success rate, but cannot be further manipulated [66]. The atomic dynamics of boron [106] and nitrogen [21, 106–108] impurities under electron irradiation have been observed, but it is difficult to work with them due to low contrast. Transition metals are mentioned here to indicate possible prospects, but were not the subject of the investigations carried out here.

Silicon
Si persists as the most suitable candidate for atomically precise manipulation because it is such a common lattice impurity [17, 109]. A high level of control when manually moving a single Si@SV through the graphene lattice is possible [42]. Using an acceleration voltage of 60 kV, the longest experimentally observed series of successfully directed exchange events of Si and C without

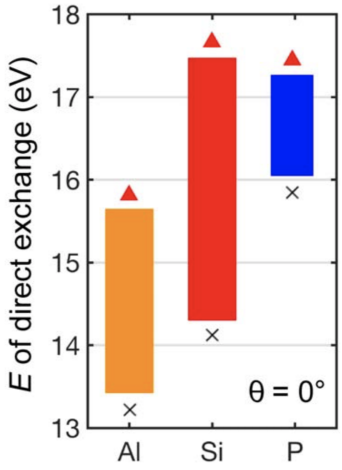

Figure 1.9: Kinetic energy ranges – transferred to the PKA – that lead to the direct exchange of the positions between a three-coordinated X@SV impurity and the PKA, compared for Al, Si, and P. The initial movement of the PKA is perpendicular to the lattice plane. (Adapted from ref. [21]. Published 2019 by the American Association for the Advancement of Science under the CC BY 4.0 license.)

any unwanted process is 34 [18]. According to simulations and experimental evidence, a four-coordinated Si@DV, which remains if a C neighbor is knocked out by the electron beam, cannot be manipulated [20, 105]. For 55 kV, the exchange-to-damage ratio is higher than for 60 kV, but the manipulation process takes ca. two orders of magnitude longer [18]. 57 kV might be the "sweet spot".

Phosphorus

After insights gained from DFT-MD simulations, it was experimentally confirmed that P seems also a candidate for single-atom manipulation. Its behavior is somewhat different from Si, and a major problem with P is the replacement process by C (see section 1.5.4), which seems significantly more active than with Si [21, 69]. Further experimental investigations could still yield interesting results.

Aluminum

Single-atom manipulation of Al dopants is promising according to a recent study [68]. DFT-MD calculations showed that the energy range for direct exchange [21] is lower than for Si, but should be roughly two times larger than for P (see also fig. 1.9). In the scope of my work, however, the use of Al dopants was not possible due to delayed sample availability and time constraints.

Iron

Iron dopants in graphene have been studied using DFT-MD calculations [110]. The direct exchange process with C works analogously to Si, Al, and P. There has been an experimental report on their behavior, but it seems likely that the impurity in question was misidentified and was Si instead [111]. However, due to their magnetic properties, manipulation experiments could be of great interest.

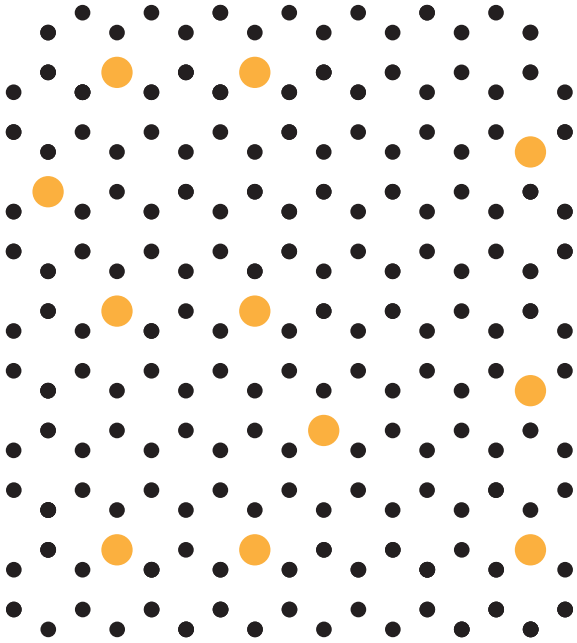

Figure 1.10: Schematics of an atomic pattern comprising substitutional atoms in graphene. The filled circles represent C (black) and other (yellow) atoms, for example Si.

1.6.2 Controlled single-atom manipulation

Single-atom manipulation of Si impurities in graphene with atomic precision at a certain level of control [20, 100] was carried out within a few years after the explanation of the electron-beam induced Si–C bond inversion process (see section 1.5.2). Consequently, higher control was demonstrated by directing a Si atom to circulate in a single hexagon of the graphene lattice and by manipulating a Si atom 34 steps in a preferential direction [18]. The primary objectives of my work were to gain more knowledge of any physics that is related to high-control single-atom manipulation. The secondary objectives were the development of automation software (see section 2.7.3 and section 3.5.1) that takes over the so far needed STEM user inputs during manipulation work.

Finally, the ultimate goal was the controlled single-atom manipulation of multiple Si impurities into an arbitrary pattern. An example of an ordered heteroatomic structure with 11 manipulated atoms is schematically illustrated in fig. 1.10, although to control so many impurity atoms, most likely Si, and to bring them so close together by single-atom manipulation remains an open challenge.

Meanwhile, two individual Si atoms must not approach closer than a defined number of lattice sites during the manipulation process, because the embedding energy of Si is reduced by ca. 0.5–1.5 eV per atom for separations lower than three sites [17, 112]. Therefore, it is difficult (if not impossible) to move Si atoms that are nearest or second-nearest neighbors away from each other again. Furthermore, it was observed for a Si atom separated by two lattice sites from another Si moved towards the latter under 60 keV electron irradiation (without spot irradiation targeted onto the corresponding C neighbor) [17]. In another observation of second-nearest Si neighbors, one of the impurities was replaced by C [113]. As for third-nearest and fourth-nearest neighbors, there exist various nonequivalent configurations, and the respective energy reductions have only partially been clarified so far [112].

1.6.2.1 Non-disruptive versus terminating processes

As highlighted at the beginning of section 1.5, cross sections can be assigned to any processes under electron irradiation. The ratio of these cross sections indicates the suitability for (controlled) single-atom manipulation, because only three-coordinated X@SV can be manipulated. Both the jump-to-damage ratio as well as the manipulation rate (per unit time) are functions of the electron kinetic energy [18, 21]. Therefore, it is crucial to find and use the optimal electron energy, which should feature a high jump-to-damage ratio and retain a practicable manipulation rate.

The following processes (1–3) leave behind a manipulable X@SV configuration and are, thus, *beneficial* for manipulating single atoms.

Process 1: Direct exchange (also referred to as "jump")
The beam-induced bond inversion process of X–C, as discussed in section 1.5.2, leads to a direct position exchange between an impurity X@SV and one of its three neighboring C atoms. From another viewpoint, it can be expected that many (if not most) of the observed exchanges take place due to the (direct) bond inversion process. However, the actual process dynamics are not accessible to direct observation, since the corresponding atomic movement takes place at the 100 fs time scale.

Process 2: Stone–Wales transformation
Thus, it may be that some of the observed X–C exchange events are attributable to SW defects that relax rapidly to the configuration with an inverted X–C bond (see section 1.5.3).

Process 3: Double jump
It is occasionally observed that a Si impurity moves by two lattice sites between the acquisition of an image and the subsequent one (see [18] and also according to my personal experience). It is assumed that it is a combined process of two exchange processes.

In analogy to the non-disruptive processes, let us also recall the *undesired* ones (4 and 5). If one of these occurs, single-atom manipulation cannot be continued using the same impurity atom.

Process 4: KO displacement of the PKA
As mentioned in section 1.6, four-coordinated Si@DV, as well as Al@DV and P@DV atoms, are not manipulable. Dynamics of Al-C_3N sites have recently been observed [68], but it is unclear if these can be controlled.

Process 5: Replacement of the impurity by C
If the impurity gets replaced by C (see section 1.5.4), it is no longer present in the lattice and thus obviously lost for further manipulation.

2 Methods

In this chapter, the methods used in this work will be explained. First, the experimental equipment will be described. This will be followed by an overview of the preparation of the investigated graphene samples. Then, the methodology for characterizing the electron beam of the used STEM will be documented, and the experimentally observed as well as theoretically predicted cross sections of electron-induced atom displacements in graphene will be described. Further, the used regression algorithms and the applied method for the propagation of uncertainties and stochastic measurement errors[1] will be recorded explicitly. Finally, the software packages developed in the course of this work will be described with respect to the tasks at hand.

2.1 Instrumentation

2.1.1 Nion UltraSTEM 100

The most important instrument used is a Nion UltraSTEM 100 scanning transmission electron microscope, which is installed in Vienna. A photo of the Nion instrument in Vienna and a general design layout for dedicated STEMs are depicted in fig. 2.1. The instrument's most important characteristics are listed on the manufacturer website[2]. The Nion UltraSTEM 100 is a probe-corrected dedicated STEM with an acceleration voltage ranging from 40 to 100 kV. The system design present in Vienna includes extra pumping for an objective area pressure $\lesssim 10^{-9}$ mbar (this is two to three orders of magnitude lower than for most other STEM instruments), with the gun pressure ranging from 10^{-10} to 10^{-11} mbar. The device has a coherent beam cold field emission gun (FEG) with a brightness of $\beta > 10^9$ A cm^{-2} sr^{-1} and the probe diameter in the focal plane is ca. 1.2 Å, which is going to be important for our purposes, since the accuracy of some studies highly depends on the precise determination of the probe's size as well as its shape. Furthermore, the instrument has the built-in option to use a cartridge featuring an electrical connection between external contacts and pins on the sample holder, which allows electrothermal in situ experiments (see section 2.1.3).

The basic configuration of a Nion UltraSTEM 100 includes both a MAADF and a HAADF detector. For this work, primarily the first one was used, whose semi-angle of collection range is 58 to 200 mrad. The MAADF detector was precisely characterized by the manufacturer, who measured an average maximum intensity proportional to $Z^{1.64}$ based on images of $_5$B, $_6$C, $_7$N, and $_8$O atoms in hexagonal boron nitride [23].

Nion microscopes are controlled by two software applications, Nion AS2 and Nion Swift[3]. For the purposes of this work, AS2 simply communicates with both the electrical backplanes and the front-

[1] These are also called random errors, in contrast to systematic biases.
[2] https://nion.com/products.html
[3] https://nionswift.readthedocs.io/en/latest/index.html

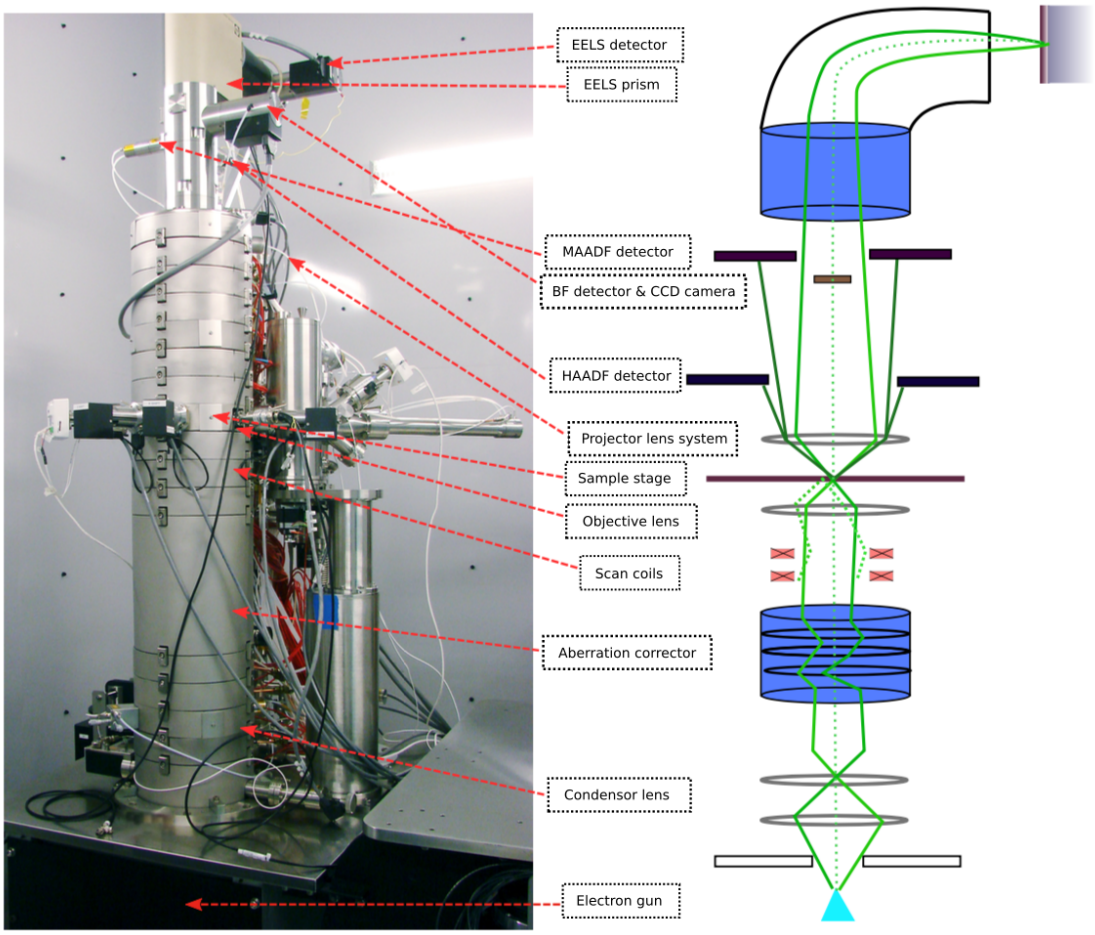

Figure 2.1: Photo and schematics of the core components of the Nion UltraSTEM 100 installed in Vienna. (Adapted from ref. [113], courtesy of M. Tripathi.)

end application Swift. A small description of Swift, though, is more relevant to this work, since it is the application with which the microscopist directly interacts. It is open source and features an application programming interface (API) that allows any user or third party to develop custom extensions [114]. Crucially, most of the experimental measurements within the framework of my research work were not feasible without customized Nion Swift plug-ins that precisely accomplish sophisticated data acquisition and image filtering tasks (as will be discussed in section 2.7).

2.1.1.1 Electron energy-loss spectroscopy

The Nion UltraSTEM 100 located in Vienna is equipped with an electron energy-loss (EEL) spectrometer (PEELS 666, Gatan Inc.[4]) and an electron-multiplying charge-coupled device (EM-CCD) camera (iXon Ultra 897, Andor[5]). The analytical technique electron energy-loss spectroscopy (EELS) is used to measure the kinetic energy loss of electrons due to interaction with a specimen. Pioneered in 1948 [115], it is mostly applied in the combination with (S)TEM. The primary electrons are nearly monochromatic, meaning that their energy spread is small compared to possible

[4]https://www.gatan.com
[5]Part of the Oxford Instruments Group, https://andor.oxinst.com.

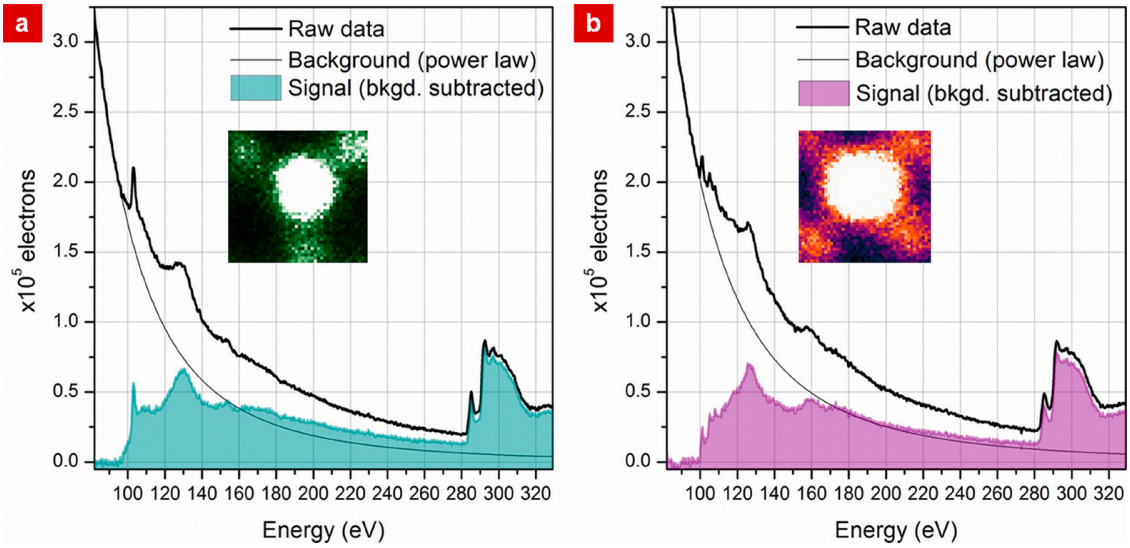

Figure 2.2: EEL spectra of Si impurities in graphene. (a) Three-coordinated Si@SV. (b) Four-coordinated Si@DV. The peak with onset at ca. 284 eV corresponds to the carbon K edge [117]. (Reproduced with permission from ref. [109]. Copyright 2013 American Chemical Society.)

losses in the EEL spectrum. The energy loss is due to inelastic scattering, mainly caused by electron-electron interactions (as introduced in section 1.5) [116]. The scattered intensities need to be dispersed as a function of kinetic energy, which is done by guiding the electrons through a magnetic prism. Spatially split by energy, the electrons are collected by a multi-channel detector, in our case the scintillator-coupled EMCCD camera (see upper parts in fig. 2.1).

An EEL spectrum can be split into a zero-loss, a low-loss, and a high-loss region. The most intense feature is the zero-loss peak (ZLP), which is created through unscattered electrons. Its full width at half maximum (FWHM) is used to specify the energy resolution. The low-loss region lies between the ZLP and about 50 eV and contains peaks corresponding to plasmons and valence excitations. Core excitations cause an energy loss in the high-loss region (above 50 eV), where characteristic peaks – ionization edges – are found that serve the unambiguous identification of chemical elements. Above the onset of an ionization edge, there are smaller features – corresponding to the fine structure – which allow the analysis of the local bonding and the environment of the ionized atoms [113, 116].

In this work, the elements Al, Si, and P needed to be distinguished, so the only interest was in the ionization edges. These are labeled *K, L, M, ...* (standard spectroscopic notation). For the three above-mentioned elements, the $L_{2,3}$ edges ($2p$-orbitals with a total angular momentum quantum number $j = 1/2, 3/2$) are in the same order of magnitude, but the energy differences among them are much larger than the resolution of typical EELS instrumentation: the onsets are at ca. 73 eV for Al, ca. 99 eV for Si, and ca. 132 eV for P [117]. The EEL spectra of Si@SV and Si@DV in graphene [109] are depicted in fig. 2.2. The spectra for Al [68] and P [69] are similar in shape, with the edge onsets instead being at the energies given above.

2.1.2 UHV system

Modern experimental research in physics often takes place at the edge between technical possibilities and limitations. For the examination of materials with high-resolution electron microscopes, it is extremely useful to have in situ apparatuses – e.g. for sample cleaning, heating, vapor deposition, tomography, etc. – at hand. They allow simultaneous alteration of the material under investigation and image acquisition or an alternating workflow. The main advantage of these techniques is that the sample remains in a controlled atmosphere, with no exposure to ambient. However, it can be impossible or technically unfeasible to integrate a specific instrument in a microscope assembly, and such solutions may not be commercially available.

The Nion UltraSTEM 100 in Vienna has two in situ components attached to it, a gas leak valve and a laser unit, the latter of which is described in section 2.1.3. Its outstanding unique property among STEM devices is that its column is connected[6] for sample insertion to the CANVAS[7] system [118], an extended UHV system (see fig. 2.3) containing a transfer system, storage space for ca. 75 (S)TEM samples, an evaporation chamber with a variety of integrated devices, and ports to a load lock for taking in and out samples, a glove box under argon atmosphere with another sample entry, and a combined atomic force and scanning electron microscope (AFSEM, GETec Microscopy[8]). The entire system is kept at pressures in the 10^{-9} to 10^{-10} mbar range, which conserves samples for the long term and has – soon after its installation in 2017 – allowed numerous studies in connection with the controlled alteration of materials [63, 72, 95, 119] and the growth of new ones [120].

2.1.3 In situ and in UHV devices for sample alteration

In the present section, the devices relevant for my studies are briefly described. Experimental work with the microwave argon plasma source (see below) was mostly carried out by other group members. That efforts also yielded some graphene samples with a high number (ca. 10) of silicon impurities within an area a few tens of nm^2 in size.

Column laser unit
An in situ diode-pumped solid-state laser (473 nm, Cobolt Blues 25, Cobolt AB[9]) with a radiation power up to 100 mW is aimed through a shutter (pulse lengths $\gtrsim 100$ µs), focusing optics (resulting in a diameter of ca. 26 µm in the focal plane, respectively an area of ca. 560 $µm^2$ [68]), and a viewport into the objective area of the Nion UltraSTEM 100 . It is suitable to reduce the ubiquitous hydrocarbon contamination coverage on graphene surfaces by evaporating it or making it accumulate at separated contamination spots with large clean sample regions in between [121].

Microwave Ar^+ plasma source and laser unit in plasma chamber
A microwave plasma generator emitting low-energy Ar^+ ions was used for vacancy creation in graphene [63]. This treatment was used to incorporate, in a subsequent step, Si (see section 1.3.4.1) as well as Al (see section 3.4.2) atoms into the lattice by recombination with the vacancies created beforehand. The measured ion energy was approximately Gaussian-distributed with a mean of ca. 170 eV and a standard deviation of ca. 30 eV. The exposure time was 300 s and the ion irradiation dose ca. 3×10^{13} cm^{-2}.

[6] The entire vacuum space is separated into individual sections by gate valves with Cu seals.
[7] Abbreviation for controlled alteration of nanomaterials in vacuum down to the atomic scale.
[8] https://www.getec-afm.com/afsem
[9] Part of HÜBNER Photonics, https://hubner-photonics.com.

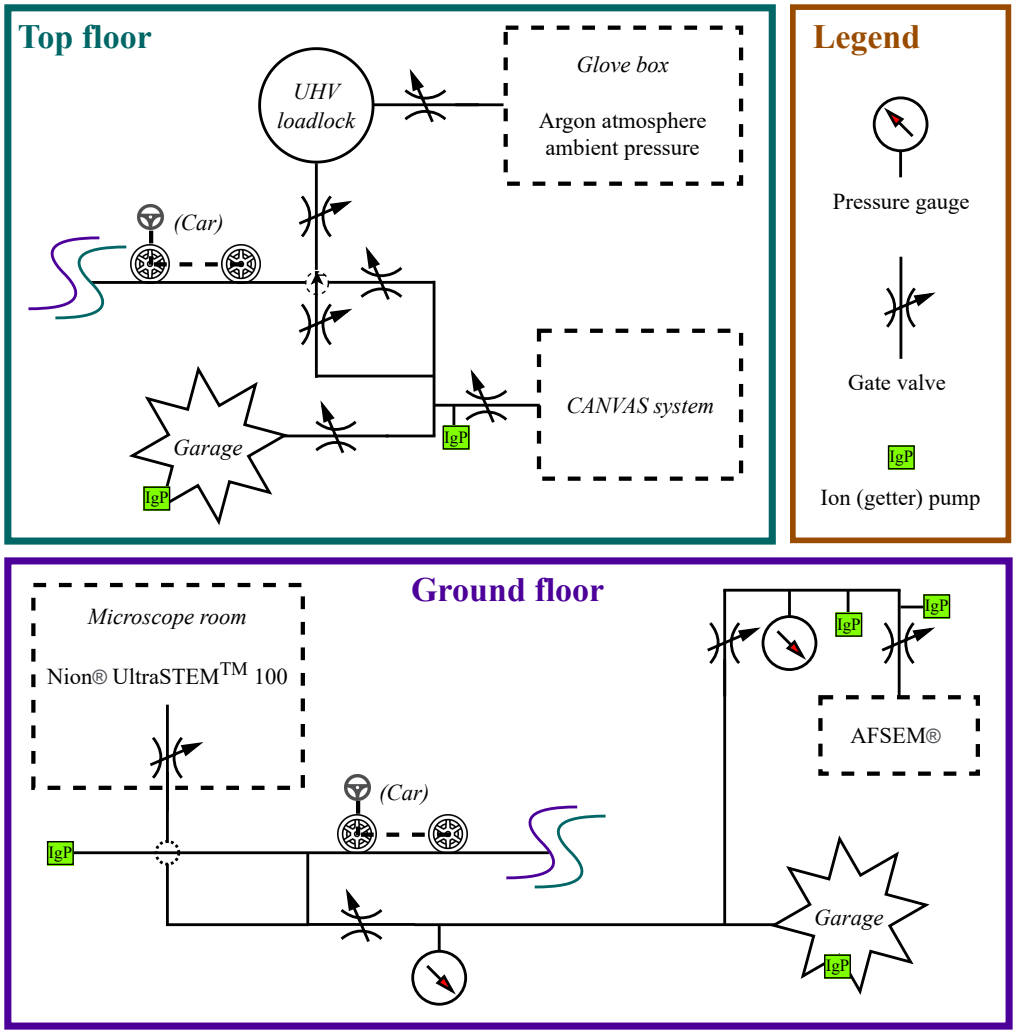

Figure 2.3: Schematics of the UHV system run by the Physics of Nanostructured Materials group in Vienna. The transportation of the samples, on the "pucks" accommodating them, is accomplished via cars, each of which can carry up to three pucks.

A specimen as clean as possible is needed for incorporating atoms directly into the lattice. Therefore, the sample used for the voltage-dependent cross-section measurement reported in section 3.3.1 was simultaneously irradiated with laser light to elevate the sample temperature and attenuate hydrocarbon buildup during the Ar plasma irradiation. The irradiance (power density) on the sample spot was ca. 200 $\mathrm{mW\,mm^{-2}}$ [68].

In situ electrical sample heater

All experiments at elevated temperature were conducted with "type 1" samples (see section 2.2) that were transferred onto a chip with electrical contacts. The chip is mounted in a TEM holder with an integrated electrical circuit (Fusion, Protochips Inc.[10]). A current can be passed through the heating coil of the chip, which heats the sample. The temperature is controllable based on the manufacturer's calibration (per chip). After consultation with the manufacturer, the uncertainty of the temperature was estimated as ± 2 % in relative terms.

[10] https://www.protochips.com

2.2 Preparation of graphene samples

Two different sample types were used. The first ("type 1") was commercial monolayer graphene grown by chemical vapor deposition (CVD) – Easy Transfer, Graphenea S.A.[11] – and transferred either onto a perforated/holey silicon nitride support grid grown on a silicon substrate (PELCO, Ted Pella, Inc.[12]), or onto a Protochip (see section 2.1.3). The silicon nitride chips had a membrane thicknesses of 50 nm and a hole diameter $d = 2.5$ µm and have been used for the voltage-dependent measurement involving silicon (as will be discussed section 3.3.1). The latter chips enable electrothermal measurements in situ by passing a current through the heating coil of the chip. These have been used for all temperature-dependent measurement (sections 3.2.1 and 3.3.2).

The second ("type 2") were commercial TEM gold grids with Quantifoil holey carbon (2 µm in diameter) and suspended monolayer graphene (Graphenea, S.A.). These samples can typically be used to tune a Nion UltraSTEM 100 in a time-efficient manner and were, thus, suitable to extensively test the developed software packages run during microscopy experiments (section 2.7).

2.2.1 Increasing the density of substitutional impurities

The efforts of our collaborators[13] in Vienna and at the MIT gave us access to "type 1" specimens with low densities of Al [68] and P [21] impurities, and high densities of Si.

Al incorporation after Ar plasma treatment
The incorporation of Al into monolayer graphene was done by two-step substitution of carbon as introduced in section 1.3.4.1, using the low-energy Ar^+ plasma source described in section 2.1.3. To bring Al close to the vacancies created due to the plasma irradiation [63], an Al target (99.999 % purity, Sigma-Aldrich[14]) was thermally evaporated by heating to 955 °C. The vacuum chamber base pressure was ca. 5×10^{-10} mbar, and the Al partial pressure was kept at ca. 1×10^{-8} mbar during evaporation. An evaporation time of 20 s resulted in a high density of Al clusters ca. 5 nm in diameter attached to the specimen surface, and single Al dopants in the graphene lattice [68].

Si incorporation yield after Ar plasma treatment
The density of Si impurities in graphene can be increased by two-step substitution of carbon. This works even without an external Si source since that element can almost always be found in the hydrocarbon contamination attached to the surface of the graphene monolayer. A fraction of the vacancies created by the low-energy Ar^+ plasma recombines with diffusing Si adatoms, for which the surface diffusion barrier on graphene was calculated to be ca. 0.06 eV [72, 81], substantially smaller than for C (0.40–0.47 eV, see section 1.4.1). After exposure of a suspended graphene lattice to 50 eV Ar^+ plasma irradiation with a dose of ca. 1 ion per nm^2, a Si density of 0.15 nm^{-2} was reported [72], which corresponds to an atomic concentration of ca. 0.4 %. About two thirds of the Si atoms were incorporated in single vacancies, and one third in double vacancies.

P-doped graphene
Graphene with substitutional P impurities can be grown on a Cu foil using CVD with a triphenylphosphine ($C_{18}H_{15}P$) precursor. Details on the fabrication procedure are given in ref. [21]. We received a sample transferred onto a Protochip heating holder (section 2.1.3) from our collaborators.

[11] https://www.graphenea.com
[12] https://www.tedpella.com
[13] Research groups of Jani Kotakoski, University of Vienna, and Ju Li, Massachusetts Institute of Technology.
[14] https://www.sigmaaldrich.com

2.2.2 In situ sample cleaning

To execute my cross-section measurements as well as my controlled single-atom manipulation experiments, clean graphene areas at least 10 nm^2 in size (and ideally much larger) were needed. On TEM samples, a large fraction of the suspended monolayer graphene is typically covered by hydrocarbon contamination, even after chemical cleaning methods and annealing at ca. 150 °C for ca. 9 to 12 hours upon loading into the UHV system.

Therefore, to obtain large areas of clean graphene while viewing the sample under the microscope, two methods were used. The *laser cleaning method* (by local heating; see section 2.1.3 and ref. [121]) was applied whenever the contamination coverage was too high (fig. 2.4) or mobile contamination covered the lattice in the FOV and thereby hindered the experimental measurement.

The second way of cleaning arose from the experimental setup for temperature-dependent measurements (as will be discussed in sections 3.2.1 and 3.3.2), since this allowed heating the sample up to ca. 1000 °C. If suspended monolayer graphene becomes subject to such treatment, part of the surface contamination will pull together to some extent, but will not be evaporated. Mobile contamination, though, will be significantly reduced for ca. 2 to 3 hours. However, the heating cycles as well as keeping the sample at high temperatures will degrade silicon-based sample substrates. The degradation was not quantified, but a rough estimate is that a sample as described in section 2.1.3 is unusable for microscopy after 30 experiments at or above 500 °C for more than 10 hours.

2.2.2.1 Laser cleaning parameters

The laser parameters suitable to clean the lattice were in the same order of magnitude for both "type 1" (silicon nitride, 50 nm thick membrane) and "type 2" (Quantifoil) samples. That being said, the intensity and the exposure must further be fine-tuned for every individual sample.

As for "type 1" samples with a thickness of 50 nm, a good starting point to remove mobile contamination was found at 10 mW in terms of nominal power[15] and 5 ms in terms of exposure time. To remove the part of the contamination that adheres slightly and is not attracted by the electron beam to the same extent as mobile contamination, $\geq$ 20 mW is likely needed for 5 ms, but this has to be done very carefully since 40 mW power with the same illumination time can destroy large areas of such a sample.

In the case of "type 2" samples, a nominal power of 15 to 20 mW and an exposure time of 2 to 5 ms have proven as a reference point to obtain large spots of atomically clean lattice (see fig. 2.4), albeit these values should be taken with care and always reduced when first attempting on another sample. To remove mobile contamination, a nominal power of 3 to 7 mW with the above-mentioned exposure time is recommended, or 15 mW and 500 to 1000 µs, alternatively.

Hint: If no cleaning effect has occurred the first time, it is recommended to incrementally increase one of the parameters, preferentially the exposure time, by at most 20 % per step (rule of thumb).

[15] Only fraction of the light intensity enters the column due to losses in the optical system.

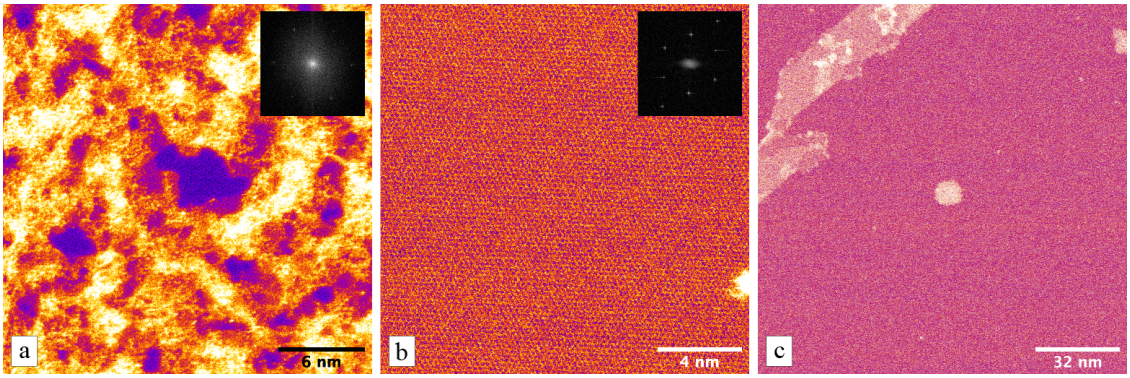

Figure 2.4: Typical contamination coverage of suspended monolayer graphene and effect of laser cleaning (MAADF-STEM images). (a) Image of a 25×25 nm^2 region of suspended monolayer graphene with high hydrocarbon contamination coverage (bright speckled contrast). The fast Fourier transform (FFT) is shown as an inlay at the top right corner; the peaks corresponding to atomic distances in the graphene monolayer are not particularly pronounced. (b) Image of a region 17×17 nm^2 in size directly after cleaning with the column laser unit described in section 2.1.3. The power and the exposure time of the laser unit were set to 20 mW and 5 ms, respectively. The peaks in the FFT (inlay at the top right corner) are strongly pronounced. (c) Overview of a clean 256×256 nm^2 large region ca. two hours after laser cleaning. The bright areal contrast in the upper left corner is multilayer graphene with adhesive contamination (either coating the layers or enclosed by the individual layers). The bright square-shaped contrast in the center is accumulated mobile contamination after the beam has been scanned across that region for ca. one minute.

2.3 Characterization of the electron beam

The calibration of the beam current was a prerequisite for the quantification of irradiation effects and the description of scattering processes in terms of cross sections. Further, determining the size and shape of the electron probe was essential to explaining the healing of vacancies in pristine graphene by carbon adatom migration competing with the creation of vacancies by electron knock-on damage.

2.3.1 Calibration of the beam current

The beam current I_B cannot be directly measured during the acquisition of STEM images. Instead, the virtual objective aperture (VOA) current I_VOA is tracked by Nion AS2 and saved to image metadata by Nion Swift. For the acquisition of a calibration function $I_\mathrm{B}(I_\mathrm{VOA})$, the beam current was assumed to be equal to the current hitting the EELS drift tube if no sample was present in the column and no electric tension was applied to the EELS prism. The drift tube was connected to electrical ground via an Ohmic resistor (resistance: $R = 10$ MΩ). The voltage drop across the resistor, U_B, was directly measured as a function of I_VOA and converted to the beam current, using Ohm's law ($I_\mathrm{B} = U_\mathrm{B}/R$). Then, a linear least-squares (LSQ) fit of the model function

$$I_\mathrm{B}(I_\mathrm{VOA}) = a_1 I_\mathrm{VOA} + a_2, \tag{2.1}$$

which is linear in I_VOA, was performed. The beam current was gauged so often that a calibration line was available for each cross-section measurement between two weeks before and after the measurement.

2.3.2 Reconstruction of the probe shape

This section is based on original work in the supplemental material of Publication I [122]. The conceptual design as well as the development of the software was done by colleagues.

The shape of a STEM probe can be estimated by comparing a simulated and an experimental image [123]. Instead of maximizing their correlation, minimizing their difference is a similar way to reconstruct the probe shape. The image intensity at pixel location (x, y) is modeled by

$$I_{\text{model}}(x, y|\boldsymbol{a}, \boldsymbol{c}, b) = \sum_i g(x, y|x_i, y_i, \boldsymbol{a}, \boldsymbol{c}) + b \tag{2.2}$$

as a superposition of rotationally symmetric probes g, one at each atomic position (x_i, y_i), with an additive background b. This yields good approximations for images of 2D materials [64]. The atomic positions are found in the experimental image, using the fully convolutional neural network (FCNN) described in section 2.7.3.1. As for the probe, the ansatz

$$g(x, y|x_i, y_i, \boldsymbol{a}, \boldsymbol{c}) = \sum_j a_j \exp\left(-\left((x - x_i)^2 + (y - y_i)^2\right)/c_j\right) \tag{2.3}$$

with the parameter sets $\boldsymbol{a} = \{a_1, a_2, \ldots, a_N\}$ and $\boldsymbol{c} = \{c_1, c_2, \ldots, c_N\}$ is made. They are optimized by minimizing the (sum of the squared) intensity difference between I_{model} and the experimental image intensity $I_{\text{experiment}}$:

$$\min_{\boldsymbol{a},\boldsymbol{c},b} \quad \sum_{x,y} \left(I_{\text{model}}(x, y|\boldsymbol{a}, \boldsymbol{c}, b) - I_{\text{experiment}}(x, y)\right)^2 \tag{2.4}$$

This was numerically solved by a gradient descent algorithm [124], implemented using the PyTorch library [125]. The method described above will provide ambiguous probe shapes if applied to experimental images of an ideal lattice, e.g. pristine graphene. Thus, it is crucial to use an image with defects.

2.4 Cross sections of atom displacements

A main objective of my work was the measurement of cross sections for various electron-beam induced processes (see section 1.5) in pristine graphene and graphene with substitutional impurities in the lattice. Thereby, these stochastic processes were quantified for different electron kinetic energies (different acceleration voltages) and at different temperatures. Further, the interpretation of results as well as the discovery and the explanation of physical relationships were further tasks that were partially accomplished in the scope of this thesis.

2.4.1 Experimental measurements

This section is based on original work in Publication I [30] and the corresponding supplemental material [122].

Before data was acquired, we made considerations about the establishment of a default experimental method and the conception of a standardized computer-aided analysis procedure (fostering reproducibility and a smooth workflow).

The experimentally observed cross section σ^{obs} can be approximated once the electron dose N_{e} impinging on the region of interest (ROI, as will be discussed in section 2.4.1.2) has been measured and the number of events N^{obs} caused by this irradiation dose has been counted. Given the expectation value of the electron dose per event λ, the experimental cross section can be calculated via

$$\sigma^{\mathrm{obs}} = \frac{1}{\rho_A \lambda} \quad \text{with} \quad \rho_A = 2\frac{1}{A_{\mathrm{UC}}} = \frac{4}{a_{\mathrm{gra}}^2\sqrt{3}}, \tag{2.5}$$

for areal atomic density ρ_A; A_{UC} is the graphene unit cell area, and a_{gra} is the lattice constant of graphene. The experiment design (as described later in section 2.4.1.3) ensured that what was observed constituted a homogeneous Poisson process [126]. Using Bayesian parameter estimation [127], the posterior mean (PM) solution is given by

$$\lambda^{\mathrm{PM}} = \overline{N_{\mathrm{e}}}\frac{N^{\mathrm{obs}}}{N^{\mathrm{obs}} - 1}, \tag{2.6}$$

where $\overline{N_{\mathrm{e}}}$ is the arithmetic mean of the individual electron doses, after each of which exactly one event was observed. As for the uncertainty $\Delta\lambda^{\mathrm{PM}}$, the square root of the variance of the PM solution is used:

$$\Delta\lambda^{\mathrm{PM}} := \sqrt{\mathrm{var}\left(\lambda^{\mathrm{PM}}\right)} = \overline{N_{\mathrm{e}}}\frac{1}{\sqrt{N^{\mathrm{obs}} - 2}} \tag{2.7}$$

The accuracy and the robustness of the calculated cross-section estimate increase with the number of observed events. In the present case, the uncertainty of the used estimator is proportional to $\approx 1/\sqrt{N^{\mathrm{obs}}}$ according to eq. (2.7). Therefore, we aimed to collect 50 to 100 electron doses for each measuring point, which was defined either by the temperature or the acceleration voltage.

When using stationary spot irradiation (i.e. keeping the electron beam parked on an atom) [17, 18] and ADF detector voltage feedback [18, 128], it is in principle possible to derive the irradiation dose on the atom based on the two-dimensional probe density profile in units of electrons per unit area, which is given by the beam current (see section 2.3.1) and the shape of the probe (see section 2.3.2). In practice, however, it is difficult to perform the measurement that way and the dose uncertainties are much higher than for the measurement method described in section 2.4.1.

2.4.1.1 Signal-to-noise ratio and perception limit

According to the Weber-Fechner law [129], the intensity perceived by a human is sense-specific and logarithmic in terms of the physical intensity. For low relative intensity differences between a feature and the background (or another feature), the Weber contrast

$$C(S_{\mathrm{f}}, S_{\mathrm{b}}) := \frac{S_{\mathrm{f}} - S_{\mathrm{b}}}{S_{\mathrm{b}}}, \tag{2.8}$$

is often used. S_{f} and S_{b} represent the stimuli intensity of the feature and the background, respectively. For comparison, the physical signal-to-noise ratio (SNR) is simply given by

$$\mathrm{SNR} = \frac{S_{\mathrm{signal}}}{S_{\mathrm{noise}}}, \tag{2.9}$$

where S_{signal} and S_{noise} are the average intensities of the "signal" (in our context: atom) and the "noise" (in our context: vacuum), respectively.

Regarding the visual sense, a rule of thumb is that the perception limit for relative differences is ca. 5 % according to eq. (2.8), however, this no longer holds in case the human-eye recognition has to be fast (say in less than a second). Even though the displayed contrast can dynamically be set in Nion Swift and the STEM images were live-filtered (as will be discussed in section 2.7.2) during acquisition to suppress noise with high spatial frequencies, it was unrealistic to sense an atom-to-background contrast of only $C = \pm 5$ % quickly enough. Instead, the typical operation regime described in the following section 2.4.1.2 led to typical atom-to-background contrast values of 15 to 25 %, or an SNR between 13 : 10 and 5 : 4, respectively.

In addition, the software package for atomic structure recognition developed by my colleagues (section 2.7.3.1) can be used immediately after image acquisition. The neural network outperforms human-eye recognition in cases for which it was trained by deep learning [130], though it was not evaluated in detail what contrast or SNR thresholds it can handle.

2.4.1.2 ROI and choosing the optimal scan parameters

The most useful experimental approach was to first take care of *maximizing the electron dose rate* that impinges on the ROI, which is the area that can be assigned to the atom(s) studied (differing among the investigated effects). By our convention, that area is obtained from applying a Voronoi decomposition [131, 132] to the graphene sheet (see fig. 2.5). Later, it will also be called the area that "corresponds to" the atom(s), though it has nothing to do with atomic radii.

Maximizing the dose minimizes the time needed to observe a certain count of events and can be accomplished by either increasing the beam current (by tip flashes or by increasing the gun extraction voltage), which is limited by the stability of the electron gun tip, or by lowering the field of view (FOV) and, hence, increasing the dose density rate impinging on the ROI. In the case of pristine graphene, where the ROI is the entire FOV, the latter option does not increase the rate of events under investigation (details on that specific measurement below). If dynamics involving impurities are investigated, however, it will be useful to choose the FOV as small as possible. To ensure the validity of the measurement, though, it is required that the FOV contains a margin of ca. 2 Å at all edges of the ROI. The electron dose impinging on the ROI will then be homogeneously distributed due to the beam movement. Further, unavoidable specimen drifts have to be compensated. The microscopist has to regularly recenter the ROI. Independent from the requested magnitude of the stage shift in the xy-plane, the mechanical stage will be shifted by $\gtrsim 1.5$ Å due to technical limitations[16].

The frame time t_f is predominantly determined by the product of the number of pixels and the dwell time per pixel, $N_x \times N_y \times t_\mathrm{p}$, and is further increased to a small extent by probe flyback times from the end of a scan line (or image) to the beginning of the next one. On the one hand, it was beneficial to use a t_f as low as possible, because this would bring about the *best possible time resolution*. On the other hand, decreasing t_f will lower the SNR if the FOV remains equal, so the best working regime is when the image contrast is at or just above the SNR limit.

The number of pixels can be considered a spatial sampling rate. To resolve all sample features, a minimum number of pixels per unit length is necessary, the magnitude of which is not discussed in detail here. As long as the pixel density is sufficiently high (regarding graphene, this always applies if there are $\gtrsim 25$ pixels per Å), the informational content of the image is determined by

[16] Please do not misunderstand: It is a wonder that the stage can do such small mechanical shifts.

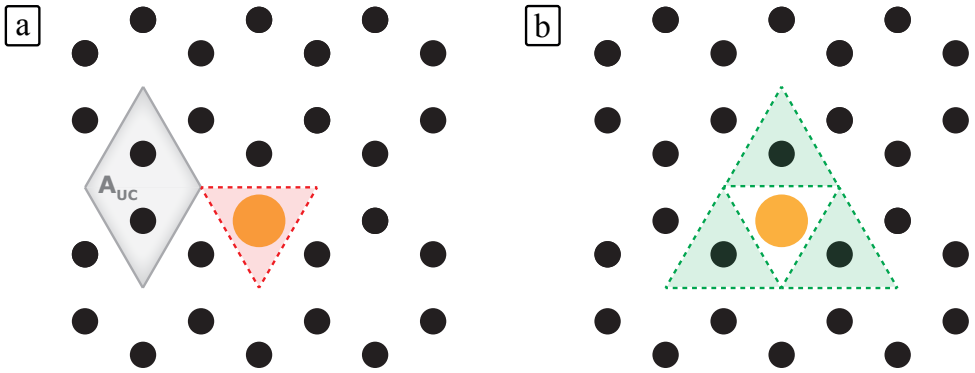

Figure 2.5: Schematics of the regions of interest (ROIs) for different irradiation effects involving three-coordinated impurities in graphene. (a) Replacement of a three-coordinated impurity atom by a C atom; the ROI is the Voronoi cell corresponding to the impurity atom (dash-bordered and shaded in red). (b) Positional exchange of an impurity atom and a C neighbor and KO displacement of a C neighbor; the ROI consists of the Voronoi cells of the three C neighbors (dash-bordered and shaded in green).

the detection time per unit area, in contrast to the pixel density. Concretely, if the FOV is ca. 1×1 nm^2, the scan setting $N_x = N_y = 256$ and $t_\mathrm{p} = 8$ µs results in virtually the same information quality as $N_x = N_y = 512$ and $t_\mathrm{p} = 2$ µs, since their products are equal. Once this equality had been noticed and verified, only the first setting was used.

Knock-on cross section of pristine graphene

The ROI is the entire FOV, since every atom in the field of view is identical. In the SNR limit regime, the frame time is proportional to the chosen FOV (in unit area). A smaller field of view and a lower frame time leads to higher time resolution, although the dose density rate and, thus, the event rate for knock-on damage of pristine graphene stays the same. Nonetheless, a reduction of the FOV has the effect that a larger proportion of the viewed atoms is located at the edge of the FOV. Therefore, a larger fraction of the events will happen at the edge, which will pose the risk of unnoticed events and impact the validity of the experiment. Consequently, the FOV cannot be chosen arbitrarily small. The predominantly used settings in the temperature-dependent KO cross-section measurement (as will be discussed in section 3.2.1) were FOV $\approx 1 \times 1$ nm^2 and 256×256 pixels with a pixel dwell time of $t_\mathrm{p} = 8$ µs.

Cross sections of effects involving impurities in graphene

If the ROI is only a fraction of the FOV (see fig. 2.5), the effective electron dose can be calculated via

$$N_\mathrm{e}^\mathrm{eff} = N_\mathrm{e} \frac{\mathrm{ROI}}{\mathrm{FOV}}, \tag{2.10}$$

where N_e is the (total) electron dose, calculated according to eq. (2.12). For replacement of the impurity by C, the ROI is the area that corresponds to one atom, which is 1/2 of the graphene unit cell area A_UC (neglecting lattice distortions). This means that, here, the assumption that the replacement process is due to electrons impinging on the Voronoi cell of the X@SV impurity. For X-C exchange events and knock-on displacements of a C neighbor, the ROI is $3/2 \times A_\mathrm{UC}$. This situation is also shown in fig. 2.5.

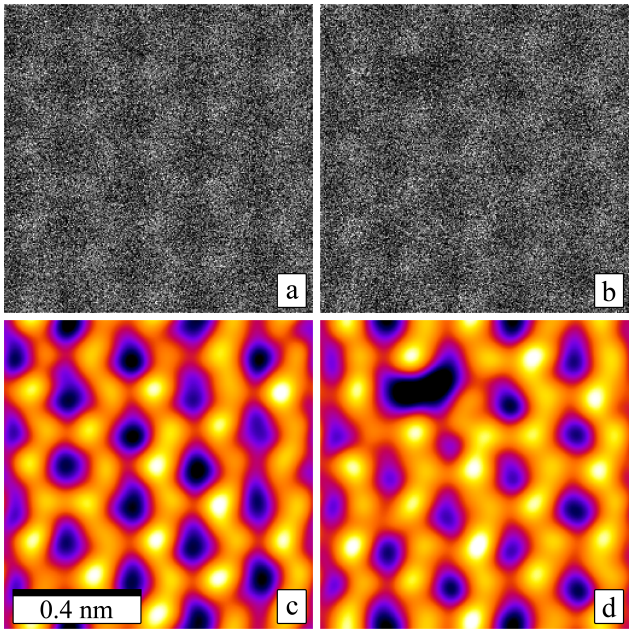

Figure 2.6: MAADF-STEM images of a graphene monolayer before and after electron KO damage ($E_e = 90$ keV). (a, b) Raw images. (c, d) Colored double Gaussian-filtered images. In (b) and (d), there is a single vacancy V_1(5-9) in the upper left corner of the image. The temperature was ca. 100 °C, the pixel dwell time was $t_p = 16$ µs, the number of pixels is $N_x \times N_y = 256 \times 256$ px, and the FOV is ca. 1×1 nm^2. See fig. 3.5 for a schematic illustration of the structure. (Reproduced from Publication I [30]. Published 2022 by Elsevier Ltd. under the CC BY 4.0 license.)

For the voltage-dependent measurement involving Si (section 3.3.1), a frame time of $t_f \approx 0.5$ s ($256 \times 256 \times 8$ µs) and a FOV of either 0.8×0.8 nm^2 (50 keV) or 1×1 nm^2 (65 and 70 keV) was used.

During the temperature-dependent measurement involving Si and P (section 3.3.2), the subscan option of Nion Swift was used. The pixel dwell time as well as the spatial sampling rate were kept constant at $t_p = 8$ µs and 256 pixel nm^{-1}, while the subscan FOV was varied between ca. 0.8×0.8 and 1.2×1.2 nm^2 (thus containing ca. 200×200 to 300×300 pixels).

2.4.1.3 Data acquisition

This section is based on original work in Publication I [30].

First, the experimental approach and the procedure are explained using the example of temperature-dependent KO cross-section measurement of pristine graphene (as will be discussed in section 3.2.1). In fig. 2.6, MAADF-STEM images of pristine graphene immediately before and after a KO damage event at an electron kinetic energy of 90 keV are depicted. Whenever the number of atoms was not conserved, the acquisition was stopped and the FOV was shifted to a pristine region, which amounts to observing a homogeneous Poisson process [126]. When a topological atom-conserving defect, e.g. an SW 5577 defect [56, 133], was noticed and immediately followed by an atom loss, the series was stopped and excluded from any further evaluations (also if such a sequence was observed during the later analysis), because the local threshold energies and cross sections would be different to those of the pristine lattice. However, if the hexagonal structure was restored in

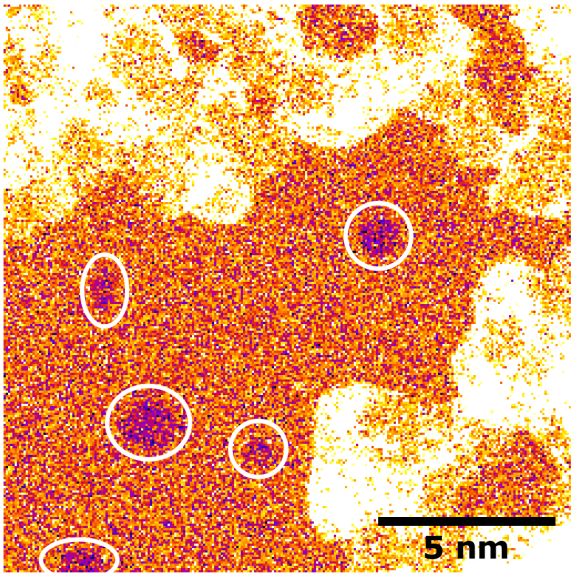

Figure 2.7: MAADF-STEM image of a graphene monolayer (intermediate speckled contrast) with holes created by 90 keV electron irradiation (dark contrast, encircled in white). Bright areas are hydrocarbon contamination. The FOV is ca. 16×16 nm^2.

the subsequent frame, the acquisition was uninterruptedly continued. To facilitate the reader's understanding, a holey graphene monolayer after measuring multiple knock-on damage events at 800 °C is depicted in fig. 2.7. Many of the created vacancies subsequently grew to larger holes by further atom loss under electron irradiation.

As for cross sections involving impurities (section 3.3), some aspects differ slightly. To describe the measurement completely: whenever an impurity exchanged its position with a C neighbor, the acquisition was continued, since the final state is equivalent to the initial state concerning the observable. Whenever a C neighbor was knocked out, leaving a four-coordinated impurity behind, or the impurity was replaced by C, the acquisition was stopped and the FOV was shifted to a region containing a single X@SV. In the very rare case of directly observed SW defects involving an impurity atom, the acquisition was either continued or stopped, depending on whether the structure immediately relaxed back to the hexagonal structure or was followed by a KO displacement of any atom in the FOV.

To make defect detection by the human eye easier (and, in many cases, possible in the first place), the images were blurred by a double-Gaussian kernel [23, 134] during acquisition (see section 2.7.2). All image series were saved, either in a Nion Swift data item or directly in a TIFF file, using the Nion Swift VCR plug-in described in section 2.7.1. The ones related to the KO cross-section measurements of pristine graphene, which is a dataset consisting of just under 200000 images in total, were searched for missing atoms manually with ImageJ [135]. The frame series belonging to the voltage-dependent measurement with the participation of Si impurities (section 3.3.1) consist of ca. 13000 images, which were also checked manually. The 2100 images in the series in connection with the temperature-dependent measurement involving Si and P impurities (section 3.3.2) were analyzed with the assistance of an iPython notebook [136] utilizing a deep learning-based algorithm for recognition of the local structure in (S)TEM images [137].

2.4.1.4 Poisson analysis

This section is based on original work in Publication I [30] and the corresponding supplemental material [122].

Data evaluation after image acquisition is described using the example of temperature-dependent measurement of the KO cross section of graphene (as will be discussed in section 3.2.1). The following can readily be translated to apply to all other investigated processes: in eqs. (2.11) and (2.13), the subscript "KO" has to be replaced by the corresponding abbreviation (as will be introduced in section 3.3) and N_e has to be substituted with $N_\mathrm{e}^\mathrm{eff} = N_\mathrm{e} \times \mathrm{ROI/FOV}$ (eq. (2.10)).

For an individual KO displacement event in pristine graphene, the observed cross section can be calculated by eq. (2.5):

$$s_\mathrm{KO}^\mathrm{obs} = \frac{1}{\rho_A N_\mathrm{e}}, \tag{2.11}$$

where N_e is the electron dose, and ρ_A is the areal atomic density of graphene. Both the VOA current and the frame time were saved to image metadata for every individual frame. The electron dose was calculated by summing up the individual frame doses, which result from the beam current (as a function of the VOA current according to eq. (2.1)) and the frame time:

$$N_\mathrm{e} = \frac{1}{e}\left(\left(\sum_{j=1}^{\delta-1} t_j I_{\mathrm{B},j}\right) + \frac{t_\delta}{2} I_{\mathrm{B},\delta}\right), \tag{2.12}$$

where e is the elementary charge, t_j is the frame time of the j-th frame, $I_{\mathrm{B},j}$ is the beam current during the acquisition of the j-th frame, and δ is the index of the defect frame. The defect frame was counted only half. In the case of image series continued after a positional exchange between an impurity and a C neighbor, the first frame was counted half as well.

For multiple electron doses, the statistical estimator of the cross section is calculated based on the expected dose per event (see eq. (2.6)) and given by

$$\sigma_\mathrm{KO}^\mathrm{obs} = \frac{1}{\rho_A \lambda^\mathrm{PM}} = \frac{1}{\rho_A \overline{N_\mathrm{e}}} \frac{N_\mathrm{KO}^\mathrm{obs} - 1}{N_\mathrm{KO}^\mathrm{obs}}, \tag{2.13}$$

where $\overline{N_\mathrm{e}}$ is the arithmetic mean of the doses, and $N_\mathrm{KO}^\mathrm{obs}$ is the number of observed KO events.

2.4.2 Theoretical model for the knock-on displacement cross section of pristine graphene

This section is based on original work in the supplemental material of Publication I [122].

The kinetic energy transfer E due to an elastic collision between an impinging electron (mass m_0, initial kinetic energy E_e) and a nucleus (mass M, initial velocity v parallel to the momentum of the electron) can be derived from relativistic energy-momentum conservation. As a function of the electron scattering angle θ, it is given by [90]

$$E(E_\mathrm{e}, v, \theta) = \frac{1}{2Mc^2}\left[(Mvc)^2 + 2\left(1 - \cos\theta\right) B(E_\mathrm{e}, v)\right] \tag{2.14}$$

with

$$B(E_\mathrm{e}, v) := E_\mathrm{e}\left(E_\mathrm{e} + 2m_0c^2\right) + Mvc\sqrt{E_\mathrm{e}\left(E_\mathrm{e} + 2m_0c^2\right)}, \tag{2.15}$$

where c is the speed of light in vacuum, and E_{max} is the maximum transferred energy for backscattering at an angle of $\theta = 180°$, which was introduced in eq. (1.4):

$$E_{\mathrm{max}}\left(E_{\mathrm{e}}, v\right) := E\left(E_{\mathrm{e}}, v, \theta = 2\pi\right). \tag{2.16}$$

Assuming that the displacement threshold energy T_{d} (see section 1.5.1) of a lattice atom is isotropic, Mott scattering [138, 139] with the McKinley and Feshbach expansion [140] yields the KO displacement cross section as a function of E_{e} and v [89, 90, 93, 141]:

$$\begin{aligned}\tilde{\sigma}_{\mathrm{KO}}^{\mathrm{theor}}(E_{\mathrm{e}}, v) = 4\pi &\left(\frac{Ze^2}{8\pi\epsilon_0 m_0 c^2 \gamma\beta^2}\right)^2 \\ &\left\{\frac{E_{\mathrm{max}}}{T_{\mathrm{d}}} - 1 - \beta^2 \log\left(\frac{E_{\mathrm{max}}}{T_{\mathrm{d}}}\right)\right. \\ &\left. + \pi Z\alpha\beta\left[2\sqrt{\frac{E_{\mathrm{max}}}{T_{\mathrm{d}}}} - \log\left(\frac{E_{\mathrm{max}}}{T_{\mathrm{d}}}\right) - 2\right]\right\}.\end{aligned} \tag{2.17}$$

Z is the atomic number, e is the elementary charge, ϵ_0 is the vacuum permittivity, and α is the fine structure constant. The relativistic factor of the impinging electron is given by $\beta(E_{\mathrm{e}}) = \{1 - (1 + E_{\mathrm{e}}/m_0/c^2)^{-2}\}^{1/2}$ and its Lorentz factor by $\gamma(E_{\mathrm{e}}) = \left(1 - \beta^2\right)^{-1/2}$. The KO displacement cross section as a function of the electron kinetic energy E_{e} and the temperature T is given by [93]

$$\sigma_{\mathrm{KO}}^{\mathrm{theor}}(E_{\mathrm{e}}, T) = \int_{-\infty}^{\infty} \Theta\left(E_{\mathrm{max}}\left(E_{\mathrm{e}}, v\right) - T_{\mathrm{d}}\right) p(v, T) \tilde{\sigma}_{\mathrm{KO}}^{\mathrm{theor}}(E_{\mathrm{e}}, v)\, dv, \tag{2.18}$$

where Θ is the Heavyside step function and $p(v, T)$ is the out-of-plane velocity distribution [93]

$$p(v, T) = \frac{1}{v_{\mathrm{rms}}(T)\sqrt{2\pi}} \exp\left(-\frac{v^2}{2(v_{\mathrm{rms}}(T))^2}\right), \tag{2.19}$$

whose width is determined by the temperature-dependent root mean square velocity $v_{\mathrm{rms}}(T)$ (square root of eq. (1.5)). As for the numerical integration in eq. (2.18), the limits have to be chosen such that the contributing velocity domain, i.e. the range for which $E_{\mathrm{max}}(E_{\mathrm{e}}, v) \geq T_{\mathrm{d}}$, is fully sampled. Since out-of-plane phonon modes become more populated with increasing temperature, the KO cross section according to eq. (2.18) is expected to increase with rising temperature [93].

2.4.2.1 Generalization to other elastic effects with threshold energies

The McKinley and Feshbach cross-section model outlined above has a universal character in the context of elastic electron-nucleus interactions. Equations (2.17)–(2.19) can be generalized for any elastic process with threshold energies (lower and/or upper threshold). Exemplary for the case of X-C bond inversion introduced in section 1.5.2, abbreviated by "XCDex" for direct exchange of the position between an X@SV impurity and a C neighbor, the elastic cross section is modeled by

$$\sigma_{\mathrm{XCDEx}}^{\mathrm{theor}}(E_{\mathrm{e}}, T) = \sigma_{\mathrm{KO}}^{\mathrm{theor}}(E_{\mathrm{e}}, T)|_{T_{\mathrm{XCDEx}}} - \sigma_{\mathrm{KO}}^{\mathrm{theor}}(E_{\mathrm{e}}, T)|_{T_{\mathrm{d}}}, \tag{2.20}$$

where $\sigma_{\mathrm{KO}}^{\mathrm{theor}}(E_{\mathrm{e}}, T)$ according to eq. (2.18) is evaluated twice, once at the KO displacement threshold energy T_{d} (second term) and once at the lower direct exchange threshold energy T_{XCDEx} in place of T_{d} (first term). Please note that the subscript "KO" is semantically incorrect for the first term, but the notation was kept for clarity.

2.4.2.2 Shortcomings

As supplementary information, please note that eqs. (2.17), (2.18), and (2.20) exclusively consider a single electronic state, which is connected to a state-specific atomic displacement (or direct exchange) threshold energy. The latter is typically calculated for the ground state. Thus, the presented model does not take excited and/or ionized states created due to inelastic scattering into account. It is noted in advance that the experimental cross sections for "XCEx" (exchange of the position between an X@SV impurity and a C neighbor) measured in this work cannot be explained by an elastic model with the form of eq. (2.20). This model will thus deliberately not be compared to the experimental data. Inelastic contributions to the total KO cross section are beyond the scope of this thesis. They can potentially be described in the framework of Bethe theory [142].

As mentioned in section 1.5.1, thermal perturbations of the lattice cause variations in the displacement threshold energy T_d [98], the effect of which is higher at elevated temperatures. Finally, the three-dimensional description (instead of the "$z-$only" model presented above) of electron KO damage of graphene, taking into account scattering events with $\theta < \pi$ and arbitrary azimuth angle of $0 \leq \phi \leq 2\pi$, was recently modeled and studied by a colleague [143].

2.5 Calculation of the carbon adatom migration barrier on graphene

This section is based on original work in Publication I [122]. The DFT simulations were carried out by colleagues.

The carbon adatom migration barrier was theoretically estimated by nudged elastic band (NEB) calculations using the density functional (DFT) theory package GPAW [144]. The finite-difference basis with a grid spacing of 0.18 Å, a 6×6 graphene supercell, and a $6 \times 6 \times 1$ Monkhorst-Pack **k**-point mesh were used. The convergence criterion for the forces was 0.02 eV/Å. The inclusion of dispersion corrections can influence the barrier heights [145, 146]. Thus, three different exchange-correlation functionals have been used: the Perdew-Burke-Ernzerhof functional (PBE) [48], the Tkatchenko-Scheffler (TS) [147] van der Waals (vdW) correction on top of the PBE functional (PBE-TS), and the C09-vdW functional [148], which explicitly treats vdW interactions.

2.6 Regression algorithms and error propagation

Model curves were fitted to experimental data by numerical algorithms. The individual uncertainty of the data points has been taken into account, which yields *weighted* regression methods. As for linear least squares[17] (LSQ) regression, the used SciPy [151] function `optimize.curve_fit`[18] has input parameters for uncertainties, so the latter were be handed over directly. The nonlinear LSQ regression with a trust region reflective algorithm [152] was implemented by using the SciPy

[17] Invention of the least squares method is attributed to Adrien-Marie Legendre [149] and Carl Friedrich Gauss [150].
[18] https://docs.scipy.org/doc/scipy/reference/generated/scipy.optimize.curve_fit.html

module `optimize.least_squares`[19] and the variance-weighted residual variance

$$\tilde{r}^2 = wr^2 = w\left(y_{\text{data}} - y_{\text{fit}}\right)^2, \tag{2.21}$$

where r are the residuals and w are the weights. The latter are given by

$$w = \frac{1}{\left(\Delta y_{\text{data}}\right)^2}, \tag{2.22}$$

where Δy_{data} is the error of the data point. In the case of manually implemented nonlinear LSQ, the residual variance with the same weighting was used. Finally, for orthogonal distance regression (ODR) [153], the SciPy package `odr`[20] was used, which accepts uncertainties regarding both the abscissa and the ordinate.

2.6.1 Propagation of uncertainties and random errors

Parts of this section are based on original work in Publication I [30] and the corresponding supplemental material [122].

While biases (systematical errors) have been avoided to the best of my knowledge, random errors and statistical uncertainties were propagated through the numerical evaluation.

Say a dependent variable is given as a function $f(\boldsymbol{x})$ of the independent variables (parameters) $\boldsymbol{x} = (x_1, x_2, ..., x_n)$. If it is expedient to specify an uncertainty $\Delta f(\boldsymbol{x})$ and to attribute it to the uncertainty or the random error Δx_i of the parameters and the covariance $\text{cov}(x_i, x_j)$ in case of correlated parameters, the so-called variance formula [154] (formerly known as 'Gaussian error propagation') can be used:

$$\left(\Delta f(\boldsymbol{x})\right)^2 = \sum_i \left(\Delta x_i \frac{\partial f(\boldsymbol{x})}{\partial x_i}\right)^2 + \sum_{i \neq j} \frac{\partial f(\boldsymbol{x})}{\partial x_i} \frac{\partial f(\boldsymbol{x})}{\partial j} \text{cov}(x_i, x_j). \tag{2.23}$$

The application of eq. (2.23) in relevant cases is broken down below:

1. Beam current I_{B}, eq. (2.1):

$$\Delta I_{\text{B}} = \sqrt{\left(I_{\text{VOA}} \Delta a_1\right)^2 + \left(\Delta a_2\right)^2 + 2 I_{\text{VOA}} \text{cov}\left(a_1, a_2\right) + \left(a_1 \Delta I_{\text{VOA}}\right)^2}, \tag{2.24}$$

   where $\text{cov}\left(a_1, a_2\right)$ is the covariance of the calibration parameters, obtained from linear LSQ regression using `scipy.optimize.curve_fit`. No correlation was considered between either of the parameters and the VOA current I_{VOA}.

2. Observed cross section σ^{obs}, eq. (2.5):

$$\Delta \sigma^{\text{obs}} = \sqrt{\left(-\frac{1}{\rho_A \lambda^2} \Delta \lambda\right)^2} = \frac{\Delta \lambda}{\rho_A \lambda^2} = \frac{\sigma^{\text{obs}}}{\lambda} \Delta \lambda, \tag{2.25}$$

   where ρ_A is the areal atomic density (of graphene), and λ is the expected electron dose per event.

[19] https://docs.scipy.org/doc/scipy/reference/generated/scipy.optimize.least_squares.html
[20] https://docs.scipy.org/doc/scipy/reference/odr.html

3. Theoretical KO cross section $\sigma_{\mathrm{KO}}^{\mathrm{theor}}$ as a function of the displacement threshold energy T_{d} and the root mean square velocity v_{rms}, eq. (2.18):

$$\Delta\sigma_{\mathrm{KO}}^{\mathrm{theor}} = \sqrt{\left(\frac{\partial\sigma}{\partial T_{\mathrm{d}}}\Delta T_{\mathrm{d}}\right)^2 + \left(\frac{\partial\sigma}{\partial v_{\mathrm{rms}}}\Delta v_{\mathrm{rms}}\right)^2 + 2\frac{\partial\sigma}{\partial T_{\mathrm{d}}}\frac{\partial\sigma}{\partial v_{\mathrm{rms}}}\mathrm{cov}\left(T_{\mathrm{d}}, v_{\mathrm{rms}}\right)}, \tag{2.26}$$

where $\mathrm{cov}\left(T_{\mathrm{d}}, v_{\mathrm{rms}}\right)$ is the covariance of T_{d} and v_{rms}, which was obtained from nonlinear LSQ regression using `scipy.optimize.least_squares`.

4. Carbon adatom migration barrier E_{m} on graphene according to the Arrhenius formalism:

   By logarithmizing eq. (3.8), we obtain the model function y with the parameters b_1 and b_2, which is linear in inverse temperature $1/T$:

$$y\left(\frac{1}{T}\right) := \log\left(k_{\mathrm{KO}}^{\mathrm{theor}}(T) - k_{\mathrm{KO}}^{\mathrm{obs}}(T)\right) = \underbrace{-\frac{E_{\mathrm{m}}}{k_{\mathrm{B}}}}_{=:b_1}\frac{1}{T} + \underbrace{\log A}_{=:b_2}, \tag{2.27}$$

   where $k_{\mathrm{KO}}^{\mathrm{theor}}$ is the theoretical KO rate, $k_{\mathrm{KO}}^{\mathrm{obs}}$ is the observed KO rate, k_{B} is the Boltzmann constant, and A is the pre-exponential factor. The uncertainty according to the variance formula is given by

$$\Delta y = \frac{1}{|k_{\mathrm{KO}}^{\mathrm{theor}} - k_{\mathrm{KO}}^{\mathrm{obs}}|}\sqrt{\left(\Delta k_{\mathrm{KO}}^{\mathrm{obs}}\right)^2 + \left(\Delta k_{\mathrm{KO}}^{\mathrm{theor}}\right)^2}. \tag{2.28}$$

   The uncertainty of $k_{\mathrm{KO}}^{\mathrm{obs}}$ (eq. (3.1)) is

$$\Delta k_{\mathrm{KO}}^{\mathrm{obs}} = N_{\mathrm{KO}}^{\mathrm{obs}}\sqrt{\left(-\frac{1}{t_{\mathrm{tot}}^2}\Delta t_{\mathrm{tot}}\right)^2} = k_{\mathrm{KO}}^{\mathrm{obs}}\frac{\Delta t_{\mathrm{tot}}}{t_{\mathrm{tot}}}, \tag{2.29}$$

   where $N_{\mathrm{KO}}^{\mathrm{obs}}$ is the number of observed KO events, and $t_{\mathrm{tot}} = \sum_i t_i$ is the total time of irradiation (eq. (3.2)). The uncertainty of the latter is given by

$$\Delta t_{\mathrm{tot}} = \sqrt{\sum_i \left(\Delta t_i\right)^2}. \tag{2.30}$$

   As for $k_{\mathrm{KO}}^{\mathrm{theor}}$ (eq. (3.3)), the uncertainty is

$$\Delta k_{\mathrm{KO}}^{\mathrm{theor}} = \frac{\rho_A}{e}\sqrt{\left(\sigma_{\mathrm{KO}}^{\mathrm{theor}}\Delta\overline{I_{\mathrm{B}}}\right)^2 + \left(\overline{I_{\mathrm{B}}}\Delta\sigma_{\mathrm{KO}}^{\mathrm{theor}}\right)^2}, \tag{2.31}$$

   where $\overline{I_{\mathrm{B}}}$ is the mean beam current, whose uncertainty is given by the standard error of the mean [155]:

$$\Delta\overline{I_{\mathrm{B}}} = \frac{\mathrm{std}\left(I_{\mathrm{B}}\right)}{\sqrt{n}}, \tag{2.32}$$

   where $\mathrm{std}\left(I_{\mathrm{B}}\right)$ is the standard deviation of measured beam-current values, and n is their number. The error of the migration barrier results from

$$\Delta E_{\mathrm{m}} = k_{\mathrm{B}}\Delta b_1, \tag{2.33}$$

   where Δb_1 was obtained from ODR (y as a function of $1/T$, eq. (2.27)) using `scipy.odr`.

5. Expectation value of positional exchanges before KO damage, eq. (3.22):

$$\begin{aligned}\Delta E(M) &= \sqrt{\left(\frac{\Delta\sigma_{\mathrm{SiCEx}}}{\sigma_{\mathrm{SiCKO}}}\right)^2 + \left(-\frac{\sigma_{\mathrm{SiCEx}}}{\sigma^2_{\mathrm{SiCKO}}}\Delta\sigma_{\mathrm{SiCKO}}\right)^2} \\ &= \frac{1}{\sigma_{\mathrm{SiCKO}}}\sqrt{\left(\Delta\sigma_{\mathrm{SiCEx}}\right)^2 + \left(E(M)\Delta\sigma_{\mathrm{SiCKO}}\right)^2}, \end{aligned} \tag{2.34}$$

   where σ_{SiCEx} is the cross section for positional exchange between a Si@SV impurity and a C neighbor, and σ_{SiCKO} is the cross section for KO displacement of a C neighbor.

Further, the uncertainty of the observed KO cross section according to the extended healing rate model (eq. (3.17)) when using the DFT-calculated carbon adatom migration barrier, was calculated via

$$\Delta\sigma^{\mathrm{DFT}}_{\mathrm{KO}} = \Delta\sigma^{\mathrm{LSQ}}_{\mathrm{KO}}\frac{\sum\tilde{r}^2_{\mathrm{DFT}}}{\sum\tilde{r}^2_{\mathrm{LSQ}}}, \tag{2.35}$$

where $\tilde{r}^2_{\mathrm{DFT}}$ is the weighted residual variance for the one-parametric LSQ regression using the DFT-calculated barrier, and $\tilde{r}^2_{\mathrm{LSQ}}$ is the weighted residual variance for the two-parametric LSQ regression (both given by eq. (2.21)).

2.7 Developed software packages

The present section represents a description of the purpose and the functionality of the software packages that I either developed or extended in the scope of my work. All packages have been pushed onto an internal Git repository server of the Physics of Nanostructured Materials (PNM) group and can be requested on demand, some of them are additionally published under the free GPL-v3 license on Phaidra[21] and/or GitHub[22], as summarized in the chapter 'Outputs'.

2.7.1 Image recording

When saving consecutive ADF-STEM images and their metadata, it can be beneficial to wrap them together and store them in a single data unit, be it a data item in a Nion Swift library or a file in TIFF format. The image metadata needed to contain experimental parameters and scan timings (i.e. the electron beam current, the field of view, the pixel dwell time, the line time, the probe flyback time, and the microsecond-precise timestamp of when the image was fully acquired). For this purpose, a PNM-internal Nion Swift plug-in called "Video Cam Recorder" (VCR) was used. It communicates with Nion Swift via its Python API [114] and waits for the completion of a new MAADF (or HAADF) image. For this work, some run-time issues were fixed, which resulted in a stable and fluent execution of both the plug-in and Nion Swift. Further, the following features were implemented, removing several shortcomings:

- The core functionality of the plug-in (record and save) was implemented according to the producer-consumer design pattern [156].

[21] Phaidra is the repository for the permanent secure storage of digital assets at the University of Vienna (https://phaidra.univie.ac.at).
[22] https://www.github.com

- Subtasks not updating any graphical user interface (GUI) elements are not run in the main thread of Nion Swift.
- The function `numpy.empty` is utilized to pre-allocate ca. 2 GB of RAM (arbitrary value). Whenever the image stacks being recorded grows larger than that, another 2 GBs are pre-allocated.
- An option to directly save a TIFF file on the file system was added.

2.7.2 Live image filtering

The image stacks for the cross-section measurements reported in section 3.2.1 and section 3.3 were acquired at the limit in terms of the SNR (see section 2.4.1.1). In these raw images, the human eye can reliably recognize whether there is an atom missing in the graphene lattice, but this generally takes longer than the frame time. Thus, a Nion Swift plug-in that is capable of applying a double-Gaussian filter [23, 134] to the live image data item was developed. In the filtered image, which gets updated with a short delay ($\lesssim 100$ ms) after the raw image, the human eye can detect missing atoms quickly enough. At the time of writing this thesis, the functionality of the plug-in had already been implemented as a core feature of Nion Swift, though not based on my development.

2.7.3 Automated single-atom manipulation

In cooperation with several former and present researchers of our group, a modular Nion Swift plug-in with the title Nion Swift Atom Manipulator was written. It is capable of autonomously arranging substitutional impurity atoms in graphene in an arbitrary user-defined pattern. The object-oriented programming approach offers software interfaces wherever needed.

The overall task was divided as listed in table 2.1 and some individual tasks were contributed by others. The architecture is intended to be as modular and reusable as possible, while the user interface is embedded in the Nion Swift environment. Technically, there is the joint module 2 for the tasks (b) and (c), and the individual modules 1, 3, and 4, which manage the tasks (a), (d), and (g). Task (f) is embedded in all modules. Each module is executed in a dedicated thread, but their in- and outputs depend on each other.

Table 2.1: Atom Manipulator: Overview of tasks, modules, and contributors.

AM ... Andreas Mittelberger AP ... Andreas Postl CH ... Christoph Hofer
CM ... Clemens Mangler JM ... Jacob Madsen TS ... Toma Susi

Task		Module		Contributor(s)
(a)	Structure recognition	1	Structure recognition	JM, TS, AP
(b)	Bond detection	2	Structural pathfinding	CH, AP
(c)	Structural pathfinding			AP, TS
(d)	ADF detector feedback	3	TractorBeam	CM, TS, AP, AM
(f)	Microscope control	*	(integrated in 1-4)	AP
(g)	Systems integration	4	Manipulation	AP, JM

2.7.3.1 Structure recognition

Fully convolutional neural networks (FCNNs) [157] are used to detect the atomic structure and identify chemical elements in atomically resolved STEM images [158]. An image analysis tool using a deep learning [130, 137] algorithm was developed by Dr. Jacob Madsen, whom I assisted in acquiring training data, troubleshooting cases of incorrect results, and improving the performance in terms of execution speed. First, the structure recognition module performs a spatial calibration of the image scale. This is accomplished either in reciprocal space by the package "Fourier scale calibration" [159] or in real space by multiple invocations of the FCNN with the sampling rate (in pixels per unit length) as a varying input parameter. Then, the module calls the FCNN to determine atom positions [160], identify atomic and large-scale impurities [63], and assigns their belonging to a chemical element (without any EEL spectra) [161]. The back end of the standalone "Nion Swift Structure Recognition" plug-in, which is available on Phaidra [162], is called by the Atom Manipulator plug-in [163]. The structure detected by this module will be illustrated in figs. 2.9, 2.10, and 3.16.

2.7.3.2 Bond detection

Another piece of code covers the detection of bonds after the atom positions are determined. Here, ideas by our group have been realized. The implemented bond algorithm makes sure that carbon atoms are considered to have a shared bond if their inter-atomic distance is below a user-defined threshold, but also that each carbon atom has at most four bonds, and that there occur no triangles in the saved bond configuration.

2.7.3.3 Structural pathfinding

This task is to ascertain the fewest possible number of manipulation events, i.e. the shortest total path length, to move an arbitrary number N of impurity atoms into a user-defined configuration consisting of N target (lattice) sites, at each of which an atom is located.

Approaches to the definition of a metric
The path length is defined by the number of necessary X-C exchange events, in contrast to the Euclidean distance [164] between atoms i and j, which is given by

$$d_{ij} := \left((x_i - x_j)^2 + (y_i - y_j)^2 \right)^{1/2} \tag{2.36}$$

in Cartesian coordinates. Thus, another metric had to be found and defined before the mutual assignment of impurities and target sites.

The idea of three-parametric "unit cell coordinates" (κ, λ, η) was contrived, as illustrated in fig. 2.8. The first two coordinates – κ and λ – unambiguously refer to the unit cell, and the third coordinate – $\eta = 0, 1$ – refers to the sublattice. A metric applicable to pristine graphene was defined. It is similar to the taxicab metric[23] [165], the principle of which dates back to H. Minkowski [166]. The distance in terms of the number of bonds (to be inverted) is given by

$$\delta_{ij} := 2 \max \left(|\kappa_i - \kappa_j|, |\lambda_i - \lambda_j|, |\xi_{ij}| \right) + \epsilon_{ij}, \tag{2.37}$$

[23] Synonyms: city-block metric, Manhattan metric.

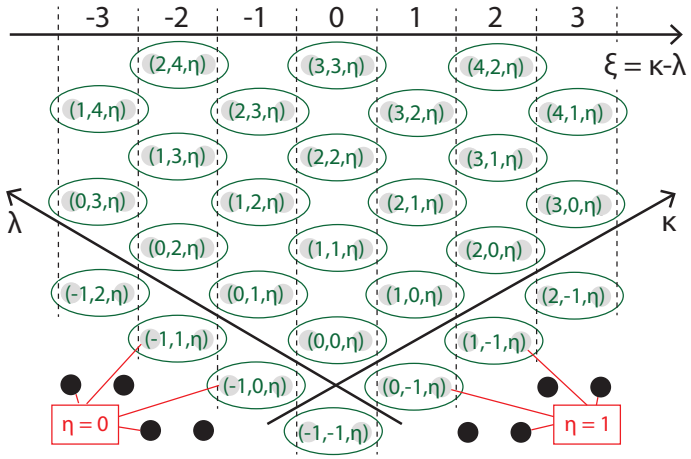

Figure 2.8: Concept of a three-parametric coordinate system (κ, λ, η) for monolayer graphene. The first two coordinates give the position of a unit cell in two zigzag directions (congruent with conventional lattice vectors, which are typically denoted as $\boldsymbol{a_1}$ and $\boldsymbol{a_2}$), and the third coordinate refers to the sublattice. The auxiliary coordinate $\xi = \kappa - \lambda$ gives the position along an armchair direction.

with the directional armchair separation

$$\xi_{ij} = (\kappa_j - \lambda_j) - (\kappa_i - \lambda_i), \tag{2.38}$$

and the sublattice correction term

$$\epsilon_{ij} := (\eta_j - \eta_i)\,\mathrm{sgn}\left((\eta_j - \eta_i)\xi_{ij}\right), \tag{2.39}$$

where sgn is the signum function with the alternative definition

$$\mathrm{sgn}(a) := \begin{cases} -1 & \text{if } a < 0 \\ 1 & \text{if } a \geq 0. \end{cases} \tag{2.40}$$

The expression according to eq. (2.39) seems more complicated than it factually is. To explain based on fig. 2.8: if both atoms are in the same sublattice, ϵ_{ij} will be zero. If atom i is in the left sublattice ($\eta = 0$), atom j is in the right sublattice ($\eta = 1$), and j is further right – or further left – than i, then ϵ_{ij} will be one or minus one. The situation for i in the right sublattice and j in the left one is analogous. It turned out, however, that this implementation is not practical because it is disadvantageous in two respects. First, the computational effort to find the coordinate set (κ, λ, η) for every detected atomic position is tremendously high, because the positions have to be sorted based on Cartesian coordinates and the lattice vectors (in κ- as well as λ-direction) have to be determined accurately. Second, if the detected structure deviates from the hexagonal in some region (due to lattice defects or contamination), these coordinates, as well as the metric, will not be applicable.

As a consequence, the embedding of the atoms was switched to a fully object-oriented approach. Every atom is instantiated, treated as an object, and has a property `neighbors`, containing all other atom objects with which it was found to have a bond (see section 2.7.3.2). Using a custom neighbor-based metric (also based on the taxicab metric), the distance between atoms i and j in

terms of the number of bonds (to be inverted) is recursively given by

$$c_{ij} := \begin{cases} 0 & \text{if } j = i \\ 1 & \text{if } j \in \text{neighbors}(i) \\ 1 + c_{kj} & \text{else,} \end{cases} \tag{2.41}$$

where k is the neighbor of i (or one of i's neighbors*) with the least Euclidean distance (eq. (2.36)) to j among all neighbors of i. In computational regards, this is the most efficient solution so far. For M impurity atoms and N target sites, a M-by-N cost matrix C is saved. Its matrix elements are c_{ij}.

*Note: Commonly, different paths from the site i to j through the graphene lattice may have the same length due to symmetry reasons, thus any chosen metric can result in an ambiguity of the shortest path.

Mutual assignment of substitutional atoms and target sites: Cost minimization
The *minimization of the total path length*, counted as the number of positional exchanges, is carried out as follows. Consider a set $\{\boldsymbol{x}_{\mathrm{s}_i}\}$, $i = 1, 2, ..., M$, of source positions and a set $\{\boldsymbol{x}_{\mathrm{t}_j}\}$, $j = 1, 2, ..., N$ (with $N \leq M$), of target positions, the latter of which constitutes a user-defined end configuration consisting of N substitutional atoms. The total task is a set $\{a_j\}$, $i = 1, 2, ..., N$, of subtasks. Subtask a_j is defined as: "Put one substitutional atom to position $\boldsymbol{x}_{\mathrm{t}_i}$". If a subset of N substitutional atoms are considered workers on the initial positions $\{\boldsymbol{x}_{\mathrm{s}_i}\}$, $i = 1, 2, ..., N$, the total task is abstracted to a linear assignment problem (LAP). Such problems can be solved using the SciPy [151] function `optimize.linear_sum_assignment`, which is an implementation of the Jonker-Volgenant algorithm [167, 168], a variant of the Kuhn-Munkres algorithm (Hungarian method) [169, 170]. The function yields the minimum cost of the total task, meaning that it minimizes the sum of the single path lengths. This is done by optimally picking *one element per column* from the cost matrix C. If there are either more heteroatoms than target positions or vice versa ($M \neq N$), the total cost will also be optimized with regard to the $\min(M, N)$-element subset to be selected, which rises the computational effort by a factor $\binom{\max(M,N)}{\min(M,N)}$. In figure fig. 2.9, the resulting paths for manipulating multiple substitutional atoms to a recognizable pattern are depicted based on simulated ADF-STEM images.

Application of restrictive rules after cost optimization
The LAP's minimum cost solution is a set of subpaths where individual subpaths do not intersect at a single cross-over. A proof is omitted here, but this seems immediately obvious – and no exception was found during extended tests with the graphene structure. However, some of the paths may lead along equal partial routes. Additionally, the subpath of an impurity might direct it close to the position of another impurity. Since two Si atoms can likely not be moved away from each other once they are close (significantly reduced embedding energy per Si atom if the atom separation is below three lattice sites, see section 1.6.2), it must be forbidden that any two substitutional atoms become nearest or second-nearest neighbors at any time – except in the final configuration, if the user sets this by defining the target sites.

This rule was addressed with different approaches. For the initial subpath sequence, the subpaths were sorted by length in ascending order. The subpaths are analyzed regarding *proximity conflicts* – as described above – one after the other, starting with the first subpath in the sequence. If the subpath of an impurity is blocked by another impurity, one of its nearest neighbors or one of

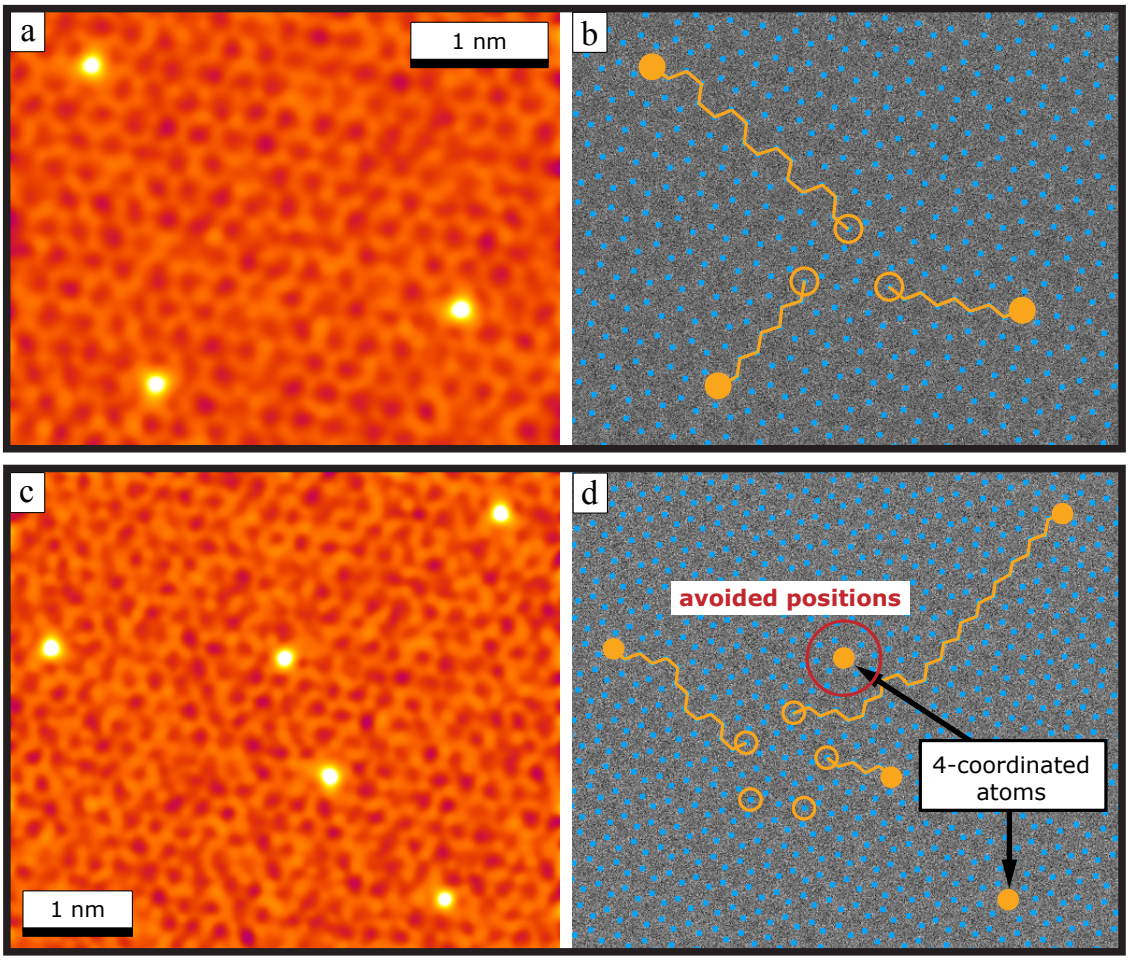

Figure 2.9: Structural pathfinding: Resulting subpaths for manipulating multiple impurities to a given pattern. The set of subpaths was optimized using the Hungarian method. (a, c) Colored Gaussian-filtered simulated ADF-STEM images of suspended monolayer graphene with Si impurities. (b, d) Raw images with overlays for the recognized atomic positions (filled blue squares for C, filled orange circles for Si), the user-defined target sites (non-filled orange circles), and the calculated individual paths (solid orange lines). Four-coordinated impurities are automatically excluded, and their nearest as well as second-nearest neighbors are avoided (red circle).

its second-nearest neighbors, a non-blocked alternative subpath[24] will be calculated. The initially calculated subpath will be substituted if the non-blocked subpath has the same length (as noted above, sites might have multiple connecting paths with the same length). Otherwise, if the non-blocked subpath is longer, a *case distinction* will be made (the impurity's subpath dealt with at the time will be referred to as blocked subpath):

1. If the blocked subpath leads over the initial position of another impurity (*direct block*) that is planned to be moved later according to the current subpath sequence, the subpath of the blocking impurity will be placed before the blocked subpath. Additionally, if the target site of a directly blocking impurity causes a blockage – either directly or indirectly (due to neighbors), and disregarding whether the blocking subpath was initially planned earlier or later – the target sites of the two concerned impurities will be exchanged (see fig. 2.10b). This

[24] This might not be the shortest of all available non-blocked paths.

concept was described and similarly put into practice with scanning tunneling microscopy (STM) on a larger scale [9]. The procedure does not increase the total path length, since the rear parts of both concerned subpaths start at the initial site of the blocking impurity.

2. If the blocked subpath leads across a nearest or second-nearest neighbor of another impurity (*indirect block 1*) that is planned to be moved earlier, the blocking subpath will be placed after the blocked one. Then, the algorithm is reinitialized based on the altered subpath sequence (fig. 2.10c). To prevent endless loops, such subpath swaps can be applied at most once to the same impurity pair.

3. If the blocked subpath leads via a nearest or second-nearest neighbor of another impurity (*indirect block 2*) that is planned to be moved later, a procedure analogous to direct blocks will be proposed: the blocking subpath will be suggested at an earlier point in the sequence, and if the target site of an indirectly blocking impurity causes a blockage, exchange of the corresponding target sites will be proposed. Then, the summed length of the two hypothetical subpaths will be calculated. If, and only if, the sum is strictly smaller than the non-blocked subpath (as discussed before this case distinction) added together with the blocking subpath, the proposal will be put into effect. Otherwise, the non-blocked subpath will be used (fig. 2.10d and f).

4. Cases 1 to 3 will be applied iteratively if a blockage is caused by multiple impurities, starting with the impurity that is last along the blocked subpath.

This behavior comes with the risk of obtaining a total amount of jumps that is larger than the shortest non-conflicting subpath set by a comparably small number, because in contrast to ref. [9], not only the impurity atoms but also their nearest and second-nearest neighbors need to be considered. Path optimization with these boundary conditions is a challenge, and further optimization could improve this module slightly.

2.7.3.4 ADF detector feedback

Our research group wrote a Nion Swift plug-in that reads out the voltage from a Keithley[25] measurement unit directly connected with the MAADF or HAADF detector inside the microscope. The application detects voltage rises and drops. After comparing them with a user-defined threshold for the relative change in voltage, interprets them as X-C exchange events or specimen drifts during the spot irradiation of a C neighbor [18]. The functionality of the standalone "TractorBeam" plug-in [171] is mirrored in the TractorBeam module of the Atom Manipulator.

2.7.3.5 Microscope control

This task is about starting scans before the structure recognition module (Tasks (a) and (b)) is called, stopping scan mode after an image was completed, directing the electron beam to move an impurity along the path calculated by the pathfinding module (Task (c)), and re-scanning after the TractorBeam module detected a "jump" event or "drift", or timed out (Task (d)). The Nion Swift API is used to translate software commands to hardware control signals. The implementation of this task into the various modules was the centerpiece of my work's automation part.

[25] Keithley Instruments, LLC; https://www.tek.com/keithley.

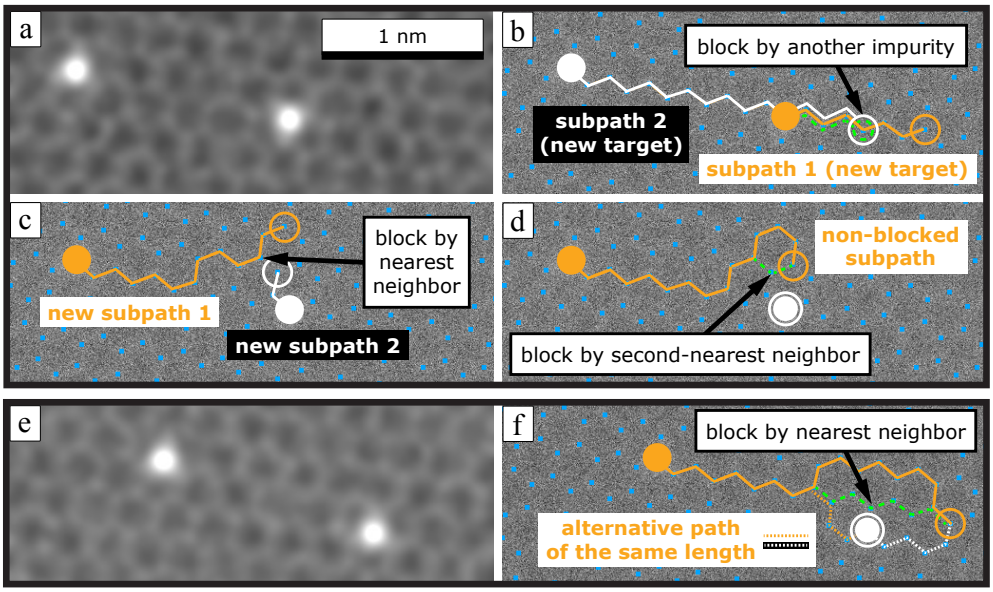

Figure 2.10: Structural pathfinding: Resolution of two conflicting subpaths using different strategies. (a, e) Gaussian-filtered ADF-STEM of suspended monolayer graphene with Si impurities. (b-d, and f) Raw images with overlays for the recognized atomic positions (filled blue squares for C, filled circles for Si), the user-defined target sites (non-filled circles), and the calculated individual subpaths (solid and dashed lines). (b) Initially, the subpath (green dashed line) of the Si atom more right in the image (orange) leads to the target site more left in the image (white). This causes a direct blockage of the other silicon's subpath, which corresponds to a case 1 proximity conflict according to the main text. To resolve it, the corresponding target sites are exchanged. (c) The nearest neighbor of the right impurity's target site causes a blockage. Initially, the execution of its subpath – shorter than the other – is planned first. This case 2 proximity conflict is resolved by exchanging the subpath execution order. (d) The subpath (green dashed line) of the impurity more left in the image (orange) is blocked by the second-nearest neighbor of an impurity that is located at its target site (white). This is a case 3 proximity conflict, resolved by using the non-blocked subpath as indicated, since moving the right impurity to the upper target site and, subsequently, moving the left impurity to the remaining target position, results in an equally long total path. (e) Similar to (d), with a nearest neighbor causing the blockage. The alternative path of the same length is indicated by short-dashed lines.

2.7.3.6 Systems integration

The last part, the so-called atom manipulation module, ensures the communication among the above-mentioned modules via events and listeners and calls the individual modules either one by one (mode B, "Single execution") or sequentially and continuously (mode A, "Auto Manipulation"). There is another endless mode ("Live Analysis") where imaging never stops[26] but the TractorBeam module is skipped. Furthermore, the module offers the features to work with simulated ADF-STEM data and manually create a fresh live data item in Nion Swift. Finally, there is an option to automatically save all frames being created during execution in mode B, both the raw data as well as with graphical overlays indicating the atomic positions and the optimized paths. Using this option is a must for scientific reproducibility and should guarantee that complete experimental data is stored.

[26]Once the structure recognition module has finished processing an image, it is fed with the next complete image.

Description of the working procedure

Once a sample region with incorporated impurity atoms has been found by the user, the structure recognition module needs to be manually called once and fed with an atomically resolved image. Then, the user can define a pattern of target sites. From there, the demanded user input demand is minimal: press the button "Start Atom Manipulator". The computer is then commanded to control the instrument and autonomously rearrange multiple impurities in graphene by single-atom manipulation to form a pattern (e.g. a character, a quantum corral, ...) [19]. Note that this is accomplished in a way that is very close to the best possible one (accurate structure recognition, almost optimal path, rapid and precise beam movement), potentially eliminating human error and optimizing the probability of a successful outcome.

3 Results and discussion

This chapter presents the results obtained during the thesis research. First, the electron beam will be characterized: on the one hand, the calibration of the beam current is essential for determining any cross sections of beam-induced effects. On the other hand, a precise reconstruction of the electron-probe shape was necessary to conclusively interpret the temperature-dependent electron KO cross-section measurement of pristine graphene, which will be dealt with in the second section. The observed radiation hardness of graphene at elevated temperatures will be reproduced by an elaborated model describing electron knock-on damage with counteracting healing of vacancies due to the recombination with surface-diffusing carbon adatoms.

Then, cross-section measurements of electron-beam induced atom displacements associated with three-coordinated impurities in graphene will be reported. At ambient temperature, dynamics involving Si@SV will be quantified for electron kinetic energies from 50 to 70 keV. Following the presentation of the analyzed data, the success probability for single-atom manipulation of Si@SV will be discussed. For 60 keV, further data for dynamics involving Si@SV, as well as P@SV, at temperatures from ambient to ca. 1000 °C will be discussed.

Subsequently, the incorporation of Al into graphene using two different experimental methods – ion implantation, and two-step substitution of C – will be evaluated. It is noteworthy that both methods, especially two-step substitution, produced specimens with an increased density of substitutional Si impurities.

The last section will first address my efforts to advance high-control single-atom manipulation in graphene using STEM. The first operations of the developed software to perform automated manipulation of multiple Si atoms will be documented. Finally, my experimental proceedings in the context of the manipulation of multiple Si atoms to a pattern will be covered.

3.1 Characterization of the electron beam

3.1.1 Calibration data for the beam current

As described in section 2.3.1, the beam current I_B was regularly measured as a function of the VOA current I_{VOA}, which is tracked and saved to image metadata by Nion software. Its error was assumed to be $\Delta I_{VOA} = 1$ nA. In table 3.1, the calibration parameters a_1 and a_2 according to eq. (2.1) are summarized for all measurement series. To show in an exemplary way, the beam current measurements and the calibration lines for an acceleration voltage $U = 70$ kV are depicted in fig. 3.1. These measurements belong to the scope of the voltage-dependent cross sections of dynamics involving Si@SV impurities (as will be discussed in section 3.3.1).

Table 3.1: Parameters and their standard errors for all beam-current calibrations at different acceleration voltages U and on different dates, obtained from a least-squares fit with the model function $I_\mathrm{B} = a_1 I_\mathrm{VOA} + a_2$ (see eq. (2.1)), where I_B is the beam current, and I_VOA is the virtual objective aperture current.

V-dep. ... voltage-dependent
T-dep. ... temperature-dependent

U [kV]	Date	a_1 [10^{-3}]	Δa_1 [10^{-3}]	a_2 [pA]	Δa_2 [pA]	Measurement	Notes
50	2022-01-13	1.083	0.010	-0.34	0.09	V-dep., Si	
60	2019-10-10	4.331	0.013	0.60	0.40	T-dep., Si/P	*
65	2022-03-02	1.004	0.013	1.10	0.20	V-dep., Si	
70	2022-01-18	1.266	0.004	-0.09	0.07	V-dep., Si	
70	2022-02-16	1.112	0.009	1.71	0.13	V-dep., Si	
90	2020-03-11	1.808	0.012	1.50	0.50	T-dep., pristine	
90	2020-05-06	1.504	0.008	3.50	0.40	T-dep., pristine	
90	2020-05-21	1.790	0.020	5.60	0.60	T-dep., pristine	
90	2020-06-05	1.669	0.020	8.30	1.30	T-dep., pristine	
90	2021-06-11	1.438	0.030	0.70	0.70	T-dep., pristine	
90	2021-06-30	2.815	0.050	0.80	0.80	T-dep., pristine	**

* The offset of the electrical measurement unit was not measured, but instead estimated by extrapolation. Further, please note that a new tip (electron source) was installed shortly before this measurement, which is why the typical beam current was higher when compared to all later measurements.
** Outlier (possibly related to a dirty tip). The related experiment, i.e. the data point at $T = 45$ °C ≈ 318 K of the temperature-dependent KO cross sections of pristine graphene (see section 3.2.1), was excluded from any further analyses.

3.1.2 Electron-probe shape

The probe shape reconstructed by the algorithm described in section 2.3.2 and applied to a MAADF-STEM image featuring a point defect is depicted in fig. 3.2. Four Gaussian components in the probe shape $g(x, y)$ according to eq. (2.3) were sufficient[1]. The fit parameters are summarized in table 3.2 and the resulting superposition has a full width at half maximum (FWHM) of (1.16 ± 0.01) Å. Note that a single Gaussian curve leads to qualitatively similar results.

Table 3.2: Fit values for the reconstruction model $g = \sum_j a_j \exp\left(-(...)/c_j\right)$ of the electron-probe shape (see eq. (2.3) for the full notation). j is the running index, a_j is the height of the j-th Gaussian component, and $\sigma_j = \sqrt{c_j/2}$ is the standard deviation of the j-th component.

j	a_j [arb. u.]	σ_j [Å]
1	4.0727	0.4426
2	2.6470	0.4885
3	0.6514	0.7139
4	0.4172	1.3252

[1] Adding more components does not lead to an improvement in accuracy.

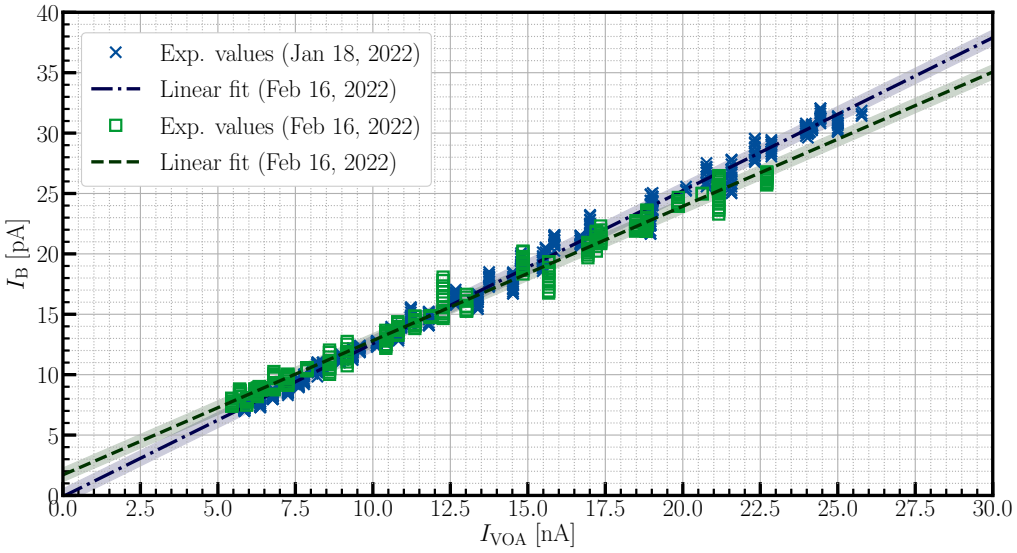

Figure 3.1: Beam current I_B as a function of the virtual objective aperture current I_{VOA} at an acceleration voltage of 70 kV.

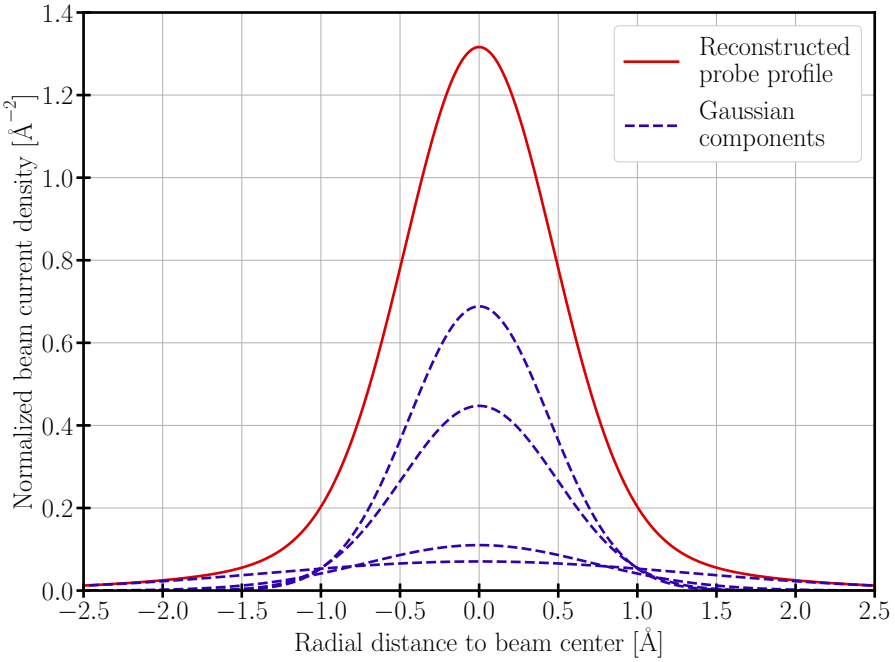

Figure 3.2: Reconstructed beam-current density as a function of the radial distance to the beam center, fitted by four Gaussian components. (Adapted from Publication I [30]. Published 2022 by Elsevier Ltd. under the CC BY 4.0 license.)

3.2 Electron knock-on damage of pristine graphene

This section is based on original work in Publication I [30] and the corresponding supplemental material [122].

The initial aim of the experimental study that Publication I is based on was the measurement of the electron knock-on damage cross section for pristine graphene as a function of the temperature, from ambient to 1000 °C. Since the experimental results ought to be statistically robust, a large enough set of electron doses for individual KO events was to be measured at each temperature. At an electron kinetic energy of 60 keV, which is standard for STEM investigations of graphene, the KO damage rate is virtually zero and thus the acquisition of such data is not possible. In contrast, the KO cross section for 90 keV electrons is in the range of 5–20 mb at ambient temperature [93] (^{12}C lattice atoms). For a typical beam current of 50 pA, this yields a predicted KO displacement event rate of ca. 0.35–1.45 min^{-1} (one per 40–170 s) according to eq. (3.3). Therefore, an acceleration voltage of 90 kV seemed to fit well for this purpose. Furthermore, it should be noted that tremendously rising displacement rates were expected with increasing temperature (see section 2.4), and in order to still be able to accurately time-resolve the damage effects, the maximum operating voltage (100 kV) of the Nion UltraSTEM 100 was not selected.

3.2.1 Temperature-dependent knock-on cross section at 90 keV

In stark contrast to the prediction based on the first-principles model (see section 2.4.2), the calculated observed KO cross section $\sigma_{\mathrm{KO}}^{\mathrm{obs}}(T)$ does not increase with temperature, but rather decreases (see table 3.3). This contradicts the vibration-assisted KO model for $\sigma_{\mathrm{KO}}^{\mathrm{theor}}(E_{\mathrm{e}}, T)$ (eq. (2.18)), according to which the cross section must increase with rising temperature. As phonon modes are increasingly thermally occupied, $\sigma_{\mathrm{KO}}^{\mathrm{obs}}(T)$ does not represent the true temperature-dependent KO cross section. Moreover, no significant difference with regard to varying frame acquisition times from 2 to 0.5 s was observed. Therefore, further analyses were performed with data merged for each temperature, as listed in table 3.3.

As will be described in section 3.2.3, the (hypothesized) reason for the discrepancy between experiment and theory is thermally activated carbon adatom migration and recombination with vacancies, so that a fraction of the latter heals out before observation in the STEM image.

3.2.2 Refinement of the displacement threshold energy and the root mean square velocity of the nuclei

Estimates for the displacement threshold energy T_{d} as well as the out-of-plane root mean square velocity of the nuclei $v_{\mathrm{rms}}(T)$ were given in section 1.5.1. Both variables may be subject to inaccuracies, and each of them is included as a parameter in the KO model for $\sigma_{\mathrm{KO}}^{\mathrm{theor}}(E_{\mathrm{e}}, T)$ according to eq. (2.18). The experimental KO cross section at 90 keV was accurately measured at ambient temperature ((11.3 ± 0.8) mb, see table 3.3). Hence, it was used along with earlier measurements for 85, 95, and 100 keV [93] to refine T_{d} as well as $v_{\mathrm{rms}}(T)$ within reasonable limits.

A nonlinear regression was performed to fit $\sigma_{\mathrm{KO}}^{\mathrm{theor}}(E_{\mathrm{e}}, T)$ to the combined energy-dependent data at ambient temperature, which is listed in table 3.4. The values $T_{\mathrm{d}} = (21.03 \pm 0.10)$ eV and $v_{\mathrm{rms}}(300\ \mathrm{K}) = (590 \pm 20)\ \mathrm{m\,s^{-1}} = (1.05 \pm 0.03) \times v_{\mathrm{rms}}^{\mathrm{phDOS}}(300\ \mathrm{K})$ were obtained by variance-

Table 3.3: Temperature-dependent cross section for KO damage of pristine graphene at an electron kinetic energy of 90 keV. The datasets for different scan parameters (pixel dwell time, number of pixels, FOV) were merged with respect to the temperature T. $\overline{I_B}$ is the mean beam current, N_{KO}^{obs} is the number of observed KO damage events, σ_{KO}^{obs} is the observed KO cross section, and σ_{KO}^{theor} is the theoretical KO cross section according to the McKinley and Feshbach model (see eq. (2.18)). ΔT is approximately 2 % of the absolute value. (Adapted from the Supplemental Material of Publication I [122]: the values for the mean beam current were corrected and supplemented with uncertainties.)

T [K]	$\overline{I_B}$ [pA]	N_{KO}^{obs}	σ_{KO}^{obs} [mb]	σ_{KO}^{theor} [mb]
300	116.6 ± 0.2	196	11.3 ± 0.8	10.7
333	127.6 ± 0.2	108	10.6 ± 1.3	12.9
373	128.8 ± 0.2	179	9.7 ± 0.9	16.0
473	106.4 ± 0.1	86	2.8 ± 0.3	26.5
573	123.5 ± 0.2	132	6.0 ± 0.6	41.1
673	115.5 ± 0.1	138	2.5 ± 0.2	59.9
873	107.0 ± 0.1	183	3.9 ± 0.4	108.7
1073	140.8 ± 0.1	52	3.6 ± 0.8	169.8

Table 3.4: Voltage-dependent cross section for KO damage of pristine at ambient temperature. E_e is the electron kinetic energy, N_{KO}^{obs} is the observed number of KO damage events, and σ_{KO}^{obs} is the observed cross section. For the cross-section values with asymmetric errors (ref. [93]), the weights $w = 2/\left((\Delta^+)^2 + (\Delta^-)^2\right)$ were used in the nonlinear LSQ regression described in the main text.

E_e [keV]	N_{KO}^{obs}	σ_{KO}^{obs} [mb]	$\Delta^+\sigma_{KO}^{obs}$ [mb]	$\Delta^-\sigma_{KO}^{obs}$ [mb]	Origin	Notes
85	15	1.2	0.8	0.5	[93]	
90	196	11.3	0.8	0.8	this study	
90	21	11	10	5	[93]	*
95	67	57	24	17	[93]	
100	61	330	120	90	[93]	

* In the regression, this value was superseded by our more accurate new measurement.

weighted least squares (LSQ) with a trust region reflective algorithm [152]. The experimental data points and the fit curve are depicted in fig. 3.3.

3.2.3 Vacancy healing by recombination with diffusing carbon adatoms

The discrepancy between the knock-on model for elastic electron-nucleus interaction according to eq. (2.18) (as will be illustrated with a green line in fig. 3.6) and the experimental results can be explained by short-lived vacancies that are not accessible to observation because they get healed out by carbon adatoms soon after creation. If there is any energy barrier involved in the healing of vacancies, the process rate must have a temperature dependence and the proportion of undetected vacancies will increase with rising temperatures. A model which describes this should provide information about the highest involved barrier. Thus, under the assumption that the surface-diffusion of carbon adatoms governs vacancy healing (rather than the lattice incorporation itself), it was possible to measure their migration energy barrier, which is described in detail below.

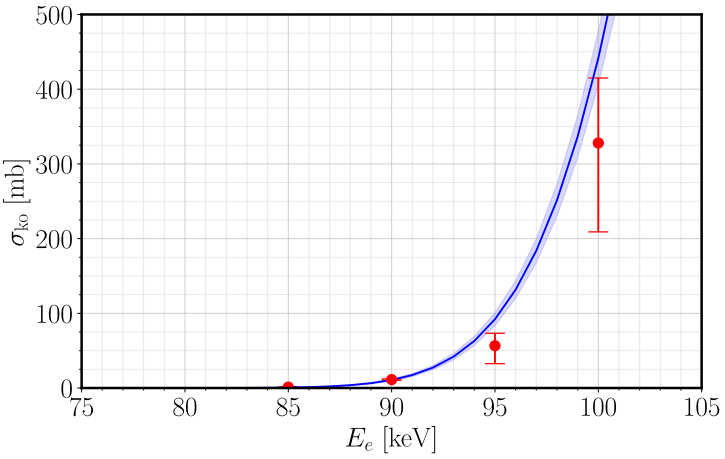

Figure 3.3: Cross section for KO damage of pristine graphene as a function of the incident electron kinetic energy at ambient temperature: Experimental values (red points) and the theoretical curve according to the McKinley and Feshbach model (blue line, see eq. (2.18)). (Reproduced from the Supplemental Material of Publication I [122]. Published 2022 by Elsevier Ltd. under the CC BY 4.0 license.)

The observed KO cross section is close to the theoretical one at temperatures up to ca. 350 K, which implies that the recombination rate of carbon adatoms and vacancies is low compared to the rate of further atom loss next to a vacancy at typical beam currents of 50–100 pA with an electron kinetic energy of 90 keV. At higher temperatures, in contrast, the recombination rate greatly exceeds even the highest possible frame acquisition rate of 2 s^{-1} (see section 2.4.1.2). In the following, the effect is quantified step-wise with increasing elaboration, which provides an explanation of the increased radiation hardness of graphene samples at elevated temperatures.

In terms of knock-on damage rates (events per unit time), the experimentally observed rate at a given temperature T is simply given by

$$k_{\mathrm{KO}}^{\mathrm{obs}}(T) = \frac{N_{\mathrm{KO}}^{\mathrm{obs}}(T)}{t_{\mathrm{tot}}(T)}, \tag{3.1}$$

where $N_{\mathrm{KO}}^{\mathrm{obs}}(T)$ is the number of observed KO events and $t_{\mathrm{tot}}(T)$ is the total time of irradiation. The latter is the sum of the individual irradiation times $t_i(T)$ until a KO event:

$$t_{\mathrm{tot}}(T) = \sum_i t_i(T). \tag{3.2}$$

The errors of the times $t_i(T)$ were assumed to be half of the frame time ($\Delta t_i(T) = t_{\mathrm{f}}/2$). The theoretically predicted rate is

$$k_{\mathrm{KO}}^{\mathrm{theor}}(T) = \frac{I_{\mathrm{B}}}{e}\,\rho_A\,\sigma_{\mathrm{KO}}^{\mathrm{theor}}(T), \tag{3.3}$$

with I_B being the beam current, e the elementary charge, and ρ_A the areal atomic density of graphene. For the calculation of eq. (3.3), the arithmetic mean $\overline{I\mathrm{B}}$ of all beam-current values measured at a given temperature was used. The difference between $k_{\mathrm{KO}}^{\mathrm{obs}}$ and $k_{\mathrm{KO}}^{\mathrm{theor}}$ is assumed to be healing rate of vacancies

$$k_{\mathrm{h}}(T) = k_{\mathrm{KO}}^{\mathrm{theor}}\,(I_{\mathrm{B}}, T) - k_{\mathrm{KO}}^{\mathrm{obs}}(T). \tag{3.4}$$

On the other hand, the vacancy healing rate can be put in relation with an energy barrier E_b via the semi-empirical Arrhenius dependence [75]

$$k_\mathrm{h}(T) = A \exp\left(-\frac{E_\mathrm{b}}{k_\mathrm{B}T}\right), \tag{3.5}$$

where A is the pre-exponential rate constant and k_B the Boltzmann constant. Vacancy healing can very likely be described by a chain process consisting of the surface diffusion of a carbon adatom and the recombination of a vacancy with an adatom that diffused into its immediate proximity. Then, two process rates and two energy barriers are involved, one each for adatom migration and recombination. After postulating that the recombination barrier E_r is negligible, the barrier E_b can be substituted with the adatom migration barrier E_m. Combining eqs. (3.4) and (3.5) yields

$$k_\mathrm{KO}^\mathrm{theor}(T) - k_\mathrm{KO}^\mathrm{obs}(T) \overset{E_\mathrm{r}=0}{=} A \exp\left(-\frac{E_\mathrm{m}}{k_\mathrm{B}T}\right). \tag{3.6}$$

Note: The assumption that the healing process is governed by the surface migration of carbon adatoms is maintained from here.

The evaluation of the simplified Arrhenius model (see eq. (3.6)) is depicted in a semi-logarithmic Arrhenius plot (see fig. 3.4) and yields a carbon adatom migration barrier of $E_\mathrm{m} = (157 \pm 8)$ meV, in contradiction to the 0.40–0.44 eV obtained from our DFT calculations (see below for detail). The Arrhenius treatment is too naive in this context and does not allow a valid interpretation of this particular experiment. At temperatures above 400 K, the observed cross section and, hence, the damage rates are very low compared to the expectation. The observed values could be called "noise": the predicted damage rate according to eq. (3.3) without subtraction of the observed damage rate yield a similar energy barrier under the Arrhenius treatment. Furthermore, the pre-exponential factor A is close to the frame rate, which demonstrates another constraint of the applied measuring method: disregarding the size of the observed vacancy, only one knock-on event was counted per vacancy. Hypothetically, the highest observed KO rate would, thus, be equal to the frame acquisition frequency.

Rather than applying the simple Arrhenius formalism, it seems physically justified to first state that vacancy healing is likely much faster *on average* than KO damage between 400 and 1073 K, and to note that some vacancies can yet be observed occasionally. To correctly describe this observation, the nature of the experiment must be explicitly accounted for: the scanning electron probe is moving, both causes and observes knock-on damage, and has a finite current density distribution. Hence, the time between the vacancy creation and its (possible) observation varies, depending on where it is created with respect to the position of the electron probe.

This knowledge motivated the extension of the Arrhenius healing rate model according to (3.6) and the consideration of a temperature-dependent healing probability $P_\mathrm{h}(T)$. It is determined by the fraction of vacancies that heal out before observation and can be used to redefine the healing rate as a fraction of the theoretical knock-on rate:

$$k_\mathrm{h}(T) := P_\mathrm{h}(T) k_\mathrm{KO}^\mathrm{theor}(T) \tag{3.7}$$

Further, a new effectively observed damage rate is obtained by combining eqs. (3.4) and (3.7):

$$k_\mathrm{KO}^\mathrm{obs}(T) = k_\mathrm{KO}^\mathrm{theor}(T)\,(1 - P_\mathrm{h}(T))\,. \tag{3.8}$$

As the next step in the elaboration of the model, the healing probability $P_\mathrm{h}(T)$ is described by the probability distributions of the random variables involved in the vacancy healing process. The

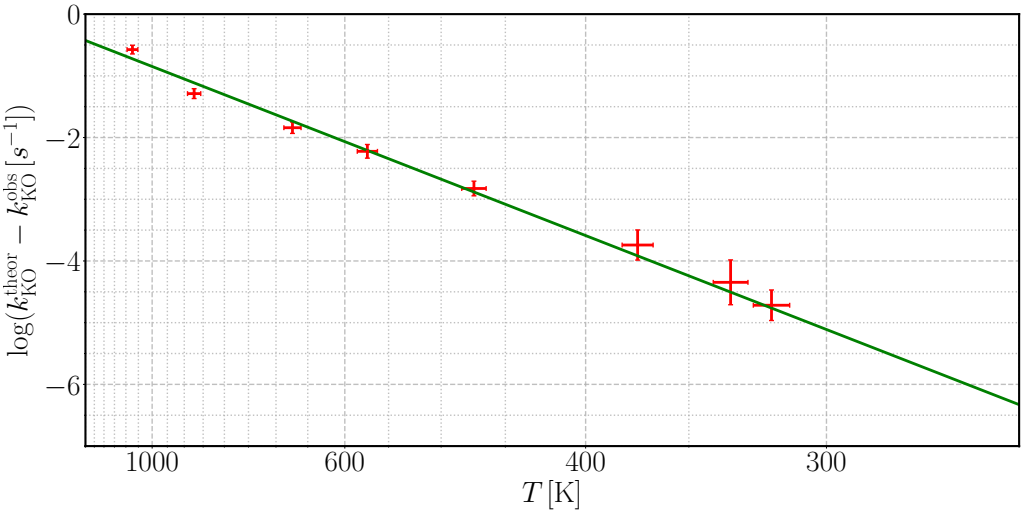

Figure 3.4: Vacancy healing rate as a function of the inverse temperature in semi-logarithmic representation (Arrhenius plot). The experimental estimates (red points) are based on the difference between the McKinley and Feshbach model and the observed knock-on rate (see table 3.3, cross-section values converted to rates using eqs. (3.1) and (3.3)). The linear fit (green line) was obtained from orthogonal distance regression. (Adapted from the Supplemental Material of Publication I [122]: the aspect ratio and the appearance of the grid were changed, $k_{\mathrm{KO}}^{\mathrm{predict}}$ was relabeled to $k_{\mathrm{KO}}^{\mathrm{theor}}(T)$, and the calculation of $k_{\mathrm{KO}}^{\mathrm{theor}}(T)$ was done using corrected values for the mean beam current. Originally published 2022 by Elsevier Ltd. under the CC BY 4.0 license.)

movement and the shape of the finite electron probe are neglected for the moment, meaning that a defect created during the acquisition of a given image can be observed in the subsequent image at the earliest.

It is assumed that migrating adatoms perform a random walk [172]. Then, the defect is not observable if the number of adatom migration steps within a frame time (random variable $n_{\mathrm{f}}(T)$) is greater than (or equal to) the number of steps needed to reach and heal a vacancy (random variable n_{h}). Whether an adatom undertakes an individual migration step or not, on the one hand, constitutes a Bernoulli process [173]. $n_{\mathrm{f}}(T)$ is a thermodynamical quantity that obeys a binomial distribution and can be approximated [174] by a normal distribution with a mean of

$$\mu(T) = t_{\mathrm{f}} f_0 \exp\left(-\frac{E_{\mathrm{m}}}{k_{\mathrm{B}} T}\right), \tag{3.9}$$

where t_{f} denotes the frame time, and f_0 the migration attempt frequency (4×10^{12} s^{-1}, literature value for carbon interstitials in graphite [82]). After how many migration steps an adatom arrives in the immediate proximity of a vacancy, on the other hand, constitutes a Poisson process [126]. n_{h} is purely statistical, obeys a geometric distribution, whose continuous analog is the exponential distribution [175], and is governed by the adatom concentration

$$c_{\mathrm{ad}} := \frac{N_{\mathrm{ad}}}{N_{\mathrm{lat-at}}}, \tag{3.10}$$

where N_{ad} is the number of adatoms and $N_{\mathrm{lat-at}}$ is the number lattice atoms. Furthermore, the expected average vacancy size N_{v} (1.6 ± 0.2 in our data) needs to be accounted for, since to fully heal multivacancies, they have to be reached by multiple adatoms. To focus on the most essential,

the parameter ν of the exponential distribution is given by

$$\nu = -\frac{1}{N_\mathrm{v}} \log\left(1 - \frac{2}{3} c_\mathrm{ad}\right), \tag{3.11}$$

in the sense that $p_\mathrm{h}(n_\mathrm{h}|\nu) = \nu \exp(-n_\mathrm{h}\nu)$ is the probability density function (PDF) of the distribution of n_h. The expectation value of n_h is given by

$$E(n_\mathrm{h}) = \frac{1}{\nu}. \tag{3.12}$$

To explain the validity of eq. (3.12), we consider single vacancies (SVs) only ($N_\mathrm{v} = 1$) and perform a first-order Taylor expansion ($\log(1-x) \approx -x$):

$$E(n_\mathrm{h}^\mathrm{SV}) = E(n_\mathrm{h})|_{N_\mathrm{v}=1} = -\frac{1}{\log\left(1 - \frac{2}{3} c_\mathrm{ad}\right)} \approx \frac{3}{2 c_\mathrm{ad}} = \underbrace{\frac{3}{2} N_\mathrm{lat-at}}_{=N_\mathrm{lat-b}} \frac{1}{N_\mathrm{ad}} = \frac{N_\mathrm{lat-b}}{N_\mathrm{ad}}, \tag{3.13}$$

where $N_\mathrm{lat-b}$ is the number of carbon-carbon bonds in the lattice. As described in section 1.4.1, the energetically favored adatom sites are the bridge sites on top of the carbon-carbon bond centers. Hence, there is one adatom site per bond ($N_\mathrm{ad-sites} = N_\mathrm{lat-b}$). We find $E(n_\mathrm{h}^\mathrm{SV}) \approx N_\mathrm{ad-sites}/N_\mathrm{ad}$, which means that that the average number of needed migration steps to arrive at an SV is just the number of available sites per adatom. This was also shown via Monte Carlo simulations [176, 177].

After defining the quotient random variable $Q(T) = n_\mathrm{f}(T)/n_\mathrm{h}$, the healing probability can be written as

$$P_\mathrm{h}(T) = \Pr\left(Q(T) \geq 1\right), \tag{3.14}$$

where $\Pr(Q(T) \geq 1)$ is the complementary cumulative distribution function (tail distribution) of $Q(T)$ at one. It can be approximated by the cumulative distribution function $\Pr(n_\mathrm{h} \leq n_\mathrm{f}(T)|\nu)$ of n_h for the expectation value of $n_\mathrm{f}(T)$, which yields

$$P_\mathrm{h}(T) = \int_0^{\mu(T)} \nu \exp(-\nu k)\, \mathrm{d}k = 1 - \exp(-\nu\mu(T)). \tag{3.15}$$

Inserting eq. (3.9), eq. (3.11), and eq. (3.15) into eq. (3.8) leads to

$$k_\mathrm{KO}^\mathrm{obs}(T) = k_\mathrm{KO}^\mathrm{theor}(T) \left(1 - \frac{2}{3} c_\mathrm{ad}\right)^{\frac{1}{N_\mathrm{v}} t_\mathrm{f} f_0 \exp\left(\frac{-E_\mathrm{m}}{k_\mathrm{B} T}\right)}, \tag{3.16}$$

a relation that can also be expressed in terms of cross sections by substituting the theoretical defect formation rate $k_\mathrm{KO}^\mathrm{theor} \to \sigma_\mathrm{KO}^\mathrm{theor}$ and the defect observation rate $k_\mathrm{KO}^\mathrm{obs} \to \sigma_\mathrm{KO}^\mathrm{obs}$. The correct normalization with respect to the beam current is conserved by this substitution, because $k_\mathrm{KO} = (I_\mathrm{B}/e)\, \rho_A \sigma_\mathrm{KO}$. The predicted result according to eq. (3.16) will be illustrated in fig. 3.6 (dashed purple line), using the DFT-calculated adatom migration barrier. At temperatures above 500 K, the healing probability according to eq. (3.15) is close to one for typical frame times of ca. 0.5 s. This does not correctly describe the experimental outcome, because vacancies can be observed across all investigated temperatures.

Finally, the movement and the shape of the scanning electron probe are taken into account. The positions of the created vacancies with respect to the probe position are, in reality, statistically distributed corresponding to the electron probe current density profile. The time between a KO

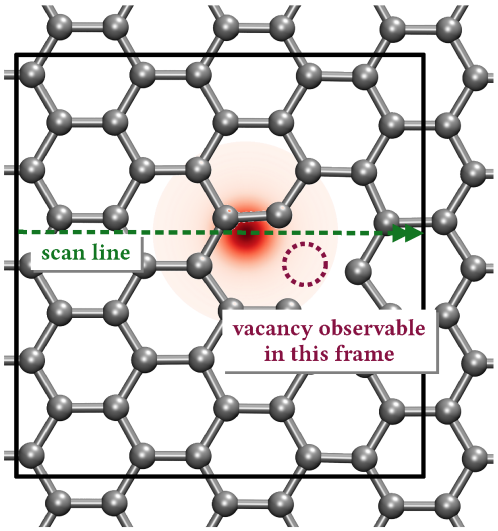

Figure 3.5: Schematic representation of a graphene monolayer with a single vacancy (marked with a dashed purple circle) caused by the electron probe's "leading" tail. The defect can be observed within the same scan frame (marked with a black rectangle). (Adapted from Publication I [30]. Published 2022 by Elsevier Ltd. under the CC BY 4.0 license.)

event and the detection (or the overlooking) of a vacancy can be as low as a few pixel dwell times, but also almost as high as the frame time. Precisely stated, if the "leading" tail of the probe causes the vacancy (see fig. 3.5), the probability for healing before observation will significantly be lowered, because the vacancy will almost immediately be recorded. Including both the electron-probe shape $g(x, y)$ according to eq. (2.3) and replacing the frame time with the probability mass function of the detection time $t_\mathrm{d}(x, y)$ in eq. (3.16) yields

$$k_\mathrm{KO}^\mathrm{obs}(T) = k_\mathrm{KO}^\mathrm{theor}(T) \sum_{x,y} \left(1 - \frac{2}{3} c_\mathrm{ad}\right)^{\frac{1}{N_\mathrm{v}} t_\mathrm{d}(x,y) f_0 \exp\left(\frac{-E_\mathrm{m}}{k_\mathrm{B} T}\right)} g(x, y), \tag{3.17}$$

where x and y are discrete spatial coordinates of a pixel location, ranging from 0 to $N_x - 1$ and from 0 to $N_y - 1$, where N_x and N_y are the pixel counts along the respective direction. Since the detection time only depends on the vacancy's position relative to the probe position, the calculation can be performed using a fixed central probe and a varying vacancy position (without loss of generality).

The extended healing rate model according to eq. (3.17) yields a qualitative match of our data. However, the model contains two unknowns, namely the carbon adatom migration barrier E_m and the adatom concentration c_ad. The former can be estimated via first-principles simulations, but the latter is essentially unknown. Different sets $(E_\mathrm{m}, c_\mathrm{ad})$ fit to our data. Thus, the prediction according to the extended model was evaluated twice: first, E_m was fixed to the average DFT value taking into account van der Waals interactions (0.415 eV, see below) and c_ad was optimized with a one-parametric variance-weighted nonlinear LSQ algorithm, and second, both E_m and c_ad were subjected to a two-parametric optimization. The predicted cross-section values are visualized in fig. 3.6 (purple and orange line). The two-parametric fit yielded (0.33 ± 0.03) eV), where the given uncertainty excludes any parameter correlation (between E_m and c_ad), since it was obtained using an adatom concentration value fixed to its two-parametric optimum. The line corresponding to

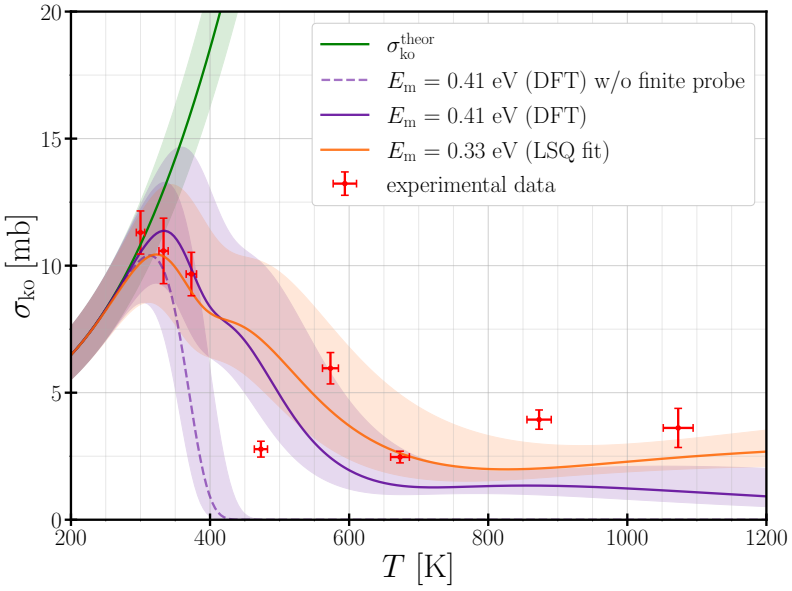

Figure 3.6: Cross section for KO damage of pristine graphene as a function of the temperature, at an electron kinetic energy of 90 keV: Experimental values (red points), theoretical curve according to the McKinley and Feshbach model (green line, see eq. (2.18)), and the prediction according to an extended model (orange as well as purple lines, see eqs. (3.16) and (3.17)). Both forms of the latter describe knock-on damage with counteracting vacancy healing. The movement and the shape of the STEM probe, which lead to a variation in defect detection time, are considered only in the second form (solid purple line for the DFT-calculated carbon adatom migration barrier, solid orange line for the LSQ optimized barrier). (Reproduced from Publication I [30]. Published 2022 by Elsevier Ltd. under the CC BY 4.0 license.)

the best estimator (orange) crosses the one-parametric one at ca. 415 K and lies higher at elevated temperatures, which better describes the experimental observations.

Last, it has to be noted that the Taylor expansions of eq. (3.16) as well as eq. (3.17) up to the first order, i.e. $(1 - x(c_{\mathrm{ad}}))^{a(f_0)} \approx 1 - a(f_0)x(c_{\mathrm{ad}})$ in terms of simplified variables, contains the product of the adatom concentration c_{ad} and the attempt frequency f_0. Thus, counteracting changes in these two variables are indistinguishable and whenever one variable is set to a seemingly expected value, the other one will decrease to an implausible order of magnitude. In concrete values: $c_{\mathrm{ad}} = 10^{-3}$ nm^{-2} implies 0.8×10^{8} s^{-1}, whereas the expected $f_0 = 4 \times 10^{12}$ s^{-1} [82] leads to a very low $c_{\mathrm{ad}} = 2.0 \times 10^{-6}$ nm^{-2}. So, either the adatom concentration is much lower than what to expect on typical graphene samples, or the model according to eq. (3.17) misses effects that are required to consistently explain the result. The product values are $(0.8 \pm 0.4) \times 10^{6}$ nm^{-2}s^{-1} for the two-parametric LSQ optimization and $(0.8 \pm 0.5) \times 10^{7}$ nm^{-2}s^{-1} for the one-parametric optimization using the DFT-calculated barrier. The given uncertainty value for the two-parametric solution is based on the criterion $\Delta\sigma_{\mathrm{KO}}^{\mathrm{LSQ}}/\sigma_{\mathrm{KO}}^{\mathrm{LSQ}} = 20$ % at 1073 K, and the uncertainty of the one-parametric fit results using the DFT-calculated barrier were set proportional to the ratio of the corresponding variance-weighted residual variances (eq. (2.21)).

As supplementary notes, the migration of single vacancies and the DFT results for the carbon adatom migration barrier are discussed. SVs are observed across the entire temperature range from 300 to 1073 K. Imaging the surrounding structure of an SV takes about 0.2 s (= 40 % of a frame time), which indicates that the migration takes longer in spite of an expected migration

barrier of ca. 1 eV (see section 1.4.2). Indeed, such a low barrier would imply that SVs can never be observed at elevated temperatures, which is not the case in our extensive experimental data.

The spin-polarized DFT values for the carbon adatom migration barrier E_{m} are 0.44 eV for the PBE functional, 0.43 eV for PBE-TS, and 0.40 eV for C09-vdW. The inclusion of dispersion interactions has little effect on E_{m}. The apparent over-estimation by DFT might be explainable by temperature-dependent entropic and vibrational effects altering the Gibbs free energy as well as quantum zero-point effects [178], though the relative error heavily depends on the system and the diffusion path [179] and can thus not be estimated at this point.

3.3 Electron-beam induced atom displacements at impurities

This section reports on the cross-section measurements of beam-driven dynamics involving three-coordinated X@SV impurities in graphene, with X being a placeholder for Si or P. For Si@SV, a voltage-dependent measurement in a range from 50 to 70 kV as well as a temperature-dependent measurement in a range from ambient to 1000 °C were carried out. The latter was done using a P-doped graphene sample (see section 2.2.1), where the primary aim was the acquisition of temperature-dependent data regarding P@SV.

The investigated effects are the KO displacement of a C atom neighboring X@SV (section 1.5.1), the positional exchange of X@SV and a C neighbor (sections 1.5.2 and 1.5.3), and the replacement of X@SV by C (section 1.5.4). For brevity of notation, these effects are abbreviated as "XCKO", "XCEx", and "XRepC".

Since XCEx events are desired in the context of single-atom manipulation, these are presented and discussed before the spurious XCKO as well as XRepC events. Furthermore, a hypothetical itemization of the effectively observable cross section for SiCEx events will be provided in section 3.3.1.1. First, SW transformations relaxing back to the hexagonal structure might be involved. Second, double positional exchanges (from one frame to the subsequent one) are treated like single positional exchanges in the data analyses.

3.3.1 Voltage-dependent cross-section measurement for Si@SV

The cross sections for SiCEx, SiCKO, and SiRepC events were measured at electron kinetic energies of 50, 60, 65, and 70 keV. The experimental results (including values based on refs. [17, 18]) are summarized in table 3.5 and graphically presented in three separate figures, one each for the investigated events.

As for SiCEx (see fig. 3.7), no events were observed at 50 keV. The total electron dose impinging on the three C neighbors of the Si@SV was taken into account to calculate an upper bound of the cross section (3.7 mb). At 55 keV, there is a notable onset ((7.1 ± 1.0) mb) according to the cross section based on electron doses from ref. [18]. At 60 keV, the electron doses from ref. [17] yield a cross section of (530 ± 90) mb, which is ca. three times larger than our new data ((150 ± 30) mb). A similar deviation is also present for SiCKO events at 60 keV, which implies that the discrepancy may be explained due to the different measuring and calculation methods applied in refs. [17] and [18]. The SiCEx cross section shows a further increase above 60 keV, which flattens from 65 keV (ca. 640 mb) to 70 keV (ca. 750 mb).

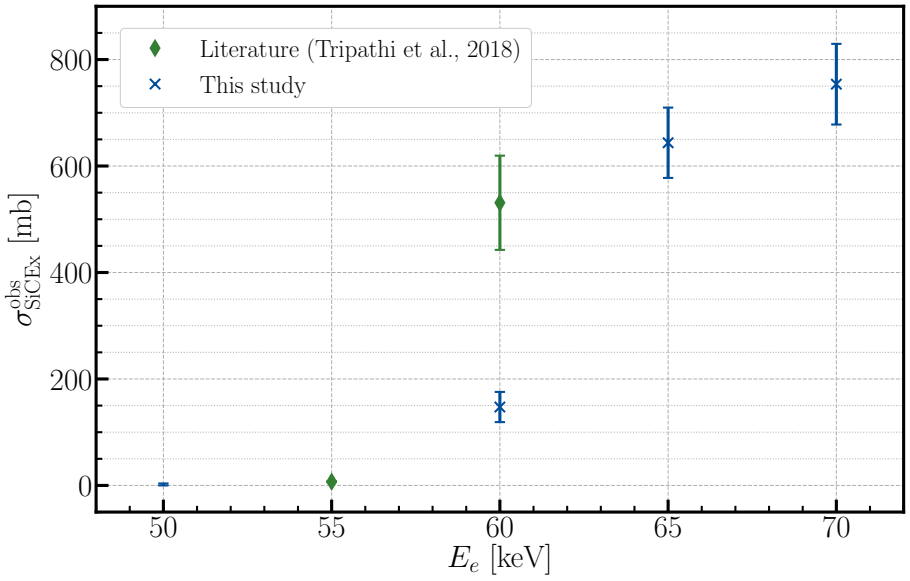

Figure 3.7: SiCEx: Observed cross section $\sigma^{\mathrm{obs}}_{\mathrm{SiCEx}}$ for the positional exchange between a Si@SV impurity and a neighboring C atom as a function of the electron kinetic energy E_e, at ambient temperature. The error bar at $E_e = 50$ keV is to be understood as an estimate for the upper limit, since no corresponding events were observed.

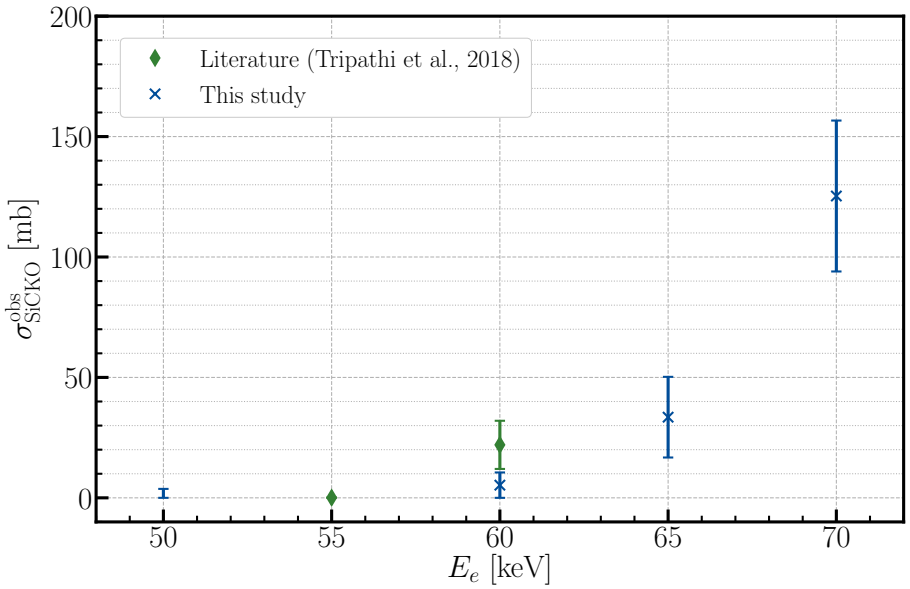

Figure 3.8: SiCKO: Observed cross section $\sigma^{\mathrm{obs}}_{\mathrm{SiCKO}}$ for the knock-on displacement of a C atom neighboring a Si@SV impurity as a function of the electron kinetic energy E_e, at ambient temperature. The error bar at $E_e = 50$ keV is to be understood as an estimate for the upper limit, since no corresponding events were observed.

The cross-section values for SiCKO (see fig. 3.8) feature an upward trend with increasing electron energy. There was no SiCKO event observed at 50 keV, resulting in 3.7 mb for the upper bound of the cross section. At 55 keV, one individual dose is provided in ref. [18], which gives a cross section of ca. 0.07 mb. Hence, almost no damage occurs at and below 55 keV. The doses for 60 keV that

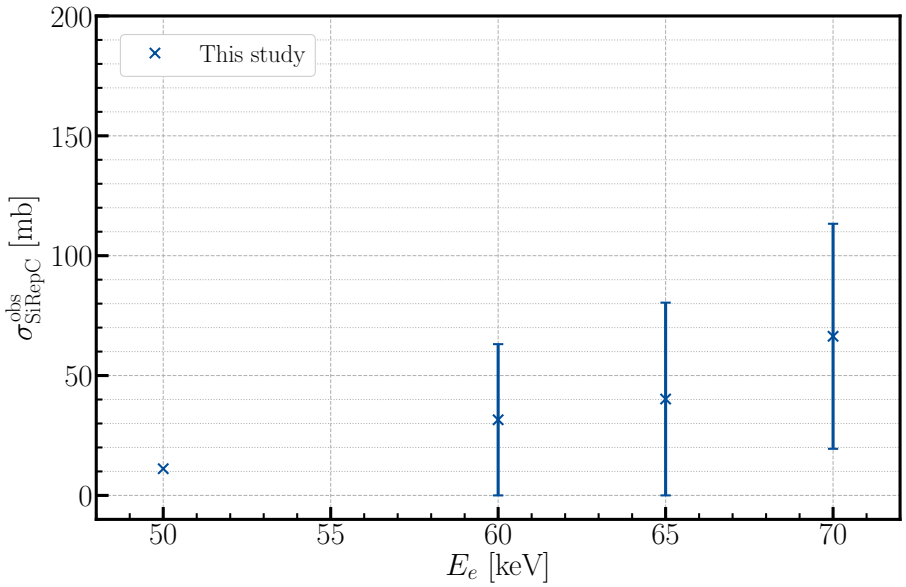

Figure 3.9: SiRepC: Observed cross section $\sigma^{\mathrm{obs}}_{\mathrm{SiRepC}}$ for the beam-induced replacement of a Si@SV impurity by a C atom as a function of the electron kinetic energy E_e, at ambient temperature. The cross section at $E_e = 50$ keV is to be regarded as a rough estimate, since the uncertainty of the expected electron dose λ^{PM} according to eq. (2.7) diverges for only two observed events.

were provided from ref. [17] result in (22 ± 10) mb (300 times larger than for 55 keV), whereas the new 60 keV data contains only one event, corresponding to an estimated cross section of ca. 5 mb. Above 60 keV, the SiCKO cross section rises further and reaches $(130 \pm 30$ mb) at 70 keV.

Regarding SiRepC (see fig. 3.9), the cross-section estimates show a slight rise with increasing electron energy, although the uncertainties according to table 3.5 are large and might the true accuracy might yet be overestimated, because the number of observed events is small for every investigated electron energy (2, 3, 3, and 4).

3.3.1.1 Success probability for single-atom manipulation of Si@SV

The cross sections discussed above represent interaction probabilities. At each electron energy, the ratio of the cross sections for SiCEx and SiCKO is a good indicator of the suitability for single-atom manipulation, because the probability that an effect occurs (before the other) can be stated in terms of the individual cross sections. SiCKO irreversibly leads to a four-coordinated Si@DV that cannot be further manipulated.

Further, SiRepC also terminates single-atom manipulation, but only a part of the cross section reported above may interfere. These are based on the assumption that SiRepC is a beam-induced process when irradiating the Si@SV itself (its Voronoi cell, respectively; see section 2.4.1.2 and fig. 2.5), although the role of the electron beam in the process is actually unknown. In contrast, a manipulation experiment is done by spot irradiation of a C neighbor. If the electron probe is centered on a C neighbor, a small fraction of the beam electrons will impinge on the Si@SV. The electron dose impinging on the Voronoi cell of the Si@SV could be calculated on the basis of the probe shape, but this dose is almost certainly different from the dose that contributes to SiRepC events. The latter dose is not easily identifiable, simply owing to the fact that the values reported

Table 3.5: Observed cross sections σ^{obs} for different electron kinetic energies E_e and beam-induced processes involving a Si@SV impurity, at ambient temperature. N^{obs} is the number of observed events. The values from refs. [18] and [17] have been recalculated based on the provided electron dose values**.

SiCEx	Positional exchange between Si@SV and one of its C neighbors
SiCKO	Knock-on displacement of a C neighbor of Si@SV
SiRepC	Replacement of Si@SV by C

E_e [keV]	event	N^{obs} *	σ^{obs} [mb]	$\Delta\sigma^{\text{obs}}$ [mb]	Origin	Notes
50	SiCEx	0	≤ 3.7	n.a.	this study	
50	SiCKO	0	≤ 3.7	n.a.	this study	
50	SiRepC	2	11.1	n.a.	this study	
55	SiCEx	49	7.1	1.0	[18]	**
55	SiCKO	1	0.07	n.a.	[18]	* and **
55	SiRepC	n.a.	n.a	n.a.		
60	SiCEx	29	150	30	this study	
60	SiCEx	38	530	90	[17]	**
60	SiCKO	1	5.3	n.a.	this study	*
60	SiCKO	8	22	10	[17]	**
60	SiRepC	3	30	30	this study	
65	SiCEx	97	640	70	this study	
65	SiCKO	6	33	17	this study	
65	SiRepC	3	40	40	this study	
70	SiCEx	101	750	80	this study	
70	SiCKO	18	130	30	this study	
70	SiRepC	4	70	50	this study	

* If $N^{\text{obs}} = 1$, the posterior mean solution according to eq. (2.6) will diverge. Instead, $\lambda = N_e$ was used, where N_e is the only measured electron dose.
** The dose values were acquired by our research group in 2014 and 2018, and originate from different measuring and calculation methods.

above are based on homogeneous dose distribution and the Voronoi segmentation of the monolayer (see section 2.4.1.2). However, if the beam has a different role and the replacement process happens mainly due to irradiation of a C neighbor, dividing the reported SiRepC cross section by three (for the number of C neighbors) will make the values directly comparable to the cross sections of the other effects. As the beam's influence is unclear, it is also uncertain how the likelihood for SiRepC during spot irradiation of a C neighbor varies due to sample drift, since they change the electron dose impinging on the C neighbor and the Si@SV itself. Finally, independent from the exact process dynamics, the higher the cross section for SiRepC calculated based on whatever assumption, the higher is the probability for replacement due to the repeated image scans in a manipulation experiment (see section 3.5, esp. fig. 3.16).

In general terms before simplifications: given the starting configuration Si@SV surrounded by a pristine C lattice and using spot irradiation of a C neighbor, the probability that the next structural change is the event α_0 (and not any other) is given by

$$p_{\alpha_0} = \frac{\sigma_{\alpha_0}}{\sum_\alpha \sigma_\alpha}, \tag{3.18}$$

with σ_α denoting cross sections and α indicating the effects (section 1.6.2.1): "SiCDEx" for the direct exchange of Si and C, "SW" for a Stone–Wales transformation involving the Si@SV, "SiCDEx^2" for a double jump of the Si@SV (presumably double direct exchange of Si and C), SiCKO as introduced above, and "SiRepC@C-Irr" for Si replacement by C (from outside of the lattice) while a C neighbor is spot-irradiated.

To approximate: the cross section for SiRepC@C-Irr could be a third of the given cross sections for SiRepC, but a different fraction could also be justifiable. On condition that the probe shape is equal among different acceleration voltages, that fraction will remain the same. However, an absolute quantification of SiRepC@C-Irr would only be possible based on a specific measurement of that effect.

SW transformations are not only reversible, but half of them effectively result in exchanged positions of the Si atom and a neighboring C (see section 1.5.3). The SW(55-77) defect configuration with Si is almost never observed, since its lifetime under electron irradiation is very short, owing to the low activation energy for relaxing back to the hexagonal configuration (lower than 1 eV [21]). Hence, the question ≪Is the quantity supposed to be measured identical to what was measured?≫ must be asked. Whatever the cross section for this SW transformation is, half of it will lie hidden in the experimental values for the SiCEx cross section.

Last, double jumps, despite not being the intended outcome, just *disrupt control* in a single-atom manipulation series, but the experiment can be continued afterwards. They have an effective cross section $\sigma_{\mathrm{SiCDEx2}}$, which could (presumably) be disassembled into $\sigma_{\mathrm{SiCDex}} \times \epsilon(\sigma_{\mathrm{SiCDex}})$, where $\epsilon(\sigma_{\mathrm{SiCDex}})$ is an efficiency factor describing the likelihood for a second direct exchange before the initial one was observed. The latter is given by $\epsilon(\sigma_{\mathrm{SiCDex}}) = \sigma_{\mathrm{SiCDex}} \rho_A N_{\mathrm{e}}^{\mathrm{Ex1-Ex2}}$, where $N_{\mathrm{e}}^{\mathrm{Ex1-Ex2}}$ is the electron dose impinging on the C neighbors between the individual exchange events. However, since double jumps occur very rarely, these were not separately analyzed in section 3.3.1 and treated like single jumps in the scope of my work.

Based upon the above, a heuristic approach is pursued. As noted above, any observed SW(55-77) defects involving the Si@SV impurity are ignored, since they are observed very rarely. For the purposes of the following consideration, direct exchange, half of the SW transformation, and double exchanges are summed up to the effectively observable exchange cross section for Si and C

$$\sigma_{\mathrm{SiCEx}} = \sigma_{\mathrm{SiCDEx}} + \frac{1}{2}\sigma_{\mathrm{SW}} + \sigma_{\mathrm{SiCDEx2}}. \tag{3.19}$$

The cross section for SiRepC@C-Irr cannot be quantified due to insufficient data. Then, the single-event probability p_m that the Si@SV configuration remains intact after an observed change in structure, which will also be called "manipulation success probability", is simply given by

$$p_m = \frac{\sigma_{\mathrm{SiCEx}}}{\sigma_{\mathrm{SiCEx}} + \sigma_{\mathrm{SiCKO}}}. \tag{3.20}$$

The random variable M shall be defined as the *count of positional exchanges* (preserving the manipulable Si@SV) *until* the Si@SV configuration gets *irreversibly altered* by SiCKO, neglecting SiRepC@C-Irr events. It obeys a geometric distribution (see ref. [180]) with the probability mass function (PMF)

$$\Pr(M = k \,|\, p_m) = p_m^k (1 - p_m). \tag{3.21}$$

The expectation value

$$E(M) = \frac{p_m}{1 - p_m} = \frac{\sigma_{\mathrm{SiCEx}}}{\sigma_{\mathrm{SiCKO}}}, \tag{3.22}$$

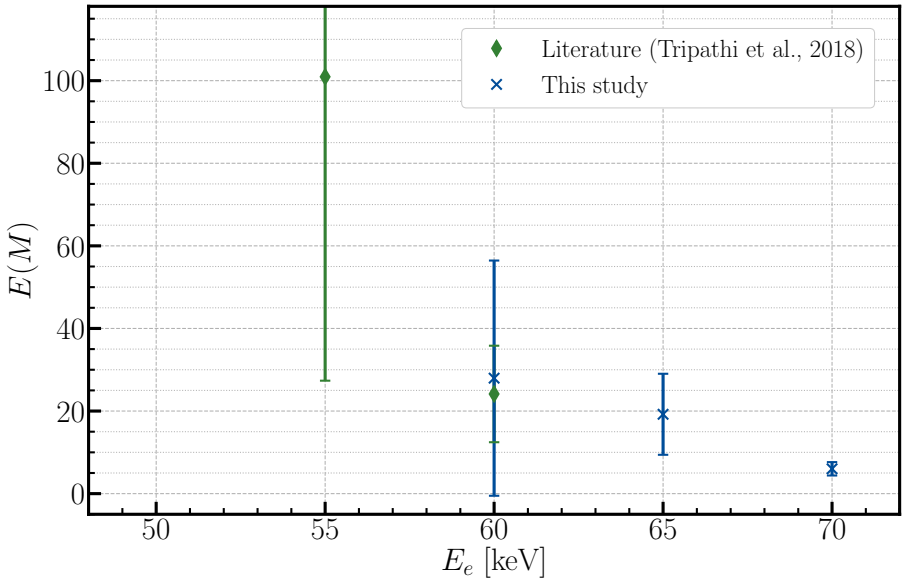

Figure 3.10: Suitability of different electron kinetic energies E_e for single-atom manipulation of Si@SV: expectation value $E(M)$ as a function of the electron kinetic energy E_e, where M is the count of SiCEx events before SiCKO, disregarding SiRepC@C-Irr.

and the variance

$$\mathrm{var}(M) = \frac{p_m}{(1-p_m)^2} = \frac{\sigma_\mathrm{SiCEx}\,(\sigma_\mathrm{SiCEx}+\sigma_\mathrm{SiCKO})}{\sigma^2_\mathrm{SiCKO}} = E(M)\,(E(M)+1) \tag{3.23}$$

are of crucial importance for the purpose of single-atom manipulation with high control. A further matter of particular interest is the probability that $M \geq k$, i.e. the complementary cumulative distribution function (CCDF) of M, evaluated at k:

$$\Pr(M \geq k \,|\, p_m) = \sum_{l=k}^{\infty} \Pr(M = l \,|\, p_m) = 1 - \sum_{l=0}^{k-1} \Pr(M = l \,|\, p_m) = 1 - \sum_{l=0}^{k-1} p_m^k (1-p_m). \tag{3.24}$$

It gives the probability that the number of exchanges before knock-on damage is no less than k.

To evaluate eqs. (3.22)–(3.24), which are characterizing the distribution of M, new experimental data is available for electron kinetic energies of 60, 65, and 70 keV (see table 3.5). At 50 keV, neither a SiCKO nor a SiCEx event has been observed, thus no information regarding M can be derived. Further, there is previous data available regarding SiCKO and SiCEx at 55 keV [18] and 60 keV [17]. The cross-section values might deviate by an unknown factor owing to the different measuring and calculation methods, but this factor may be the same across all values, making the ratios and thus p_m according to eq. (3.20) as well as M directly comparable with the new data.

The expectation value $E(M)$ as a function of the electron kinetic energy E_e is depicted in fig. 3.10 and listed in table 3.6. The propagated uncertainty $\Delta E(M)$ according to eq. (2.34) depends on the errors of both influencing cross-section values. This results in especially large uncertainties for the old 55 keV and the new 60 keV data, since there is only one SiCKO dose each. As similarly reported in ref. [18], at 55 keV, the best estimator for the expectation value $E(M)$ is drastically higher than at 60 keV (100 vs. 24 for the old 55 and 60 keV data, and 28 for the new 60 keV data), although the errors are large and the error ranges eventually overlap.

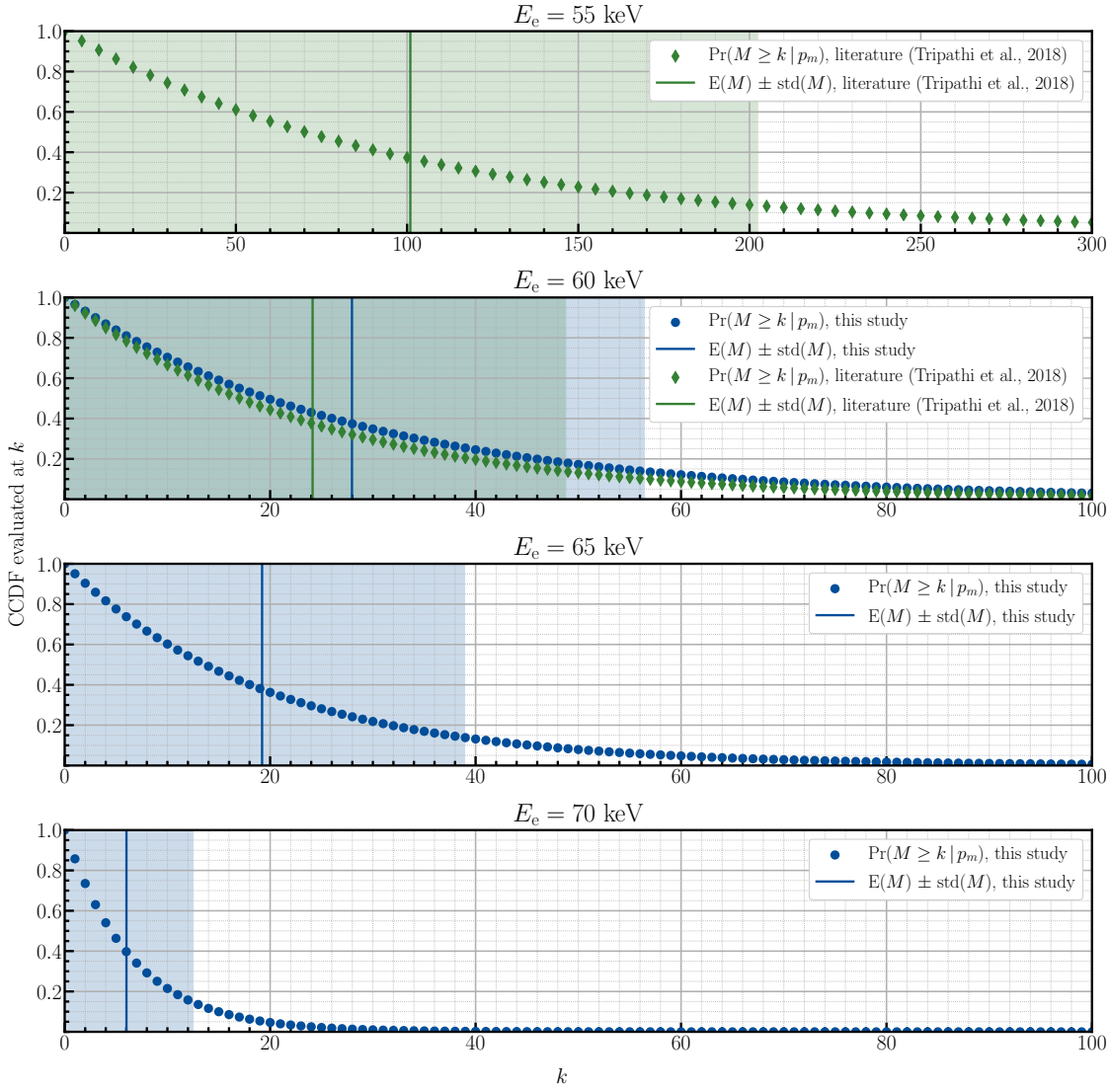

Figure 3.11: Suitability of different electron kinetic energies E_e for single-atom manipulation of Si@SV: complementary cumulative distribution function of M, evaluated at k, for electron kinetic energies $E_e = 55$, 60, 65, and 70 keV. M is the count of SiCEx events before SiCKO, disregarding SiRepC@C-Irr. The shaded areas indicate the standard deviation $\mathrm{std}(M) = \sqrt{\mathrm{var}(M)} \approx E(M)$.

Table 3.6: Suitability of different electron kinetic energies E_e for single-atom manipulation of Si@SV: expectation value $E(M)$ for different electron kinetic energies, where M is the count of SiCEx events before SiCKO, disregarding SiRepC@C-Irr.

E_e [keV]	$E(M)$	$\Delta E(M)$	Source
55	100	70	[18]
60	24	12	[18]
60	28	28	this study
65	19	10	this study
70	6	2	this study

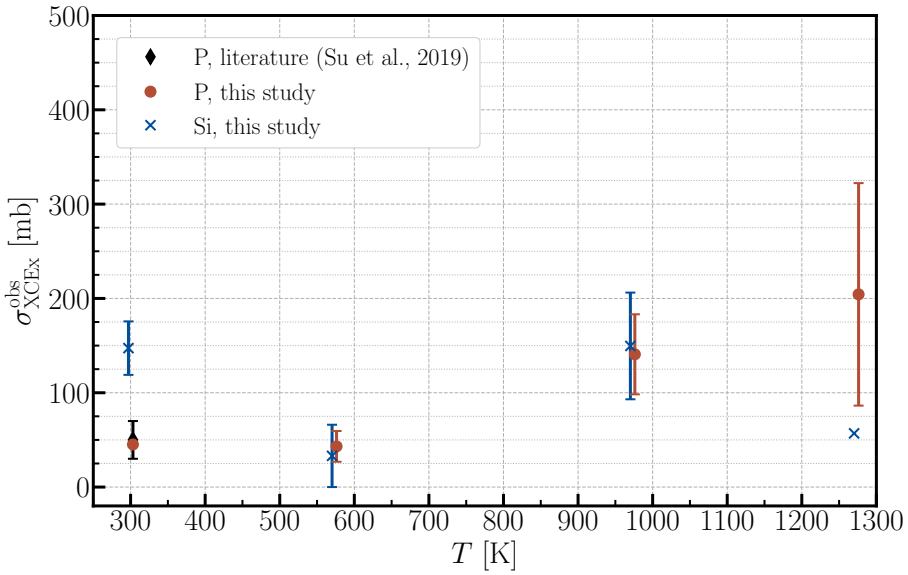

Figure 3.12: SiCEx & PCEx: Observed cross section $\sigma^{\mathrm{obs}}_{\mathrm{XCEx}}$ for the positional exchange between a Si@SV or P@SV impurity and a neighboring C atom as a function of the temperature T, at an electron kinetic energy of 60 keV. To reduce overlaps in the illustration of the data points, the latter have been offset on the abscissa by -3 K for Si and by 3 K for P. The cross sections for PCEx at 300 K and PCEx at 1273 K are to be regarded as estimates with very high uncertainty, since eq. (2.7) cannot be used for less than three observed events.

Evaluation of the higher kinetic energies in the new data yields an estimate of $E(M) = 19 \pm 10$ for 65 keV, which is not significantly lower than the 60 keV value (28 ± 28). At 70 keV, the expected number of SiCEx events before SiCKO seemingly drops to a lower level (6 ± 2).

In fig. 3.11, the CCDF of M according to eq. (3.24) is illustrated for different electron kinetic energies. This offers a insightful presentation of the success to be expected from single-atom manipulation experiments with Si@SV and concludes the discussion of this measurement series.

3.3.2 Temperature-dependent cross-section measurement for Si@SV and P@SV

The cross sections for XCKO, XCEx, and XRepC events involving Si@SV and P@SV were measured at 300 K (ambient temperature), 573 K, 973 K, and 1273 K. The chemical species (Si or P) were individually identified via EELS (analysis carried out by collaborators in MIT[2]). The experimental results (including values for P@SV from ref. [21]) are summarized in table 3.7 and graphically presented in three figures, one each for SiCEx & PCEx, SiCKO & PCKO, and SiRepC & PRepC.

As for positional exchanges (SiCEx and PCEx, see fig. 3.12), the cross-section values for Si impurities do not show a monotonous trend, but rather rise and fall. The data contains only three electron doses for 573 K and only one for 1273 K. Thus, these two data points are not statistically robust. The error for 573 K according to eq. (2.25) might underestimate the true error. Although the upper bound of the cross section at 573 K is lower than the lower bounds at 300 K and 973 K, that difference might not be significant. No error estimate can be given for

[2]Research group of Ju Li, Massachusetts Institute of Technology.

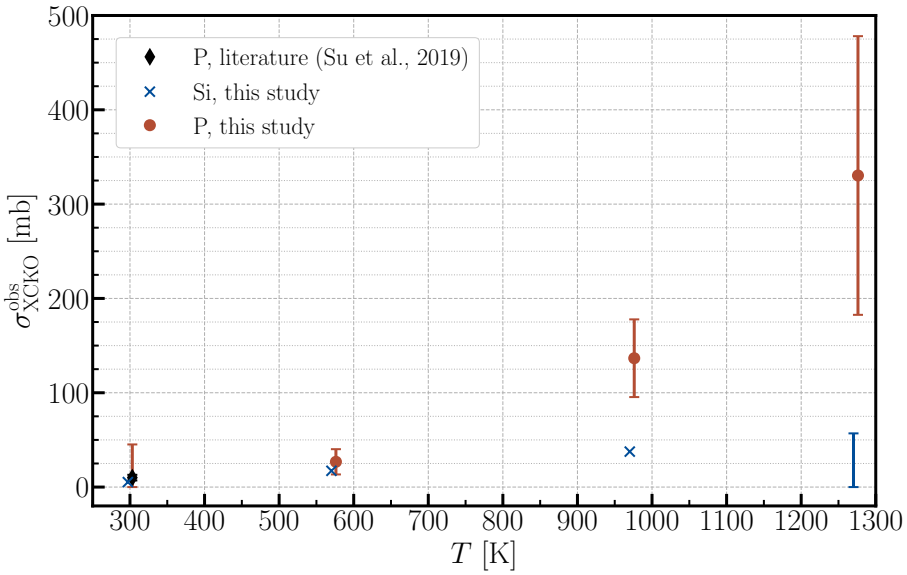

Figure 3.13: SiCKO & PCKO: Observed cross section $\sigma^{\mathrm{obs}}_{\mathrm{XCKO}}$ for the knock-on displacement of a C atom neighboring a Si@SV or P@SV impurity as a function of the temperature T, at an electron kinetic energy of 60 keV. To reduce overlaps in the illustration of the data points, the latter have been offset on the abscissa by -3 K for Si and by 3 K for P. The PCKO error bar at $T = 300$ K and the SiCKO error bar at $T = 1273$ K are to be understood as estimates for the upper limit, since no corresponding events were observed. The cross sections for SiCKO at 573 K as well as 973 K are to be regarded as estimates with very high uncertainty, since eq. (2.7) cannot be used for less than three observed events.

the 1273 K data point (57 mb). The actual cross section could be at the same level as (or at a higher level than) the value at 973 K ((150 ± 60) mb). The cross section for exchange of P and C is a little more robust and shows an upward trend from 300 to 1273 K. The ambient temperature data point (45 mb) is based on a single dose value, but matches literature ((50 ± 20) mb [21]), which also supports the validity of both measurement methods. When directly comparing Si and P, there is only a significant difference at ambient temperature, with SiCEx events having a three times larger cross section than PCEx.

Due to the low cross section for SiCKO (depicted in fig. 3.13), there is a lack of data across all temperatures (1, 1, 2, and 0 electron dose values). Nevertheless, there is an indication that the cross section increases with growing temperature (300 K: 5.3 mb, 573 K: 17 mb, 973 K: 40 mb, 1273 K: no greater than 57 mb). The PCKO cross section shows a more pronounced upward trend with increasing temperature, rising from 45 mb as an upper bound at ambient temperature (literature: (10 ± 3) mb [21]) to (330 ± 150) mb at 1273 K.

Regarding the replacement by C (SiRepC and PRepC, see fig. 3.14), the cross section for Si is increased at elevated temperatures (plateau at ca. 150 mb) when compared to ambient temperature ((30 ± 30) mb), although the number of observed events is small (3, 4, 3, and 1) and the cross sections could thus have a greater error than specified according to eq. (2.25). Concerning P, the replacement cross section at ambient temperature estimated based on one electron dose value (134 mb) is about four times higher than for Si. There is no significant upward or downward trend with rising temperature. Note that the literature value at ambient temperature ((70 ± 20) mb [21]) is only half as large as the new value from this study. The literature value might be more

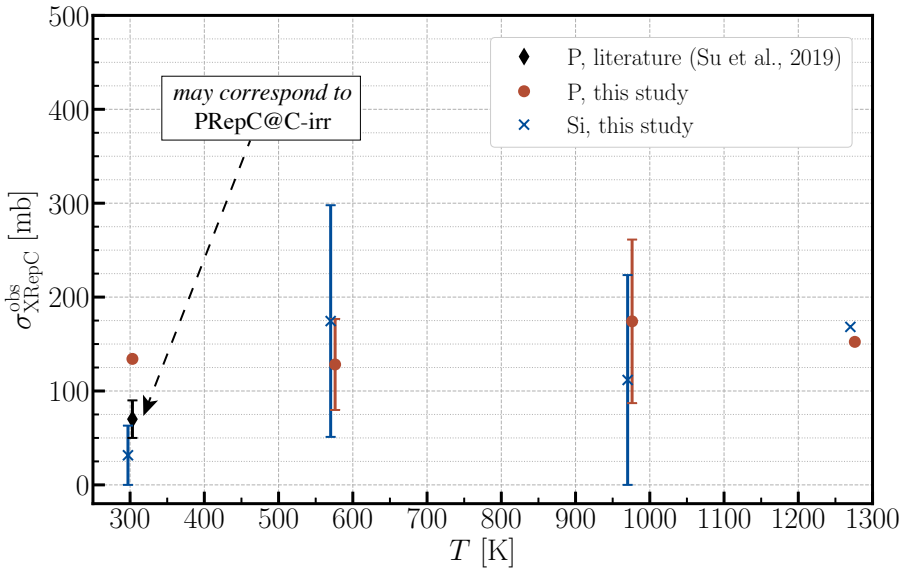

Figure 3.14: SiRepC & PRepC: Observed cross section $\sigma^{\mathrm{obs}}_{\mathrm{XRepc}}$ for the beam-induced replacement of a Si@SV or P@SV impurity by a C atom as a function of the temperature T, at an electron kinetic energy of 60 keV. To reduce overlaps in the illustration of the data points, the latter have been offset on the abscissa by -3 K for Si and by 3 K for P. The cross sections for PRepC at 300 K as well as 1273 K and for SiRepC at 1273 K, are to be regarded as estimates with very high uncertainty, since eq. (2.7) cannot be used for less than three observed events. The literature value for 300 K may correspond to the effect PRepC@C-Irr instead.

comparable to one third of the cross section measured here, because the first was measured based on spot irradiation of a C neighbor, corresponding to the effect "PRepC@C-Irr" instead (as discussed for Si in section 3.3.1.1).

Furthermore, the suitability of P@SV for single-atom manipulation at 60 keV can be briefly discussed based on the cross sections at ambient temperature. Although the new data at hand have large uncertainties, the indication of a large PRepC cross section when compared to the PCEx cross section implies that single-atom manipulation of P@SV is hardly feasible. As mentioned in section 1.3.4, the same conclusion was already drawn in the literature [21].

Table 3.7: Observed cross sections σ^{obs} for different temperatures T and beam-induced processes involving Si@SV and P@SV impurities, at an electron kinetic energy of 60 keV. N^{obs} is the number of observed events. ΔT is approximately 2 % of the absolute value.

SiCEx	Positional exchange between Si@SV and one of its C neighbors
SiCKO	Knock-on displacement of a C neighbor of Si@SV
SiRepC	Replacement of Si@SV by C
PCEx	Positional exchange between P@SV and one of its C neighbors
PCKO	Knock-on displacement of a C neighbor of P@SV
PRepC	Replacement of P@SV by C

T [K]	Element	Event	N^{obs} *	σ^{obs} [mb]	$\Delta\sigma^{\mathrm{obs}}$ [mb]	Origin	Notes
300	Si	SiCEx	29	150	30	this study	
300	Si	SiCKO	1	5.3	n.a.	this study	*
300	Si	SiRepC	3	30	30	this study	
300	P	PCEx	1	45	n.a.	this study	*
300	P	PCEx	2	50	20	[21]	**
300	P	PCKO	0	≤ 45	n.a.	this study	
300	P	PCKO	1	10	3	[21]	**
300	P	PRepC	1	135	n.a.	this study	*
300	P	PRepC	7	70	20	[21]	**
573	Si	SiCEx	3	30	30	this study	
573	Si	SiCKO	1	17	n.a.	this study	*
573	Si	SiRepC	4	170	120	this study	
573	P	PCEx	9	43	16	this study	
573	P	PCKO	6	27	13	this study	
573	P	PRepC	9	130	50	this study	
973	Si	SiCEx	9	150	60	this study	
973	Si	SiCKO	2	40	n.a.	this study	
973	Si	SiRepC	3	110	110	this study	
973	P	PCEx	13	140	40	this study	
973	P	PCKO	13	140	40	this study	
973	P	PRepC	6	170	90	this study	
1273	Si	SiCEx	1	57	n.a.	this study	*
1273	Si	SiCKO	0	≤ 57	n.a.	this study	
1273	Si	SiRepC	1	170	n.a.	this study	*
1273	P	PCEx	5	200	120	this study	
1273	P	PCKO	7	330	150	this study	
1273	P	PRepC	1	150	n.a.	this study	*

* If $N^{\mathrm{obs}} = 1$, the posterior mean solution according to eq. (2.6) will diverge. Instead, $\lambda = N_{\mathrm{e}}$ was used, where N_{e} is the only measured electron dose.
** These values originate from different measuring and calculation methods Furthermore, the provided PRepC cross section may correspond to the effect PRepC@C-Irr instead.

3.4 Evaluation of implantation experiments

3.4.1 Al ion implantation

In an effort to create samples with Al@SV sites, ion implantation experiments with Al^+ were carried out by collaborators in Dresden[3]. The chosen ion implantation energies were 35, 50, and 65 eV. Two samples each were delivered, which were examined in Vienna with STEM to evaluate the implantation yields.

A total sample area of ca. 1.5×10^5 nm^2 has been searched for clean lattice regions. Typical images of the graphene monolayer covered by hydrocarbon contamination are depicted in fig. 3.15. A graphene lattice area of ca. 8000 nm^2, a fraction of which was pure by itself and the other fraction being cleaned by laser-heating (see section 2.1.3 and 2.2.2.1), has been searched for individual Al atoms. No Al was detected via EELS (no onset for the $L_{2,3}$ peak at ca. 73 eV [117]). Instead, individual Si atoms were found, evident due to an onset for the $L_{2,3}$ edge at ca. 99 eV [109] (see also section 2.1.1.1). The electron beam was scanned over contamination areas (appearing bright in the images) several times and EELS spectra were acquired, which did not provide any evidence of Al, either.

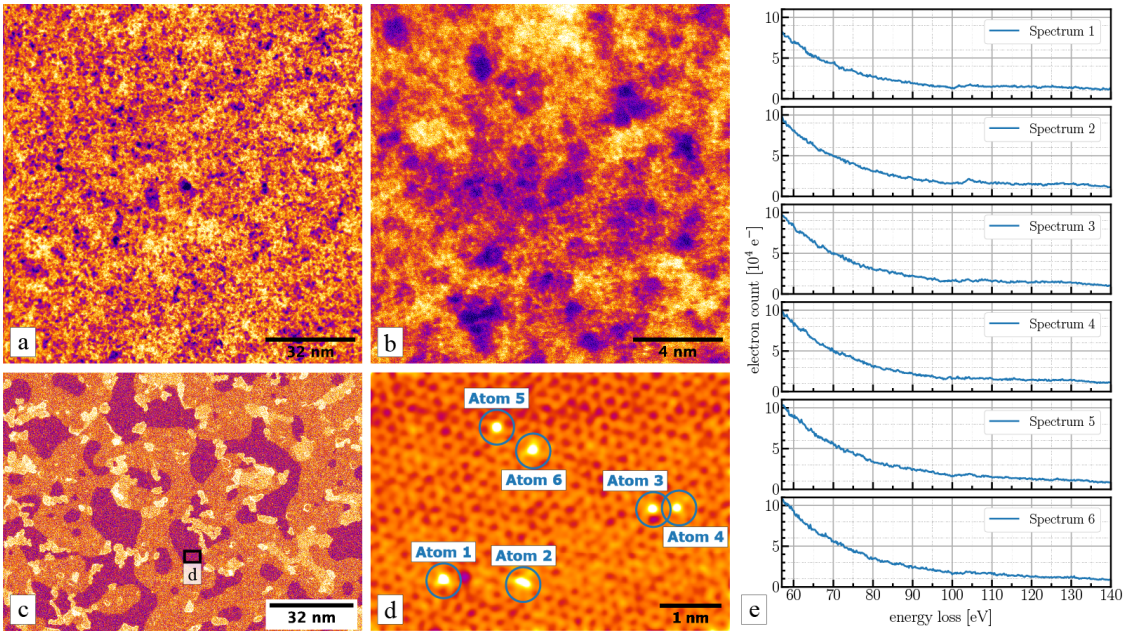

Figure 3.15: MAADF-STEM images of graphene samples after Al^+ ion implantation experiments. (a-b) Overviews of regions (a) 128×128 nm^2 and (b) 16×16 nm^2 in size, covered by hydrocarbon contamination (bright speckled contrast) with small regions of clean free-standing monolayer graphene (dark contrast). (c) Overview of a 130×100 nm^2 region after laser cleaning with a nominal power of 20 mW and an exposure time of 2 ms. (d) Atomically resolved image of a graphene monolayer with substitutional impurities (FOV $= 8 \times 6$ nm^2). All individual impurity atoms found (encircled and labeled in blue) were identified as Si via EELS. (e) Electron energy-loss spectra acquired with an accumulation time of ca. 5 s. During acquisition, the beam was positioned on the corresponding atom numbered in (d).

[3]Research group of Ulrich Kentsch, TU Dresden.

3.4.2 Al and Si incorporation after Ar plasma treatment

As discussed before, the ion implantation experiments for Al were not successful, but sample fabrication carried out by colleagues [68] was finally successful via two-step substitution of carbon (see sections 1.3.4.1 and 2.2.1).

Furthermore, the density of Si impurities in the graphene lattice is much higher in samples treated by Ar^+ plasma irradiation than in commercially available samples. Therefore, such plasma-irradiated samples were used for the voltage-dependent cross-section measurement involving Si@SV impurities (see section 3.3.1) as well as, partly, for the single-atom manipulation experiments which will be reported below.

3.5 High-control automated single-atom manipulation to patterns

3.5.1 Automation software

All demanded software to perform single-atom manipulation in an automated manner exists and is ready to use as a result of this and related work. The Nion Swift plug-in "Atom Manipulator" is open-source software and published under the GPL-3.0 license on Phaidra [163] and GitHub[4]. The tasks it accomplishes were described in section 2.7.3. Here, two information graphics are provided, one describing the functionalities (see fig. 3.17) and the other the main modes of operation (fig. 3.18).

The first successful operation of the Nion Swift Atom Manipulator, on the 7th of June, 2021, was captured in a video, which is available on Phaidra [181]. During the video, a Si@SV impurity is automatically moved by three lattice sites in the intended direction along the shortest path to its user-defined target site, after which the Si@SV exchanges its position with a carbon neighbor other than the desired one. In total, this individual Si atom exchanged its position with a C neighbor six times, after which one of its carbon neighbors was displaced, leaving behind a non-manipulable Si@DV. Note that the implemented path finding algorithm (section 2.7.3.3) is capable of working with multiple impurities and target sites and optimizes the total path length in that case.

An automated single-atom manipulation experiment using a further developed version of the plug-in is presented in fig. 3.16. Perfect control was achieved for four manipulation steps. After the two Si@SV were moved to a separation of only 4 lattice sites for the second time, one of the impurities moved towards the other autonomously after a loss of one or two C atoms (not unambiguously resolved). Subsequently, one of the Si atoms was lost and the defect reconstructed to a Si@DV.

[4] https://github.com/arpostl/nionswift_atom_manipulator

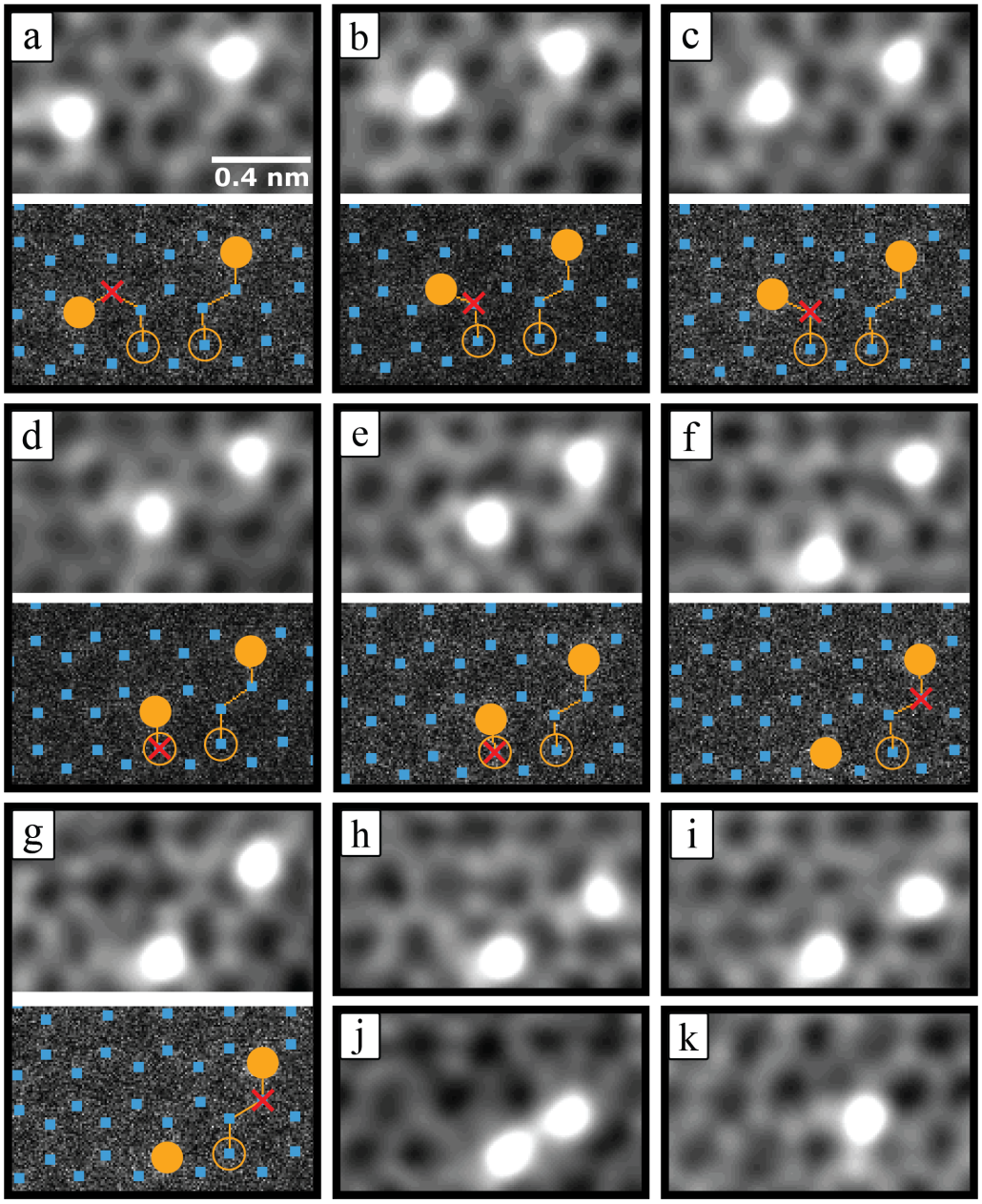

Figure 3.16: Atom Manipulator: MAADF-STEM image series recorded during an automated single-atom manipulation experiment with two individual Si@SV impurities, achieving high control. (a-g) Gaussian-filtered (top) and the corresponding raw image (bottom) with overlays for the recognized atomic positions (filled blue squares for C, filled orange circles for Si), the user-defined target sites (non-filled orange circles), the calculated paths (orange lines), and the position of the electron beam (red cross). The four positional exchanges of the Si@SV and the respective spot-irradiated C neighbor, i.e. (b) compared to (a), (d) compared to (c), (f) compared to (e), and (h) compared to (g), were automatically detected by ADF voltage feedback (increased electron intensity for Si when compared to C). Neither a Si jump nor specimen drift was detected during a 15 s (set as the maximum time before acquiring a new image) spot irradiation of the C atom marked by a red cross in (b), (d), and (f). In these cases, a rescan of the region was performed automatically, after which the spot irradiation was continued based upon the new images (c), (e), and (g). (h-k) Gaussian-filtered images after control in terms of single-atom manipulation was lost. One of the Si impurities moved nearer to the other in (j), and was lost in the next frame (k).

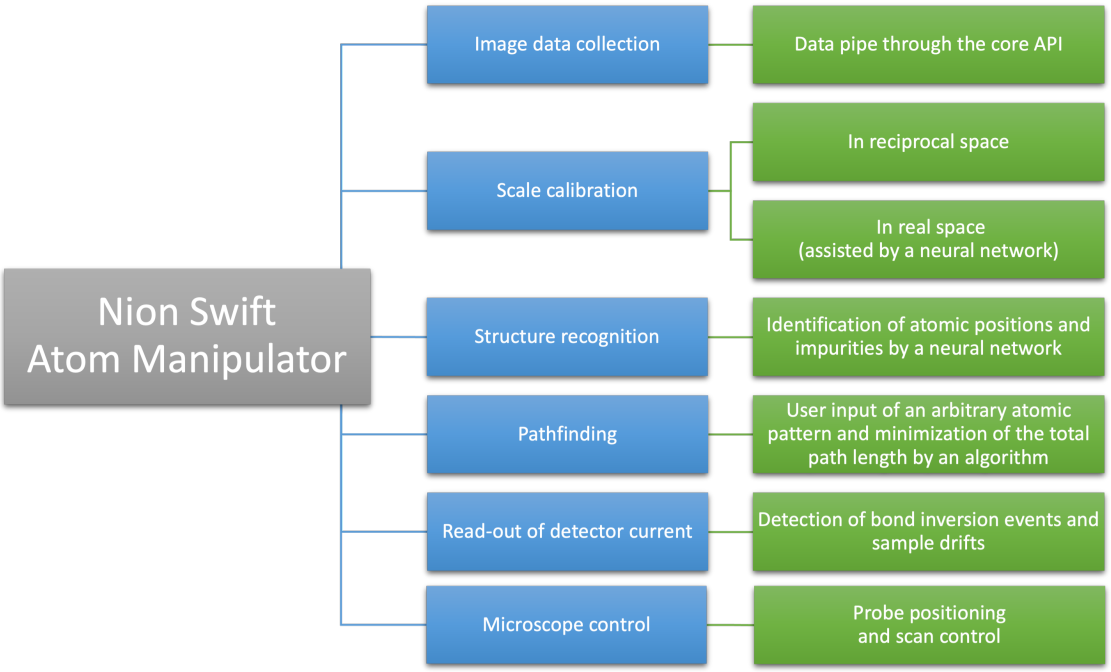

Figure 3.17: Atom Manipulator: Infographics to give an overview of the functionalities. The subtasks (blue boxes) and their descriptions (green boxes) are interpreted in a slightly different way when compared to section 2.7.3 and table 2.1, because this graphic is used to present the software online [163]. It is therefore aimed at people who have not read this thesis.

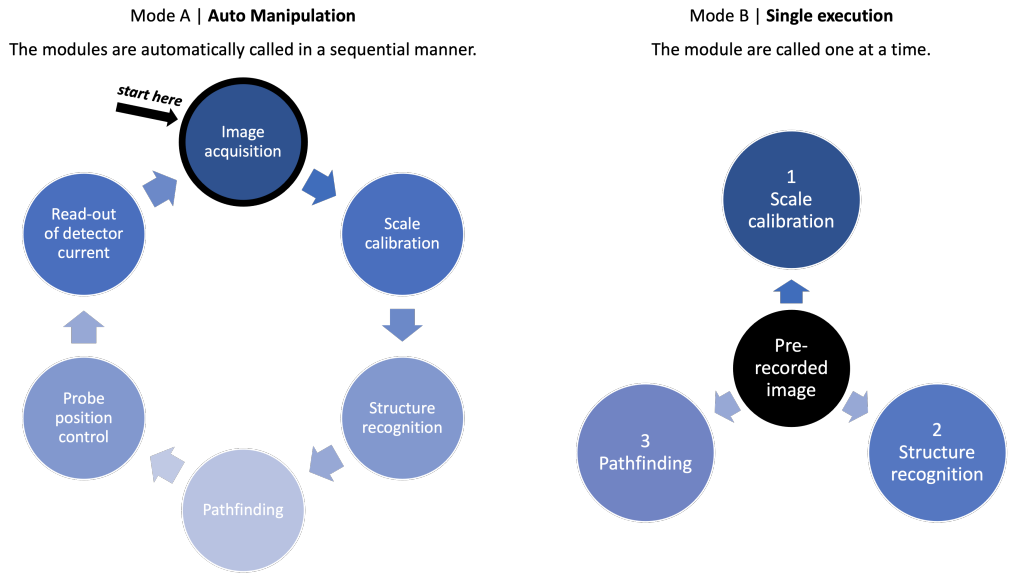

Figure 3.18: Atom Manipulator: Infographics describing the two main operation modes according to section 2.7.3.

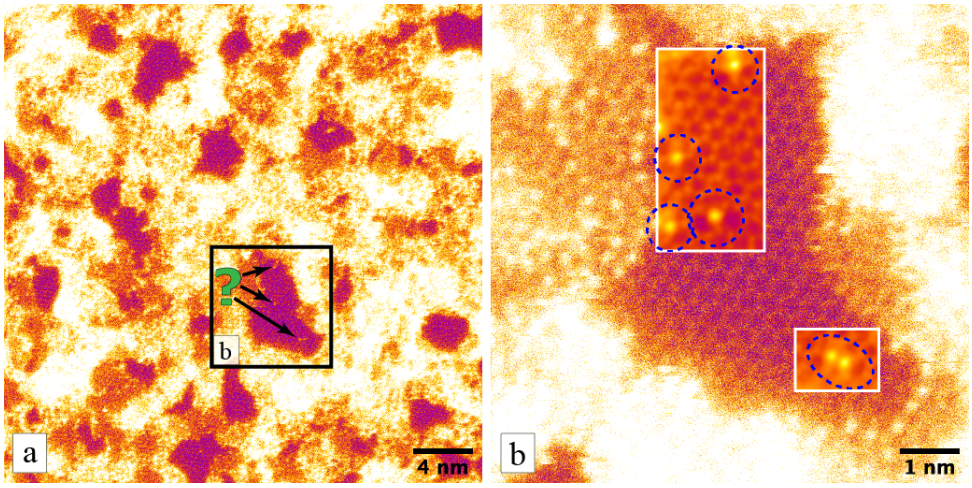

Figure 3.19: Contamination coverage and non-manipulable Si dopants in suspended monolayer graphene (MAADF-STEM images). (a) Overview of a 32×32 nm^2 region with high coverage of hydrocarbon contamination (bright speckled contrast) and clean graphene regions in between (dark contrast). The arrows near the center of the image point to individual Si atoms, which are recognizable at this resolution. Their bonding configuration and the surrounding atomic structure are not resolved. It is thus unclear whether the Si impurities are manipulable. (b) Atomically resolved image of this graphene region. The small monolayer patch is coated by hydrocarbon contamination (bright speckled contrast) at all edges of the image. A total of six Si atoms (marked with blue dashed ellipses) are incorporated into the clean lattice region, three of which are four-coordinated, involved in a topological/structural defect (large white rectangle: top right, middle left, bottom left), or very near to the surrounding contamination. One Si atom (large white rectangle: bottom center) is three-coordinated but also involved in a topological/structural defect. The other two Si atoms (small white rectangle) are bonded to each other, and the structure is not clearly resolved: likely, the Si atoms sit together in a trivacancy. None of these Si atoms are suitable for single-atom manipulation.

3.5.2 Experimental proceedings

Five full days were used for testing and debugging the automation software (see above) on-site at the Nion UltraSTEM 100. Two full days and thirteen half-days were further spent exclusively to push towards high-control single-atom manipulation of silicon and to possibly surpass recent achievements [18, 100]. At this point, it must be admitted that we did not succeed in deliberately bringing more than two atoms close to each other and forming a user-defined pattern, such as schematically illustrated in fig. 1.10 for eleven atoms. There were samples available for which the graphene monolayer had a high density of substitutional silicon (for examples, see fig. 3.19a), though they usually also exhibited high contamination coverage. Among these, two particular samples were not sensitive to laser cleaning because the TEM grid region seemed to be in the geometric shadow of the laser irradiation.

As for the most promising samples, it was typically still difficult to find several silicon atoms close to each other. If silicon atoms were found, it often turned out – after switching to smaller fields of view and higher frame times – that at least two of the three targeted Si atoms either sat in a double vacancy or featured another non-manipulable configuration, as exemplarily shown in fig. 3.19b and fig. 3.20a.

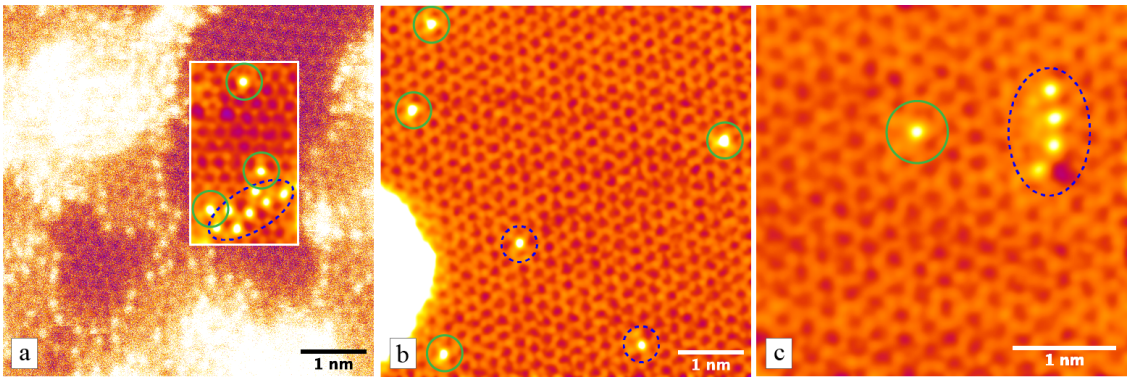

Figure 3.20: Atomically resolved MAADF-STEM images of non-manipulable and manipulable Si impurities in suspended monolayer graphene. (a) The Si atoms in the region featuring a SiC-like structure with topological defects (marked with a blue dashed ellipse) are not manipulable. The other three Si atoms (marked with green solid circles) are Si@SV, have no bond with any other Si, and, thus, their suitability for single-atom manipulation was checked. However, the two atoms close to the SiC-like structure could not be moved away from the latter, which was expected according to section 1.6.2. The atom at the top of the image is near a defective structure (to the left), in which the Si got stuck after this image was taken due to a jump in the unintended direction. (b) A total of six Si atoms were found within a region ca. 6×6 nm^2 in size, two of which turned out to be in the non-manipulable Si@DV structure (marked with blue dashed circles). The other four Si@SV (marked with green solid circles) could not be brought close to each other in the course of the experiment, because three of them each lost a C neighbor due to KO displacement. (c) Four individual Si atoms (marked with a blue dashed ellipse) are located near a vacancy and involved in a topological/structural defect. There was thus only one manipulable Si@SV (marked with a solid green circle).

The rare case that at least three three-coordinated and, thus, manipulable silicon atoms were found in close proximity to each other (say within a square $5\times$ 5 nm^2) was encountered ca. 5 times. Then, an acceleration voltage of 57 keV was used, since this remains the assumed "sweet spot"[5] for single-atom manipulation of Si@SV (see section 1.3.4 as well as section 3.3.1, esp. fig. 3.10). Some encouraging intermediate configurations (after the start and before the end of a single-atom manipulation experiment) for controlled manipulation to patterns are depicted in fig. 3.20. Yet, every attempt to create a smaller scale pattern out of three silicon atoms failed. At least two of them became four-coordinated or trapped otherwise before their positions could be aligned. For every individual Si atom, this happened either without targeted spot irradiation (noticed in images taken later on) or after a relatively low number (fewer than ca. 5) of successfully induced position exchanges between Si and a C neighbor. At 57 keV, such cases are suspected to be "the unlucky ones", since the expectation value $E(M)$ according to eq. (3.22) is just the cross-section ratio $\sigma_{\mathrm{SiCEx}} : \sigma_{\mathrm{CKO}}$, which is assumed to lie above the estimated $E(M)$ for 60 keV (ca. 25, see discussion in section 3.3.1.1 and fig. 3.10).

Therefore, we must conclude that high-control multi-atom manipulation and the creation of arbitrary impurity atom patterns in graphene remains an open challenge, though all of the pieces for further progress have been put together by the work described in this thesis.

[5] Reasonably high exchange rates, low KO cross section for the carbon neighbors.

4 Conclusion

Based on temperature-dependent knock-on damage cross sections of graphene, the first experimental estimate for the carbon adatom migration barrier on graphene was reported, i.e. (0.33±0.03) eV. The developed vacancy healing model during STEM imaging also provides an explanation for the radiation hardness of graphene at elevated temperatures. The new measurement and analysis approach might be suitable to measure the adatom (adparticle) migration barrier of other species on other 2D materials as well.

Beam-induced dynamics of Si@SV impurities in graphene were studied: at ambient temperature, the cross section for the positional exchange between Si@SV and one of its carbon neighbors rises rapidly in the electron kinetic energy range from 50 to 65 keV, where the increase flattens out up to 70 keV. At the latter energy, the exchange cross section reaches a value of ((750 ± 80) mb). In the investigated energy range, the cross section for the knock-on displacement of a Si@SV impurity's carbon neighbor is one to two orders of magnitude lower than for positional exchanges, although it rises in the entire range from 50 to 70 keV, where it takes a value of ((130 ± 30) mb). This behavior is as expected (apart from the exchange cross section at 70 keV) and the ratio of the above-mentioned cross sections is in good agreement with the literature. Regarding the replacement of Si@SV by carbon, no significant dependence on the electron energy was measured, though there is an indication for a slight elevation of the cross section with increasing energy.

At 60 keV, all three above-mentioned dynamics were also measured at elevated temperatures. The general lack of data at temperatures above ambient has to be considered. However, the exchange cross section shows no statistically evident trend as a function of the temperature, varying between ca. 30 and 150 mb. Furthermore, there are indications for the knock-on displacement of a carbon neighbor and the replacement by carbon: the cross section of the former effect appears to rise from ca. 5 mb at ambient temperature to ca. 50 mb at 1000–1300 K, and the cross section of the latter is seemingly increased at elevated temperatures.

Regarding P@SV impurities, for the most part, the results for 60 keV and at ambient temperature agree well with the literature. Across all investigated temperatures, the cross sections for the exchange with a carbon neighbor and for the knock-on displacement of a carbon neighbor are similar to each other, ranging from ca. 40 mb at ambient temperature to ca. 200 mb for exchange and ca. 300 mb for knock-on damage at ca. 1300 K. The cross section for P@SV replacement by carbon does not seem to be a function of the temperature.

The suitability for single-atom manipulation was considered in detail: in the case of Si@SV and in the electron kinetic energy range from 55 to 70 keV, the expected number of exchanges before knock-on damage, leading to a non-manipulable Si@DV, steadily decreases with increasing electron kinetic energy. Moreover, the reported cross sections for the replacement of Si@SV by carbon can give hints for how likely a manipulation experiment gets aborted due to replacement, although the lack of a known atomistic mechanism means that the area involved in calculating the values

is not unambiguously defined. Finally, single-atom manipulation with P@SV impurities is not as promising as with Si@SV at 60 keV, which also confirms previous studies.

A comprehensive software application, embedded as a plug-in in a microscopy suite, was developed to perform automated single-atom manipulation of impurities in graphene. The required user input for single-atom manipulation was, thereby, reduced to a minimum. The first proof of work was recorded, and the application was successfully used for single-atom manipulation by myself as well as colleagues. High control in the automated single-atom manipulation of two individual Si@SV impurities was achieved.

4.1 Pitfalls and experimental difficulties

Sample availability and interplay of other components
From the very beginning of my work, there was agreement among the involved researchers that the availability of samples suitable for high-control single-atom manipulation is one of the greatest factors that can hinder or delay experiments with substitutional impurities other than silicon. There was one sample with P and Si dopants available that eventually allowed temperature-dependent measurements, but unfortunately, it degraded before I could collect all desired data. Ion implantation of Al did not work out, though the two-step implantation carried out by colleagues very recently did [68]. Furthermore, in case a suitable sample was available in principle, further hindrances generally originate from the fact that these experiments require a lot of individual systems (microscopy software, customized plug-ins, CUDA computation, laser apparatus, voltage flashover protection) to work together and simultaneously.

Limitations on single-atom manipulation
One the one hand, 55 kV remains the most safe acceleration voltage for controlled single-atom manipulation of Si@SV. On the other hand, though, the average waiting time (using typical beam currents) for a single positional exchange is as large as ca. 1.5 min [18]. Using an acceleration voltage between 55 kV and 60 kV is promising, as mentioned in the introductory section 1.6.1 and recapped in section 3.3.1.1. Both 60 as well as 65 kV offer high rates for positional exchanges between Si@SV and a carbon neighbor, but both the knock-on damage as well as the replacement rate are moderately high. 70 kV is too high for controlled single-atom manipulation of Si@SV.

Updates of required software
Accepting the challenge of developing embedded applications comes with the burden of software dependencies. Whenever a used package – Nion Swift being the most critical in the context of my work – receives updates, those come with the risk that dependent code has to be adapted. The developed modules and packages for this work are no exception in that regard, and most of them needed regular revisions. This situation will not change in the future, and outside developers are invited to contribute to the packages published under the free GPL-v3 copyleft license.

4.2 Outlook

While the time of my PhD studies has passed too quickly to perform cross-section measurements involving Al@SV impurities and to do more automated single-atom manipulation experiments at high control, we now have much more experimental data related to beam-induced irradiation effects of graphene and its Si@SV impurity. The cross-section data presented in chapter 3, especially those for Si@SV at different electron kinetic energies, will become subject to comparison with a theoretical model including inelastic effects, using the framework of Bethe theory [142].

One of the easiest recognizable patterns made out of three points is an imitation of a lowercase ”i”, and I personally have a lot of faith in producing that arrangement of Si@SV impurities in graphene by single-atom manipulation. Future researchers are cordially invited to actively use the Nion Swift Atom Manipulator and write a letter – or indeed larger and more complicated patterns.

Outputs

First-authored journal article publications

- Publication I

  A. Postl, P. P. P. Hilgert, A. Markevich, J. Madsen, K. Mustonen, J. Kotakoski, T. Susi, Indirect measurement of the carbon adatom migration barrier on graphene, Carbon 196 (2022) 596-601.

  DOI: 10.1016/j.carbon.2022.05.039

  Contribution of A.P.: Investigation, Methodology, Visualization, Formal analysis, Software, Writing – original draft, preparation, Writing – review & editing.

- Manuscript in preparation

  Postl et al., (2022), "Electron irradiation cross sections for graphene's silicon impurities"

  Contribution of A.P.: Investigation, Methodology, Visualization, Formal analysis, Software, Writing.

Other publications

- J. Madsen, A. Postl, T. Susi, Automated Real-time Analysis of Atomic-resolution STEM Images, Microscopy and Microanalysis 25 (S2) (2019) 166–167.

  DOI: 10.1017/S1431927619001569

  Contribution of A.P.: Software testing.

- A. Postl, J. Madsen, P. P. P. Hilgert, M. T. Schreiber, J. Kotakoski, T. Susi, Temperature-dependent displacement cross section of graphene and its impurities: measuring the carbon adatom migration barrier, Microscopy and Microanalysis 27 (S1) (2021) 3340–3340.

  DOI: 10.1017/S143192762101148X

  (related to Publicaton I)

- G. Zagler, M. Stecher, A. Trentino, F. Kraft, C. Su, A. Postl, M. Längle, C. Pesenhofer, C. Mangler, E. H. Ahlgren, A. Markevich, A. Zettl, J. Kotakoski, T. Susi, K. Mustonen, Beam-driven dynamics of aluminium dopants in graphene, 2D Materials (2022).

  DOI: 10.1088/2053-1583/ac6c30

  Contribution of A.P.: Investigation.

- A. Postl, T. A. Bui, F. Kraft, A. Chirita, G. Leuthner, H. Inani, C. Mangler, K. Mustonen, J. Kotakoski, T. Susi, Adventures in Atomic Resolution in situ STEM, Microscopy and Microanalysis 28 (S1) (2022) 2342-2343.

  DOI: 10.1017/S1431927622008996

  (related to Publication I)

Software

- Nion Swift plug-in "Nion Swift Atom Manipulator"

  The package is described in sections 2.7 and 3.5.1. In the latter, some results of the first operations are documented.

  Available on Phaidra [163].

  DOI: 11353/10.1586606

- Nion Swift plug-in "eLabFTW" (fork)

  This package was forked from the "Nionswift Elabftw Plugin"[1] project by Sherjeel Shabih, HU Berlin, and is published under the GPL-3.0 license. It serves the purpose to write electronic lab notes into an instance of the open source laboratory notebook software eLabFTW [182] directly out of Nion Swift.

  Available on Phaidra [183].

  DOI: 11353/10.1591066

- Contributions to pre-existent Nion Swift plug-ins and Python-based analysis packages

  Some effort was put into the further development of PNM-internal software packages that facilitated my own work or made it possible in the first place:

  - Nion Swift plug-in "VCR" (Video Cam Recorder) – see section 2.7.1.
  - Nion Swift plug-in "TractorBeam", and the contained hardware function library `adf_feedback` – see section 2.7.3.4.
  - Nion Swift plug-in "Nion Swift Structure Recognition" – see section 2.7.3.1.
  - `pnm_poisson`, an analysis package for particle dose values originating from a Poisson process – see section 2.4.1.
  - `pnm_cs`, a function library for knock-on damage cross sections – see section 2.4.2.

  These packages are available on internal GIT repository servers and can be requested on demand.

  Available on Phaidra: TractorBeam [171], and Nion Swift Structure Recognition [162].

[1] https://github.com/shabihsherjeel/nionswift_elabftw_plugin

Bibliography

[1] P. R. Wallace, The Band Theory of Graphite, Physical Review 71 (9) (1947) 622–634. doi:10.1103/PhysRev.71.622.

[2] A. K. Geim, K. S. Novoselov, The rise of graphene, Nature Materials 6 (3) (2007) 183–191. doi:10.1038/nmat1849.

[3] C. Lee, X. Wei, J. W. Kysar, J. Hone, Measurement of the Elastic Properties and Intrinsic Strength of Monolayer Graphene, Science 321 (5887) (2008) 385–388. doi:10.1126/science.1157996.

[4] K. S. Novoselov, A. K. Geim, S. V. Morozov, D. Jiang, Y. Zhang, S. V. Dubonos, I. V. Grigorieva, A. A. Firsov, Electric Field Effect in Atomically Thin Carbon Films, Science 306 (5696) (2004) 666–669. doi:10.1126/science.1102896.

[5] K. S. Novoselov, S. V. Morozov, T. M. G. Mohinddin, L. A. Ponomarenko, D. C. Elias, R. Yang, I. I. Barbolina, P. Blake, T. J. Booth, D. Jiang, J. Giesbers, E. W. Hill, A. K. Geim, Electronic properties of graphene, physica status solidi (b) 244 (11) (2007) 4106–4111. doi:10.1002/pssb.200776208.

[6] A. A. Balandin, S. Ghosh, W. Bao, I. Calizo, D. Teweldebrhan, F. Miao, C. N. Lau, Superior Thermal Conductivity of Single-Layer Graphene, Nano Letters 8 (3) (2008) 902–907. doi:10.1021/nl0731872.

[7] R. Bennewitz, J. N. Crain, A. Kirakosian, J.-L. Lin, J. L. McChesney, D. Y. Petrovykh, F. J. Himpsel, Atomic scale memory at a silicon surface, Nanotechnology 13 (4) (2002) 499–502. doi:10.1088/0957-4484/13/4/312.

[8] D. M. Eigler, E. K. Schweizer, Positioning single atoms with a scanning tunnelling microscope, Nature 344 (6266) (1990) 524–526. doi:10.1038/344524a0.

[9] F. E. Kalff, M. P. Rebergen, E. Fahrenfort, J. Girovsky, R. Toskovic, J. L. Lado, J. Fernández-Rossier, A. F. Otte, A kilobyte rewritable atomic memory, Nature Nanotechnology 11 (11) (2016) 926–929. doi:10.1038/nnano.2016.131.

[10] O. L. Krivanek, N. Dellby, A. R. Lupini, Towards sub-Å electron beams, Ultramicroscopy 78 (1) (1999) 1–11. doi:10.1016/S0304-3991(99)00013-3.

[11] P. E. Batson, N. Dellby, O. L. Krivanek, Sub-ångstrom resolution using aberration corrected electron optics, Nature 418 (6898) (2002) 617–620. doi:10.1038/nature00972.

[12] R. P. Feynman, There's plenty of room at the bottom, Resonance 16 (9) (2011) 890–905. doi:10.1007/s12045-011-0109-x.

[13] A. V. Crewe, J. Wall, A scanning microscope with 5 Å resolution, Journal of Molecular Biology 48 (3) (1970) 375–393. doi:10.1016/0022-2836(70)90052-5.

[14] A. V. Crewe, J. Wall, J. Langmore, Visibility of Single Atoms, Science 168 (3937) (1970) 1338–1340. doi:10.1126/science.168.3937.1338.

[15] H. Sawada, F. Hosokawa, T. Kaneyama, T. Ishizawa, M. Terao, M. Kawazoe, T. Sannomiya, T. Tomita, Y. Kondo, T. Tanaka, Y. Oshima, Y. Tanishiro, N. Yamamoto, K. Takayanagi, Achieving 63 pm Resolution in Scanning Transmission Electron Microscope with Spherical Aberration Corrector, Japanese Journal of Applied Physics 46 (6L) (2007) L568. doi:10.1143/JJAP.46.L568.

[16] R. Erni, M. D. Rossell, C. Kisielowski, U. Dahmen, Atomic-Resolution Imaging with a Sub-50-pm Electron Probe, Physical Review Letters 102 (9) (2009) 096101. doi:10.1103/PhysRevLett.102.096101.

[17] T. Susi, J. Kotakoski, D. Kepaptsoglou, C. Mangler, T. C. Lovejoy, O. L. Krivanek, R. Zan, U. Bangert, P. Ayala, J. C. Meyer, Q. Ramasse, Silicon–Carbon Bond Inversions Driven by 60-keV Electrons in Graphene, Physical Review Letters 113 (11) (2014) 115501. doi:10.1103/PhysRevLett.113.115501.

[18] M. Tripathi, A. Mittelberger, N. A. Pike, C. Mangler, J. C. Meyer, M. J. Verstraete, J. Kotakoski, T. Susi, Electron-Beam Manipulation of Silicon Dopants in Graphene, Nano Letters 18 (8) (2018) 5319–5323. doi:10.1021/acs.nanolett.8b02406.

[19] T. Susi, D. Kepaptsoglou, Y.-C. Lin, Q. M. Ramasse, J. C. Meyer, K. Suenaga, J. Kotakoski, Towards atomically precise manipulation of 2D nanostructures in the electron microscope, 2D Materials 4 (4) (2017) 042004. doi:10.1088/2053-1583/aa878f.

[20] T. Susi, J. C. Meyer, J. Kotakoski, Manipulating low-dimensional materials down to the level of single atoms with electron irradiation, Ultramicroscopy 180 (2017) 163–172. doi:10.1016/j.ultramic.2017.03.005.

[21] C. Su, M. Tripathi, Q.-B. Yan, Z. Wang, Z. Zhang, C. Hofer, H. Wang, L. Basile, G. Su, M. Dong, J. C. Meyer, J. Kotakoski, J. Kong, J.-C. Idrobo, T. Susi, J. Li, Engineering single-atom dynamics with electron irradiation, Science Advances 5 (5) (2019) eaav2252. doi:10.1126/sciadv.aav2252.

[22] D. B. Williams, C. B. Carter, Transmission electron microscopy: A textbook for materials science, Springer Science+ Business Media, LLC, 1996.

[23] O. L. Krivanek, M. F. Chisholm, V. Nicolosi, T. J. Pennycook, G. J. Corbin, N. Dellby, M. F. Murfitt, C. S. Own, Z. S. Szilagyi, M. P. Oxley, S. T. Pantelides, S. J. Pennycook, Atom-by-atom structural and chemical analysis by annular dark-field electron microscopy, Nature 464 (7288) (2010) 571–574. doi:10.1038/nature08879.

[24] W. H. Bragg, W. L. Bragg, The reflection of X-rays by crystals, Proceedings of the Royal Society of London. Series A, Containing Papers of a Mathematical and Physical Character 88 (605) (1913) 428–438. doi:10.1098/rspa.1913.0040.

[25] J. Kotakoski, C. Mangler, J. C. Meyer, Imaging atomic-level random walk of a point defect in graphene, Nature Communications 5 (1) (Dec. 2014). doi:10.1038/ncomms4991.

[26] E. J. Kirkland, On the optimum probe in aberration corrected ADF-STEM, Ultramicroscopy 111 (11) (2011) 1523–1530. doi:10.1016/j.ultramic.2011.09.002.

[27] K. Watanabe, N. Nakanishi, T. Yamazaki, M. Kawasaki, I. Hashimoto, M. Shiojiri, Effect of incident probe on HAADF STEM images, physica status solidi (b) 235 (1) (2003) 179–188. doi:10.1002/pssb.200301354.

[28] T. Sasaki, H. Sawada, E. Okunishi, F. Hosokawa, T. Kaneyama, Y. Kondo, K. Kimoto, K. Suenaga, Evaluation of probe size in STEM imaging at 30 and 60kV, Micron 43 (4) (2012) 551–556. doi:10.1016/j.micron.2011.10.010.

[29] M. Saeed Muhammad, T.-S. Choi, 3D shape recovery by image focus using Lorentzian-Cauchy function, in: 2010 IEEE International Conference on Image Processing, 2010, pp. 4065–4068. doi:10.1109/ICIP.2010.5653557.

[30] A. Postl, P. P. P. Hilgert, A. Markevich, J. Madsen, K. Mustonen, J. Kotakoski, T. Susi, Indirect measurement of the carbon adatom migration barrier on graphene, Carbon 196 (2022) 596–601. doi:10.1016/j.carbon.2022.05.039.

[31] J. Lin, O. Cretu, W. Zhou, K. Suenaga, D. Prasai, K. I. Bolotin, N. T. Cuong, M. Otani, S. Okada, A. R. Lupini, J.-C. Idrobo, D. Caudel, A. Burger, N. J. Ghimire, J. Yan, D. G. Mandrus, S. J. Pennycook, S. T. Pantelides, Flexible metallic nanowires with self-adaptive contacts to semiconducting transition-metal dichalcogenide monolayers, Nature Nanotechnology 9 (6) (2014) 436–442. doi:10.1038/nnano.2014.81.

[32] G. H. Ryu, H. J. Park, J. Ryou, J. Park, J. Lee, G. Kim, H. S. Shin, C. W. Bielawski, R. S. Ruoff, S. Hong, Z. Lee, Atomic-scale dynamics of triangular hole growth in monolayer hexagonal boron nitride under electron irradiation, Nanoscale 7 (24) (2015) 10600–10605. doi:10.1039/C5NR01473E.

[33] S. Wang, H. Li, H. Sawada, C. S. Allen, A. I. Kirkland, J. C. Grossman, J. H. Warner, Atomic structure and formation mechanism of sub-nanometer pores in 2D monolayer MoS2, Nanoscale 9 (19) (2017) 6417–6426. doi:10.1039/C7NR01127J.

[34] S. M. Gilbert, G. Dunn, A. Azizi, T. Pham, B. Shevitski, E. Dimitrov, S. Liu, S. Aloni, A. Zettl, Fabrication of Subnanometer-Precision Nanopores in Hexagonal Boron Nitride, Scientific Reports 7 (1) (2017) 15096. doi:10.1038/s41598-017-12684-x.

[35] N. Clark, L. Nguyen, M. J. Hamer, F. Schedin, E. A. Lewis, E. Prestat, A. Garner, Y. Cao, M. Zhu, R. Kashtiban, J. Sloan, D. Kepaptsoglou, R. V. Gorbachev, S. J. Haigh, Scalable Patterning of Encapsulated Black Phosphorus, Nano Letters 18 (9) (2018) 5373–5381. doi:10.1021/acs.nanolett.8b00946.

[36] J. Lin, S. T. Pantelides, W. Zhou, Vacancy-Induced Formation and Growth of Inversion Domains in Transition-Metal Dichalcogenide Monolayer, ACS Nano 9 (5) (2015) 5189–5197. doi:10.1021/acsnano.5b00554.

[37] Z. Liu, Z. Fei, C. Xu, Y. Jiang, X.-L. Ma, H.-M. Cheng, W. Ren, Phase transition and in situ construction of lateral heterostructure of 2D superconducting α/β Mo2C with sharp interface by electron beam irradiation, Nanoscale 9 (22) (2017) 7501–7507. doi:10.1039/C7NR01609C.

[38] F. R. Eder, J. Kotakoski, U. Kaiser, J. C. Meyer, A journey from order to disorder — Atom by atom transformation from graphene to a 2D carbon glass, Scientific Reports 4 (2014). doi:10.1038/srep04060.

[39] J. Su, X. Zhu, In-situ TEM observation of preferential amorphization in single crystal Si nanowire, Nanotechnology 29 (23) (2018) 235703. doi:10.1088/1361-6528/aab6eb.

[40] S. Jesse, Q. He, A. R. Lupini, D. N. Leonard, M. P. Oxley, O. Ovchinnikov, R. R. Unocic, A. Tselev, M. Fuentes-Cabrera, B. G. Sumpter, S. J. Pennycook, S. V. Kalinin, A. Y. Borisevich, Atomic-Level Sculpting of Crystalline Oxides: Toward Bulk Nanofabrication with Single Atomic Plane Precision, Small 11 (44) (2015) 5895–5900. doi:10.1002/smll.201502048.

[41] B. C. Bayer, R. Kaindl, M. Reza Ahmadpour Monazam, T. Susi, J. Kotakoski, T. Gupta, D. Eder, W. Waldhauser, J. C. Meyer, Atomic-Scale in Situ Observations of Crystallization and Restructuring Processes in Two-Dimensional MoS2 Films, ACS Nano 12 (8) (2018) 8758–8769. doi:10.1021/acsnano.8b04945.

[42] O. Dyck, S. Kim, S. V. Kalinin, S. Jesse, Placing single atoms in graphene with a scanning transmission electron microscope, Applied Physics Letters 111 (11) (2017) 113104. doi:10.1063/1.4998599.

[43] B. M. Hudak, J. Song, H. Sims, M. C. Troparevsky, T. S. Humble, S. T. Pantelides, P. C. Snijders, A. R. Lupini, Directed Atom-by-Atom Assembly of Dopants in Silicon, ACS Nano 12 (6) (2018) 5873–5879. doi:10.1021/acsnano.8b02001.

[44] P. Hohenberg, W. Kohn, Inhomogeneous Electron Gas, Physical Review 136 (3B) (1964) B864–B871, publisher: American Physical Society. doi:10.1103/PhysRev.136.B864.

[45] E. Schrödinger, Quantisierung als Eigenwertproblem, Annalen der Physik 385 (13) (1926) 437–490. doi:10.1002/andp.19263851302.

[46] M. Born, W. Heisenberg, Zur Quantentheorie der Molekeln, in: Original Scientific Papers Wissenschaftliche Originalarbeiten, Springer, 1985, pp. 216–246. doi:10.1007/978-3-642-61659-4_16.

[47] W. Kohn, L. J. Sham, Self-Consistent Equations Including Exchange and Correlation Effects, Physical Review 140 (4A) (1965) A1133–A1138. doi:10.1103/PhysRev.140.A1133.

[48] J. P. Perdew, K. Burke, M. Ernzerhof, Generalized Gradient Approximation Made Simple, Physical Review Letters 77 (18) (1996) 3865–3868, publisher: American Physical Society. doi:10.1103/PhysRevLett.77.3865.

[49] J. C. Meyer, C. Kisielowski, R. Erni, M. D. Rossell, M. F. Crommie, A. Zettl, Direct Imaging of Lattice Atoms and Topological Defects in Graphene Membranes, Nano Letters 8 (11) (2008) 3582–3586. doi:10.1021/nl801386m.

[50] F. Banhart, J. Kotakoski, A. V. Krasheninnikov, Structural Defects in Graphene, ACS Nano 5 (1) (2011) 26–41. doi:10.1021/nn102598m.

[51] O. V. Yazyev, S. G. Louie, Topological defects in graphene: Dislocations and grain boundaries, Physical Review B 81 (19) (2010) 195420. doi:10.1103/PhysRevB.81.195420.

[52] L. Liu, M. Qing, Y. Wang, S. Chen, Defects in Graphene: Generation, Healing, and Their Effects on the Properties of Graphene: A Review, Journal of Materials Science & Technology 31 (6) (2015) 599–606. doi:10.1016/j.jmst.2014.11.019.

[53] L. Li, S. Reich, J. Robertson, Defect energies of graphite: Density-functional calculations, Physical Review B 72 (18) (2005) 184109. doi:10.1103/PhysRevB.72.184109.

[54] C. G. Van de Walle, J. Neugebauer, First-principles calculations for defects and impurities: Applications to III-nitrides, Journal of Applied Physics 95 (8) (2004) 3851–3879. doi:10.1063/1.1682673.

[55] P. Badziag, W. S. Verwoerd, W. P. Ellis, N. R. Greiner, Nanometre-sized diamonds are more stable than graphite, Nature 343 (6255) (1990) 244–245. doi:10.1038/343244a0.

[56] A. J. Stone, D. J. Wales, Theoretical studies of icosahedral C60 and some related species, Chemical Physics Letters 128 (5-6) (1986) 501–503. doi:10.1016/0009-2614(86)80661-3.

[57] J. Ma, D. Alfè, A. Michaelides, E. Wang, Stone-Wales defects in graphene and other planar sp2-bonded materials, Physical Review B 80 (3) (2009) 033407. doi:10.1103/PhysRevB.80.033407.

[58] J. Kotakoski, A. V. Krasheninnikov, U. Kaiser, J. C. Meyer, From Point Defects in Graphene to Two-Dimensional Amorphous Carbon, Physical Review Letters 106 (10) (2011) 105505. doi:10.1103/PhysRevLett.106.105505.

[59] R. Ishikawa, S. D. Findlay, T. Seki, G. Sánchez-Santolino, Y. Kohno, Y. Ikuhara, N. Shibata, Direct electric field imaging of graphene defects, Nature Communications 9 (1) (2018) 3878. doi:10.1038/s41467-018-06387-8.

[60] H. A. Jahn, E. Teller, F. G. Donnan, Stability of polyatomic molecules in degenerate electronic states - I—Orbital degeneracy, Proceedings of the Royal Society of London. Series A - Mathematical and Physical Sciences 161 (905) (1937) 220–235. doi:10.1098/rspa.1937.0142.

[61] A. A. El-Barbary, R. H. Telling, C. P. Ewels, M. I. Heggie, P. R. Briddon, Structure and energetics of the vacancy in graphite, Physical Review B 68 (14) (2003) 144107. doi:10.1103/PhysRevB.68.144107.

[62] A. Krasheninnikov, P. Lehtinen, A. Foster, R. Nieminen, Bending the rules: Contrasting vacancy energetics and migration in graphite and carbon nanotubes, Chemical Physics Letters 418 (1-3) (2006) 132–136. doi:10.1016/j.cplett.2005.10.106.

[63] A. Trentino, J. Madsen, A. Mittelberger, C. Mangler, T. Susi, K. Mustonen, J. Kotakoski, Atomic-Level Structural Engineering of Graphene on a Mesoscopic Scale, Nano Letters 21 (12) (2021) 5179–5185. doi:10.1021/acs.nanolett.1c01214.

[64] E. H. Åhlgren, J. Kotakoski, A. V. Krasheninnikov, Atomistic simulations of the implantation of low-energy boron and nitrogen ions into graphene, Physical Review B 83 (11) (Mar. 2011). doi:10.1103/PhysRevB.83.115424.

[65] C. Rao, K. Gopalakrishnan, A. Govindaraj, Synthesis, properties and applications of graphene doped with boron, nitrogen and other elements, Nano Today 9 (3) (2014) 324–343. doi:10.1016/j.nantod.2014.04.010.

[66] M. Tripathi, A. Markevich, R. Böttger, S. Facsko, E. Besley, J. Kotakoski, T. Susi, Implanting Germanium into Graphene, ACS Nano 12 (5) (2018) 4641–4647. doi:10.1021/acsnano.8b01191.

[67] A. Trentino, K. Mizohata, G. Zagler, M. Längle, K. Mustonen, T. Susi, J. Kotakoski, E. H. Åhlgren, Two-step implantation of gold into graphene, 2D Materials 9 (2) (2022) 025011. doi:10.1088/2053-1583/ac4e9c.

[68] G. Zagler, M. Stecher, A. Trentino, F. Kraft, C. Su, A. Postl, M. Längle, C. Pesenhofer, C. Mangler, E. H. Åhlgren, A. Markevich, A. Zettl, J. Kotakoski, T. Susi, K. Mustonen, Beam-driven dynamics of aluminium dopants in graphene, 2D Materials (May 2022). doi:10.1088/2053-1583/ac6c30.

[69] T. Susi, T. P. Hardcastle, H. Hofsäss, A. Mittelberger, T. J. Pennycook, Clemens Mangler, R. Drummond-Brydson, A. J. Scott, J. C. Meyer, J. Kotakoski, Single-atom spectroscopy of phosphorus dopants implanted into graphene, 2D Materials 4 (2) (2017) 021013. doi:10.1088/2053-1583/aa5e78.

[70] D. Usachov, O. Vilkov, A. Grüneis, D. Haberer, A. Fedorov, V. K. Adamchuk, A. B. Preobrajenski, P. Dudin, A. Barinov, M. Oehzelt, C. Laubschat, D. V. Vyalikh, Nitrogen-Doped Graphene: Efficient Growth, Structure, and Electronic Properties, Nano Letters 11 (12) (2011) 5401–5407. doi:10.1021/nl2031037.

[71] H. Wang, Q. Wang, Y. Cheng, K. Li, Y. Yao, Q. Zhang, C. Dong, P. Wang, U. Schwingenschlögl, W. Yang, X. X. Zhang, Doping Monolayer Graphene with Single Atom Substitutions, Nano Letters 12 (1) (2012) 141–144. doi:10.1021/nl2031629.

[72] H. Inani, K. Mustonen, A. Markevich, E.-X. Ding, M. Tripathi, A. Hussain, C. Mangler, E. I. Kauppinen, T. Susi, J. Kotakoski, Silicon Substitution in Nanotubes and Graphene via Intermittent Vacancies, The Journal of Physical Chemistry C 123 (20) (2019) 13136–13140. doi:10.1021/acs.jpcc.9b01894.

[73] P. O. Lehtinen, A. S. Foster, A. Ayuela, A. Krasheninnikov, K. Nordlund, R. M. Nieminen, Magnetic Properties and Diffusion of Adatoms on a Graphene Sheet, Physical Review Letters 91 (1) (2003) 017202. doi:10.1103/PhysRevLett.91.017202.

[74] K. Oura, V. Lifshits, A. Saranin, A. Zotov, M. Katayama, Elementary Processes at Surfaces II. Surface Diffusion, in: Surface Science: An Introduction, Springer Science & Business Media, Chapter 13, 2013, pp. 325–341.

[75] S. Arrhenius, Über die Reaktionsgeschwindigkeit bei der Inversion von Rohrzucker durch Säuren, Zeitschrift für Physikalische Chemie 4U (1) (1889) 226–248. doi:10.1515/zpch-1889-0416.

[76] B. Song, G. F. Schneider, Q. Xu, G. Pandraud, C. Dekker, H. Zandbergen, Atomic-Scale Electron-Beam Sculpting of Near-Defect-Free Graphene Nanostructures, Nano Letters 11 (6) (2011) 2247–2250. doi:10.1021/nl200369r.

[77] R. Zan, Q. M. Ramasse, U. Bangert, K. S. Novoselov, Graphene Reknits Its Holes, Nano Letters 12 (8) (2012) 3936–3940. doi:10.1021/nl300985q.

[78] A. V. Krasheninnikov, K. Nordlund, P. O. Lehtinen, A. S. Foster, A. Ayuela, R. M. Nieminen, Adsorption and migration of carbon adatoms on carbon nanotubes: Density-functional *ab initio* and tight-binding studies, Physical Review B 69 (7) (2004) 073402. doi:10.1103/PhysRevB.69.073402.

[79] G. Henkelman, H. Jónsson, Improved tangent estimate in the nudged elastic band method for finding minimum energy paths and saddle points, The Journal of Chemical Physics 113 (22) (2000) 9978–9985. doi:10.1063/1.1323224.

[80] A. V. Krasheninnikov, K. Nordlund, Ion and electron irradiation-induced effects in nanostructured materials, Journal of Applied Physics 107 (7) (2010) 071301. doi:10.1063/1.3318261.

[81] L. Xian, M. Y. Chou, Diffusion of Si and C atoms on and between graphene layers, Journal of Physics D: Applied Physics 45 (45) (2012) 455309. doi:10.1088/0022-3727/45/45/455309.

[82] P. Thrower, R. Mayer, Point defects and self-diffusion in graphite, Physica Status Solidi A, Applied Research 47 (1) (1978) 11–37. doi:10.1002/pssa.2210470102.

[83] R. Ishikawa, R. Mishra, A. R. Lupini, S. D. Findlay, T. Taniguchi, S. T. Pantelides, S. J. Pennycook, Direct Observation of Dopant Atom Diffusion in a Bulk Semiconductor Crystal Enhanced by a Large Size Mismatch, Phys. Rev. Lett. 113 (15) (2014) 155501. doi:10.1103/PhysRevLett.113.155501.

[84] C. Li, Y.-Y. Zhang, T. J. Pennycook, Y. Wu, A. R. Lupini, N. Paudel, S. T. Pantelides, Y. Yan, S. J. Pennycook, Column-by-column observation of dislocation motion in CdTe: Dynamic scanning transmission electron microscopy, Applied Physics Letters 109 (14) (2016) 143107. doi:10.1063/1.4963765.

[85] T. Furnival, R. K. Leary, E. C. Tyo, S. Vajda, Q. M. Ramasse, J. M. Thomas, P. D. Bristowe, P. A. Midgley, Anomalous diffusion of single metal atoms on a graphene oxide support, Chemical Physics Letters 683 (2017) 370–374. doi:10.1016/j.ultramic.2016.05.005.

[86] A. W. Robertson, B. Montanari, K. He, C. S. Allen, Y. A. Wu, N. M. Harrison, A. I. Kirkland, J. H. Warner, Structural Reconstruction of the Graphene Monovacancy, ACS Nano 7 (5) (2013) 4495–4502. doi:10.1021/nn401113r.

[87] J. D. Wadey, A. Markevich, A. Robertson, J. Warner, A. Kirkland, E. Besley, Mechanisms of monovacancy diffusion in graphene, Chemical Physics Letters 648 (2016) 161–165. doi:10.1016/j.cplett.2016.02.005.

[88] F. Banhart, Irradiation effects in carbon nanostructures, Reports on Progress in Physics 62 (8) (1999) 1181. doi:10.1088/0034-4885/62/8/201.

[89] A. Zobelli, A. Gloter, C. P. Ewels, G. Seifert, C. Colliex, Electron knock-on cross section of carbon and boron nitride nanotubes, Physical Review B 75 (24) (2007) 245402. doi:10.1103/PhysRevB.75.245402.

[90] T. Susi, J. C. Meyer, J. Kotakoski, Quantifying transmission electron microscopy irradiation effects using two-dimensional materials, Nature Reviews Physics 1 (6) (2019) 397–406. doi:10.1038/s42254-019-0058-y.

[91] K. I. Bolotin, K. J. Sikes, Z. Jiang, M. Klima, G. Fudenberg, J. Hone, P. Kim, H. L. Stormer, Ultrahigh electron mobility in suspended graphene, Solid State Communications 146 (9) (2008) 351–355. doi:10.1016/j.ssc.2008.02.024.

[92] J. C. Meyer, F. Eder, S. Kurasch, V. Skakalova, J. Kotakoski, H. J. Park, S. Roth, A. Chuvilin, S. Eyhusen, G. Benner, A. V. Krasheninnikov, U. Kaiser, Accurate Measurement of Electron Beam Induced Displacement Cross Sections for Single-Layer Graphene, Physical Review Letters 108 (19) (2012) 196102. doi:10.1103/PhysRevLett.108.196102.

[93] T. Susi, C. Hofer, G. Argentero, G. T. Leuthner, T. J. Pennycook, C. Mangler, J. C. Meyer, J. Kotakoski, Isotope analysis in the transmission electron microscope, Nature Communications 7 (1) (2016) 13040. doi:10.1038/ncomms13040.

[94] G. T. Leuthner, S. Hummel, C. Mangler, T. J. Pennycook, T. Susi, J. C. Meyer, J. Kotakoski, Scanning transmission electron microscopy under controlled low-pressure atmospheres, Ultramicroscopy (Feb. 2019). doi:10.1016/j.ultramic.2019.02.002.

[95] G. T. Leuthner, T. Susi, C. Mangler, J. C. Meyer, J. Kotakoski, Chemistry at graphene edges in the electron microscope, 2D Materials 8 (3) (2021) 035023. doi:10.1088/2053-1583/abf624.

[96] O. Cretu, Y.-C. Lin, K. Suenaga, Inelastic electron irradiation damage in hexagonal boron nitride, Micron 72 (2015) 21–27. doi:10.1016/j.micron.2015.02.002.

[97] S. Kretschmer, T. Lehnert, U. Kaiser, A. V. Krasheninnikov, Formation of Defects in Two-Dimensional MoS_2 in the Transmission Electron Microscope at Electron Energies below the Knock-on Threshold: The Role of Electronic Excitations, Nano Letters 20 (4) (2020) 2865–2870. doi:10.1021/acs.nanolett.0c00670.

[98] A. I. Chirita Mihaila, T. Susi, J. Kotakoski, Influence of temperature on the displacement threshold energy in graphene, Scientific Reports 9 (1) (2019) 12981. doi:10.1038/s41598-019-49565-4.

[99] T. Fließbach, Mechanik: Lehrbuch zur Theoretischen Physik I, Springer Spektrum Berlin, Heidelberg, 2015. doi:10.1007/978-3-642-55432-2.

[100] O. Dyck, S. Kim, E. Jimenez-Izal, A. N. Alexandrova, S. V. Kalinin, S. Jesse, Building Structures Atom by Atom via Electron Beam Manipulation, Small 14 (38) (2018) 1801771. doi:10.1002/smll.201801771.

[101] K. Mustonen, A. Hussain, C. Hofer, M. R. A. Monazam, R. Mirzayev, K. Elibol, P. Laiho, C. Mangler, H. Jiang, T. Susi, E. I. Kauppinen, J. Kotakoski, J. C. Meyer, Atomic-Scale Deformations at the Interface of a Mixed-Dimensional van der Waals Heterostructure, ACS Nano 12 (8) (2018) 8512–8519. doi:10.1021/acsnano.8b04050.

[102] T. Susi, M. Scardamaglia, K. Mustonen, M. Tripathi, A. Mittelberger, M. Al-Hada, M. Amati, H. Sezen, P. Zeller, A. H. Larsen, C. Mangler, J. C. Meyer, L. Gregoratti, C. Bittencourt, J. Kotakoski, Intrinsic core level photoemission of suspended monolayer graphene, Physical Review Materials 2 (7) (2018). doi:10.1103/PhysRevMaterials.2.074005.

[103] J. Tuček, K. Holá, G. Zoppellaro, P. Błoński, R. Langer, M. Medved', T. Susi, M. Otyepka, R. Zbořil, Zigzag sp2 Carbon Chains Passing through an sp3 Framework: A Driving Force toward Room-Temperature Ferromagnetic Graphene, ACS Nano 12 (12) (2018) 12847–12859. doi:10.1021/acsnano.8b08052.

[104] T. Susi, J. Madsen, U. Ludacka, J. J. Mortensen, T. J. Pennycook, Z. Lee, J. Kotakoski, U. Kaiser, J. C. Meyer, Efficient first principles simulation of electron scattering factors for transmission electron microscopy, Ultramicroscopy 197 (2019) 16–22. doi:10.1016/j.ultramic.2018.11.002.

[105] R. Nieman, A. J. A. Aquino, T. P. Hardcastle, J. Kotakoski, T. Susi, H. Lischka, Structure and electronic states of a graphene double vacancy with an embedded Si dopant, The Journal of Chemical Physics 147 (19) (2017) 194702. doi:10.1063/1.4999779.

[106] U. Bangert, W. Pierce, D. M. Kepaptsoglou, Q. Ramasse, R. Zan, M. H. Gass, J. A. Van den Berg, C. B. Boothroyd, J. Amani, H. Hofsäss, Ion Implantation of Graphene—Toward IC Compatible Technologies, Nano Letters 13 (10) (2013) 4902–4907. doi:10.1021/nl402812y.

[107] J. C. Meyer, S. Kurasch, H. J. Park, V. Skakalova, D. Künzel, A. Groß, A. Chuvilin, G. Algara-Siller, S. Roth, T. Iwasaki, U. Starke, J. H. Smet, U. Kaiser, Experimental analysis of charge redistribution due to chemical bonding by high-resolution transmission electron microscopy, Nature Materials 10 (3) (2011) 209–215. doi:10.1038/nmat2941.

[108] Y.-C. Lin, P.-Y. Teng, C.-H. Yeh, M. Koshino, P.-W. Chiu, K. Suenaga, Structural and Chemical Dynamics of Pyridinic-Nitrogen Defects in Graphene, Nano Letters 15 (11) (2015) 7408–7413. doi:10.1021/acs.nanolett.5b02831.

[109] Q. M. Ramasse, C. R. Seabourne, D.-M. Kepaptsoglou, R. Zan, U. Bangert, A. J. Scott, Probing the Bonding and Electronic Structure of Single Atom Dopants in Graphene with Electron Energy Loss Spectroscopy, Nano Letters 13 (10) (2013) 4989–4995. doi:10.1021/nl304187e.

[110] A. V. Markevich, M. Baldoni, J. H. Warner, A. I. Kirkland, E. Besley, Dynamic Behavior of Single Fe Atoms Embedded in Graphene, The Journal of Physical Chemistry C 120 (38) (2016) 21998–22003. doi:10.1021/acs.jpcc.6b06554.

[111] A. W. Robertson, B. Montanari, K. He, J. Kim, C. S. Allen, Y. A. Wu, J. Olivier, J. Neethling, N. Harrison, A. I. Kirkland, J. H. Warner, Dynamics of Single Fe Atoms in Graphene Vacancies, Nano Letters 13 (4) (2013) 1468–1475. doi:10.1021/nl304495v.

[112] D. Nosraty Alamdary, J. Kotakoski, T. Susi, Structure and Energetics of Embedded Si Patterns in Graphene, physica status solidi (b) 254 (11) (2017) 1700188. doi:10.1002/pssb.201700188.

[113] M. Tripathi, Modifying low-dimensional materials using energetic charged particles, Dissertation, University of Vienna (2019).

[114] M. Murfitt, C. Meyer, G. Skone, N. Dellby, O. Krivanek, Open-Source Python Scripting and Analysis with Nion Swift, Microscopy and Microanalysis 19 (S2) (2013) 782–783. doi:10.1017/S1431927613005904.

[115] J. Hillier, On the Investigation of Specimen Contamination in the Electron Microscope, Journal of Applied Physics 19 (3) (1948) 226–230. doi:10.1063/1.1715049.

[116] R. F. Egerton, Electron Energy-Loss Spectroscopy in the Electron Microscope, Springer Science & Business Media, 2011.

[117] C. C. Ahn, Transmission electron energy loss spectrometry in materials science and the EELS atlas, John Wiley & Sons, 2006.

[118] C. Mangler, J. Meyer, A. Mittelberger, K. Mustonen, T. Susi, J. Kotakoski, A Materials Scientist's CANVAS: A System for Controlled Alteration of Nanomaterials in Vacuum Down to the Atomic Scale, Microscopy and Microanalysis 28 (S1) (2022) 2940–2942. doi:10.1017/S1431927622011023.

[119] K. Mustonen, C. Hofer, P. Kotrusz, A. Markevich, M. Hulman, C. Mangler, T. Susi, T. J. Pennycook, K. Hricovini, C. Richter, J. C. Meyer, J. Kotakoski, V. Skákalová, Toward Exotic Layered Materials: 2D Cuprous Iodide, Advanced Materials 34 (9) (2022) 2106922. doi:10.1002/adma.202106922.

[120] G. Zagler, M. Reticcioli, C. Mangler, D. Scheinecker, C. Franchini, J. Kotakoski, CuAu, a hexagonal two-dimensional metal, 2D Materials 7 (4) (2020) 045017. doi:10.1088/2053-1583/ab9c39.

[121] M. Tripathi, A. Mittelberger, K. Mustonen, C. Mangler, J. Kotakoski, J. C. Meyer, T. Susi, Cleaning graphene: Comparing heat treatments in air and in vacuum, physica status solidi (RRL) – Rapid Research Letters 11 (8) (2017) 1700124. doi:10.1002/pssr.201700124.

[122] Supplemental Material of [30]: Appendix A, Supplementary Data, Multimedia component 1 at https://doi.org/10.1016/j.carbon.2022.05.039. Another supplementary data item (Jupyter notebook) contains the code used to simulate our extended model.

[123] C. Hofer, V. Skákalová, J. Haas, X. Wang, K. Braun, R. S. Pennington, J. C. Meyer, Atom-by-atom chemical identification from scanning transmission electron microscopy images in presence of noise and residual aberrations, Ultramicroscopy 227 (2021) 113292. doi:10.1016/j.ultramic.2021.113292.

[124] S. Ruder, An overview of gradient descent optimization algorithms (2017). doi:10.48550/arXiv.1609.04747.

[125] A. Paszke, S. Gross, F. Massa, A. Lerer, J. Bradbury, G. Chanan, T. Killeen, Z. Lin, N. Gimelshein, L. Antiga, A. Desmaison, A. Kopf, E. Yang, Z. DeVito, M. Raison, A. Tejani, S. Chilamkurthy, B. Steiner, L. Fang, J. Bai, S. Chintala, PyTorch: An Imperative Style, High-Performance Deep Learning Library, in: H. Wallach, H. Larochelle, A. Beygelzimer, F. d. Alché-Buc, E. Fox, R. Garnett (Eds.), Advances in Neural Information Processing Systems 32, Curran Associates, Inc., 2019, pp. 8024–8035.

[126] J. F. C. Kingman, Poisson processes, Vol. 3, Clarendon Press, 1992.

[127] W. Von der Linden, V. Dose, U. Von Toussaint, Bayesian parameter estimation, in: Bayesian Probability Theory: Applications in the Physical Sciences, Cambridge University Press, Chapter 14, 2014, pp. 233–235. doi:10.1017/CBO9781139565608.

[128] O. Dyck, S. Kim, A. Borisevich, B. M. Hudak, A. R. Lupini, S. V. Kalinin, S. Jesse, Atomic Manipulation on a Scanning Transmission Electron Microscope Platform using Real-Time Image Processing and Feedback, Microscopy and Microanalysis 24 (S1) (2018) 534–535. doi:10.1017/S1431927618003161.

[129] G. T. Fechner, Elemente der Psychophysik, Vol. 2, Breitkopf u. Härtel, 1860.

[130] Y. LeCun, Y. Bengio, G. Hinton, Deep learning, Nature 521 (7553) (2015) 436–444. doi:10.1038/nature14539.

[131] G. Voronoi, Nouvelles applications des paramètres continus à la théorie des formes quadratiques. Deuxième mémoire. Recherches sur les parallélloèdres primitifs., Journal für die reine und angewandte Mathematik (Crelles Journal) 1908 (134) (1908) 198–287. doi:10.1515/crll.1908.134.198.

[132] G. Voronoi, Nouvelles applications des paramètres continus à la théorie des formes quadratiques. Premier mémoire. Sur quelques propriétés des formes quadratiques positives parfaites., Journal für die reine und angewandte Mathematik (Crelles Journal) 1908 (133) (1908) 97–102. doi:10.1515/crll.1908.133.97.

[133] J. Kotakoski, J. C. Meyer, S. Kurasch, D. Santos-Cottin, U. Kaiser, A. V. Krasheninnikov, Stone-Wales-type transformations in carbon nanostructures driven by electron irradiation, Physical Review B 83 (24) (2011) 245420. doi:10.1103/PhysRevB.83.245420.

[134] O. L. Krivanek, N. Dellby, M. F. Murfitt, M. F. Chisholm, T. J. Pennycook, K. Suenaga, V. Nicolosi, Gentle STEM: ADF imaging and EELS at low primary energies, Ultramicroscopy 110 (8) (2010) 935–945. doi:10.1016/j.ultramic.2010.02.007.

[135] C. A. Schneider, W. S. Rasband, K. W. Eliceiri, NIH Image to ImageJ: 25 years of image analysis, Nature Methods 9 (7) (2012) 671–675. doi:10.1038/nmeth.2089.

[136] F. Perez, B. E. Granger, IPython: A System for Interactive Scientific Computing, Computing in Science & Engineering 9 (3) (2007) 21–29. doi:10.1109/MCSE.2007.53.

[137] J. Madsen, P. Liu, J. Kling, J. B. Wagner, T. W. Hansen, O. Winther, J. Schiøtz, A Deep Learning Approach to Identify Local Structures in Atomic-Resolution Transmission Electron Microscopy Images, Advanced Theory and Simulations 1 (8) (2018) 1800037. doi:10.1002/adts.201800037.

[138] N. F. Mott, N. H. D. Bohr, The scattering of fast electrons by atomic nuclei, Proceedings of the Royal Society of London. Series A, Containing Papers of a Mathematical and Physical Character 124 (794) (1929) 425–442. doi:10.1098/rspa.1929.0127.

[139] N. F. Mott, R. H. Fowler, The polarisation of electrons by double scattering, Proceedings of the Royal Society of London. Series A, Containing Papers of a Mathematical and Physical Character 135 (827) (1932) 429–458. doi:10.1098/rspa.1932.0044.

[140] W. A. McKinley, H. Feshbach, The Coulomb Scattering of Relativistic Electrons by Nuclei, Physical Review 74 (12) (1948) 1759–1763. doi:10.1103/PhysRev.74.1759.

[141] F. Seitz, J. Koehler, Solid state physics vol. 2, Academic Press, New York, 1956.

[142] H. Bethe, Zur Theorie des Durchgangs schneller Korpuskularstrahlen durch Materie, Annalen der Physik 397 (3) (1930) 325–400. doi:10.1002/andp.19303970303.

[143] A. Chirita, A. Markevich, M. Tripathi, N. A. Pike, M. J. Verstraete, J. Kotakoski, T. Susi, Three-dimensional ab initio description of vibration-assisted electron knock-on displacements in graphene, Physical Review B 105 (23) (2022) 235419. doi:10.1103/PhysRevB.105.235419.

[144] J. Enkovaara, C. Rostgaard, J. J. Mortensen, J. Chen, M. Dułak, L. Ferrighi, J. Gavnholt, C. Glinsvad, V. Haikola, H. Hansen, others, Electronic structure calculations with GPAW: a real-space implementation of the projector augmented-wave method, Journal of Physics: Condensed Matter 22 (25) (2010) 253202. doi:10.1088/0953-8984/22/25/253202.

[145] T. P. Hardcastle, C. R. Seabourne, R. Zan, R. M. D. Brydson, U. Bangert, Q. M. Ramasse, K. S. Novoselov, A. J. Scott, Mobile metal adatoms on single layer, bilayer, and trilayer graphene: An ab initio DFT study with van der Waals corrections correlated with electron microscopy data, Physical Review B 87 (19) (2013) 195430. doi:10.1103/PhysRevB.87.195430.

[146] S. Thinius, M. M. Islam, P. Heitjans, T. Bredow, Theoretical study of Li migration in lithium–graphite intercalation compounds with dispersion-corrected DFT methods, The Journal of Physical Chemistry C 118 (5) (2014) 2273–2280. doi:10.1021/jp408945j.

[147] A. Tkatchenko, M. Scheffler, Accurate Molecular Van Der Waals Interactions from Ground-State Electron Density and Free-Atom Reference Data, Physical Review Letters 102 (7) (2009) 073005. doi:10.1103/PhysRevLett.102.073005.

[148] V. R. Cooper, Van der Waals density functional: An appropriate exchange functional, Physical Review B 81 (16) (2010) 161104, publisher: American Physical Society. doi:10.1103/PhysRevB.81.161104.

[149] A. M. Legendre, Nouvelles méthodes pour la détermination des orbites des comètes, Firmin Didot, Paris, 1806.

[150] H. W. Sorenson, Least-squares estimation: from Gauss to Kalman, IEEE Spectrum 7 (7) (1970) 63–68. doi:10.1109/MSPEC.1970.5213471.

[151] P. Virtanen, R. Gommers, T. E. Oliphant, M. Haberland, T. Reddy, D. Cournapeau, E. Burovski, P. Peterson, W. Weckesser, J. Bright, S. J. van der Walt, M. Brett, J. Wilson, K. J. Millman, N. Mayorov, A. R. J. Nelson, E. Jones, R. Kern, E. Larson, C. J. Carey, I. Polat, Y. Feng, E. W. Moore, J. VanderPlas, D. Laxalde, J. Perktold, R. Cimrman, I. Henriksen, E. A. Quintero, C. R. Harris, A. M. Archibald, A. H. Ribeiro, F. Pedregosa, P. van Mulbregt, SciPy 1.0: fundamental algorithms for scientific computing in Python, Nature Methods 17 (3) (2020) 261–272. doi:10.1038/s41592-019-0686-2.

[152] A. R. Conn, N. I. Gould, P. L. Toint, Trust region methods, SIAM, 2000.

[153] P. T. Boggs, J. E. Rogers, Orthogonal distance regression, Contemporary Mathematics 112 (1990) 183–194. doi:10.6028/NIST.IR.89-4197.

[154] H. H. Ku, others, Notes on the use of propagation of error formulas, Journal of Research of the National Bureau of Standards 70 (4) (1966) 263–273.

[155] D. G. Altman, J. M. Bland, Standard deviations and standard errors, BMJ 331 (7521) (2005) 903. doi:10.1136/bmj.331.7521.903.

[156] E. Gamma, R. Helm, R. Johnson, R. E. Johnson, J. Vlissides, others, Design patterns: elements of reusable object-oriented software, Pearson Deutschland GmbH, 1995.

[157] J. Long, E. Shelhamer, T. Darrell, Fully convolutional networks for semantic segmentation, in: Proceedings of the IEEE conference on computer vision and pattern recognition, 2015, pp. 3431–3440.

[158] M. Ziatdinov, O. Dyck, A. Maksov, X. Li, X. Sang, K. Xiao, R. R. Unocic, R. Vasudevan, S. Jesse, S. V. Kalinin, Deep Learning of Atomically Resolved Scanning Transmission Electron Microscopy Images: Chemical Identification and Tracking Local Transformations, ACS Nano 11 (12) (2017) 12742–12752. doi:10.1021/acsnano.7b07504.

[159] J. Madsen, Python package "Fourier Scale Calibration",
Permanent link: https://phaidra.univie.ac.at/o:1589265. doi:11353/10.1589265.

[160] J. Madsen, A. Postl, T. Susi, Automated Real-time Analysis of Atomic-resolution STEM Images, Microscopy and Microanalysis 25 (S2) (2019) 166–167. doi:10.1017/S1431927619001569.

[161] J. Schiøtz, J. Madsen, B. J. G. Østergaard, A. S. Dreisig, P. Liu, S. Helveg, O. Winther, J. Kling, J. B. Wagner, T. W. Hansen, Using Neural Networks to Identify Atoms in HRTEM Images, Microscopy and Microanalysis 25 (S2) (2019) 216–217. doi:10.1017/S1431927619001818.

[162] J. Madsen, A. Postl, T. Susi, Python package "Nion Swift Structure Recognition".
Permanent link: https://phaidra.univie.ac.at/o:1589267. doi:11353/10.1589267.

[163] A. Postl, J. Madsen, C. Hofer, C. Mangler, A. Mittelberger, T. Susi, Python package "Nion Swift Atom Manipulator".
Permanent link: https://phaidra.univie.ac.at/o:1586606. doi:11353/10.1586606.

[164] P.-E. Danielsson, Euclidean distance mapping, Computer Graphics and Image Processing 14 (3) (1980) 227–248. doi:10.1016/0146-664X(80)90054-4.

[165] E. F. Krause, Taxicab geometry: An adventure in non-Euclidean geometry, Courier Corporation, 1986.

[166] H. Minkowski, Geometrie der Zahlen, BG Teubner, 1910.

[167] R. Jonker, A. Volgenant, A shortest augmenting path algorithm for dense and sparse linear assignment problems, Computing 38 (4) (1987) 325–340. doi:10.1007/BF02278710.

[168] D. F. Crouse, On implementing 2D rectangular assignment algorithms, IEEE Transactions on Aerospace and Electronic Systems 52 (4) (2016) 1679–1696. doi:10.1109/TAES.2016.140952.

[169] H. W. Kuhn, The Hungarian method for the assignment problem, Naval Research Logistics Quarterly 2 (1-2) (1955) 83–97. doi:10.1002/nav.3800020109.

[170] J. Munkres, Algorithms for the assignment and transportation problems, Journal of the society for industrial and applied mathematics 5 (1) (1957) 32–38.

[171] C. Mangler, A. Mittelberger, A. Postl, T. Susi, Python package "Nion Swift TractorBeam".
Permanent link: https://phaidra.univie.ac.at/o:1541616. doi:11353/10.1541616.

[172] K. Pearson, The Problem of the Random Walk, Nature 72 (1865) (1905) 294–294. doi:10.1038/072294b0.

[173] J. Bernoulli, Ars conjectandi, opus posthumum: accedit tractatus de seriebus infinitis, et epistola Gallice scripta de ludo pilæ reticularis, Impensis Thurnisiorum Fratrum, 1713.

[174] A. De Moivre, The doctrine of chances: A method of calculating the probabilities of events in play, Routledge, 2020. doi:10.4324/9780203041352.

[175] F. M. Dekking, C. Kraaikamp, H. P. Lopuhaä, L. E. Meester, A Modern Introduction to Probability and Statistics: Understanding Why and How, Springer Science & Business Media, 2005.

[176] S. Ulam, R. D. Richtmyer, J. von Neumann, Statistical methods in neutron diffusion, Los Alamos National Laboratory 551 (1947) 1–22.

[177] N. Metropolis, S. Ulam, The monte carlo method, Journal of the American statistical association 44 (247) (1949) 335–341. doi:10.1080/01621459.1949.10483310.

[178] G. Henkelman, A. Arnaldsson, H. Jónsson, Theoretical calculations of CH4 and H2 associative desorption from Ni(111): Could subsurface hydrogen play an important role?, The Journal of Chemical Physics 124 (4) (2006) 044706. doi:10.1063/1.2161193.

[179] A. Zobelli, C. P. Ewels, A. Gloter, G. Seifert, Vacancy migration in hexagonal boron nitride, Physical Review B 75 (9) (2007) 094104. doi:10.1103/PhysRevB.75.094104.

[180] W. Von der Linden, V. Dose, U. Von Toussaint, Combinatorics, in: Bayesian Probability Theory: Applications in the Physical Sciences, Cambridge University Press, Chapter 4, 2014, pp. 62–66. doi:10.1017/CBO9781139565608.

[181] Beta test of the Nion Swift Atom Manipulator (video).
Permanent link: https://phaidra.univie.ac.at/o:1586599.

[182] N. CARPi, A. Minges, M. Piel, eLabFTW: An open source laboratory notebook for research labs., J. Open Source Softw. 2 (12) (2017) 146. doi:10.21105/joss.00146.

[183] S. Shabih, A. Postl, Python package "Nion Swift eLabFTW plug-in" (fork).
Permanent link: https://phaidra.univie.ac.at/o:1591066. doi:11353/10.1591066.

Appendix

1. First-authored journal article (peer-reviewed):

   A. Postl, P. P. P. Hilgert, A. Markevich, J. Madsen, K. Mustonen, J. Kotakoski, T. Susi, Indirect measurement of the carbon adatom migration barrier on graphene, Carbon 196 (2022) 596-601. doi:10.1016/j.carbon.2022.05.039

2. Co-authored journal article (peer-reviewed):

   G. Zagler, M. Stecher, A. Trentino, F. Kraft, C. Su, A. Postl, M. Längle, C. Pesenhofer, C. Mangler, E. H. Ahlgren, A. Markevich, A. Zettl, J. Kotakoski, T. Susi, K. Mustonen, Beam-driven dynamics of aluminium dopants in graphene, 2D Materials (2022). doi:10.1088/2053-1583/ac6c30

3. Conference proceedings article

   J. Madsen, A. Postl, T. Susi, Automated Real-time Analysis of Atomic-resolution STEM Images, Microscopy and Microanalysis 25 (S2) (2019) 166–167. doi:10.1017/S1431927619001569

4. Conference proceedings article

   A. Postl, J. Madsen, P. P. P. Hilgert, M. T. Schreiber, J. Kotakoski, T. Susi, Temperature-dependent displacement cross section of graphene and its impurities: measuring the carbon adatom migration barrier, Microscopy and Microanalysis 27 (S1) (2021) 3340–3340. doi:10.1017/S143192762101148X

5. Conference proceedings article

   A. Postl, T. A. Bui, F. Kraft, A. Chirita, G. Leuthner, H. Inani, C. Mangler, K. Mustonen, J. Kotakoski, T. Susi, Adventures in Atomic Resolution in situ STEM, Microscopy and Microanalysis 28 (S1) (2022) 2342-2343. doi:10.1017/S1431927622008996

6. Conference poster

   A. Postl, J. Madsen, P. Hilgert, M. Schreiber, J. Kotakoski, T. Susi, Temperature-dependent displacement cross section of graphene: Measuring the carbon adatom migration barrier, M&M 2021 (Microscopy & Microanalysis Meeting 2021)

Carbon 196 (2022) 596–601

Contents lists available at ScienceDirect

Carbon

journal homepage: www.elsevier.com/locate/carbon

Indirect measurement of the carbon adatom migration barrier on graphene

Andreas Postl [a,b,*], Pit Pascal Patrick Hilgert [a], Alexander Markevich [a], Jacob Madsen [a], Kimmo Mustonen [a], Jani Kotakoski [a], Toma Susi [a,**]

[a] University of Vienna, Faculty of Physics, Boltzmanngasse 5, A-1090, Vienna, Austria
[b] University of Vienna, Vienna Doctoral School in Physics, Boltzmanngasse 5, A-1090, Vienna, Austria

ARTICLE INFO

Keywords:
Surface diffusion
Graphitic surfaces
TEM
DFT

ABSTRACT

Although surface diffusion is critical for many physical and chemical processes, including the epitaxial growth of crystals and heterogeneous catalysis, it is particularly challenging to directly study. Here, we estimate the carbon adatom migration barrier on freestanding monolayer graphene by quantifying its temperature-dependent electron knock-on damage. Due to the fast healing of vacancies by diffusing adatoms, the damage rate decreases with increasing temperature. By analyzing the observed damage rates at 300–1073 K using a model describing our finite scanning probe, we find a barrier of (0.33 ± 0.03) eV.

1. Introduction

Transmission electron microscopy (TEM) allows exposing specimens to electrons impinging with high kinetic energy (typically up to 200–300 keV) and imaging the effects in-situ with atomic resolution. Recent work has established that electron irradiation can be used to sculpt materials [1–5], induce phase transitions [6,7], locally amorphize [8,9] or crystallize [10,11] structures, and even to manipulate individual covalently bound atoms [12–15]. Diffusion processes of fundamental importance have also been directly studied in some materials, although unavoidably these observations have been influenced by the energetic electron beam [16–18].

Understanding the interaction between probe electrons and the sample has become crucial to correctly apply and interpret such experiments [19]. The investigation of irradiation effects in carbon nanostructures has been a field of intense research during the last decades [20–22]. Recently, progress in sample preparation of two-dimensional materials and advances in the theoretical models have, especially in graphene, enabled the quantitative description of so-called knock-on damage resulting from elastic electron-nucleus collisions enhanced by atomic vibrations [23,24], whereas inelastic scattering and its contribution to damage are still harder to describe [19,25]. However, with notable exceptions (albeit not at atomic resolution [26]), thus far the effect of temperature on such processes has been rarely quantified.

In this study, our initial aim was to determine the temperature-dependence of the electron knock-on damage cross section for pristine graphene, which is in the range of 5–20 mb[1] for 90 keV electrons and ^{12}C lattice atoms at ambient temperature [24]. Based on a first-principles model of the cross section, one should expect to observe tremendously increasing knock-on damage rates for elevated temperatures due to the higher population of out-of-plane phonon modes [24] and the thermal perturbation of the lattice [27]. In stark contrast to that prediction, the detected damage rates do not increase with temperature, but rather decrease.

The reason must be thermally activated carbon adatom migration and recombination with defects. This has been directly observed for vacancies and larger holes in graphene [24,28] as well as at its impurity sites [29,30], even at room temperature, and also indirectly studied for carbon nanotubes under electron irradiation [31]. A carbon adatom on top of a graphene layer bonds at a C–C bridge site and has to overcome an energy barrier, estimated to be in the range of 0.40–0.47 eV [32,33], to migrate from one minimum to another. At elevated temperatures, this migration is enhanced, and thus the proportion of vacancies which get healed before they are detected increases with increasing temperature.

Even so, we do observe vacancies all across the investigated temperature range from 300 to 1073 K. Recording the atomic structure surrounding single or double vacancies takes about 0.2 s, which indicates that even at the highest temperature, the vacancy migration must take longer than this. We are able to use the discrepancy between predicted and observed damage rates of electron knock-on damage by

* Corresponding author. University of Vienna, Faculty of Physics, Boltzmanngasse 5, A-1090, Vienna, Austria.
** Corresponding author.
E-mail addresses: andreas.postl@univie.ac.at (A. Postl), toma.susi@univie.ac.at (T. Susi).
[1] abbreviation of "millibarn"; 1 mb = 10^{-31} m^2.

https://doi.org/10.1016/j.carbon.2022.05.039
Received 23 February 2022; Received in revised form 27 April 2022; Accepted 18 May 2022
Available online 23 May 2022

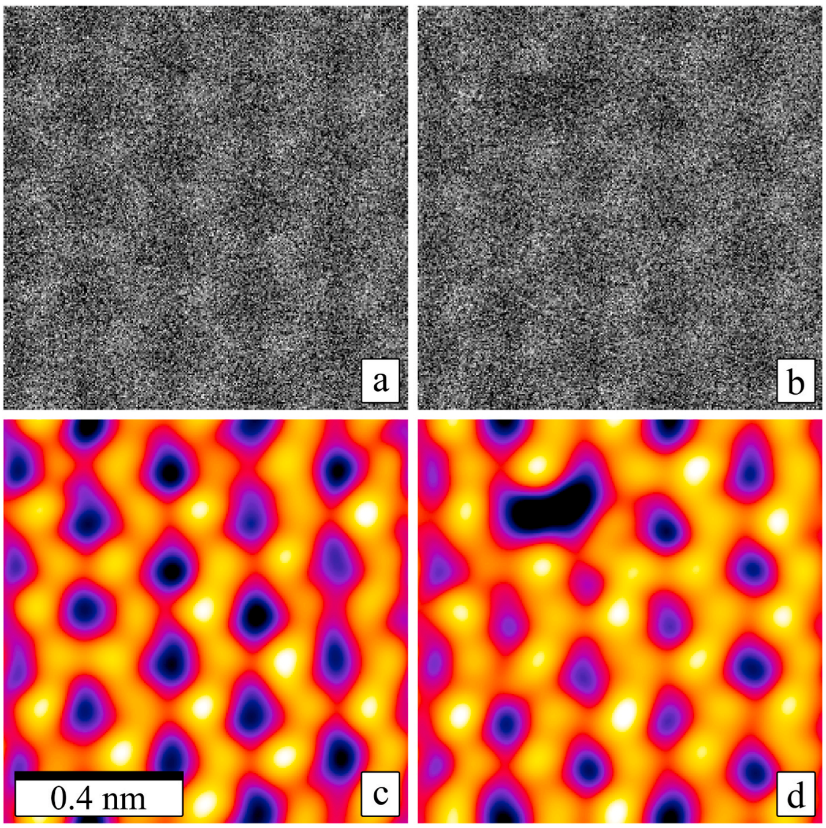

Fig. 1. Raw (a, b) and colored double Gaussian-filtered (c, d) medium-angle ADF-STEM images before (a, c) and after (b, d) a knock-on damage event at 100 °C. Field of view: 1 × 1 nm^2, pixel dwell time: 16 μs, 256 × 256 px. See Fig. 2 (a) for a schematic illustration of the structure. (A colour version of this figure can be viewed online.)

90 keV electrons at elevated temperatures to provide an indirect experimental estimate of the migration barrier. Importantly, we need to account for the fact that the same scanning electron beam both creates and observes the damage to correctly describe the experiments. Our analysis indicates a barrier value of (0.33 ± 0.03) eV (in line with the 0.25 eV estimated inside nanotubes [31]), which is the first measurement for graphene that has been reported to date.

2. Materials and methods

As samples, we used commercial monolayer graphene (Easy Transfer, Graphenea S.A.), which was transferred onto a chip with an electron-transparent window and electrical contacts for resistive heating, and placed in an in-situ TEM holder with an integrated electrical circuit (Fusion, Protochips Inc.). To heat the sample, a current was passed through the heating coil of the chip. The heating power and temperature were controlled based on the manufacturer's per-chip calibration, and the precision of the set temperature was estimated to be ±2%.

All experimental images were acquired using a Nion UltraSTEM 100, a probe-corrected scanning transmission electron microscope (STEM) [34], operated at 90 keV with a probe convergence semi-angle of 30 mrad. Crucially, our objective area pressure is near ultra-high vacuum ($\lesssim 1 \times 10^{-9}$ mbar), which minimizes any spurious effects of chemical etching. The origin of carbon adatoms is either the contamination on the sample or the residual gas in the objective area of the microscope. In our case, the latter appears unlikely due to the near ultra-high vacuum conditions.

The electron beam was scanned across fields of view of roughly 1 × 1 nm^2 or 2 × 2 nm^2, which initially contained pristine graphene and were located away from any surface contamination, and recorded medium-angle annular dark field (MAADF; 60–200 mrad collection semi-angle) image series of consecutive frames.

As illustrated in Fig. 1, we stopped the acquisition whenever we recognized a defect that did not conserve the number of atoms, as opposed to e.g. a Stone-Wales (SW) 5577 defect [35,36]. The frame time was set to as low as possible while retaining atomic resolution and, to enhance contrast, used double-Gaussian filtering [37] of the raw images during acquisition. However, if we found (either during the acquisition or the later analysis) that such an SW 5577 defect was immediately followed by a defect that did not conserve the number of atoms, we excluded that series from any further evaluations, as the local threshold energy for the vacancy creation would not correspond to that of the pristine lattice.

The observed cross section for an individual knock-on event $\sigma_{\mathrm{ko},i}^{\mathrm{obs}}$ was calculated according to $\sigma_{\mathrm{ko},i}^{\mathrm{obs}} = e/(I_{\mathrm{B}} t_{\mathrm{tot},i} \rho_A)$, where e is the elementary charge, I_{B} the beam current, $t_{\mathrm{tot},i}$ the time elapsed until the detection of the atom loss, and ρ_A the areal atomic density of graphene. Repeating this measurement, starting with pristine graphene every time, amounts to observing a homogeneous Poisson process [38], such as in radioactive decay. Thus, the expectation value of the cross section can be estimated with the posterior mean in the context of Bayesian parameter estimation [39]: $\sigma_{\mathrm{ko}}^{\mathrm{obs}} = \sum_{i=1}^{N} \sigma_{\mathrm{ko},i}^{\mathrm{obs}}/(N-1)$ (for detail, see Ref. [40]).

After obtaining sufficient data to perform statistical analyses (60 or more series per temperature and frame acquisition time), we examined

each recorded image series to identify the first frame in which at least one atom was missing (henceforth referred to as defect frame). The total electron count $N_{e^-} = I_B t_{tot}$ up to that point was calculated with the assistance of image metadata and the above-mentioned beam current calibration. For the defect frame itself, we counted half of the frame time and neglected the (x, y) position of the defect in the frame.

To accurately estimate the beam current during imaging, we related it to the current from electrons hitting the virtual objective aperture (VOA) of our STEM, which is recorded when images are taken (for the calibration curve, see Ref. [40]). The beam current as a function of the VOA current was recorded at least every other week when the experiments were conducted.

To estimate the theoretical carbon adatom migration barrier, we performed nudged elastic band calculations using the density functional (DFT) theory package GPAW [41]. We used the finite-difference basis with grid spacing of 0.18 Å, 6 × 6 graphene supercell, 6 × 6 × 1 Monkhorst-Pack **k**-point mesh and convergence criterion of 0.02 eV/Å for the forces. Since the inclusion of dispersion corrections has been shown to influence barrier heights [42,43], we used both the Tkatchenko-Scheffler (TS) [44] van der Waals (vdW) correction on top of the Perdew-Burke-Ernzerhof (PBE) exchange-correlation functional or an explicit treatment of vdW interactions via the C09-vdW functional [45]. Our results show that inclusion of dispersion interactions has little effect on the barrier.

3. Results and discussion

At temperatures up to ~350 K, the recombination rate of carbon adatoms and vacancies is low compared to the rate of further atom loss under irradiation with typical beam currents of 50–100 pA at 90 keV, as indicated by an observed knock-on cross section that is close the theoretical one. At more elevated temperatures, the recombination rate rapidly rises and greatly exceeds even our highest frame acquisition rate at an acceptable signal-to-noise ratio limit, which was about two frames per second (pixel dwell time: 8 µs, 256 × 256 pixels) in our setup (for estimated rates, see Ref. [40]). Thus, graphene samples mainly show increased radiation hardness at elevated temperatures, as has been remarked before [28,46]. However, this effect was not quantified until now. Furthermore, we did not observe a difference with respect to a variation of frame acquisition time from 2 to 0.5 s. Thus, we merged our data for each temperature.

Although it turned out that our measurement cannot be used to calculate the true temperature-dependent knock-on cross section, in the following we use the term "observed cross section" with the symbol σ_{ko}^{obs}. To begin with, we slightly revised the parameters of our knock-on damage cross section model, incorporating our additional 90 keV room-temperature data. Due to possible phonon modeling inaccuracies, we used a parameter uncertainty for the out-of-plane root-mean-square velocity of the nuclei $v_{rms}(T)$ and refitted the threshold energy T_d (for detail, see Ref. [40]). Variance-weighted least squares with a trust region reflective algorithm [47] yielded $T_d = (21.03 \pm 0.10)$ eV with $v_{rms}(300\ \mathrm{K}) = (590 \pm 20)\ \mathrm{ms}^{-1}$.

By assuming that the discrepancy between the experimentally observed $k_{ko}^{obs}(I_B, T)$ and the predicted $k_{ko}^{theor} = (I_B/e)\,\rho_A\,\sigma_{ko}^{theor}$ knock-on damage rates, with I_B being the beam current, e the elementary charge and ρ_A the areal atomic density of graphene, is equal to the healing rate of vacancies $k_h(T)$,

$$k_{ko}^{theor}(I_B, T) - k_{ko}^{obs}(T) = k_h(T), \tag{1}$$

we can state an Arrhenius dependence [48] of the healing rate on the migration energy barrier E_m as

$$k_h(T) \approx^{E_r=0} A \exp\left(-\frac{E_m}{k_B T}\right), \tag{2}$$

where A is the pre-exponential rate constant, T the absolute temperature, k_B the Boltzmann constant, and E_r the energy barrier for the recombination of a vacancy and a carbon adatom in immediate proximity, which we assume to be negligible compared to E_m. This naive treatment yields $E_m = (150 \pm 6)$ meV for the adatom migration barrier (see Ref. [40]). The resulting pre-exponential factor is close to the frame acquisition frequency, which underscores a limitation of the applied measuring method; since we counted only one knock-on event per vacancy irrespective of its size, the maximum observed damage rate would be equal to the frame rate. Eq. (2) would hold if k_{ko}^{theor} were much higher than the healing rate $k_h(T)$. For temperatures above 400 K, however, the observed cross section values are very low ($\lesssim 5$ mb). Despite the fact that the healing of vacancies is on average much faster than knock-on damage for temperatures up to 1073 K, we are occasionally able to observe them, namely if a created vacancy is not healed before it can be observed (for modeled rates, see Ref. [40]).

To correctly describe these observations, we must explicitly account for the nature of the experiment: the images are recorded by a scanning electron probe with a finite current density distribution (Fig. 2). Thus, the time between the creation of a vacancy and its observation depends on where it is created with respect to the probe. This motivates an extension of the reduced healing rate model of Eq. (2) to explicitly account for this probability.

To start with, we redefine the healing rate as a fraction of the theoretical knock-on rate determined by probability $P_h(T)$ for a vacancy to be healed before observation

$$k_{ko}^{theor}(T) k_h(T) = P_h(T), \tag{3}$$

which can be combined with Eq. (1) to obtain a new effective observed damage rate

$$k_{ko}^{obs}(T) = k_{ko}^{theor}(T)(1 - P_h(T)). \tag{4}$$

An accurate description of $P_h(T)$ must contain the involved random variables via their probability distributions. A defect can not be observed if the number of adatom migration steps within a frame time ($n_f(T)$) is greater than the number of steps needed to reach a vacancy to heal it (n_h). Specifically, the healing probability is the value of the complementary cumulative distribution function (tail distribution) of the random variable $Q(T) = n_f(T)/n_h$ at 1. The number of migration steps is normally distributed with a mean of

$$\mu(T) = t_f f_0 \exp\left(-\frac{E_m}{k_B T}\right), \tag{5}$$

where t_f is the frame time, and f_0 the migration attempt frequency ($4 \times 10^{12}\ \mathrm{s}^{-1}$ as reported for carbon interstitials in graphite [49]). The number of surface diffusion steps that N_v adatoms need to reach the immediate proximity of a vacancy with (on average) N_v missing atoms is exponentially distributed with the parameter

$$\nu = -\frac{1}{N_v} \log\left(1 - \frac{2}{3} c_{ad}\right), \tag{6}$$

where c_{ad} is the number of adatoms per lattice atom (adatom concentration), and the prefactor 2/3 accounts for the number of lattice atoms per bond. In our data, the average vacancy size is $N_v = 1.6 \pm 0.2$ (see Ref. [40]).

The tail distribution of the ratio $Q(T)$ can be approximated (see Ref. [40]) by the cumulative distribution function of n_h at the expectation value of $n_f(T)$,

$$P_h(T) = \int_0^{\mu(T)} \nu \exp(-\nu k)\,\mathrm{d}k = 1 - \exp(-\nu \mu(T)), \tag{7}$$

which, together with Eqs. (4)–(6), leads to

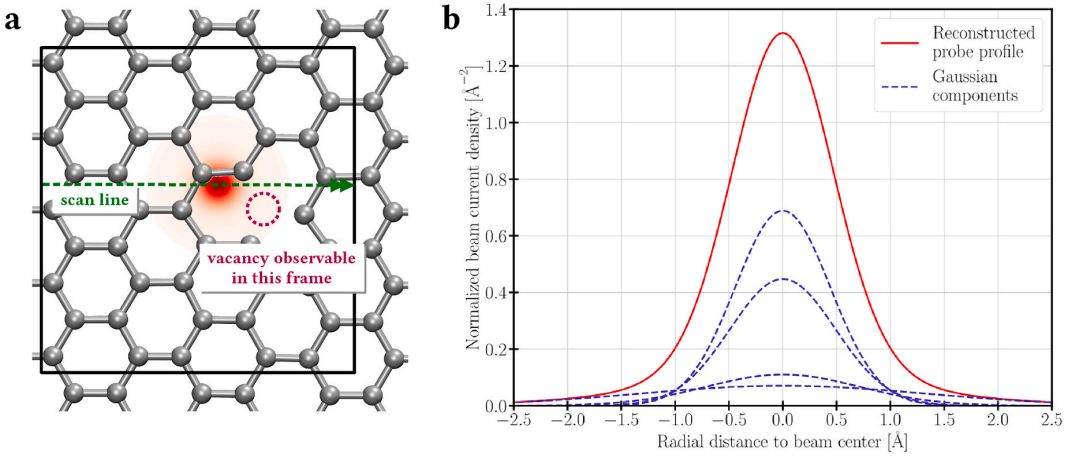

Fig. 2. (a) Schematic illustration of the graphene lattice and a single vacancy (dashed purple circle) created by the "leading" tail of the scanning electron probe and observed within the same scan frame (black rectangle). (b) Radial plot of the beam current density profile fitted by four Gaussian components. (A colour version of this figure can be viewed online.)

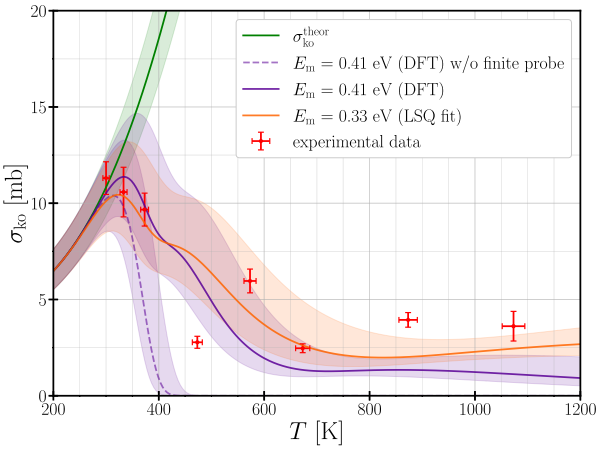

Fig. 3. Knock-on damage cross section as a function of temperature: experimental observations (red points), theoretical model (green line), and an extended model describing the damage rate with counteracting vacancy healing and the effect of a scanning electron probe with a finite extent, resulting in a varying detection time, and the measured shape (orange line for a least-squares fitted migration barrier and purple for the DFT barrier). See the text for description of the underlying adatom concentrations and error estimates. (A colour version of this figure can be viewed online.)

$$k_{ko}^{obs}(T) = k_{ko}^{theor}(T)\left(1-\frac{2}{3}c_{ad}\right)^{\frac{1}{N_V}t_f f_0 \exp\left(\frac{-E_m}{k_B T}\right)}. \quad (8)$$

Eq. (8) can be expressed in terms of cross sections by substituting the theoretical defect formation rate $k_{ko}^{theor} \to \sigma_{ko}^{theor}$ and the defect observation rate $k_{ko}^{obs} \to \sigma_{ko}^{obs}$, which conserves the correct normalization with respect to the beam current, since $k_{ko} = (I_B/e)\rho_A \sigma_{ko}$. At temperatures above 500 K and for typical frame times $t_f \approx 0.5$ s, the healing probability resulting from eq. (7) is close to 1 (Fig. 3), which would imply that despite their increasing creation, no vacancies can be observed.

The remaining crucial missing piece of the model is the movement and the shape of the electron probe, which leads to a statistical distribution of the positions of the created vacancies with respect to the probe position. Depending on this relationship, the time between the creation of a vacancy and its detection varies from just a few pixel dwell times to almost one frame time, with a probability distribution corresponding to the electron probe current density profile. In particular, if the "leading" tail of the electron probe, i.e. the electrons impinging on the sample where the scan has not yet reached, causes the knock-on event, we will almost immediately record the vacancy giving it little chance to heal (Fig. 2). Conversely, if the lattice atom is ejected at a position that the beam center has already crossed by that time, the detection time will be roughly one frame time, and the vacancy very likely has already healed before it can be observed.

Taking into account the electron probe shape based on a beam current density profile $g(x, y)$ determined by optimizing a model of the probe in an image simulation to reproduce the observed image contrast [40] (Fig. 2, approximated by a full width at half maximum of ~ 1.16 Å; note that a simple Gaussian shape leads to qualitatively similar results) and the detection time distribution $t_d(x, y)$ instead of a constant t_f, completes a final elaboration of our model that qualitatively matches our experimental data (see Fig. 3, and [40] for more detail):

$$k_{ko}^{obs}(T) = k_{ko}^{theor}(T)\sum_{x,y}\left(1-\frac{2}{3}c_{ad}\right)^{\frac{1}{N_V}t_d(x,y) f_0 \exp\left(\frac{-E_m}{k_B T}\right)} g(x,y). \quad (9)$$

There are two unknowns in the model, namely the migration barrier E_m and the adatom concentration c_{ad}, the former of which can be estimated via first-principles simulations. The calculated values with spin polarization are 0.44 eV, 0.43 eV, and 0.40 eV for PBE, PBE-TS, and C09-vdW, respectively.

Several choices of model parameters (E_m, c_{ad}) fit our data. In Fig. 3, our extended model is illustrated for migration barrier values of 0.41 (DFT-vdW average, purple curves) and 0.33 eV (weighted nonlinear least-squares fit (LSQ), orange curve), with the latter better describing our experimental observations, especially at higher temperatures. The statistical uncertainty of the LSQ-fitted barrier is 0.03 eV for fixed values of adatom concentration and migration attempt frequency. Temperature-dependent entropic and vibrational contributions to the Gibbs free energy as well as quantum zero-point effects [50] could modify the barrier and thus explain the seeming 25% over-estimation by DFT, but since these strongly depend on the system and diffusion path [51], we cannot estimate their relative magnitude.

Our model has one unfortunate feature: The first-order Taylor expansion of Eq. (8), i.e. $(1-x)^a \approx 1 - ax$, contains the product of adatom concentration c_{ad} and attempt frequency f_0 so that changes in their values are essentially indistinguishable. Whenever one factor is set to a seemingly reasonable value, the other will decrease to an order of

magnitude that seems implausible. For $E_m = 0.33$ eV, an adatom concentration of 10^{-3} nm^{-2} implies an attempt frequency of only 0.8×10^8 s^{-1}, whereas for $f_0 = 4 \times 10^{12}$ s^{-1}, it leads to a very low concentration of $c_{ad} = 2.0 \times 10^{-6}$ nm^{-2}. Either effective adatom concentrations are lower than we expect, or some effects missing from our model are required to explain the discrepancy. In Fig. 3, the values of the product $c_{ad} \times f_0$ are $(0.8 \pm 0.4) \times 10^6$ nm^{-2}s^{-1} for the LSQ fit, and $(0.8 \pm 0.5) \times 10^7$ nm^{-2}s^{-1} for the DFT results. For LSQ at 1073 K, the criterion $\Delta\sigma_{ko}/\sigma_{ko} = 20\%$ was used to estimate the uncertainty of the concentration, and those of the DFT fits were set proportional to the ratios of the weighted residual variances.

4. Conclusions

We have provided the first experimental estimate of the carbon adatom migration barrier on graphene, which not only provides a useful test of widely applied modeling approaches, but also may help improve commonly used graphene growth and heat treatment techniques. Potentially, when combined with the creation and characterization of vacancies [52] and the in-situ deposition of other elements, the presented approach could also be used to estimate migration barriers for other diffusing species [53], though carbon co-diffusion will remain a complicating factor. Further experiments at higher electron energies and temperatures might give insights into additional processes such as the adatom desorption barrier and the limits of the harmonic approximation for the phonon-derived vibrational velocities.

CRediT authorship contribution statement

Andreas Postl: Investigation, Methodology, Visualization, Formal analysis, Software, Writing – original draft, preparation, Writing – review & editing. **Pit Pascal Patrick Hilgert:** Investigation. **Alexander Markevich:** Investigation, Writing – review & editing. **Jacob Madsen:** Software, Investigation, Writing – review & editing. **Kimmo Mustonen:** Supervision. **Jani Kotakoski:** Methodology, Software, Writing – review & editing. **Toma Susi:** Conceptualization, Supervision, Funding acquisition, Writing – original draft, preparation, Writing – review & editing.

Declaration of competing interest

The authors declare that they have no known competing financial interests or personal relationships that could have appeared to influence the work reported in this paper.

Acknowledgements

This work has received funding from the European Research Council (ERC) under the European Union's Horizon 2020 research and innovation programme (Grant agreement No. 756277-ATMEN) and the Vienna Doctoral School in Physics (VDS-P). Computational resources from the Vienna Scientific Cluster (VSC) are gratefully acknowledged.

Appendix A. Supplementary data

Supplementary data to this article can be found online at https://doi.org/10.1016/j.carbon.2022.05.039.

References

[1] J. Lin, O. Cretu, W. Zhou, K. Suenaga, D. Prasai, K.I. Bolotin, N.T. Cuong, M. Otani, S. Okada, A.R. Lupini, J.-C. Idrobo, D. Caudel, A. Burger, N.J. Ghimire, J. Yan, D. G. Mandrus, S.J. Pennycook, S.T. Pantelides, Flexible metallic nanowires with self-adaptive contacts to semiconducting transition-metal dichalcogenide monolayers, Nat. Nanotechnol. 9 (6) (2014) 436–442, https://doi.org/10.1038/nnano.2014.81.

[2] G.H. Ryu, H.J. Park, J. Ryou, J. Park, J. Lee, G. Kim, H.S. Shin, C.W. Bielawski, R. S. Ruoff, S. Hong, Z. Lee, Atomic-scale dynamics of triangular hole growth in monolayer hexagonal boron nitride under electron irradiation, Nanoscale 7 (24) (2015) 10600–10605, https://doi.org/10.1039/C5NR01473E.

[3] S. Wang, H. Li, H. Sawada, C.S. Allen, A.I. Kirkland, J.C. Grossman, J.H. Warner, Atomic structure and formation mechanism of sub-nanometer pores in 2D monolayer MoS2, Nanoscale 9 (19) (2017) 6417–6426, https://doi.org/10.1039/C7NR01127J.

[4] S.M. Gilbert, G. Dunn, A. Azizi, T. Pham, B. Shevitski, E. Dimitrov, S. Liu, S. Aloni, A. Zettl, Fabrication of subnanometer-precision nanopores in hexagonal boron nitride, Sci. Rep. 7 (1) (2017) 15096, https://doi.org/10.1038/s41598-017-12684-x.

[5] N. Clark, L. Nguyen, M.J. Hamer, F. Schedin, E.A. Lewis, E. Prestat, A. Garner, Y. Cao, M. Zhu, R. Kashtiban, J. Sloan, D. Kepaptsoglou, R.V. Gorbachev, S. J. Haigh, Scalable patterning of encapsulated black phosphorus, Nano Lett. 18 (9) (2018) 5373–5381, https://doi.org/10.1021/acs.nanolett.8b00946.

[6] J. Lin, S.T. Pantelides, W. Zhou, Vacancy-induced formation and growth of inversion domains in transition-metal dichalcogenide monolayer, ACS Nano 9 (5) (2015) 5189–5197, https://doi.org/10.1021/acsnano.5b00554.

[7] Z. Liu, Z. Fei, C. Xu, Y. Jiang, X.-L. Ma, H.-M. Cheng, W. Ren, Phase transition and in situ construction of lateral heterostructure of 2D superconducting/Mo2C with sharp interface by electron beam irradiation, Nanoscale 9 (22) (2017) 7501–7507, https://doi.org/10.1039/C7NR01609C.

[8] F. R. Eder, J. Kotakoski, U. Kaiser, J. C. Meyer, A journey from order to disorder — atom by atom transformation from graphene to a 2D carbon glass, Sci. Rep. 4 (Feb. 2014). doi:10.1038/srep04060.

[9] J. Su, X. Zhu, In-situ TEM observation of preferential amorphization in single crystal Si nanowire, Nanotechnology 29 (23) (2018), 235703, https://doi.org/10.1088/1361-6528/aab6eb.

[10] S. Jesse, Q. He, A.R. Lupini, D.N. Leonard, M.P. Oxley, O. Ovchinnikov, R. R. Unocic, A. Tselev, M. Fuentes-Cabrera, B.G. Sumpter, S.J. Pennycook, S. V. Kalinin, A.Y. Borisevich, Atomic-Level sculpting of crystalline oxides: toward bulk nanofabrication with single atomic plane precision, Small 11 (44) (2015) 5895–5900, https://doi.org/10.1002/smll.201502048.

[11] B.C. Bayer, R. Kaindl, M. Reza Ahmadpour Monazam, T. Susi, J. Kotakoski, T. Gupta, D. Eder, W. Waldhauser, J.C. Meyer, Atomic-Scale in situ observations of crystallization and restructuring processes in two-dimensional MoS2 films, ACS Nano 12 (8) (2018) 8758–8769, https://doi.org/10.1021/acsnano.8b04945.

[12] T. Susi, J. Kotakoski, D. Kepaptsoglou, C. Mangler, T.C. Lovejoy, O.L. Krivanek, R. Zan, U. Bangert, P. Ayala, J.C. Meyer, Q. Ramasse, Silicon–carbon bond inversions driven by 60-keV electrons in graphene, Phys. Rev. Lett. 113 (11) (2014), 115501, https://doi.org/10.1103/PhysRevLett.113.115501.

[13] T. Susi, J.C. Meyer, J. Kotakoski, Manipulating low-dimensional materials down to the level of single atoms with electron irradiation, Ultramicroscopy 180 (2017) 163–172, https://doi.org/10.1016/j.ultramic.2017.03.005.

[14] O. Dyck, S. Kim, S.V. Kalinin, S. Jesse, Placing single atoms in graphene with a scanning transmission electron microscope, Appl. Phys. Lett. 111 (11) (2017) 113104, https://doi.org/10.1063/1.4998599.

[15] B.M. Hudak, J. Song, H. Sims, M.C. Troparevsky, T.S. Humble, S.T. Pantelides, P. C. Snijders, A.R. Lupini, Directed atom-by-atom assembly of dopants in silicon, ACS Nano 12 (6) (2018) 5873–5879, https://doi.org/10.1021/acsnano.8b02001.

[16] R. Ishikawa, R. Mishra, A.R. Lupini, S.D. Findlay, T. Taniguchi, S.T. Pantelides, S. J. Pennycook, Direct observation of dopant atom diffusion in a bulk semiconductor crystal enhanced by a large size mismatch, Phys. Rev. Lett. 113 (15) (2014) 155501, https://doi.org/10.1103/PhysRevLett.113.155501.

[17] C. Li, Y.-Y. Zhang, T.J. Pennycook, Y. Wu, A.R. Lupini, N. Paudel, S.T. Pantelides, Y. Yan, S.J. Pennycook, Column-by-column observation of dislocation motion in CdTe: dynamic scanning transmission electron microscopy, Appl. Phys. Lett. 109 (14) (2016) 143107, https://doi.org/10.1063/1.4963765.

[18] T. Furnival, R.K. Leary, E.C. Tyo, S. Vajda, Q.M. Ramasse, J.M. Thomas, P. D. Bristowe, P.A. Midgley, Anomalous diffusion of single metal atoms on a graphene oxide support, Chem. Phys. Lett. 683 (2017) 370–374, https://doi.org/10.1016/j.ultramic.2016.05.005.

[19] T. Susi, J.C. Meyer, J. Kotakoski, Quantifying transmission electron microscopy irradiation effects using two-dimensional materials, Nature Reviews Physics 1 (6) (2019) 397–406, https://doi.org/10.1038/s42254-019-0058-y.

[20] F. Banhart, Irradiation effects in carbon nanostructures, Rep. Prog. Phys. 62 (8) (1999) 1181, https://doi.org/10.1088/0034-4885/62/8/201.

[21] A. Zobelli, A. Gloter, C.P. Ewels, G. Seifert, C. Colliex, Electron knock-on cross section of carbon and boron nitride nanotubes, Phys. Rev. B 75 (24) (2007), 245402, https://doi.org/10.1103/PhysRevB.75.245402.

[22] F. Banhart, J. Kotakoski, A.V. Krasheninnikov, Structural defects in graphene, ACS Nano 5 (1) (2011) 26–41, https://doi.org/10.1021/nn102598m.

[23] J.C. Meyer, F. Eder, S. Kurasch, V. Skakalova, J. Kotakoski, H.J. Park, S. Roth, A. Chuvilin, S. Eyhusen, G. Benner, A.V. Krasheninnikov, U. Kaiser, Accurate measurement of electron beam induced displacement cross sections for single-layer graphene, Phys. Rev. Lett. 108 (19) (2012), 196102, https://doi.org/10.1103/PhysRevLett.108.196102.

[24] T. Susi, C. Hofer, G. Argentero, G.T. Leuthner, T.J. Pennycook, C. Mangler, J. C. Meyer, J. Kotakoski, Isotope analysis in the transmission electron microscope, Nat. Commun. 7 (1) (2016) 13040, https://doi.org/10.1038/ncomms13040.

[25] S. Kretschmer, T. Lehnert, U. Kaiser, A.V. Krasheninnikov, Formation of defects in two-dimensional MoS2 in the transmission electron microscope at electron energies below the knock-on threshold: the role of electronic excitations, Nano Lett. 20 (4) (2020) 2865–2870, https://doi.org/10.1021/acs.nanolett.0c00670.

[26] O. Cretu, Y.-C. Lin, K. Suenaga, Inelastic electron irradiation damage in hexagonal boron nitride, Micron 72 (2015) 21–27, https://doi.org/10.1016/j.micron.2015.02.002.

[27] A.I. Chirita Mihaila, T. Susi, J. Kotakoski, Influence of temperature on the displacement threshold energy in graphene, Sci. Rep. 9 (1) (2019) 12981, https://doi.org/10.1038/s41598-019-49565-4.
[28] R. Zan, Q.M. Ramasse, U. Bangert, K.S. Novoselov, Graphene reknits its holes, Nano Lett. 12 (8) (2012) 3936–3940, https://doi.org/10.1021/nl300985q.
[29] M. Tripathi, A. Markevich, R. Böttger, S. Facsko, E. Besley, J. Kotakoski, T. Susi, Implanting germanium into graphene, ACS Nano 12 (5) (2018) 4641–4647, https://doi.org/10.1021/acsnano.8b01191.
[30] C. Su, M. Tripathi, Q.-B. Yan, Z. Wang, Z. Zhang, C. Hofer, H. Wang, L. Basile, G. Su, M. Dong, J.C. Meyer, J. Kotakoski, J. Kong, J.-C. Idrobo, T. Susi, J. Li, Engineering single-atom dynamics with electron irradiation, Sci. Adv. 5 (5) (2019), https://doi.org/10.1126/sciadv.aav2252 eaav2252.
[31] Y. Gan, J. Kotakoski, A.V. Krasheninnikov, K. Nordlund, F. Banhart, The diffusion of carbon atoms inside carbon nanotubes, New J. Phys. 10 (2) (2008), 023022, https://doi.org/10.1088/1367-2630/10/2/023022.
[32] P.O. Lehtinen, A.S. Foster, A. Ayuela, A. Krasheninnikov, K. Nordlund, R. M. Nieminen, Magnetic properties and diffusion of adatoms on a graphene sheet, Phys. Rev. Lett. 91 (1) (2003), 017202, https://doi.org/10.1103/PhysRevLett.91.017202.
[33] A.V. Krasheninnikov, K. Nordlund, P.O. Lehtinen, A.S. Foster, A. Ayuela, R. M. Nieminen, Adsorption and migration of carbon adatoms on carbon nanotubes: density-functional *ab initio* and tight-binding studies, Phys. Rev. B 69 (7) (2004), 073402, https://doi.org/10.1103/PhysRevB.69.073402.
[34] O.L. Krivanek, T.C. Lovejoy, N. Dellby, R. Carpenter, Monochromated STEM with a 30 meV-wide, atom-sized electron probe, Microscopy 62 (1) (2013) 3–21, https://doi.org/10.1093/jmicro/dfs089.
[35] A.J. Stone, D.J. Wales, Theoretical studies of icosahedral C60 and some related species, Chem. Phys. Lett. 128 (5–6) (1986) 501–503, https://doi.org/10.1016/0009-2614(86)80661-3.
[36] J. Kotakoski, J.C. Meyer, S. Kurasch, D. Santos-Cottin, U. Kaiser, A. V. Krasheninnikov, Stone-Wales-type transformations in carbon nanostructures driven by electron irradiation, Phys. Rev. B 83 (24) (2011), 245420, https://doi.org/10.1103/PhysRevB.83.245420.
[37] O.L. Krivanek, N. Dellby, M.F. Murfitt, M.F. Chisholm, T.J. Pennycook, K. Suenaga, V. Nicolosi, Gentle STEM: ADF imaging and EELS at low primary energies, Ultramicroscopy 110 (8) (2010) 935–945, https://doi.org/10.1016/j.ultramic.2010.02.007.
[38] J.F.C. Kingman, Poisson Processes, vol. 3, Clarendon Press, 1992.
[39] W. Von der Linden, V. Dose, U. Von Toussaint, Bayesian Probability Theory: Applications in the Physical Sciences, Cambridge University Press, 2014.
[40] See Supplemental Material at [url] for details on experimental and theoretical knock-on damage cross sections, arrhenius formalism, extended healing model, adatom concentration, and probe profile determination. Furthermore, Experimental Data and Detailed Documentation of Our Uncertainty Calculation Are Attached. A Supplementary Data Item (Jupyter Notebook) Contains the Code Used to Simulate Our Extended Model.
[41] J. Enkovaara, C. Rostgaard, J.J. Mortensen, J. Chen, M. Dułak, L. Ferrighi, J. Gavnholt, C. Glinsvad, V. Haikola, H. Hansen, others, Electronic structure calculations with GPAW: a real-space implementation of the projector augmented-wave method, J. Phys. Condens. Matter 22 (25) (2010), 253202, https://doi.org/10.1088/0953-8984/22/25/253202.
[42] T.P. Hardcastle, C.R. Seabourne, R. Zan, R.M.D. Brydson, U. Bangert, Q. M. Ramasse, K.S. Novoselov, A.J. Scott, Mobile metal adatoms on single layer, bilayer, and trilayer graphene: an ab initio DFT study with van der Waals corrections correlated with electron microscopy data, Phys. Rev. B 87 (19) (2013), 195430, https://doi.org/10.1103/PhysRevB.87.195430.
[43] S. Thinius, M.M. Islam, P. Heitjans, T. Bredow, Theoretical study of Li migration in lithium–graphite intercalation compounds with dispersion-corrected DFT methods, J. Phys. Chem. C 118 (5) (2014) 2273–2280, https://doi.org/10.1021/jp408945j.
[44] A. Tkatchenko, M. Scheffler, Accurate molecular van der Waals interactions from ground-state electron density and free-atom reference data, Phys. Rev. Lett. 102 (7) (2009), 073005, https://doi.org/10.1103/PhysRevLett.102.073005.
[45] V.R. Cooper, Van der Waals density functional: an appropriate exchange functional, Phys. Rev. B 81 (16) (2010), https://doi.org/10.1103/PhysRevB.81.161104, 161104(R).
[46] B. Song, G.F. Schneider, Q. Xu, G. Pandraud, C. Dekker, H. Zandbergen, Atomic-Scale electron-beam sculpting of near-defect-free graphene nanostructures, Nano Lett. 11 (6) (2011) 2247–2250, https://doi.org/10.1021/nl200369r.
[47] A.R. Conn, N.I. Gould, P.L. Toint, Trust Region Methods, SIAM, 2000.
[48] S. Arrhenius, Über die Reaktionsgeschwindigkeit bei der Inversion von Rohrzucker durch Säuren, Z. Phys. Chem. 4U (1) (1889) 226–248, https://doi.org/10.1515/zpch-1889-0416.
[49] P. Thrower, R. Mayer, Point defects and self-diffusion in graphite, Physica Status Solidi A, Applied Research 47 (1) (1978) 11–37, https://doi.org/10.1002/pssa.2210470102.
[50] G. Henkelman, A. Arnaldsson, H. Jónsson, Theoretical calculations of CH4 and H2 associative desorption from Ni(111): could subsurface hydrogen play an important role? J. Chem. Phys. 124 (4) (2006), 044706 https://doi.org/10.1063/1.2161193.
[51] A. Zobelli, C.P. Ewels, A. Gloter, G. Seifert, Vacancy migration in hexagonal boron nitride, Phys. Rev. B 75 (9) (2007), 094104, https://doi.org/10.1103/PhysRevB.75.094104.
[52] A. Trentino, J. Madsen, A. Mittelberger, C. Mangler, T. Susi, K. Mustonen, J. Kotakoski, Atomic-Level structural engineering of graphene on a mesoscopic scale, Nano Lett. 21 (12) (2021) 5179–5185, https://doi.org/10.1021/acs.nanolett.1c01214.
[53] H. Inani, K. Mustonen, A. Markevich, E.-X. Ding, M. Tripathi, A. Hussain, C. Mangler, E.I. Kauppinen, T. Susi, J. Kotakoski, Silicon substitution in nanotubes and graphene via intermittent vacancies, J. Phys. Chem. C 123 (20) (2019) 13136–13140, https://doi.org/10.1021/acs.jpcc.9b01894.

IOP Publishing 2D Mater. 9 (2022) 035009 https://doi.org/10.1088/2053-1583/ac6c30

2D Materials

OPEN ACCESS

RECEIVED
11 February 2022

REVISED
29 April 2022

ACCEPTED FOR PUBLICATION
3 May 2022

PUBLISHED
19 May 2022

PAPER

Beam-driven dynamics of aluminium dopants in graphene

Georg Zagler[1,5,6], Maximilian Stecher[1,6], Alberto Trentino[1,5], Fabian Kraft[1], Cong Su[2,3,4], Andreas Postl[1,5], Manuel Längle[1,5], Christian Pesenhofer[1], Clemens Mangler[1], E Harriet Åhlgren[1], Alexander Markevich[1], Alex Zettl[2,3,4], Jani Kotakoski[1], Toma Susi[1,*] and Kimmo Mustonen[1,*]

[1] University of Vienna, Faculty of Physics, Boltzmanngasse 5, 1090, Austria
[2] Department of Physics, University of California, Berkeley, CA 94720, United States of America
[3] Materials Sciences Division, Lawrence Berkeley National Laboratory, Berkeley, CA 94720, United States of America
[4] Kavli Energy NanoSciences Institute at the University of California, Berkeley, CA 94720, United States of America
[5] Vienna Doctoral School in Physics, University of Vienna, Boltzmanngasse 5, Vienna 1090, Austria
[6] These authors contributed equally.
[*] Authors to whom any correspondence should be addressed.

E-mail: toma.susi@univie.ac.at **and** kimmo.mustonen@univie.ac.at

Keywords: scanning transmission electron microscopy, atomic dynamics, heteroatom doping

Supplementary material for this article is available online

Abstract

Substituting heteroatoms into graphene can tune its properties for applications ranging from catalysis to spintronics. The further recent discovery that covalent impurities in graphene can be manipulated at atomic precision using a focused electron beam may open avenues towards sub-nanometer device architectures. However, the preparation of clean samples with a high density of dopants is still very challenging. Here, we report vacancy-mediated substitution of aluminium into laser-cleaned graphene, and without removal from our ultra-high vacuum apparatus, study their dynamics under 60 keV electron irradiation using aberration-corrected scanning transmission electron microscopy and spectroscopy. Three- and four-coordinated Al sites are identified, showing excellent agreement with *ab initio* predictions including binding energies and electron energy loss spectrum simulations. We show that the direct exchange of carbon and aluminium atoms predicted earlier occurs under electron irradiation, although unexpectedly it is less probable than the same process for silicon. We also observe a previously unknown nitrogen–aluminium exchange that occurs at Al–N double-dopant sites at graphene divacancies created by our plasma treatment.

1. Introduction

Heteroatom-substituted two-dimensional (2D) materials have generated sustained research interest [1]. Applications in fuel-cells, energy storage devices, sensing, catalysis [2–5] and not least, nanoelectronics [6, 7], have motivated numerous studies of these materials. Graphene with its outstanding electronic properties [8, 9], in particular its high electron mobility [10], stands out as a promising candidate for both smaller and more capable electronic devices [11, 12]. To this end, the electronic structure of monolayer graphene may need to be manipulated to open a bandgap, e.g. by lateral confinement [13, 14] or doping [7, 15, 16].

While graphene doping has been widely studied across the periodic table [17], with the period two neighbors to carbon, N and B, being the most commonly studied dopants [18–20], direct atomic-level evidence for the incorporation of other heteroatomic substitutions is more sparse. Si [21], P [22], Ge [23], O [24, 25], and Au [26] have been conclusively detected in monolayer graphene using atomically resolved electron energy loss spectroscopy (EELS) and/or quantitative image contrast comparisons with simulations. Several other elements, including many transition metals [3, 27, 28], have been identified on the basis of either non-local spectroscopy or chemically-insensitive imaging, although the identity of the substituted atoms was not in every case conclusively proven.

Beyond possible applications, research on dopants in graphene has produced insight into a rich variety of physical phenomena discovered by atomic-level observations. Heteroatoms in graphene are often found in multiple configurations, typically bonding

either to three or four carbon neighbors [21, 29]. Aberration-corrected scanning transmission electron microscopy (STEM) can resolve their atomic configuration [30, 31], and additionally give detailed insight in the chemical structure with EELS [21, 22, 32]. Irradiation with the imaging electrons can, however, also induce dynamic structural changes in graphene [33, 34], including its heteroatom sites [35]. Indeed, utilizing the kinetic energy imparted by electrons, certain heteroatoms in graphene [29, 36, 37], single-walled carbon nanotubes (SWCNTs) [38], and within bulk silicon [39, 40] can be manipulated at atomic precision using the atomically focused STEM electron probe. This has opened new perspectives for engineering materials on the atomic level.

Period 3 elements Al, Si and P are all expected to be stable dopants in graphene [16], and to also show the richest dynamics under electron irradiation [29]. However, although there have been numerous theoretical studies on Al dopants [16, 41–43], their direct experimental detection has so far been limited to a single incidental example that was sputtered during EEL spectrum acquisition [29], and a very recent study using a chemical synthesis route [44]. However, characterization of the electron-beam stability of the Al heteroatom sites as well as their dynamics is still crucially missing, and a complementary physical post-synthesis modification route would be highly desirable.

Here, we report on Al heteroatom substitutions into graphene as well as on their electron-beam induced dynamics under 60 keV electron irradiation. We observe both three- and four-coordinated configurations whose atomically resolved EEL spectrum fine structure matches our first principles simulations. Notably, we first attempted to incorporate Al using low-energy ion implantation with Al^+ energies around 30 eV, but despite exhaustive STEM characterization of multiple samples, could not locate any implanted impurities in the lattice. This was presumably due to excessive surface contamination that was either pre-existing on the surfaces, or was introduced in the merely high-vacuum implantation chamber and/or subsequent ambient transfer. Hence, in our view, direct low-energy ion implantation remains a highly challenging method. We therefore resorted to an intermittent vacancy approach to substitute Al into graphene, which has been used earlier to substitute heavy elements [26, 45], transition metals [28], and silicon [46, 47].

Commercial monolayer graphene supported on TEM grids was first irradiated by Ar ions to create vacancies, after which Al atoms were introduced by physical vapour deposition accompanied by laser heating, substituting them into some of the vacancies. STEM was used to image the dopants and observe their dynamics, and EELS to characterize their bonding. Supporting density functional theory (DFT) simulations were used to confirm the heteroatom bonding configurations and to reveal their three-dimensional structure and energetics: as expected, Al are observed in both three- and four-coordinated configurations, thus bonding to either three or four C neighbours.

As has been previously shown for Si and P heteroatoms [29, 48] in graphene and for Si also in carbon nanotubes [38], electron irradiation of Al dopant sites is expected [29] to result in the direct exchange of Al with one of its C neighbours, facilitating its migration within the graphene lattice without the loss of atoms. Slightly higher kinetic energy transfer from the electrons can lead to C atom ejection, converting a three-coordinated configuration into a four-coordinated one. The threshold energies for these processes for three-coordinated Al substitutions were previously estimated with DFT-based molecular dynamics (MD) simulations by Su *et al* [29], but the direct exchange mechanism was not experimentally confirmed until now. We also observed theoretically predicted [49] Al–N dual-doped configurations for the first time, and found that electron irradiation can also lead to their atomic rearrangement, whose mechanism we explain by DFT/MD simulations.

2. Results and discussion

2.1. Experimental

We prepared suspended graphene monolayers by placing commercially available chemical vapour deposition graphene onto perforated SiN grids, and then dry-deposited SWCNTs onto the graphene to improve mechanical stability [50]. After standard overnight bake, the samples were introduced into our interconnected ultra-high vacuum (UHV) system, where both heteroatom substitution and subsequent STEM and EELS characterization with the Nion UltraSTEM 100 instrument were performed. Hydrocarbon contamination covering the graphene surface (see figure 1(a)) was removed [51] using a high-power-density laser aimed inside the microscope column through a viewport. The resulting cleaned surface (see figure 1(b)) as well as sample transfers in near-UHV ensured that we could achieve large atomically clean areas [47]. For detail, see section 4.

The pre-cleaned sample was transferred to a plasma chamber within the UHV system and exposed to ca. 3×10^{13} cm^{-2} of Ar ions with a mean kinetic energy of ca. 170 eV, at which primarily mono- and divacancy defects are expected to form [52]. The sample was simultaneously irradiated with a laser to elevate its temperature and to mitigate hydrocarbon buildup. The plasma treatment was followed by thermal evaporation of an Al target heated to 955 °C, producing an Al partial pressure of 10^{-8} mbar. The total evaporation time was 20 s, resulting in the

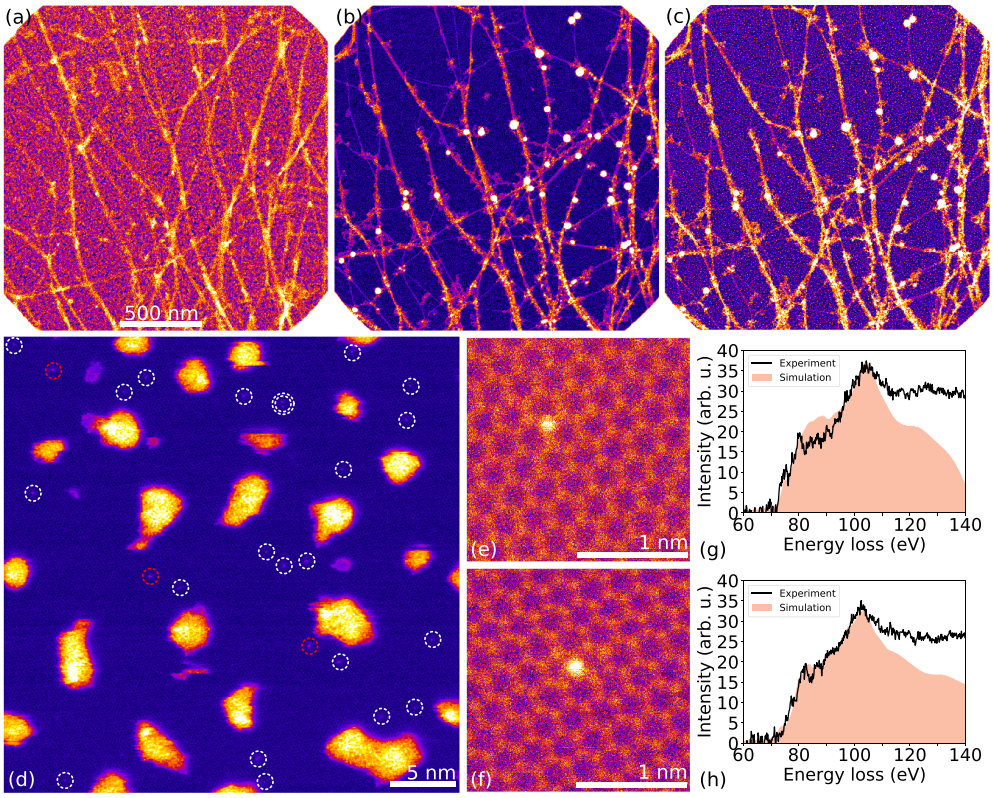

Figure 1. Al dopants substituted into suspended monolayer graphene (STEM/MAADF images and EEL spectra). (a) Overview of the specimen upon introduction to the vacuum system. Free-standing graphene and single-walled carbon nanotubes (SWCNTs, bright linear contrast) on the graphene are coated by hydrocarbon contamination (intermediate speckled areal contrast). (b) After heating with an *in-situ* laser, most contamination is removed from the graphene surface, with some contamination and heavier (bright spherical contrast) clusters remaining at the SWCNTs. (c) After ion irradiation and Al deposition, many small clusters cover the cleaned free-standing graphene (dense bright point contrast). (d) Closer view of the sample after cleaning, plasma irradiation and Al deposition. Bright contrast are nm-sized Al clusters formed after Al deposition. A total of 25 atomic sites (marked with dashed circles) in the graphene are substituted with heteroatoms. Of these, 22 sites (white) show a contrast consistent with either Al or Si heteroatoms, while three sites (red) appear clearly brighter than is expected for Al and are possibly Cu impurities remaining from the original graphene synthesis. (e) Close-up view of an Al heteroatom in a three-coordinated configuration. The corresponding EEL spectrum in (g) showing the Al $L_{2,3}$ core-loss edge (onset 73 eV). A simulated spectrum (solid filled light salmon colored area) shows good agreement with the experimental data (black line). (f) Close-up view image of an Al heteroatom in four-fold configuration. The corresponding EEL spectrum and simulation are shown in (h).

Al coverage observable in figures 1(c) and (d), where single dopants within the graphene lattice can be seen, as well as numerous Al nanoclusters. Although the heteroatom substitution yield was relatively high, roughly two thirds of the substituted heteroatoms were found to be Si instead, again highlighting its chemical affinity for graphene [47].

2.1.1. Aluminium substitutions

As expected based on our own recent experiments on both graphene and SWCNTs [47, 53] and atomistic simulations of Ar irradiation of graphene conducted by others and reported in the literature [52], the Al dopants are mainly found in single and double vacancies, corresponding to three-(Al–C_3) and four-(Al–C_4) coordinated configurations [43] (figures 1(e) and (f)), similar to Si [21, 32], Ge [23], and P [22]. Both configurations were found in roughly equal numbers in the specimens, and their measured EEL spectra are in good agreement with the simulated ones (figures 1(g) and (h); section 4).

The experimentally determined projected Al–C distances were 1.65 ± 0.05 Å (Al–C_3) and 1.96 ± 0.05 Å (Al–C_4), being in an excellent agreement with the distances calculated from relaxed DFT models (section 4), which were 1.65 and 1.95 Å, corresponding to bond lengths of 1.86 and 1.96 Å, respectively. Notably, similar to the previously studied four-coordinated silicon impurity (Si–C_4) [54], the Al–C_4 ground state is slightly non-planar with the bonding C atoms displaced from the plane by ± 0.2 Å, showing signs of tetrahedral bonding [43]. The binding energies of the Al dopants into the sites were similar at −5.95 eV (Al–C_3) and −4.76 eV (Al–C_4).

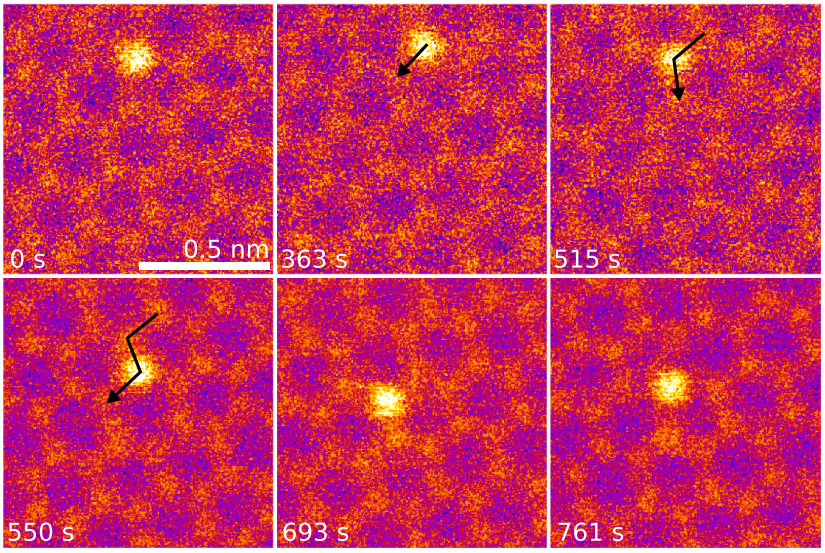

Figure 2. Three Al–C direct exchange steps both preceded and followed by conversion between four- and three-coordinated bonding. STEM/MAADF image frames selected each time a new configuration was observed. The overlaid numbers show the time elapsed since continuous recording of image series began. (**0 s**) Al heteroatom in four-coordinated (Al–C_4) configuration. (**363 s**) The bonding is converted to Al–C_3 by capture of a diffusing C adatom. (**515–693 s**) The Al–C_3 jumps three subsequent times from one lattice site to the next via direct exchanges with subsequent neighbouring C atoms. (**761 s**) The bonding configuration is converted to Al–C_3N by knock-out of a C neighbour; the atom downwards from the Al site is N (see figure 3 below).

Stone-Wales-rotated configurations containing Al were not observed in our experimental data.

2.1.2. Al–C bond inversion

Al dopants exhibit various dynamic processes induced by the 60 keV electron irradiation. In figure 2 after 363 s of continuous observation, an Al heteroatom was converted from a four-coordinated Al–C_4 to a three-coordinated Al–C_3 configuration via the capture of a C adatom into the lattice [48]. In the subsequent frames (363–693 s), the direct exchange (bond inversion) of C and Al was observed three times prior to conversion into Al–C_3-N with neighbouring a N heteroatom (see figure 3 below). For Si and P heteroatoms, migration and controlled manipulation has been demonstrated at the same electron energy [29, 34, 46]: carbon neighbours of these heteroatoms can swap atomic position with them. In this dynamical beam-induced process, an elastic momentum transfer from a single probe electron to a C atom causes it to nearly eject from the lattice, but during its upwards trajectory, the heteroatom relaxes into the created transient vacancy and the ejected atom is recaptured into the lattice at the heteroatom's original position [48].

In a more recent study [29], direct exchange was also predicted for Al–C_3 at 60 keV, with a notably lower range of threshold energies (between 13.4 and 15.7 eV) than was found for P (15.1–16.3 eV) or silicon (14.3–17.6 eV). Considering that at our beam energy, the lowest end of these energies should dominate the cross section of any elastic scattering process limited by momentum-conservation [55], we expected Al impurities to be highly mobile under electron irradiation. Instead, we found that of the seven Al–C_3 sites we observed at atomic resolution for extended periods of time (at least 5 min), only the heteroatom shown in figure 2 migrated within the lattice. Notably, this occurred at significantly higher irradiation doses than has been previously reported for P or Si [29] (for example, Si could be expected to have jumped dozens of times during the ∼13 min series covered by the figure). The ejection of a C neighbor was observed five times, but twice the resulting Al–C_4 site healed back to Al–C_3. Further studies collecting statistically robust data at multiple primary beam energies beyond our scope here will need to be performed to understand this discrepancy.

2.1.3. Aluminium–nitrogen substitutions

Aluminium, with its three valence electrons, could be expected to form strong covalent bonds with nitrogen, which has five. Al–N co-doping has been theoretically considered, and was proposed to stabilize the three-coordinated Al site [49] forming an Al–C_2N configuration (with one of the three C neighbors being substituted by N). Indeed, N co-dopants, presumably sputtered from the SiN TEM-grids during the Ar plasma irradiation, are occasionally found at Al sites in our samples, creating not only previously considered three-coordinated but also four-coordinated Al–C_3N configurations.

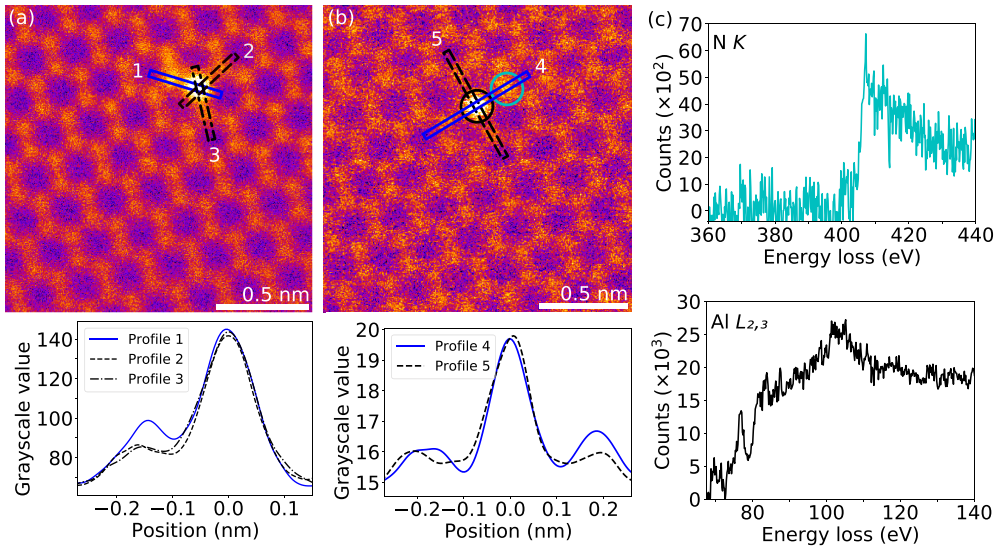

Figure 3. Al–N double-dopants in three-(Al–C_2N) and four-coordinated (Al–C_3N) configurations in the graphene lattice (STEM/MAADF images and EEL spectra). (a) Al bound to three neighbouring atoms. Line profiles of the intensity (along lines marked 1, 2 and 3) are plotted underneath after applying a low-pass filter. The atom on the top-left side of Al in profile 1 shows a higher intensity compared to the two other neighbors, consistent with a N heteroatom. (b) Al bound to four neighbouring atoms. Line profiles of the intensity (along lines marked 4 and 5) are plotted underneath after applying a low-pass filter. The atom on the top-right side of Al in profile 4 shows a higher intensity than the other neighbors, again consistent with a N heteroatom. (c) EEL spectrum (turquoise line) of the N atom encircled in turquoise in (b) with characteristic N *K* core-loss edge onset at ca. 400 eV. EEL spectrum (black line) of the central Al atom encircled in black in (b), showing an Al $L_{2,3}$ core-loss edge onset at 73 eV.

Analysis of our experimental image intensities (figure 3) reveals that Al dopants in both three- and four-coordinated configurations can have one neighbouring atom with a higher-than-carbon MAADF intensity, i.e. an element with a higher atomic number [56]. These atoms were confirmed as N using EELS, with a characteristic *K*-edge core-loss spectrum of N recorded from a Al–C_2N site shown in figure 3(c).

The experimentally determined projected Al–N distances were 1.51 ± 0.06 Å (Al–C_2N) and 1.94 ± 0.08 Å (Al–C_3N), slightly shorter than those calculated from relaxed DFT models (1.58 and 1.98 Å, corresponding to bond lengths of 1.81 and 1.98 Å, respectively). Notably, the projected Al–N distance in the three-coordinated Al–C_2N site is more than 0.1 Å longer than the Al–C distance despite only a 0.05 Å difference in the bond length, indicative of the out-of-plane distortion of the site, while in the nearly atomically flat four-coordinated site, the differences are negligible. In contrast to the purely carbon-containing Al–C_4 site, the out-of-plane displacement of the C bonding atoms in the Al–C_3N site are present only one the side of the defect that does not contain N. The binding energies of the Al dopants into the nitrogen-containing sites were −4.88 eV (Al–C_2N) and −7.13 eV (Al–C_3N), and thus while N co-doping is energetically somewhat unfavorable for the three-coordinated configuration (+1.1 eV), it is found to stabilize the four-coordinated site by as much as −2.4 eV.

2.1.4. N–Al bond inversion

We also observed non-destructive dynamics for Al–C_3N: during imaging, the Al–N bond rotates, as shown in figures 4(a)–(c). We could find only one single-step process that can explain the observed outcome, which was confirmed by our DFT/MD simulations (see figures 4(d)–(h)): energy is imparted from a probe electrons to the N atom, displacing it out of the plane so that it subsequently passes over the Al atom while remaining bound to it, followed by the Al relaxing into the vacancy left by the N. A configuration that is by symmetry equivalent to the starting point is thus reached, but the site has rotated and shifted. A similar process has been predicted for the Fe–C_4 defect [57]. In our experiment, the site changed back into its original configuration (figure 4(c)) after several seconds of further irradiation.

In the DFT/MD simulation shown in figures 4(d)–(h), this process was modelled by imparting a kinetic energy of 16.5 eV on the N atom with the initial momentum vector having a polar angle of 20 degrees from the out-of-plane *z* axis and an azimuthal angle of 20 degrees from the *x* axis (aligned along the armchair lattice direction of graphene). The same outcome was achieved also for azimuthal angles of 10 and 45 degrees, but could notably not be found in our simulations for the Al–C_4 site, which does not contain nitrogen. Although the required kinetic energy exceeds the maximum transferable energy from a 60 keV electron in the static approximation of the elastic knock-on process,

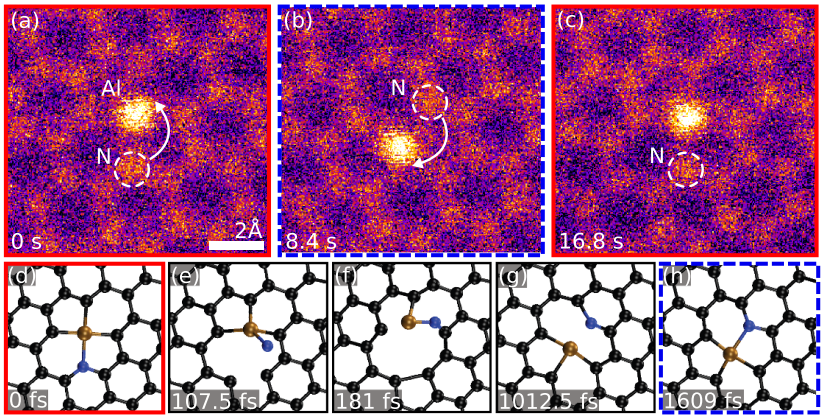

Figure 4. Rotation of the Al–C_3N site (STEM/MAADF images and DFT/MD snapshots). (a) Initial configuration. The arrow marks the movement of the N atom from the first frame (a) to the second (b). The model images below (d)–(f) show the structure with C (black), N (blue) and Al (brown) atoms. In the second frame (b), the Al has moved downwards, while the N is now upwards from it. The structure still comprises of two pentagons and two hexagons, with no atoms lost, but Al and N are bound to different C atoms apart for the left-side neighbour of Al. The arrow marks the change with respect to the next frame (c), where the site is back to its initial configuration. (d) Relaxed atomic model of Al–C_3N corresponding to (a). (e) Transfer of 16.5 eV of kinetic energy at a slight angle with respect to the plane normal displaces the N after 108 fs, rotating it out of the plane over the Al. (f) After 181 fs the N, still bound to the Al, also binds to a C upwards from the Al. (g) The Al relaxes after 1012 fs into a configuration where it is bound to three C, while the N is momentarily bound to only two C after the Al has shifted. (h) After 1609 fs, the Al–N bond is reestablished. This configuration corresponds to the intermediate frame in (b), after which the process can (by symmetry) reverse with a new electron impact and restore the configuration to the original one (frame in (c) and model in (d)).

lattice vibrations can increase this energy [58, 59] and electronic excitations may in turn lower the threshold [60, 61].

2.2. Discussion

Notably, knock-out events of the Al heteroatom itself were rare in our experiments, limited to a single one from an Al–C_2N configuration. Taking into account the total accumulated dose on all imaged Al dopants (which had several distinct local environments, so that this rough estimate should be strictly taken as an upper bound), this results in a displacement cross-section of 10^{-3} barn. Further, unlike has been observed for Si [38], Ge [23] and P [29], we did not observe any instances of Al being replaced by C during our experiments.

We expect that grain boundaries are highly reactive, and thus both creation of vacancies and incorporation of Al atoms is enhanced there. However, they are also typically covered by contamination that is particularly difficult to remove, and we did not purposefully try to find any in our specimen. The dynamical processes under electron irradiation very likely would not take place in the same way if the local lattice configuration is not perfectly hexagonal.

Our study is complementary to the recent work of Ullah *et al* [44], though there are notable differences. Although potentially easier to scale up, their chemical synthesis route necessitates the transfer of the sample from the Cu growth substrate, while our post-synthesis physical route can be applied to any free-standing graphene sample. However, they were able to achieve a higher concentration of Al, and we did not observe defects with multiple dopants. On the other hand, they detected a high concentration of oxygen in their samples, including oxidized Al nanoparticle byproducts, whereas our samples have never been exposed to ambient and our Al nanoparticles are correspondingly completely metallic (as confirmed by EELS).

Finally, although Ullah *et al* [44] certainly did substitute Al into the graphene lattice, their EEL spectra were not collected on single atoms and thus cannot spectrally distinguish different local Al–C coordinations. Further, comparing our atomically resolved spectra (figures 1(g) and (h)) with their areal acquisition, we believe that some of the shown spectral response is due to Si impurities, which their chemically insensitive high-resolution TEM imaging cannot differentiate from Al (indeed, this is challenging even with annular dark-field STEM). Thus, our results are complementary to theirs and the availability of both synthesis routes is a welcome development that is set to open up Al-doped graphene to a broad range of studies.

3. Conclusion

We substituted Al dopants into free-standing graphene via intermittent mono- and divacancies created using argon ions and filling these with aluminium from physical vapour deposition. The substituted sites were observed without ambient exposure using atomically resolved imaging and spectroscopy.

The Al were found in three- and four-coordinated configurations, bound either to three or four C atoms, but occasionally also to N dopants. Different configurations of Al dopants and Al–N dopant-pairs showed dynamical behaviour induced by the electron irradiation at a 60 keV primary beam energy. The theoretically predicted direct exchange process that has been found to enable atomically precise atom manipulation of covalently bound impurities was experimentally confirmed also for three-coordinated Al dopants, but was found to be clearly slower than expected from earlier simulations. Electron irradiation of four-coordinated Al–N double-heteroatom sites was observed to lead to a new kind of non-destructive dynamical process where the Al site rotates around one C neighbor due to beam-induced out-of-plane dynamics of the N. Our findings thus increase the tools at our disposal for engineering the properties of graphene at the atomic scale.

4. Materials and methods

4.1. Sample preparation

A monolayer graphene sample was prepared from commercially available CVD-grown graphene (Graphenea 'Easy Transfer'). The graphene, covered with a sacrificial polymer layer and originally 1 × 1 cm^2 in size, was cut with a surgical blade into a size slightly larger than the TEM grid. This was floated in a beaker filled with deionized water, and then fished out onto a perforated SiN TEM grid (Ted Pella, hole diameter of 2.5 μm) held with tweezers. After transfer, the sample was baked overnight under 10 mbar Ar/H^2 atmosphere (95/5 molar ratio) at 450 °C to remove the polymer layer, leaving regions of free-standing graphene. SWCNTs were dry-deposited on the graphene surface to reduce mechanical oscillations emerging in ultra-clean samples [50]. The sample was baked overnight in vacuum at nominal 180 °C temperature prior to introducing it into the interconnected near-UHV system (base pressure 10^{-8} mbar), where heteroatom substitution and characterization were undertaken.

4.2. Heteroatom substitution

The surface of the free-standing graphene was cleaned [51] on a μm-scale from ubiquitous hydrocarbon contamination using a *in-situ* laser diode-pumped solid-state laser (473 nm, Cobolt Blues™ 25, Cobolt AB) with added focusing optics (750 μs laser pulse, power 25 mW and spot size ca. 560 μm^2). Amorphous contamination was thereby either evaporated or accumulated at reactive areas, such as around the graphene-SWCNT interface. The pre-cleaned specimen was then transferred in near-UHV to a chamber containing a plasma generator and a diode heating laser [51].

Low-energy Ar^+ ions from the plasma generator with a current of 16.5 nA (exposure time 300 s) and anode and extractor voltages both at 0 V were used to irradiate the graphene. The measured ion energy for these parameters is approximately normally distributed with a mean of ca. 170 eV and a standard deviation of ca. 30 eV. The ion irradiation corresponds to a dose equivalent to ca. 3×10^{13} cm^{-2}. During the Ar plasma irradiation, the sample was simultaneously irradiated with ca. 100 mW of laser power spread to a spot size of ca. 0.3 × 1.5 mm^2 to elevate its temperature and to mitigate hydrocarbon buildup.

The plasma treatment was followed by thermal evaporation of an Al target (evaporation slug, 99.999%, Sigma-Aldrich) heated to 955 °C, producing an Al partial pressure of 10^{-8} mbar (the chamber base pressure was 5×10^{-10} mbar). The total evaporation time was 20 s, resulting in ∼5 nm diameter Al clusters covering large portions of the specimen, as well as single Al dopants in the graphene lattice.

4.3. Microscopy and spectroscopy

STEM medium-angle annular dark-field (MAADF) images were acquired with a Nion UltraSTEM 100 (probe convergence semiangle 30 mrad, detector semiangular range 60–200 mrad). EELS was carried out in the same instrument with a Gatan PEELS 666 spectrometer fitted with an Andor iXon 897 electron-multiplying charge-coupled device camera [22]. To estimate the beam current, we calibrated the current of electrons impinging on the virtual objective aperture, which is recorded when images are taken, against the beam current measured on the drift tube of the EELS. We used a 60 keV primary beam energy with a beam current of ca. 50 pA.

4.4. Density functional theory

DFT simulations were carried out with the grid-based projector-augmented wave (GPAW) software package [62] using the Perdew–Burke–Ernzerhof (PBE) functional [63]. Each site was placed in a 6 × 6 hexagonal supercell of graphene with periodic boundary conditions (10 Å of vacuum in the perpendicular direction between the images) and a 5 × 5 × 1 **k**-point mesh, and both the cells and the atomic structures were relaxed [64] until maximum Hellman-Feynman forces were below 0.02 eV $Å^{-1}$. The simulation scripts can be found as Supplementary Materials (available online at stacks.iop.org/TDM/9/035009/mmedia).

For the structural optimization and energetics, a plane-wave basis with a cutoff energy of 500 eV was used. Binding energies of the Al dopants were estimated by comparing the total energies of the relaxed structures to equivalent configurations where the Al atom was removed and the structure relaxed. In GPAW, the total energy of an isolated atom in vacuum is by definition zero, and thus this energy difference corresponds to the energy gained by the system when the Al atom is bound to the defect.

To further study the electron-beam-induced dynamics of the sites, MD simulations were conducted with a *dzp*-basis in the LCAO mode [65] with a grid spacing of 0.2 Å. A Velocity-Verlet timestep of 0.5 fs and a total simulation time of 1.5 ps were used. Each run started from an initial kinetic energy kick assigned to a selected atom whose magnitude was increased until a threshold energy value was found as a change in the atomic arrangement during the trajectory (as described in detail in previous work [48, 66]), and whose direction was optionally varied from the perpendicular direction [67].

EEL spectra of the Al substitutions were simulated with the CASTEP package [68] based on DFT with pseudopotentials generated on-the-fly. The structures were re-optimized using the PBE functional with a plane-wave cutoff energy of 500 eV and $3 \times 3 \times 1$ **k**-point mesh until the forces on the atoms were below 0.04 eV $Å^{-1}$. The single-atom EELS simulation of the $L_{2,3}$ response covers the transitions from the $2p$ core state of Al to 3204 unoccupied bands of the crystal without an explicit core hole included [69]. The final spectrum was broadened by the OptaDOS package [70] with adaptive broadening [71] using 1.0 eV Gaussian and 1.3 eV Lorentzian components.

Data availability statement

Open data, including scanning transmission electron microscopy image series and density functional theory relaxed structures and molecular dynamics trajectories, can be obtained from the University of Vienna repository Phaidra (https://doi.org/10.25365/phaidra.334).

Acknowledgments

Funding through the Austrian Science Fund (FWF) within projects P-31605 and M2595 and the European Research Council (ERC) under the European Union's Horizon 2020 research and innovation programme (Grant No. 756277-ATMEN) is gratefully acknowledged, as well as computational resources by the Vienna Scientific Cluster (VSC). This work was also supported in part by the Director, Office of Science, Office of Basic Energy Sciences, Materials Sciences and Engineering Division, of the US Department of Energy under Contract No. DE-AC02-05-CH1123, within the van der Waals Heterostructures Program (KCWF16), which provided for the EELS simulation. C S acknowledges National Institutes of Health (NIH S10OD023532) for providing the computational resources in the Molecular Graphics and Computation Facility of University of California at Berkeley, and the financial support of a Kavli Energy NanoScience Institute Heising-Simons Postdoctoral Fellowship. We further thank Ulrich Kentsch for experimental assistance.

Conflict of interest

The authors declare no conflicts of interest.

ORCID iDs

Georg Zagler https://orcid.org/0000-0002-2355-6189
Maximilian Stecher https://orcid.org/0000-0002-9933-5622
Alberto Trentino https://orcid.org/0000-0003-0229-3313
Manuel Längle https://orcid.org/0000-0002-4126-4059
E Harriet Åhlgren https://orcid.org/0000-0002-3876-8547
Jani Kotakoski https://orcid.org/0000-0002-1301-5266
Toma Susi https://orcid.org/0000-0003-2513-573X
Kimmo Mustonen https://orcid.org/0000-0002-0953-7299

References

[1] Zhu H, Gan X, McCreary A, Lv R, Lin Z and Terrones M 2020 *Nano Today* **30** 100829
[2] Dai J, Yuan J and Giannozzi P 2009 *Appl. Phys. Lett.* **95** 8–11
[3] Qiu H J, Ito Y, Cong W, Tan Y, Liu P, Hirata A, Fujita T, Tang Z and Chen M 2015 *Angew. Chem., Int. Ed.* **54** 14031–5
[4] Wu Z S, Ren W, Xu L, Li F and Cheng H M 2011 *ACS Nano* **5** 5463–71
[5] Jiang K *et al* 2018 *Energy Environ. Sci.* **11** 893–903
[6] Frisenda R, Molina-Mendoza A J, Mueller T, Castellanos-Gomez A and van der Zant H S 2018 *Chem. Soc. Rev.* **47** 3339–58
[7] Joucken F, Henrard L and Lagoute J 2019 *Phys. Rev. Mater.* **3** 110301
[8] Novoselov K S, Geim A K, Morozov S V, Jiang D, Zhang Y, Dubonos S V, Grigorieva I V and Firsov A A 2004 *Science* **306** 666–9
[9] Novoselov K S, Jiang Z, Zhang Y, Morozov S V, Stormer H L, Zeitler U, Maan J C, Boebinger G S, Kim P and Geim A K 2007 *Science* **315** 1379–1379
[10] Bolotin K, Sikes K, Jiang Z, Klima M, Fudenberg G, Hone J, Kim P and Stormer H 2008 *Solid State Commun.* **146** 351–5
[11] Farmer D B, Lin Y M, Afzali-Ardakani A and Avouris P 2009 *Appl. Phys. Lett.* **94** 213106
[12] Ferrari A C *et al* 2015 *Nanoscale* **7** 4598–810
[13] Han M Y, Özyilmaz B, Zhang Y and Kim P 2007 *Phys. Rev. Lett.* **98** 206805
[14] Stampfer C *et al* 2011 *Front. Phys.* **6** 271–93
[15] Wei D, Liu Y, Wang Y, Zhang H, Huang L and Yu G 2009 *Nano Lett.* **9** 1752–8
[16] Denis P A 2010 *Chem. Phys. Lett.* **492** 251–7
[17] Wang X, Sun G, Routh P, Kim D H, Huang W and Chen P 2014 *Chem. Soc. Rev.* **43** 7067–98
[18] Lv R *et al* 2012 *Sci. Rep.* **2** 586
[19] Zhao L *et al* 2013 *Nano Lett.* **13** 4659–65
[20] Bangert U, Pierce W, Kepaptsoglou D M, Ramasse Q, Zan R, Gass M H, Van den Berg J A, Boothroyd C B, Amani J and Hofsäss H 2013 *Nano Lett.* **13** 4902–7
[21] Ramasse Q M, Seabourne C R, Kepaptsoglou D M, Zan R, Bangert U and Scott A J 2013 *Nano Lett.* **13** 4989–95

[22] Susi T, Hardcastle T P, Hofsäss H, Mittelberger A, Pennycook T J, Mangler C, Drummond-Brydson R, Scott A J, Meyer J C and Kotakoski J 2017 *2D Mater.* **4** 021013
[23] Tripathi M, Markevich A, Böttger R, Facsko S, Besley E, Kotakoski J and Susi T 2018 *ACS Nano* **12** 4641–7
[24] Hofer C, Skákalová V, Haas J, Wang X, Braun K, Pennington R S and Meyer J C 2021 *Ultramicroscopy* **227** 113292
[25] Mackenzie D M A *et al* 2021 *2D Mater.* **8** 045035
[26] Trentino A, Mizohata K, Zagler G, Längle M, Mustonen K, Susi T, Kotakoski J and Åhlgren E H 2022 *2D Mater.* **9** 025011
[27] Lin P C *et al* 2021 *ACS Nano* **15** 5449–58
[28] Dyck O, Zhang L, Yoon M, Swett J L, Hensley D, Zhang C, Rack P D, Fowlkes J D, Lupini A R and Jesse S 2021 *Carbon* **173** 205–14
[29] Su C *et al* 2019 *Sci. Adv.* **5** eaav2252
[30] Xu R *et al* 2015 *Nat. Mater.* **14** 1099–103
[31] Hofer C, Skákalová V, Görlich T, Tripathi M, Mittelberger A, Mangler C, Monazam M R A, Susi T, Kotakoski J and Meyer J C 2019 *Nat. Commun.* **10** 4570
[32] Zhou W, Lee J, Nanda J, Pantelides S T, Pennycook S J and Idrobo J C 2012 *Nat. Nanotechnol.* **7** 161–5
[33] Kotakoski J, Krasheninnikov A V, Kaiser U and Meyer J C 2011 *Phys. Rev. Lett.* **106** 105505
[34] Susi T, Meyer J and Kotakoski J 2017 *Ultramicroscopy* **180** 163–72
[35] Susi T *et al* 2014 *Phys. Rev. Lett.* **113** 1–5
[36] Tripathi M, Mittelberger A, Pike N A, Mangler C, Meyer J C, Verstraete M J, Kotakoski J and Susi T 2018 *Nano Lett.* **18** 5319–23
[37] Dyck O, Kim S, Jimenez-Izal E, Alexandrova A N, Kalinin S V and Jesse S 2018 *Small* **14** 1801771
[38] Mustonen K, Markevich A, Tripathi M, Inani H, Ding E X, Hussain A, Mangler C, Kauppinen E I, Kotakoski J and Susi T 2019 *Adv. Funct. Mater.* **29** 1901327
[39] Hudak B M, Song J, Sims H, Troparevsky M C, Humble T S, Pantelides S T, Snijders P C and Lupini A R 2018 *ACS Nano* **12** 5873–9
[40] Markevich A, Hudak B M, Madsen J, Song J, Snijders P C, Lupini A R and Susi T 2021 *J. Phys. Chem.* C **125** 16041–8
[41] Ao Z M, Yang J, Li S and Jiang Q 2008 *Chem. Phys. Lett.* **461** 276–9
[42] Dai J, Yuan J and Giannozzi P 2009 *Appl. Phys. Lett.* **95** 232105
[43] Tsetseris L, Wang B and Pantelides S T 2014 *Phys. Rev.* B **89** 035411
[44] Ullah S *et al* 2022 *Nano Res.* **15** 1310–8
[45] Wang H *et al* 2012 *Nano Lett.* **12** 141–4
[46] Dyck O, Kim S, Kalinin S V and Jesse S 2017 *Appl. Phys. Lett.* **111** 113104
[47] Inani H, Mustonen K, Markevich A, Ding E X, Tripathi M, Hussain A, Mangler C, Kauppinen E I, Susi T and Kotakoski J 2019 *J. Phys. Chem.* C **123** 13136–40
[48] Susi T *et al* 2014 *Phys. Rev. Lett.* **113** 115501
[49] Denis P A, Pereyra Huelmo C and Martins A 2016 *J. Phys. Chem.* C **120** 7103–12
[50] Mustonen K *et al* 2018 *ACS Nano* **12** 8512–9
[51] Tripathi M, Mittelberger A, Mustonen K, Mangler C, Kotakoski J, Meyer J C and Susi T 2017 *Phys. Status Solidi RRL* **11** 1700124
[52] Lehtinen O, Kotakoski J, Krasheninnikov A V, Tolvanen A, Nordlund K and Keinonen J 2010 *Phys. Rev. B* **81** 153401
[53] Trentino A, Madsen J, Mittelberger A, Mangler C, Susi T, Mustonen K and Kotakoski J 2021 *Nano Lett.* **21** 5179–85
[54] Nieman R, Aquino A J A, Hardcastle T P, Kotakoski J, Susi T and Lischka H 2017 *J. Chem. Phys.* **147** 194702
[55] Susi T, Meyer J C and Kotakoski J 2019 *Nat. Rev. Phys.* **1** 397–405
[56] Krivanek O L *et al* 2010 *Nature* **464** 571–4
[57] Markevich A V, Baldoni M, Warner J H, Kirkland A I and Besley E 2016 *J. Phys. Chem.* C **120** 21998–2003
[58] Meyer J C *et al* 2012 *Phys. Rev. Lett.* **108** 196102
[59] Susi T, Hofer C, Argentero G, Leuthner G T, Pennycook T J, Mangler C, Meyer J C and Kotakoski J 2016 *Nat. Commun.* **7** 13040
[60] Susi T, Kepaptsoglou D, Lin Y C, Ramasse Q, Meyer J C, Suenaga K and Kotakoski J 2017 *2D Mater.* **4** 042004
[61] Lingerfelt D B, Ganesh P, Jakowski J and Sumpter B G 2019 *Adv. Funct. Mater.* **29** 1901901
[62] Enkovaara J *et al* 2010 *J. Phys. Condens. Matter* **22** 253202
[63] Perdew J P, Burke K and Ernzerhof M 1996 *Phys. Rev. Lett.* **77** 3865–8
[64] Tadmor E B, Smith G S, Bernstein N and Kaxiras E 1999 *Phys. Rev.* B **59** 235–45
[65] Larsen A H, Vanin M, Mortensen J J, Thygesen K S and Jacobsen K W 2009 *Phys. Rev.* B **80** 195112
[66] Susi T *et al* 2012 *ACS Nano* **6** 8837–46
[67] Zobelli A, Gloter A, Ewels C P, Seifert G and Colliex C 2007 *Phys. Rev.* B **75** 245402
[68] Clark S J, Segall M D, Pickard C J, Hasnip P J, Probert M I J, Refson K and Payne M C 2005 *Z. Kristallogr.* **220** 567–70
[69] Hardcastle T P, Seabourne C R, Kepaptsoglou D M, Susi T, Nicholls R J, Brydson R M D, Scott A J and Ramasse Q M 2017 *J. Phys.: Condens. Matter.* **29** 225303
[70] Morris A J, Nicholls R J, Pickard C J and Yates J R 2012 *J. Phys.: Conf. Ser.* **371** 012062
[71] Yates J R, Wang X, Vanderbilt D and Souza I 2007 *Phys. Rev.* B **75** 195121

doi:10.1017/S1431927619001569
Microsc. Microanal. 25 (Suppl 2), 2019

Automated Real-time Analysis of Atomic-resolution STEM Images

Jacob Madsen[1*], Andreas Postl[1] and Toma Susi[1]

[1.] Faculty of Physics, University of Vienna, Vienna, Austria.
* Corresponding author: jacob.madsen@univie.ac.at

Understanding the microstructural characteristics of materials, such as lattice defects, increasingly relies on the analysis of large numbers of images from electron and scanning probe microscopy [1]. It is now becoming routine to record series of atomic-resolution images, resulting in the generation of massive datasets. The new challenge is then analysing this data. The workflow for such analyses typically comprises the identification of atomic positions and subsequent derivation of physical quantities, such as defect concentration and strain. Conventionally, this analysis is done manually, which is slow and laborious, and the results are prone to human errors and bias.

We demonstrate an automatic method for extracting information from atomically resolved images. We take advantage of GPU acceleration and fast graph-based algorithms to enable real-time structural analysis. The method is capable of extracting high-level information such as defect type, lattice orientation and strain, as well as characteristics of the electron probe. Our method is based on two algorithms, building on recent advances in deep-learning and on computational geometry and graph theory.

The deep learning recognition model is similar to recently published results [2, 3]. A neural network is trained to identify the smallest distinguishable repeated substructures within the image, i.e. atoms or atomic columns of a particular species. We take advantage of the recent finding that deep neural networks trained using simulated data can generalise to experimental data [2]. Furthermore, by using randomisation in the generation of the synthetic images, the neural network is capable of making predictions with minimal prior assumptions of the types of defects present. Fig. 1 shows the results of the neural network applied to a noisy image of graphene with a silicon substitutional defect. A simple routine converts the predictions of the neural network to a set of 2D points representing the centres of the detected substructures, each point associated with a substructure class. We further explore the precision of the detected atom locations and their sensitivity to the imaging parameters including noise.

The geometric relationship between these points encodes further information, for example, whether the substitutional silicon atom in graphene has three or four carbon neighbours. To facilitate fast geometric analysis, we create a geometric graph from the detected points. It is crucial that the graph is stable to small perturbations of the atomic positions. We identified a type of geometric graph, called a stable Delaunay graph [4], fulfilling this criterion while being fast to construct for large numbers of points. Using simple rules localised segments of the graph can be extracted representing an atom and its surrounding neighbourhood. Each segment of the graph is compared to a library of known graph templates, representing, for example, different defect types. The similarity between a segment and a template is calculated using the symmetry invariant root-mean-squared-deviation [5]. After identifying the best matching template, further geometric analysis can be performed, such as calculating the strain.

The algorithm is invariant to scale and rotations, and effectively parameterless for a given set of structures, allowing it to operate without user input. Fig. 2 illustrates the algorithm applied to a set of points

representing a grain boundary in graphene. In this example, the algorithm identifies the individual grains by their orientation and distinguishes between different types of defects along the grain boundary.
We have implemented the method in the open source microscope control software Nion Swift [6], allowing the user to overlay the results on top of the images as they are recorded, thus providing easily understandable feedback, from which the human operator can adjust the characterisations in response. Furthermore, in an effort to enable large-scale atom manipulation [7], we are working towards an increasingly self-driving microscope, where the output of the present method is used to guide the microscope to make the necessary actions, e.g. move the scan frame or the probe position, similar to the way a self-driving car would adjust the steering wheel upon encountering an obstacle on the road [8].
References:
[1] S Pennycook and P Nellist, Scanning Transmission Electron Microscopy (Springer, New York).
[2] J Madsen et al., Advanced Theory and Simulations **1** (2018), p. 1800037.
[3] M Ziatdinov et al., ACS Nano **11** (2017), p. 12742.
[4] P Agarwal et al., Discrete Computational Geometry **54** (2015), p. 905.
[5] I Kufareva and R Abagyan, Methods in Molecular Biology **857** (2012), p. 231.
[6] C Meyer et al., Proceedings of Microscopy and Microanalysis **20** (2014), p. 1108.
[7] M Tripathi et al., Nano Letters **18** (2018), p. 5319.
[8] The work was supported by the European Research Council (ERC) Grant No. 756277-ATMEN.

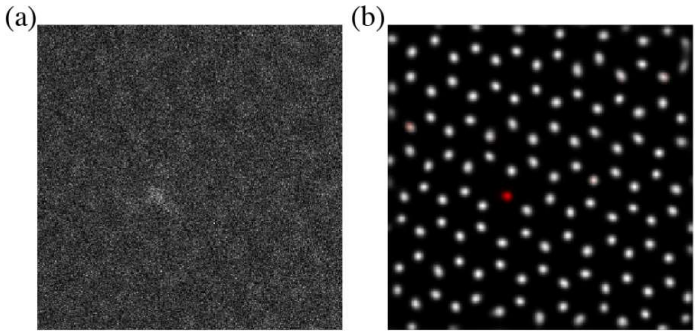

Figure 1. (a) Noisy STEM/MAADF image of graphene with a substitutional silicon defect. (b) Corresponding output of our deep learning recognition model. The white and red areas indicate positions of high likelihood for finding a carbon and a silicon atom, respectively.

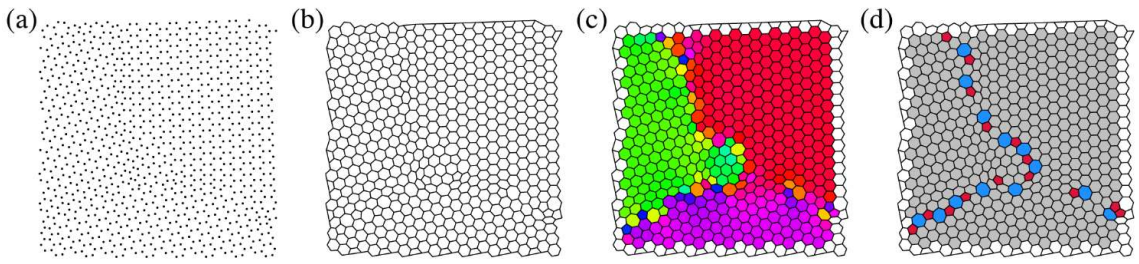

Figure 2. (a) A set of points representing the atomic positions at a grain boundary in graphene. (b) The stable Delaunay graph of the points. (c) The carbon rings of the graphene sheet are color-coded according to the orientation, assisting easy identification of different grains. (d) The carbon rings of the graphene sheet are color-coded according to their number of members. Further graph-based analysis can be used to automatically identify for example Stone-Wales defects.

https://doi.org/10.1017/S1431927619001569 Published online by Cambridge University Press

doi:10.1017/S143192762101148X
Microsc. Microanal. 27 (Suppl 1), 2021

Temperature-dependent displacement cross section of graphene and its impurities: measuring the carbon adatom migration barrier

Andreas Postl[1], Jacob Madsen[2], Pit Pascal Patrick Hilgert[2], Makoto Tokoro Schreiber[3], Jani Kotakoski[4] and Toma Susi[5]

[1]Faculty of Physics & VDS Physics, University of Vienna, Vienna, Austria, Vienna, Wien, Austria, [2]Faculty of Physics, University of Vienna, Vienna, Austria, United States, [3]Okinawa Institute of Science and Technology Graduate University (OIST), Japan, Japan, [4]Faculty of Physics, University of Vienna, Vienna, Austria, Vienna, Wien, Austria, [5]Faculty of Physics, University of Vienna, Vienna, Austria, Vienna, Austria

Surface diffusion is crucial for many physical and chemical processes, including epitaxial growth of crystals and heterogeneous catalysis. Although the phenomenon is common [1] and theoretically understood, measuring adatom migration barriers on 2D materials remains a daunting challenge. We are able to estimate the carbon adatom migration barrier on freestanding monolayer graphene, which has theoretically been predicted to be in the range of 350–500 meV [2,3], by quantifying the temperature dependence of its electron knock-on damage.

To measure damage and healing rates as accurately as possible, we use 90 keV electrons and choose the fastest possible time for image acquisition with our aberration-corrected scanning transmission electron microscope. Contrary to expectations, the damage rate decreases with increasing temperature, which is due to the fast healing of vacancies by recombination with diffusing adatoms. By comparing the predicted and observed damage rates at 300–1073 K we find a barrier of 140 meV, which is the first measurement reported to date.

We further measured the cross sections of electron-driven processes involving single silicon and phosphorus dopants in graphene at elevated temperatures. To aid in the analysis of our image series, we turned to automated structure recognition based on convolutional neural networks. By utilizing deep learning [4|, we quantified for the first time the direct exchange of carbon neighbors with the dopant in the lattice (so-called bond inversion) [5,6], the replacement of the dopants by carbon adatoms, which has emerged as a hindrance to their manipulation, and knock-on damage of a carbon neighbor, which transforms the sites from threefold to fourfold coordination, as a function of sample temperature.

We gratefully acknowledge funding from the European Research Council (ERC) under the European Unions Horizon 2020 research and innovation program (Grant agreement no. 756277-ATMEN) and the Vienna Doctoral School in Physics.

References

[1] R. Zan et al., Nano Letters 12 (2021) 3936–3940.
[2] A. V. Krasheninnikov et al., Physical Review B 69 (2004) 073402.
[3] P. O. Lehtinen et al., Physical Review Letters 91 (2003) 017202.
[4] Madsen, J. et al., Microscopy and Microanalysis 25(S2) (2019) 166-167.
[5] M. Tripathi et al., Nano Letters 18 (2018) 5319–5323.
[6] C. Su et al., Science Advances 5 (2019) eaav2252.

2342
doi:10.1017/S1431927622008996
Microsc. Microanal. 28 (Suppl 1), 2022

Adventures in Atomic Resolution *in situ* STEM

Andreas Postl[1], Thuy An Bui[1], Fabian Kraft[1], Alexandru Chirita[1], Gregor Leuthner[1], Heena Inani[1], Clemens Mangler[1], Kimmo Mustonen[1], Jani Kotakoski[1] and Toma Susi[1*]

[1.] University of Vienna, Faculty of Physics, Vienna, Austria.
* Corresponding author: toma.susi@univie.ac.at

Advances in transmission electron microscopy have enabled an increasing range of *in situ* experiments to study the effects of external perturbations including heating, electrical biasing, and controlled residual vacuum on a range of different samples. Although some trade-offs in imaging resolution and sample stability may be inevitable, with advanced instrumentation it is in many cases possible to conduct such experiments while retaining atomic resolution. *In situ* approaches make it relatively easy to obtain atomically clean surfaces, but can also reveal surprising effects from the residual vacuum composition as well as the thermal diffusion of surface adatoms.

The NionUltraSTEM 100 microscope in Vienna has been modified to enable a wide range of *in situ* experiments without compromising its excellent imaging capabilities [1]. These customizations include a viewport with a line of sight to the sample, which has allowed us to aim a laser at the specimen sitting in the column via telescope optics. This makes it possible to effectively remove amorphous carbon contamination by heating [2] as well as to mitigate mobile contamination that occasionally builds up under the beam. The laser can be precisely aligned to irradiate a ca. 560 μm^2 spot of the sample at the optical axis, minimizing thermal drift and localizing heating to the area of interest.

In terms of sample chemistry, the ultra-high vacuum (UHV) base pressure ensures that no unwanted chemical interactions can influence precise quantitative measurements of electron irradiation effects [3], revealing for example that pristine hexagonal boron nitride is remarkably stable at electron acceleration voltages below 80 keV. Further, a gas line connected into the column at the sample stage via a leak valve allows experiments at controlled atmospheres up to 10^{-6} mbar to be conducted without affecting imaging. These have revealed that oxygen is the active gas for the etching of pores in graphene, and that its armchair edges are indeed more stable than zigzag when chemical etching is not active [4].

Finally, heating experiments can be performed either using a Protochips heating insert in the standard Nion electrical cartridge, or via electrical biasing using conducting leads contacted with the sample. Using the latter, Joule heating of graphene-MoS_2 heterostructures up to estimated temperatures exceeding 2000 K has allowed us to observe the structural transformation of 2D MoS_2 into separated 3D nanocrystals of hexagonal shapes with the 2H and hybrid polytypes [5].

On the other hand, heating a monolayer graphene sample deposited on a SiN chip to temperatures between 300–1073 K using resistive heating with the Protochips Fusion chip remarkably increases its radiation hardness against otherwise damaging 90 keV irradiation [6]. This has further allowed us to estimate the carbon adatom migration barrier by quantifying how electron knock-on damage is reduced at elevated temperatures due to adatom migration and the healing of vacancies [7].

References:

[1] MT Hotz, GJ Corbin, N Dellby, OL Krivanek, C Mangler, JC Meyer, Microscopy and Microanalysis **22** Supplement S3 (2016), p. 34–35. doi: 10.1017/S1431927616001021
[2] M Tripathi, A Mittelberger, K Mustonen, C Mangler, J Kotakoski, JC Meyer, T Susi, Physica Status Solidi RRL 11 (2017), 1700124. doi:10.1002/pssr.201700124
[3] T Susi, JC Meyer, J Kotakoski, Nature Reviews Physics **1** (2019), 635. doi: 10.1038/s42254-019-0096-5
[4] GT Leuthner, T Susi, C Mangler, JC Meyer, J Kotakoski, 2D Materials **8** (2021), 035023. doi:10.1088/2053-1583/abf624
[5] H Inani, DH Shin, J Madsen, HJ Jeong, MH Kwon, N McEvoy, T Susi, C Mangler, SW Lee, K Mustonen, J Kotakoski, Advanced Functional Materials **31** (2021), 2008395. doi:10.1002/adfm.202008395
[6] T Susi, C Hofer, G Argentero, GT Leuthner, TJ Pennycook, C Mangler, JC Meyer, J Kotakoski, Nature Communications **7** (2016), 13040. doi:10.1038/ncomms13040
[7] A Postl, PPP Hilgert, A Markevich, J Madsen, K Mustonen, J Kotakoski, T Susi, arXiv (2022). https://arxiv.org/abs/2202.04485
[8] The authors acknowledge funding by the European Research Council (ERC) under the European Union’s Horizon 2020 research and innovation programme (Grant agreement No. 756277-ATMEN).

https://doi.org/10.1017/S1431927622008996 Published online by Cambridge University Press

Temperature-dependent displacement cross section of graphene: Measuring the carbon adatom migration barrier

A. Postl[1,2], J. Madsen[1], P. Hilgert[1], M. Schreiber[3], J. Kotakoski[1], T. Susi[1]

1 Faculty of Physics, University of Vienna, Vienna, Austria
2 Vienna Doctoral School in Physics, University of Vienna, Vienna, Austria
3 Okinawa Institute of Science and Technology Graduate University (OIST), Okinawa, Japan

Contact: andreas.postl@univie.ac.at, https://physnano.univie.ac.at/research/susi-group/

Surface diffusion

Crucial aspect of epitaxial growth of crystals, heterogeneous catalysis, ...

Phenomenon is common and theoretically understood [1]. State-of-the-art modeling predicts the carbon adatom migration barrier barrier to be in the range of 350-500 meV.

Measuring adatom migration energy barriers on 2D materials?

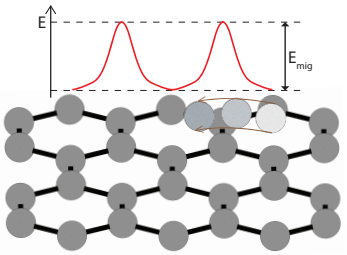

Method

Recording of subsequent STEM images and, thereby, capturing images right before a knock-on damage event and "immediately" afterwards.

Cross section analysis of this Poisson process, and the conception of observed knock-on damage event rates as the difference between competing reactions.

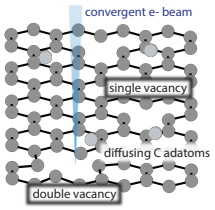

Under the assumption that vacancy healing is governed by surface migration (rather than by the recombination of vacancies with carbon adatoms):

$k_{ko}^{obs} \underset{(E_{mig} \gg E_t)}{\approx} k_{ko}^{theor} - A \exp(-E_{mig}/(k_B T))$, $k_{ko} = N_{ko}/t_{tot}$, N_{ko} ... knock-on count

Knock-on damage vs. **vacancy healing**

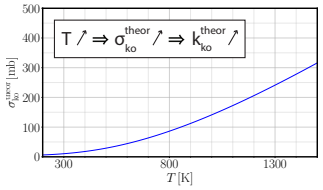

Figure 1: Theoretically predicted knock-on cross section of graphene for incident 90 keV electrons as a function of temperature (DFT-based molecular dynamics simulation) [4]

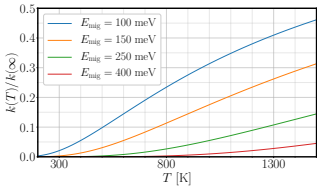

Figure 2: Temperature dependence of migration rates (normalized w.r.t. the rates at infinite temperature) for different energy barriers E_{mig}

Results

The observed damage rate instead decreases with increasing temperature, which must be due to the fast healing of vacancies by recombination with diffusing carbon adatoms.

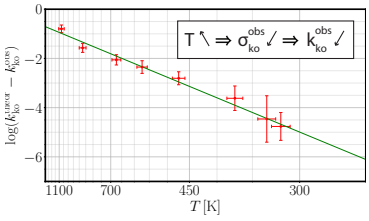

Figure 4: Arrhenius diagram; Semilogarithmic plot of the discrepancy between theoretically predicted and observed knock-on damage rates vs. inverse temperature

We compare predicted with observed damage rates at 300–1073 K and find an energy barrier of

(144 ± 12) meV for **carbon adatom migration**.

Take-Home Message

By quantifying the temperature dependence of its electron knock-on damage, we are able to experimentally estimate the C adatom migration barrier on freestanding monolayer graphene.

Albeit our estimated value is unexpectedly low, this is the first-ever reported measurement.

Experimental challenges

High accuracy for event rates required
⇒ Lowest possible frame acquisition times
⇒ Live image filtering needed for defect recognition

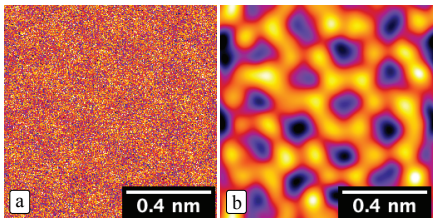

Figure 3: MAADF-STEM image of a 1 x 1 nm² section of monolayer graphene with a single vacancy (upper left corner). The frame acquisition time was 0.52 seconds. (a) Raw data, (b) double Gaussian blur

Sufficient count of knock-on events (per temperature point)
⇒ Moderate damage rates needed
⇒ 90 keV STEM electrons

We gratefully acknowledge funding from the European Research Council (ERC) under the European Unions Horizon 2020 research and innovation program (Grant agreement no. 756277-ATMEN) and the Vienna Doctoral School in Physics.

[1] R. Zan et al., Nano Letters 12 (2021) 3936–3940
[2] A. V. Krasheninnikov et al., Physical Review B 69 (2004) 073402
[3] P. O. Lehtinen et al., Physical Review Letters 91 (2003) 017202
[4] T. Susi et al., Nature communications 7(2016) 13040